Electronic conduction in linear quantum systems: Coherent transport and the effects of decoherence

Von der Fakultät für Physik
der Universität Duisburg-Essen
zur Erlangung des Grades
Dr. rer. nat.
genehmigte Dissertation
von

Matías Zilly
aus Mülheim an der Ruhr

Tag der Disputation: 16.04.2010
Referent: Prof. Dr. Dietrich E. Wolf
Korreferent: Prof. Dr. Juan Carlos Cuevas

Für María Belén

Abstract. Coherent quantum transport in linear and quasi-linear tight-binding models and the influence of decoherence are studied. For the coherent transport description, Green functions and surface Green functions of semi-infinite systems are calculated and the transmission through defects and finite tight-binding chains with and without diagonal disorder are examined. A statistical model based on the division of a large system into coherent subsystems and decoherence regions is analyzed. While on the total system level, classical rate equations interrelate electron energy distribution functions assigned to the decoherence regions, the transition rates themselves are calculated using quantum transport formalism. Thus a two-scale approach is used. For contact Fermi energies within the tight-binding band of the system without disorder, ohmic large scale behavior is observed for any finite density of decoherence regions. If the Fermi energy is outside the band, and for disordered systems, critical decoherence densities are defined. Above the critical densities, material-specific resistivities can be defined. Applying the statistical model for the effects of decoherence on DNA double strands, experimental findings for base-sequence dependent conductance are reproduced.

Contents

Abstract **v**

1 Introduction and Outline **1**

2 Quantum Transport **5**

2.1 Introduction 5
  2.1.1 The spectral function A 6
  2.1.2 The Green functions G and G^{+} 6
  2.1.3 The Green function and the total density of states (DOS) 6
  2.1.4 The correlation function G^{n} 7
2.2 Open quantum-mechanical systems: Σ, Γ, and ρ 7
2.3 Transport formulae 9
2.4 Properties of the Green function 12
  2.4.1 The Lehmann or spectral representation 12
  2.4.2 The Dyson equation 12
  2.4.3 The Kramers-Kronig relations for the Green function 13

3 Coherent Transport in Linear Systems **15**

3.1 The infinite linear tight-binding chain 15
3.2 The half-infinite linear chain 17
  3.2.1 Surface Green function of the half-infinite chain 17
  3.2.2 An alternative way of calculation: direct back-transformation 20
3.3 Transmission through a single defect 20
  3.3.1 Symmetrical coupling to left and right contact 20
  3.3.2 Different couplings to left and right contact 23
3.4 The alternating chain 24
3.5 The double chain 25
  3.5.1 Hamiltonian and its diagonalization 25
  3.5.2 Surface Green function of the half-infinite double chain 27
3.6 The triple chain 32
3.7 The n-tuple chain and the 2d tight-binding grid 32
  3.7.1 Surface Green functions for n-tuple chains 33
  3.7.2 Transmission through defects: symmetry effects 35
3.8 The DNA chain 41
  3.8.1 DNA-chain bands 41
  3.8.2 DNA surface Green function 42
3.9 Transmission of a finite chain 42
  3.9.1 The wide-band limit contact 44
  3.9.2 Transmission of the finite chain without disorder: periodicity in length and tunneling 44

3.9.3 Transmission of the finite chain with onsite disorder: localization . . 52
3.10 Conclusions 54

4 Statistical Model for the Effects of Decoherence on Electron Transport 57
4.1 Büttiker probes 58
4.2 Our approach for modelling the effects of decoherence 59
4.2.1 Decoherence regions 60
4.2.2 Phase coherence length 60
4.2.3 The decoherence regions as reservoirs: our η parameter 61
4.2.4 The rate-equations 61
4.2.5 The statistical approach 63
4.3 Application of the model to a linear tight-binding system 63
4.3.1 Model for the decoherence regions: decoherence sites and parameter η 63
4.3.2 Model for contacts and contact coupling 64
4.3.3 The decoherence length: parameter p 64
4.3.4 The effective channels and their transmissions 64
4.3.5 Rate equations 65
4.3.6 Results for the ordered chain 67
4.3.7 Results for a linear chain with onsite disorder 82
4.4 Conclusions and outlook 87

5 Model for Decoherence Effects Applied on DNA Double Strands 91
5.1 Structure of DNA double strands 91
5.2 Electronic properties of DNA 93
5.2.1 Direct measurements of conductance of DNA double strands 93
5.2.2 Tight-binding models for DNA 94
5.2.3 The extended ladder model 96
5.3 Application of the decoherence model for DNA double strands 97
5.3.1 Decoherence region 1 97
5.3.2 Decoherence region 2 99
5.3.3 Decoherence region 3 100
5.3.4 Contact model 1 101
5.3.5 Contact model 2 101
5.3.6 Contact model 3 101
5.3.7 Conductance calculations for different base sequences 102
5.4 Conclusions and outlook 105

6 Conclusions and Outlook 107

7 Summary 109

A Recommended Literature 111
A.1 Solid state physics 111
A.2 Green functions and many-particle physics 112
A.3 Nanostructures and nanoparticles 112
A.4 Mesoscopic physics 112
A.5 Quantum transport 112
A.6 Biochemistry 113

B Green functions in transport theory **115**
B.1 Definition and basic properties of time-independent Green functions 115
B.2 Non-equilibrium Green functions: the Keldysh formalism 117
B.2.1 Perturbation theory in equilibrium 117
B.2.2 Perturbation theory in non-equilibrium 123
B.2.3 Properties of the Keldysh Green functions 125
B.2.4 Derivation of the current formula 126

C Derivation of equations (4.48) and (4.49) **129**

Bibliography **133**

Zusammenfassung **145**

Danksagung **147**

Erklärung **149**

Lebenslauf **151**

1 Introduction and Outline

Nanotechnology has become one of the most active research fields in the last years. The vision and goal to design, build, and control devices and new materials on the nanometer scale for use in computation, engineering, and medicine is the driving force and inspiration for scientists all around the world.

At the University Duisburg-Essen, nanoparticles are one of the central research fields.[1] From gas-phase synthesis, experimental and theoretical characterization to application: Nanoparticles have been studied from many points of view.[2]

One of the recent milestones is the realization of a light-emitting device made of ZnO nanoparticles [142], see Figure 1.1.

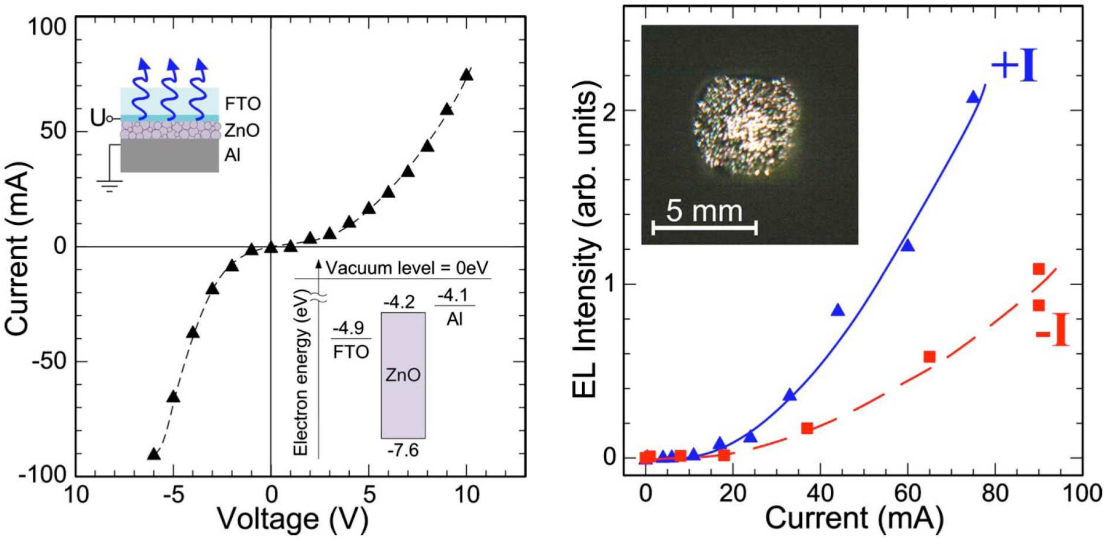

(a) I-V characteristic

(b) electroluminescence

Figure 1.1: Figures 2 and 3 of [142]. A light-emitting device made of ZnO nanoparticles. The upper inset in (a) shows the schematic of the device. The inset in (b) is a photograph of the device at a voltage of +8V.

A dc current driven through the powder of ZnO nanoparticles causes light emission. For a deeper understanding of the processes taking place in the light-emitting device, an electron transport theory for a nanoparticulate system is necessary. This theory can be approached from the points of view of quantum transport [53, 54, 58, 141], mesoscopic physics [3, 86], hopping conduction [26], and percolation theory [169, 177]. Also the relation to theory and experiment of quantum dots, Coulomb blockade, and Mott variable-range hopping has to be considered.[3] For metallic nanoparticle systems, there exists already a theoretical approach [16].

---

[1] For an overview of nanotechnology-related activities at the University, see the website of the Center for Nanointegration Duisburg-Essen, www.cenide.de.

[2] For results, see the publication list on the web-page of SFB 445: sfb445.uni-due.de.

The present thesis deals with linear and quasi-linear systems. As a rough approximation they can be seen as line representatives of the 3d nanoparticle system between two parallel 2d electrodes, where the diameter of the quasi-linear system corresponds to the phase coherence length in the medium. Yet also linear systems of nanoparticles have been realized, see Figure 1.2.

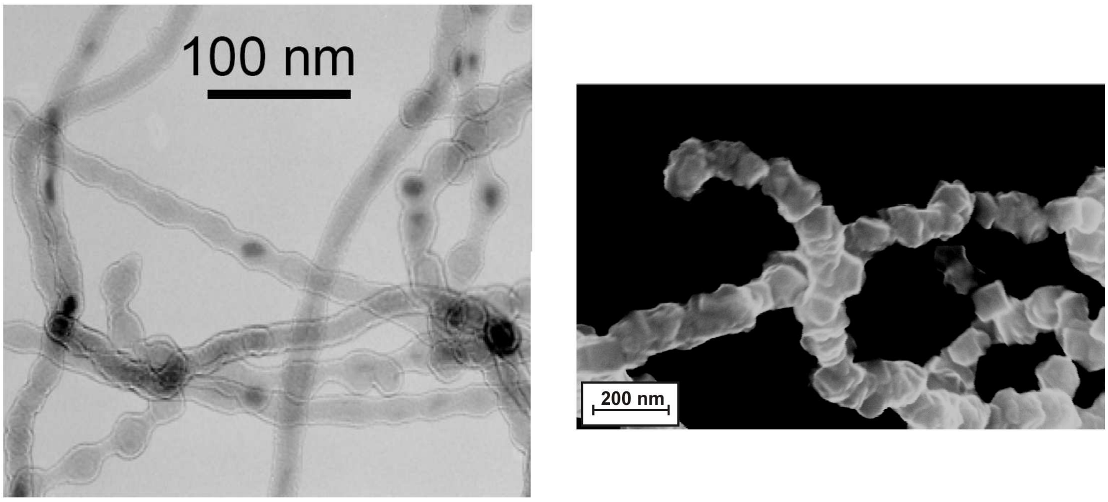

(a) Si nanoparticle chain

(b) Fe nanoparticle chain

Figure 1.2: Electron microscope pictures of nanoparticle chains. (a) from [149, Figure 1-a], (b) from [143, Figure 5.13].

Linear quantum systems also appear in other fields of research, especially molecular electronics [48, 72]. Fascinating applications of this field are expected from the use of DNA as a building block of electronic devices [56, 59, 147], or carbon nanotubes [7, 39, 60, 104], or both [127].

Regarding linear quantum systems, this thesis focuses on the effects of decoherence on the electronic conduction, which govern the transition from a quantum to a classical description. The thesis is organized as follows. Chapter 2 introduces the concepts of quantum transport. Chapter 3 discusses coherent transport in infinite linear systems, the effects of symmetry on the transmission function, transport in finite linear systems, and the properties of the finite-chain transmission function, which include even-odd effects, and localization. The model for the effects of decoherence is presented in Chapter 4. It is based on the statistical subdivision of the system under consideration into coherent regions and regions of decoherence. In Section 4.3 the model is applied to linear tight-binding systems with and without diagonal disorder. Once these systems are long enough (system size

---

[3] See e.g. [2, 5, 9, 10, 12–14, 19–22, 24, 25, 43, 64–66, 97, 105, 106, 109, 134, 139, 155, 168, 171, 174, 178, 195, 198].

$\gg$ coherence length), for chains without and with weak disorder we can define an ohmic resistivity ρ. In Chapter 5, the model for the effects of decoherence is applied to DNA double strands, yielding base sequence dependent conductance which can be compared with experimental data. The thesis finishes with conclusions and outlook in Chapter 6. The important results are summarized in Chapter 7. In the appendices, the reader can find literature recommendations, a derivation of the current formula from the Keldysh formalism, and technical details which were not included in the main text.

2 Quantum Transport

In this chapter I give an introduction to the theory of quantum transport. The aim is a straight-to-the-point derivation of the essential formulae needed in the subsequent Chapters 3–5. Therefore, here I restrain myself from applying many-body perturbation theory and Keldysh formalism[1]; instead I follow Datta [54] who in his derivation uses a physically intuitive approach without second-quantization formalism. Nonetheless the derivation is exact for the systems discussed in this thesis. For a thorough study of quantum transport I refer to the literature which I recommend in Section A.5.

2.1 Introduction

The theory of electron transport in solid-state materials has come a long way since Drude's electron-gas theory [61] of 1900 and Bloch's theorem for electrons in periodic crystals [23] of 1928. Whereas many bulk properties like electrical or thermal resistivity can be well described within Drude's framework and band-structure theory (by material-specific relaxation times, free-electron densities and effective electron masses), modern nanoscale devices require a completely different theoretical description. The reason is that by going to smaller and smaller systems, the classical concept of *conductivity* loses its sense. Once the system size comes into the range of electron phase-coherence length, the concept of a local quantity named conductivity can no longer be valid. Thus for nanoscale systems we must, instead, start from a microscopic quantum-mechanical description of conduction. This is done in this chapter. In Chapter 4, I then explain our approach of the transition from the micro to the macro scale: how to come from microscopic conductances back to a macroscopic conductivity.

To summarize this paragraph: Transport in nanoscale systems cannot be described "top-down"[2] with macroscopic concepts but rather the theory must be built "bottom-up" starting from quantum theory.

Before we come to the description of the electrical current, we have to introduce the concepts of the spectral function A, the Green function G and the correlation function G^{n}.

---

[1] In the Appendix B, the interested reader can find some notes about this formalism.

[2] Top-down and bottom-up approach are the words used by Supriyo Datta in [54, page 1–2].

2.1.1 The spectral function A

The spectral function A of a quantum-mechanical system with Hamiltonian H (eigenenergies ϵ_α) is defined as

$$A \equiv 2\pi\delta(EI - H) \tag{2.1}$$

where I is the unity operator of the same dimension as H. In real space representation this is equivalent to

$$A(\mathbf{r}, \mathbf{r}'; E) = 2\pi \sum_\alpha \phi_\alpha(\mathbf{r})\delta(E - \epsilon_\alpha)\phi_\alpha^*(\mathbf{r}') \tag{2.2}$$

where the $\phi_\alpha(\mathbf{r})$ are the eigenfunctions of H. Thus we recognize the physical meaning of the spectral function: The diagonal elements of its real-space representation are proportional to the local density of states (LDOS).

2.1.2 The Green functions G and G^+

Now we can use a representation of the delta function that leads us to the definition of the Green function of the system.

$$2\pi\delta(E - \epsilon_\alpha) = \left[\frac{2\eta}{(E - \epsilon_\alpha)^2 + \eta^2}\right]_{\eta \to 0^+} = \mathrm{i}\left[\frac{1}{E - \epsilon_\alpha + \mathrm{i}0^+} - \frac{1}{E - \epsilon_\alpha - \mathrm{i}0^+}\right] \tag{2.3}$$

Using this identity we can rewrite A

$$A(E) = 2\pi\delta(EI - H) = \mathrm{i}[\ \underbrace{\left((E + \mathrm{i}0^+) - H\right)^{-1}}_{\text{retarded Green function } G} - \underbrace{\left((E - \mathrm{i}0^+) - H\right)^{-1}}_{\text{advanced Green function } G^+}\ ] \tag{2.4}$$

and have thereby introduced the retarded and advanced Green functions G and G^+. In the following, with the term Green function we will refer to the retarded Green function, if not otherwise specified.

2.1.3 The Green function and the total density of states (DOS)

From (2.4) we can also read the relation between Green function and total density of states $D(E)$:

$$D(E) = -\frac{1}{\pi}\,\mathrm{Tr}\,[\mathrm{Im}\, G(E)] \tag{2.5}$$

where Tr is the trace of the operator.

The density of states is non-negative. This is consistent with the fact that the imaginary part of the Green function has to be non-positive[3], i.e.

$$\mathrm{Im}\, G_{ii}(E) \le 0 \tag{2.6}$$

where the index ii refers to the diagonal elements in any basis.

---

[3] The retarded Green function in time vanishes for $t < 0$. This is in accordance with the poles lying on the lower half of the complex energy plane, cf. [62].

2.1.4 The correlation function G^n

The electron-electron correlation function G^n is usually defined in time domain as

$$G^\mathrm{n}_{ij}(t,t') \equiv \langle c_j^+(t')c_i(t)\rangle \tag{2.7}$$

where c_j^+ and c_i are the electron creation and annihilation operators. In steady state, it depends only on the time difference $\tau = t - t'$, and a Fourier transform shows that in energy domain, the correlation function $G^\mathrm{n}(E)$ is nothing but the energy resolved electron density matrix, i.e.

$$\rho = \int\limits_{-\infty}^{\infty} \frac{\mathrm{d}E}{2\pi} G^\mathrm{n}(E) \tag{2.8}$$

Due to its relation to the electron density matrix, in equilibrium G^n fulfills

$$G^\mathrm{n}(E) \overset{\mathrm{eq}}{=} 2\pi f_0(E-\mu)\delta(EI - H) \tag{2.9}$$

where f_0 is the Fermi distribution and μ the chemical potential. Comparing with the definition for the spectral function (2.1) we conclude

$$G^\mathrm{n}(E) \overset{\mathrm{eq}}{=} A(E) f_0(E-\mu) \tag{2.10}$$

2.2 Open quantum-mechanical systems: Σ, Γ, and ρ

Current flow through a nanoscale system or *channel* is not possible without coupling to external voltage sources or *reservoirs*. Thus a description of the current flow through the channel has to include the effects of the reservoirs *source* and *drain*.

The total system under consideration can be described by (i) the Hamiltonians for the isolated contacts (source H_1 and drain H_2) and for the isolated channel (H) and (ii) the couplings between source and channel (τ_1) and between channel and drain (τ_2).

The Schrödinger equations for the isolated source and drain read:

$$H_1 |\Phi_{R1}\rangle = EI |\Phi_{R1}\rangle \tag{2.11}$$

$$H_2 |\Phi_{R2}\rangle = EI |\Phi_{R2}\rangle \tag{2.12}$$

Here, $|\Phi_{R1}\rangle$ and $|\Phi_{R2}\rangle$ are wave-vectors, and the Is unit matrices of the dimensions corresponding to H_1 and H_2 respectively. Let us rewrite these equations as

$$(EI - H_1 + \mathrm{i}\eta) |\Phi_{R1}\rangle = |S_1\rangle \tag{2.13}$$

$$(EI - H_2 + \mathrm{i}\eta) |\Phi_{R2}\rangle = |S_2\rangle \tag{2.14}$$

where $\eta = 0^+ I$ is a positive infinitesimal times the unit matrix. The term $\mathrm{i}\eta\,|\Phi\rangle$ represents the extraction of electrons from the contact, the term $|S\rangle$ the corresponding re-injection. If we identify $\mathrm{i}\eta\,|\Phi\rangle = |S\rangle$, mathematically we have not changed the Schrödinger equations. Nonetheless the transition from (2.11) and (2.12) to (2.13) and (2.14) represents a change in viewpoint. In the latter, the energy E is no longer an eigenenergy of the Hamiltonian. Rather, in Equations (2.13) and (2.14), E describes the energy of the excitation $|S\rangle$ from external sources. Whereas in (2.11) and (2.12), the $|\Phi\rangle$s are zero whenever E is not an eigenenergy of $H_{1,2}$, in the case of (2.13) and (2.14), the $|\Phi\rangle$s are non-zero for all energies and represent the response of the contact to external excitation. The $|\Phi\rangle$s are peaked around the eigenenergies of H_1 and H_2, the sharpness of the peaks depends on the infinitesimal 0^+.

Now, what happens if we couple the contacts to the channel? The left contact wave function $|\Phi_{R1}\rangle$ and the right contact wave function $|\Phi_{R2}\rangle$ will spill over and give rise to the wavefunction $|\psi\rangle$ of the channel which, again, excites wavefunctions $|\chi_1\rangle$ and $|\chi_2\rangle$ in reservoir 1 and 2. The composite Schrödinger equation can therefore be written as

$$\begin{pmatrix} EI - H_1 + \mathrm{i}\eta & -\tau_1^+ & 0 \\ -\tau_1 & EI - H & -\tau_2 \\ 0 & -\tau_2^+ & EI - H_2 + \mathrm{i}\eta \end{pmatrix} \begin{pmatrix} \Phi_{R1} + \chi_1 \\ \psi \\ \Phi_{R2} + \chi_2 \end{pmatrix} = \begin{pmatrix} S_1 \\ 0 \\ S_2 \end{pmatrix} \tag{2.15}$$

Using (2.13) with the first line of (2.15), and (2.14) with the third, we obtain

$$|\chi_1\rangle = G_1 \tau_1^+ |\psi\rangle \qquad \text{and} \qquad |\chi_2\rangle = G_2 \tau_2^+ |\psi\rangle \tag{2.16}$$

where

$$G_1 = (EI - H_1 + \mathrm{i}\eta)^{-1} \qquad \text{and} \qquad G_2 = (EI - H_2 + \mathrm{i}\eta)^{-1} \tag{2.17}$$

are the Green functions of the *isolated* reservoirs (i.e. without coupling to the channel). With help of (2.16) we write the middle line of (2.15) as

$$(EI - H - \Sigma_1 - \Sigma_2)\, |\psi\rangle = |S\rangle \tag{2.18}$$

where we have introduced the so-called ***self-energies***

$$\Sigma_1 = \tau_1 G_1 \tau_1^+ \qquad \text{and} \qquad \Sigma_2 = \tau_2 G_2 \tau_2^+ \tag{2.19}$$

due to the coupling to the left and right reservoir. In (2.18),

$$|S\rangle \equiv \tau_1 |\Phi_{R1}\rangle + \tau_2 |\Phi_{R2}\rangle \tag{2.20}$$

is the sum of the source terms due to source and drain.

Now we define the ***channel Green function***

$$G \equiv (EI - H - \Sigma_1 - \Sigma_2)^{-1} \tag{2.21}$$

Comparing (2.21) with (2.4) we can interpret the self-energies as a modification of H due to the coupling to the contacts. In the case that H is 1-dimensional (i.e. we have a single energy level in the channel), $\mathrm{Re}(\Sigma_1)$ represents an energy shift of the channel, and $\mathrm{Im}(\Sigma_1)$ an energy broadening due to the coupling to the source. Correspondingly Σ_2 represents shift and broadening due to the coupling to the drain. The anti-hermitian component Γ of the self-energy is also called the ***broadening matrix***.

$$\Gamma(E) = \mathrm{i}\left(\Sigma(E) - \Sigma^+(E)\right) \tag{2.22}$$

Thus combining (2.21) with (2.18) we can write the channel wavefunction as

$$|\psi\rangle = G\,|S\rangle \tag{2.23}$$

Thus we can examine

$$\begin{aligned} |\psi\rangle\,\langle\psi| &= G\,|S\rangle\langle S|\,G^+ \\ &\overset{(2.20)}{=} G\tau_1\,|\Phi_{R1}\rangle\langle\Phi_{R1}|\,\tau_1^+G^+ + G\tau_2\,|\Phi_{R2}\rangle\langle\Phi_{R2}|\,\tau_2^+G^+ \\ &+ \underbrace{G\tau_1\,|\Phi_{R1}\rangle\langle\Phi_{R2}|\,\tau_2^+G^+ + G\tau_2\,|\Phi_{R2}\rangle\langle\Phi_{R1}|\,\tau_1^+G^+}_{\text{cross terms=0}} \end{aligned} \tag{2.24}$$

where the cross terms vanish because the uncoupled wavefunctions $|\Phi_R\rangle$ of the reservoirs have no overlap.

Now, in (2.24) we recognize the projectors $|\Phi_R\rangle\langle\Phi_R|$ of the reservoirs. As we know the density operators $\rho_{1,2} = \int \frac{\mathrm{d}E}{2\pi} A_{1,2} f_{1,2}$ for the reservoirs 1 and 2, we can write

$$\begin{aligned} \rho &= \int \frac{\mathrm{d}E}{2\pi} \left(G\tau_1 A_1 \tau_1^+ G^+\right) f_1 + \left(G\tau_2 A_2 \tau_2^+ G^+\right) f_2 \\ &= \int \frac{\mathrm{d}E}{2\pi} G\Gamma_1 G^+ f_1 + G\Gamma_2 G^+ f_2 \end{aligned} \tag{2.25}$$

where we have used

$$\Gamma_{1,2} = \mathrm{i}(\Sigma_{1,2} - \Sigma_{1,2}^+) = \mathrm{i}\tau(G_{1,2} - G_{1,2}^+)\tau^+ = \tau A_{1,2}\tau^+ \tag{2.26}$$

We find in (2.25) that both f_1 and f_2 enter linearly into the density operator of the channel. This reflects the fact, that the electrons coming from source and drain do not interact inside the channel.

We conclude for the correlation function by comparing (2.25) and (2.8)

$$G^{\mathrm{n}} = G\Sigma^{\mathrm{in}}G^+ \tag{2.27}$$

where

$$\Sigma^{\mathrm{in}} = \Gamma_1 f_1 + \Gamma_2 f_2 \tag{2.28}$$

is called inscattering.

2.3 Transport formulae

For transport we have to consider the time evolution of the probability density in the channel. For the contacts we assume an equilibrium energy distribution, i.e. we can use (2.25). With the abbreviation $|\Phi_i\rangle = |\Phi_{Ri}\rangle + |\chi_i\rangle$ we consider, instead of (2.15) the time-dependent Schrödinger equation:

$$\mathrm{i}\hbar\frac{\mathrm{d}}{\mathrm{d}t}\begin{pmatrix}\Phi_1\\ \psi\\ \Phi_2\end{pmatrix} = \begin{pmatrix} H_1 - \mathrm{i}\eta & \tau_1^+ & 0 \\ \tau_1 & H & \tau_2 \\ 0 & \tau_2^+ & H_2 - \mathrm{i}\eta \end{pmatrix}\begin{pmatrix}\Phi_1\\ \psi\\ \Phi_2\end{pmatrix} \tag{2.29}$$

For the particle current $\frac{I}{e}$, e being the electronic charge, we have to look at the time evolution of $\langle\psi|\psi\rangle$:

$$\frac{I}{e} \equiv \frac{\mathrm{d}}{\mathrm{d}t}\langle\psi|\psi\rangle = \frac{\langle\psi|\tau_1|\Phi_1\rangle + \langle\psi|\tau_2|\Phi_2\rangle - \left\langle\Phi_1|\tau_1^+|\psi\right\rangle - \left\langle\Phi_2|\tau_2^+|\psi\right\rangle}{\mathrm{i}\hbar} \tag{2.30}$$

Now, the current can be divided into an inflowing and an outflowing part, using $|\Phi_i\rangle = |\Phi_{Ri}\rangle + |\chi_i\rangle$

$$\begin{aligned}\frac{I}{e} = &\frac{\overbrace{\langle\psi|\,\tau_1\,|\Phi_{R1}\rangle - \langle\Phi_{R1}|\,\tau_1^+\,|\psi\rangle}^{\text{Inflow 1}} + \overbrace{\langle\psi|\,\tau_2\,|\Phi_{R2}\rangle - \langle\Phi_{R2}|\,\tau_2^+\,|\psi\rangle}^{\text{Inflow 2}}}{\mathrm{i}\hbar} \\ - &\frac{\overbrace{\langle\chi_1|\,\tau_1^+\,|\psi\rangle - \langle\psi|\,\tau_1\,|\chi_1\rangle}^{\text{Outflow 1}} + \overbrace{\langle\chi_2|\,\tau_2^+\,|\psi\rangle - \langle\psi|\,\tau_2\,|\chi_2\rangle}^{\text{Outflow 2}}}{\mathrm{i}\hbar}\end{aligned} \tag{2.31}$$

Here “Inflow 1” and “Inflow 2” refer to the electron flow through interface 1 and 2 (“Outflow” correspondingly).

Let us focus on Inflow 1. Using $|\psi\rangle = G\,|S\rangle$ and $|S_1\rangle = \tau_1\,|\Phi_{R1}\rangle$ we find

$$\text{Inflow 1} = \frac{\langle S|\,G^+\,|S_1\rangle - \langle S_1|\,G\,|S\rangle}{\mathrm{i}\hbar} = \frac{\mathrm{Tr}\left[|S_1\rangle\langle S_1|\,A\right]}{\hbar} \tag{2.32}$$

since $|S\rangle = |S_1\rangle + |S_2\rangle$ and $\langle S_1|S_2\rangle = \langle S_2|S_1\rangle = 0$ and $\mathrm{i}\,[G - G^+] = A$.

Now, just as we came from (2.24) to (2.25) by considering the equilibrium distribution in the reservoir, we replace

$$|S_1\rangle\langle S_1| = \tau_1\,|\Phi_1\rangle\langle\Phi_1|\,\tau_1^+ \rightarrow \int \frac{\mathrm{d}E}{2\pi} f_1(E)\left[\tau_1 A_1 \tau_1^+\right] = \int \frac{\mathrm{d}E}{2\pi} f_1(E)\,[\Gamma_1] \tag{2.33}$$

and conclude

$$\text{Inflow 1} = \frac{1}{\hbar}\int \frac{\mathrm{d}E}{2\pi} f_1(E)\,\mathrm{Tr}\,[\Gamma_1 A] \tag{2.34}$$

Similarly we examine Outflow 1 using $\left|\chi_1^+\right\rangle = G_1\tau_1\,|\psi\rangle$

$$\text{Outflow 1} = \frac{\mathrm{Tr}\left[\langle\psi|\,\tau_1 G_1^+ \tau_1^+\,|\psi\rangle - \langle\psi|\,\tau_1 G_1 \tau_1^+\,|\psi\rangle\right]}{\mathrm{i}\hbar} = \frac{\mathrm{Tr}\left[|\psi\rangle\langle\psi|\,\Gamma_1\right]}{\hbar} \tag{2.35}$$

Again considering thermal equilibrium in the reservoir we find

$$\text{Outflow 1} = \frac{1}{\hbar}\int \frac{\mathrm{d}E}{2\pi}\,\mathrm{Tr}\,[\Gamma_1 G^{\mathrm{n}}] \tag{2.36}$$

Thus we have a net current through the interface 1

$$\text{Inflow 1} - \text{Outflow 1} = \frac{1}{\hbar}\int_{-\infty}^{\infty} \frac{\mathrm{d}E}{2\pi} I_1(E) \tag{2.37}$$

where

$$I_1(E) = \mathrm{Tr}\left[\Gamma_1 A\right] f_1 - \mathrm{Tr}\left[\Gamma_1 G^{\mathrm{n}}\right] \tag{2.38}$$

Now, as in the case without interaction in the channel $G^{\mathrm{n}} = A_1 f_1 + A_2 f_2$, we can rewrite (2.38) as

$$I_1(E) = \mathrm{Tr}\left[\Gamma_1 \left(A_1 + A_2\right) f_1 - \Gamma_1 \left(A_1 f_1 + A_2 f_2\right)\right] = \underbrace{\mathrm{Tr}\left[\Gamma_1 A_2\right]}_{T_{12}} \left(f_1 - f_2\right) \tag{2.39}$$

Thus we have introduced the *transmission function* T_{12} which we can further manipulate using $A \equiv \mathrm{i}\left[G - G^{+}\right] = G\Gamma G^{+} = G^{+}\Gamma G$ [4] and the fact that cyclical permutations do not change the trace, to arrive at the important *transmission formula*

$$T_{12} = \mathrm{Tr}\left[\Gamma_1 A_2\right] = \mathrm{Tr}\left[\Gamma_1 G \Gamma_2 G^{+}\right] = \mathrm{Tr}\left[\Gamma_2 G \Gamma_1 G^{+}\right] \tag{2.44}$$

Equivalently we can write

$$T_{12} = 4\,\mathrm{Tr}\left[G \mathrm{Im}(\Sigma_1) G^{+} \mathrm{Im}(\Sigma_2)\right] \tag{2.45}$$

By integrating the transmission function over the energy (cf. (2.37)) we arrive at the famous **Landauer-Büttiker formula**

$$I_{12} = \frac{e}{h} \int\limits_{-\infty}^{\infty} \mathrm{d}E\, T_{12}(E) \left(f_1(E) - f_2(E)\right) \tag{2.46}$$

This is the correct formula to be used for the calculation of the current under the following conditions:

- Both source and drain are in thermal equilibrium.
- The electron transport is coherent from the source through the channel to the drain. That means that no interaction takes place inside the channel.

In the following chapters we will use this formula mostly in the case of infinitesimal voltage drop (linear response). The limit $\mu_1 \to \mu_2$ leads to

$$G = \frac{e^2}{h} T_{12}(E = \mu) \tag{2.47}$$

---

[4] This formula is proved like this:

$$G = \left(EI - H - \Sigma\right)^{-1} \qquad \text{and} \qquad \Gamma = \mathrm{i}\left(\Sigma - \Sigma^{+}\right) \tag{2.40}$$

$$\Rightarrow \quad \left(G^{-1}\right)^{+} - G^{-1} = \Sigma - \Sigma^{+} = -\mathrm{i}\Gamma \tag{2.41}$$

which is pre-multiplied with G and post-multiplied with G^{+}, or vice versa, to obtain

$$G - G^{+} = -\mathrm{i} G\Gamma G^{+} \qquad \text{and} \qquad G - G^{+} = -\mathrm{i} G^{+}\Gamma G \tag{2.42}$$

$$\Rightarrow \quad A = G\Gamma G^{+} = G^{+}\Gamma G \tag{2.43}$$

where G is the conductance of the channel. This formula is also called **Landauer formula** [107, 108].

In the literature, e.g. [53], one often finds $G = \frac{2e^2}{h} MT$ as the Landauer formula. Here, the 2 stems from an assumed spin degeneracy, M is the number of transverse modes[5], and T the average transmission *per mode*. Our transmission function (2.44) comprises all conducting modes, therefore $T > 1$ is possible if more than a single mode contributes in the transmission, cf. Section 3.7.2.4. In this context one also speaks of conducting channels [47], [46, Chapter 6].

Also for finite bias the Landauer-Büttiker formula (2.46) can be used, yet the voltage drop has to be carefully included in the channel Hamiltonian and the self-energies. This can be done by a self-consistent determination of the potential profile within the channel and the current. For the details, see e.g. [54].

2.4 Properties of the Green function

2.4.1 The Lehmann or spectral representation

There are many ways to evaluate the Green function

$$G = \left[E + \mathrm{i}0^+ - H\right]^{-1} \tag{2.48}$$

One of them is to use the so-called Lehmann or spectral representation. If we know the eigenvectors $|\psi_i\rangle$ and eigenenergies ϵ_i of the Hamiltonian H, the Lehmann representation is

$$G = \sum_i |\psi_i\rangle\langle\psi_i| \left[E + \mathrm{i}0^+ - H\right]^{-1} = \sum_i \frac{|\psi_i\rangle\langle\psi_i|}{E + \mathrm{i}0^+ - \epsilon_i} \tag{2.49}$$

More explicitly, if H has a partly continuous spectrum

$$G = \sum_i \frac{|\psi_i\rangle\langle\psi_i|}{E + \mathrm{i}0^+ - \epsilon_i} + \int \mathrm{d}i \frac{|\psi_i\rangle\langle\psi_i|}{E + \mathrm{i}0^+ - \epsilon_i} \tag{2.50}$$

We conclude that the Green function has poles wherever $E = \epsilon_i$, and that $G(E) \propto 1/E$ for $E \to \pm\infty$.

2.4.2 The Dyson equation

The Dyson equation relates the Green function G of a perturbed system to g, the one of the unperturbed system. Let the Hamiltonian $H = H_0 + V$ be composed of the unperturbed

---

[5] The name transverse modes stems from the analogy between the electron channel and an electronic wave guide and indicates how many electrons can transmit the channel simultaneously.

Hamiltonian H_0 and some perturbation V. Then we can write

$$G = \left[E + \mathrm{i}0^+ - H\right]^{-1} = \left[E + \mathrm{i}0^+ - H_0 - V\right]^{-1} \tag{2.51}$$

$$= \left[g^{-1} - V\right]^{-1} \tag{2.52}$$

$$\Rightarrow \quad G^{-1} = g^{-1} - V \tag{2.53}$$

$$\Rightarrow \quad g = G - gVG \quad \Leftrightarrow \quad G = g + gVG \tag{2.54}$$

where from the next-to-last to the last line we have multiplied g from the left and G from the right. Equation (2.54) is called Dyson equation for the Green function. There are Dyson equations also for other functions in transport theory, e.g. in (2.27) we got to know the one for the correlation function G^{n}.

The Dyson equation offers a means for a perturbation approximation of the Green function. To n-th order, we can approximate

$$G = g + \sum_{j=1}^{n} (gV)^j \, g \tag{2.55}$$

For further information about Dyson equations and their relation to the diagrammatic formulation of many-body theory, we refer to the literature, e.g. [120, 126].

2.4.3 The Kramers-Kronig relations for the Green function

The retarded Green function $G(E)$ as a complex function of the complex variable E meets the requirements for Kramers-Kronig relations, i.e. its Fourier transform is zero for $t < 0$ (or equivalently it is analytic in the upper complex half-plane and vanishes for $|E| \to \infty$).

The Kramers-Kronig relations state that

$$G(E) = \frac{1}{\mathrm{i}\pi} \mathcal{P} \int_{-\infty}^{\infty} \mathrm{d}E' \, \frac{G(E')}{E' - E} \tag{2.56}$$

or, split into real and imaginary parts,

$$\operatorname{Re} G(E) = -\frac{1}{\pi} \mathcal{P} \int_{-\infty}^{\infty} \mathrm{d}E' \, \frac{\operatorname{Im} G(E')}{E - E'} \tag{2.57}$$

$$\operatorname{Im} G(E) = \frac{1}{\pi} \mathcal{P} \int_{-\infty}^{\infty} \mathrm{d}E' \, \frac{\operatorname{Re} G(E')}{E - E'} \tag{2.58}$$

where, $\mathcal{P}$ denotes the Cauchy principal value[6] of the integral.

---

[6] The Cauchy principal value of a function $f(x)$ with a single pole at x_0 is defined as

$$\mathcal{P} \int_{-\infty}^{\infty} \mathrm{d}x f(x) = \lim_{\epsilon \to 0^+} \left[\int_{-\infty}^{x_0 - \epsilon} \mathrm{d}x f(x) + \int_{x_0 + \epsilon}^{\infty} \mathrm{d}x f(x) \right] \tag{2.59}$$

For functions with various poles analogously.

3 Coherent Transport in Linear Systems

In this Chapter, I discuss the electron transport in idealized infinite and finite completely coherent systems. I begin with the known example of the infinite and half-infinite linear tight-binding chain, and extend the considerations to double, triple and n-tuple chains. A different treatment of similar systems can be found in [68, Section 3.8]. In the limit $n \to \infty$, the n-tuple chain converges to the 2d grid. The transmission through single defects in the chains will give us insight to the effects of symmetry. Also the known example of the alternating chain is presented. The DNA-chain is shown to be a generalized alternating chain. After the discussion of infinite and half-infinite chains I examine finite chains, where we observe even-odd effects, and length-periodicity for the transmission in ordered chains, and localization as a consequence of disorder.

3.1 The infinite linear tight-binding chain

Firstly, we will discuss the infinite linear tight-binding chain with the Hamiltonian

$$H = \sum_{i=-\infty}^{\infty} \epsilon \left|i\right\rangle\left\langle i\right| + t \left[\left|i\right\rangle\left\langle i+1\right| + \text{H.c.}^{1}\right] \tag{3.1}$$

where the onsite energy ϵ and the transfer matrix element t are the same all along the chain, cf. Figure 3.1.[2] The states $\left|i\right\rangle$ form an orthonormal system, i.e. $\left\langle i|j\right\rangle = \delta_{ij}$, $\sum_i \left|i\right\rangle\left\langle i\right| = 1$.

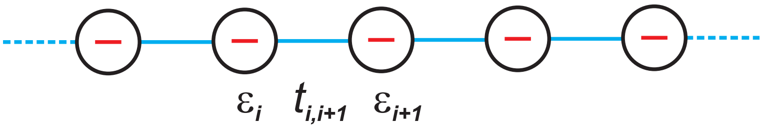

Figure 3.1: The infinite linear tight-binding chain.

For the eigenfunctions of the Hamiltonian we make the plane-wave ansatz $\left|k\right\rangle = \sum_j \mathrm{e}^{\mathrm{i}kj} \left|j\right\rangle$.

---

[1] H.c. means Hermitian conjugate, i.e. here: $\left|i+1\right\rangle\left\langle i\right|$

[2] Often, a tight-binding Hamiltonian is defined with "$-t$", underlining the fact that for electrons in conduction bands the transfer matrix element is negative. For description of hole transport it is positive.

Thus we find the eigenenergies as follows

$$H\,|k\rangle = \sum_{i,j=-\infty}^{\infty} \left(\epsilon\,|i\rangle\langle i| + t\,[|i\rangle\langle i+1| + |i+1\rangle\langle i|]\right) \mathrm{e}^{\mathrm{i}kj}\,|j\rangle \tag{3.2}$$

$$= \sum_{j=-\infty}^{\infty} \epsilon\ \mathrm{e}^{\mathrm{i}kj}\,|j\rangle + t\ \mathrm{e}^{\mathrm{i}k(j+1)}\,|j\rangle + t\ \mathrm{e}^{\mathrm{i}kj}\,|j+1\rangle \tag{3.3}$$

$$= (\epsilon + 2t\cos(k)) \sum_{j=-\infty}^{\infty} \mathrm{e}^{\mathrm{i}kj}\,|j\rangle = (\epsilon + 2t\cos(k))\,|k\rangle \tag{3.4}$$

$$\Rightarrow \quad E(k) = \epsilon + 2t\cos(k) \tag{3.5}$$

Without loss of generality, we restrict the parameter range $k \in [-\pi, \pi]$. Knowing the eigenenergy spectrum we can also determine the total density of states $D(E)$. As the states are distributed equally along the k-axis, we can write

$$D(E) = \left.\frac{\mathrm{d}k}{\pi \mathrm{d}E}\right|_E = \frac{1}{2\pi t}\frac{1}{\sqrt{1-\left(\frac{\epsilon-E}{2t}\right)^2}} \tag{3.6}$$

Here the normalization is such that $\int \mathrm{d}E D(E) = 1$. A plot of $D(E)$ can be found in Fig. 3.2. We see that the density of states diverges at the band edges.

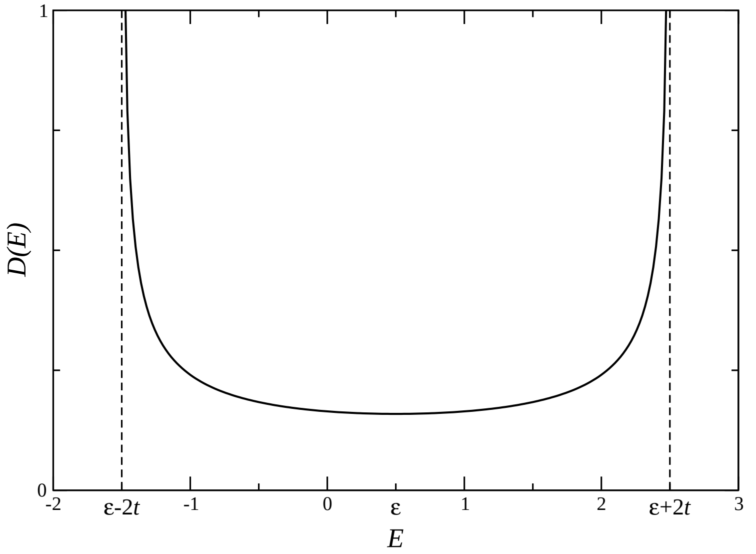

Figure 3.2: Density of states for the infinite linear tight-binding chain as defined in (3.6). The parameters were chosen $\epsilon = 0.5$, $t = 1$.

Summarizing, the infinite linear tight-binding chain has an energy spectrum given by $E(k) = \epsilon + 2t\cos(k)$, which is a cosine band between $\epsilon - 2t$ and $\epsilon + 2t$. All tight-binding chains can be mapped onto each other by taking ϵ as the origin and t as the energy unit. The eigenstates are plane waves.

3.2 The half-infinite linear chain

Transport calculations need to include a model for the reservoirs source and drain. A simple, but often used model is the half-infinite tight-binding chain or bundles of them. The principle dates back to 1971, to a work by Caroli et. al. [35] but is also applied nowadays, e.g. [40, 53, 121, 198].

First let us address the half-infinite chain in the same manner as the infinite chain, i.e. by considering the energy spectrum.

We define the Hamiltonian of the half-infinite chain as

$$H = \sum_{i=1}^{\infty} \epsilon\, |i\rangle\langle i| + t\,[|i\rangle\langle i+1| + \mathrm{H.c.}] \tag{3.7}$$

where the difference to the infinite chain is that the site index starts only at 1. For the eigenfunctions we make the ansatz

$$|k\rangle = \sum_{j=1}^{\infty} \sin(kj)\,|j\rangle \tag{3.8}$$

which essentially is also borrowed from the case of the infinite chain. With this ansatz we can find the eigenenergies

$$\begin{aligned} H\,|k\rangle &= \sum_{i,j=1}^{\infty} \epsilon \sin(kj)\,|i\rangle\langle i|j\rangle + t\sin(kj)\,|i\rangle\langle i+1|j\rangle + t\sin(kj)\,|i+1\rangle\langle i|j\rangle && (3.9)\\ &= \epsilon \sum_{j=1}^{\infty} \sin(kj)\,|j\rangle + t\sum_{j=1}^{\infty} [\sin(kj)\,|j-1\rangle + \sin(kj)\,|j+1\rangle] && (3.10)\\ &= \epsilon\,|k\rangle + t\sum_{j=1}^{\infty} [\sin(k(j+1))\,|j\rangle + \sin(k(j-1))\,|j\rangle] && (3.11)\\ &= (\epsilon + 2t\cos(k))\,|k\rangle && (3.12)\\ \Rightarrow \quad E(k) &= \epsilon + 2t\cos(k) && (3.13) \end{aligned}$$

where from the second to third row we have used $0 = \sin(k0)$, and from the third to fourth the addition theorem for the sine. The result is that the eigenenergy spectrum of the half-infinite chain is just the same as for the infinite chain, with the difference that $k \in [0, \pi]$. Therefore, also the total density of states is the same. We conclude that, although the single site energies ϵ are all the same, due to its coupling, the half-infinite chain has a continuous density of states and can thus serve as a model contact.

3.2.1 Surface Green function of the half-infinite chain

If we wish to use the half-infinite chain as a model for source and drain, we just need its surface Green function, i.e. the surface elements of its Green function. This can be seen by considering the definition of the self-energies (2.19) of source and drain. If the coupling matrix τ links the channel only to the surface of the reservoir, only the surface Green function comes into play.

In order to obtain the surface Green function we apply the Dyson equation (2.54). Imagine the half-infinite chain divided into its surface site and the rest (i.e. another half-infinite chain). As the unperturbed system (Green function g) let us consider the system in which the surface site (index 1) and the rest are uncoupled, and the coupling between surface and rest as perturbation (coupling t corresponds to perturbation V). Cf. Figure 3.3.

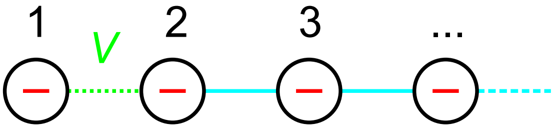

Figure 3.3: The half-infinite linear chain. For the calculation of the surface Green function we divide the system into site 1 and the rest, and consider the coupling $V = t$ between sites 1 and 2 as perturbation.

To the coupled system we assign the Green function G. The matrices have the following structure:

$$G = \begin{pmatrix} G_{11} & G_{12} & \cdots \\ G_{21} & G_{22} & \cdots \\ \vdots & \vdots & \ddots \end{pmatrix} \qquad g = \begin{pmatrix} g_{11} & 0 & 0 & \cdots \\ 0 & G_{11} & G_{12} & \cdots \\ 0 & G_{21} & G_{22} & \cdots \\ \vdots & \vdots & \vdots & \ddots \end{pmatrix} \qquad V = \begin{pmatrix} 0 & t & 0 & \cdots \\ t & 0 & 0 & \cdots \\ 0 & 0 & 0 & \cdots \\ \vdots & \vdots & \vdots & \ddots \end{pmatrix} \tag{3.14}$$

Here we have already included the fact that the unperturbed system from the second site on comprises just the same half-infinite chain which is our perturbed system. Then we consider the Dyson equation (2.54):

$$G = g + gVG \tag{3.15}$$

$$\Rightarrow \quad \left\{ \begin{array}{ll} G_{11} & = g_{11} + (gVG)_{11} = g_{11} + g_{11}V_{12}G_{21} \\ G_{21} & = g_{21} + g_{22}V_{21}G_{11} \end{array} \right\} \tag{3.16}$$

$$\Rightarrow \quad G_{11} = g_{11} + g_{11}V_{12}g_{22}V_{21}G_{11} \tag{3.17}$$

$$\underset{g_{22}=G_{11}}{\Rightarrow} \quad G_{11} = g_{11} + g_{11}t^2G_{11}^2 \tag{3.18}$$

$$\Rightarrow \quad G_{11} = \frac{1}{2t^2 g_{11}} \pm \frac{1}{2t^2}\sqrt{\frac{1}{g_{11}^2} - 4t^2} \tag{3.19}$$

$$\Rightarrow \quad G_{11} = \frac{E-\epsilon}{2t^2} \pm \frac{1}{2t^2}\sqrt{(E-\epsilon)^2 - 4t^2} \tag{3.20}$$

The ambiguity of the last line can be lifted by considering that $\operatorname{Im} G(E) \leq 0$ according to (2.6). We conclude

$$\operatorname{Im} G_{11}(E) = \begin{cases} -\frac{1}{2t^2}\sqrt{4t^2 - (E-\epsilon)^2} & \text{for } |E-\epsilon| < 2t \\ 0 & \text{else} \end{cases} \tag{3.21}$$

I.e. the imaginary part of the surface Green function is a negative half-circle with its center at ϵ. Using the Kramers-Kronig relation (2.57) we find

$$G_{11} = \begin{cases} \frac{E-\epsilon}{2t^2} + \frac{1}{2t^2}\sqrt{(E-\epsilon)^2 - 4t^2} & \text{for } E-\epsilon \leq -2t \\ \frac{E-\epsilon}{2t^2} - \mathrm{i}\frac{1}{2t^2}\sqrt{4t^2 - (E-\epsilon)^2} & \text{for } |E-\epsilon| < 2t \\ \frac{E-\epsilon}{2t^2} - \frac{1}{2t^2}\sqrt{(E-\epsilon)^2 - 4t^2} & \text{for } E-\epsilon \geq 2t \end{cases} \tag{3.22}$$

We observe that this solution is in accordance with $G(E) \propto 1/E$ for $E \to \pm\infty$, cf. (2.49). The results are plotted in Figure 3.4.

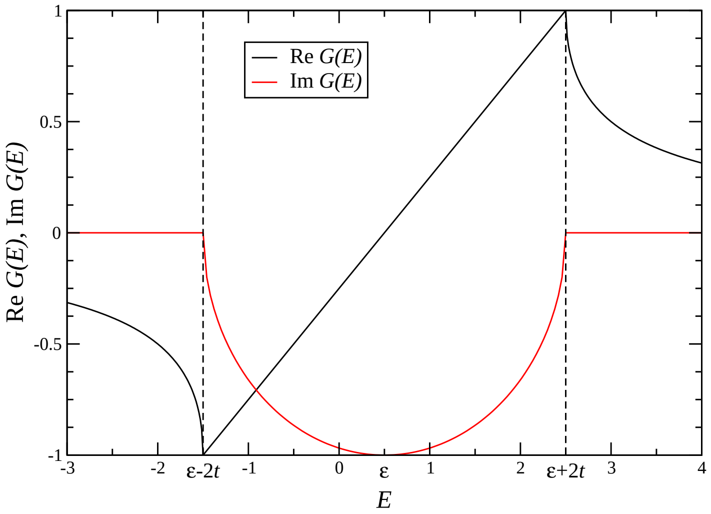

Figure 3.4: Real and imaginary part of the surface Green function of a half-infinite linear chain as defined in (3.7). The parameters were chosen $\epsilon = 0.5$, $t = 1$.

It is instructive to compare the local density of states at the surface of the chain with the one inside the infinite chain. Whereas at the surface the density of states has a maximum in the middle of the band, in the infinite chain it has a minimum and diverges at the band edges, cf. Figure 3.5.

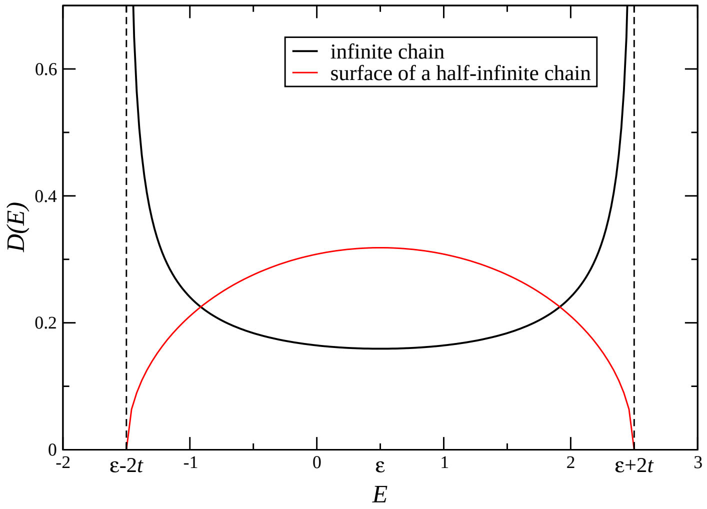

Figure 3.5: Local density of states for the infinite linear tight-binding chain in comparison with the density of states at the surface of the half-infinite chain.

3.2.2 An alternative way of calculation: direct back-transformation

There is an alternative way to calculate the surface Green function, which is to back-transform the eigenstates of the half-infinite chain from k to real space. In spectral representation (2.49), we write the Green function of the half-infinite chain as

$$G(E) = \lim_{\eta\to 0^+} \int_0^\pi \mathrm{d}k \frac{|k\rangle\langle k|}{E + \mathrm{i}\eta - 2t\cos(k)} \tag{3.23}$$

If we consider the matrix element $\langle 1|G(E)|1\rangle$, i.e. we perform a Fourier back-transformation, we obtain the surface Green function

$$G_{11} = \lim_{\eta\to 0^+} \int_0^\pi \mathrm{d}k \frac{|\langle 1|k\rangle|^2}{E + \mathrm{i}\eta - 2t\cos(k)} \tag{3.24}$$

$$= \lim_{\eta\to 0^+} \int_0^\pi \mathrm{d}k \frac{\frac{2}{\pi}\sin^2(k)}{E + \mathrm{i}\eta - 2t\cos(k)} \tag{3.25}$$

where we have inserted the normalized real-space eigenstates

$$|j\rangle = \sqrt{\frac{2}{\pi}} \int_0^\pi \mathrm{d}k \sin(jk)\,|k\rangle \tag{3.26}$$

and used the normalization of the k-eigenstates

$$\langle k|k'\rangle = \delta(k - k') \tag{3.27}$$

The elliptical integral (3.25) can be solved by application of the residue theorem and integration along a half-infinite rectangle (edges are the imaginary axis, a parallel to it through $k = \pi$, the interval $[0, \pi]$ along the real axis and a parallel to it at infinity) to obtain again (3.22). Of course, it is also tabled, cf. [78]. A general treatment on infinite lattice Green functions which involves similar integrals can be found in [62, Chapter 5] which refers to [84].

3.3 Transmission through a single defect

3.3.1 Symmetrical coupling to left and right contact

Knowing the surface Green function of the half-infinite chain we can use it as reservoir for transport calculations. As the simplest example we consider the transport through a single site with energy ϵ_0 coupled to the left and right half-infinite chain with a hopping term t'. For simpler notation we choose $\epsilon = 0$, the onsite energy of the half-infinite chains as our energy origin, and we set $t = 1$, the intra-chain coupling as our energy unit. According to (2.19), the self-energies of the chains with respect to the single site are

$$\Sigma_{L,R} = t'^2 G_{11} \tag{3.28}$$

The Green function of the single site reads accordingly

$$G(E) = \frac{1}{E - \epsilon_0 - \Sigma_L - \Sigma_R} \tag{3.29}$$

$$= \begin{cases} \frac{1}{E(1-t'^2)-\epsilon_0-t'^2\sqrt{E^2-4}} & \text{for } E \leq -2 \\ \frac{1}{E(1-t'^2)-\epsilon_0+\mathrm{i}t'^2\sqrt{4-E^2}} & \text{for } |E| < 2 \\ \frac{1}{E(1-t'^2)-\epsilon_0+t'^2\sqrt{E^2-4}} & \text{for } E \geq 2 \end{cases} \tag{3.30}$$

By considering the imaginary part of this Green function, we obtain the local density of states at the defect:

$$D(E, \epsilon_0) = -\frac{1}{\pi} \mathrm{Im}\, G(E, \epsilon_0) = \begin{cases} \frac{1}{\pi} \frac{\frac{1}{t'^2}\sqrt{4-E^2}}{4-E^2+\left(\left(\frac{1}{t'^2}-1\right)E-\frac{1}{t'^2}\epsilon_0\right)^2} & \text{for } |E| < 2 \\ 0 & \text{else} \end{cases} \tag{3.31}$$

This is a Lorentzian in ϵ_0. This reflects the fact that by coupling to the contacts, the onsite energy of the defect becomes smeared out. For $\epsilon_0 = 0$, $t' = 1$, (3.31) is nothing but the local density of states of the infinite chain (3.6), as expected.

With the Green function (3.29) and the self-energies (3.28) we can calculate the transmission according to (2.45). As the imaginary part of $\Sigma_{L,R}$, like the one of G_{11}, is only nonzero within the band of the half-infinite chains, the transmission vanishes for all energies outside the band. This is a general feature of coherent quantum transport: Transmission is only possible for energies which lie within bands of both source and drain. Hence

$$T(E) = \begin{cases} \frac{t'^4}{t'^4+\frac{\left((1-t'^2)E-\epsilon_0\right)^2}{4-E^2}} & \text{for } |E| < 2 \\ 0 & \text{else} \end{cases} \tag{3.32}$$

In the case of $t' = 1$, $\epsilon_0 = 0$ (i.e. no defect), the transmission is the window function

$$T(E) = \begin{cases} 1 & \text{for } |E| < 2 \\ 0 & \text{else} \end{cases} \tag{3.33}$$

Of course, this is an expected result. Without defect, the transmission has to be 1 within the tight-binding band.

Case $t' = 1$, $\epsilon_0 \neq 0$. The transmission function for various parameters ϵ_0, and $t' = 1$ is plotted in Figure 3.6. We see that the single defect corresponds to a barrier: Incoming electrons are partly reflected at the defect. The maximum values of the transmission behave like a Lorentzian in the defect energy ϵ_0 for every E.

Case $\epsilon_0 = 0$, $t' \neq 1$. In Figure 3.7 the transmission function is displayed for $\epsilon_0 = 0$ with different values of t'. We see that in this case, the transmission $T(E)$ always has a peak at $E = 0$, where $T = 1$ is reached. By analyzing (3.32), we find that the transmission functions for t',$-t'$, and $\pm\frac{t'}{\sqrt{2t'^2-1}}$ are identical.

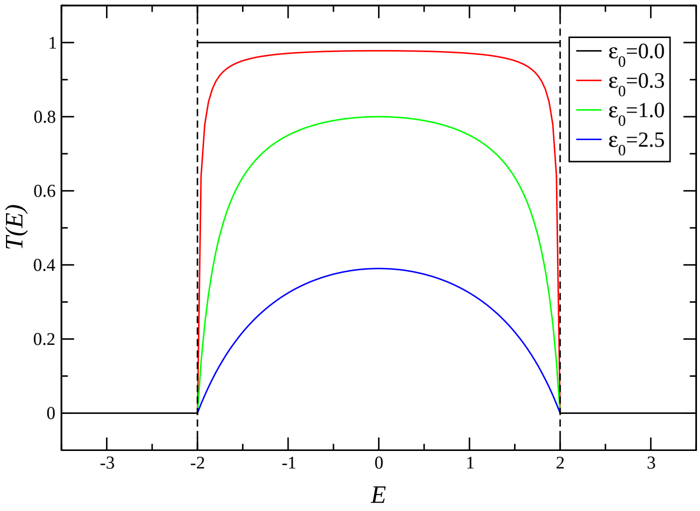

Figure 3.6: Transmission function for the linear chain (onsite energy $\epsilon = 0$, coupling $t = 1$ as the energy unit) without defect and with a single defect at three different energies ϵ_0.

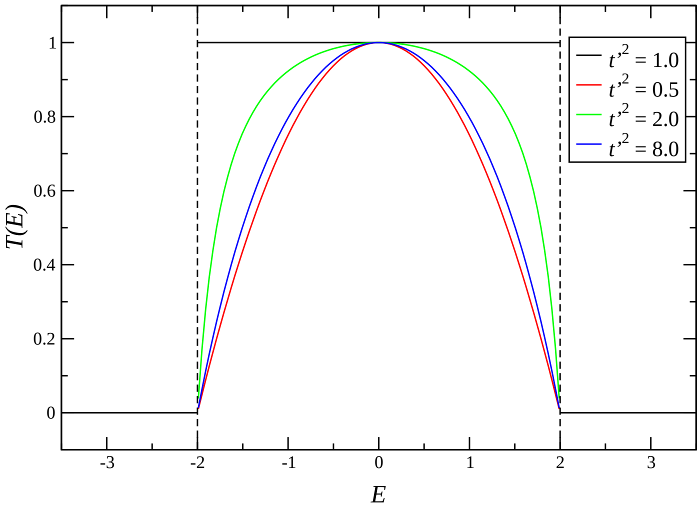

Figure 3.7: Transmission function for the linear chain without defect and with a single coupling defect with three different strengths t'. The onsite energy was chosen $\epsilon_0 = 0$. We observe that the transmission function is the same for t',$-t'$, and $\pm\frac{t'}{\sqrt{2t'^2-1}}$. $t = 1$ is our energy unit.

Case $t' \neq 1$, $\epsilon_0 \neq 0$. If the defect varies from the rest of the chain in both t' and ϵ_0, the transmission function loses its symmetry with respect to $E = 0$. Cf. Figure 3.8. In Figure 3.8 we observe that depending on the onsite energy ϵ_0 of the defect, there is an energy E for which $T = 1$, or not. The condition is that the second term in the denominator of (3.32) vanishes for E inside the band:

$$\left(1 - t'^2\right) E - \epsilon_0 = 0 \quad \wedge \quad |E| < 2 \tag{3.34}$$

It cannot be fulfilled if

$$|\epsilon_0| > 2\left|1 - t'^2\right| \tag{3.35}$$

Thus for defect energies given by this formula, no resonant tunneling is possible.

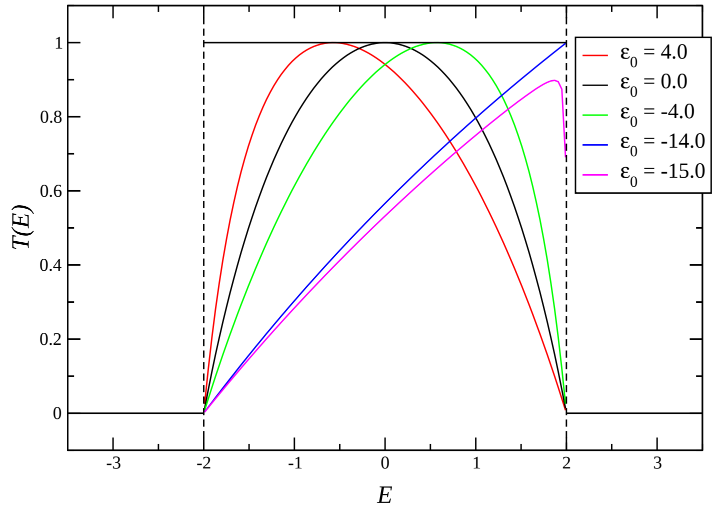

Figure 3.8: Transmission function for the linear chain without defect and with a single defect at different energies ϵ_0 coupled with $t'^2 = 8$. $t = 1$.

3.3.2 Different couplings to left and right contact

Now, let us study the single defect coupled by t_L to the left and t_R to the right half-infinite chain. Like before, for simplification of the notation we choose $\epsilon = 0$ to be the origin of the energy scale and $t = 1$ its unit. Then the transmission function reads

$$T(E) = \frac{t_L^2 t_R^2}{\frac{\left(t_L^2+t_R^2\right)^2}{4} + \frac{\left[\left(1-\frac{t_L^2+t_R^2}{2}\right)E-\epsilon_0\right]^2}{4-E^2}} \tag{3.36}$$

Some examples are plotted in Figure 3.9.

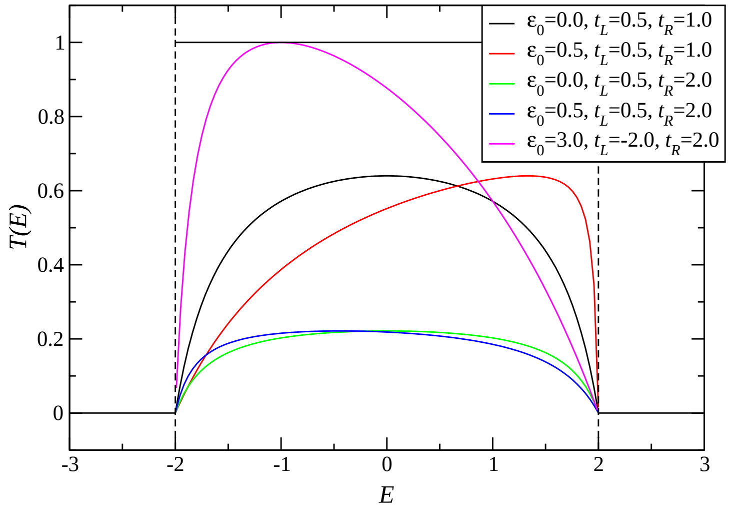

Figure 3.9: Transmission function for the linear chain with a single asymmetric defect. For the chosen parameters see the legend.

We see that here, $\frac{t_L^2+t_R^2}{2}$ plays the same role like t'^2 in the case discussed before (cf. (3.32)), i.e. maximum transmission is reached for $E = \frac{\epsilon_0}{1-\frac{t_L^2+t_R^2}{2}}$, yet the value of the maximum is given by $T = \frac{4t_L^2 t_R^2}{\left(t_L^2+t_R^2\right)^2}$. It is only $T = 1$ for $t_L = \pm t_R$.

3.4 The alternating chain

The alternating chain is composed of two types of sites (onsite energies ϵ and $-\epsilon$) which are coupled by the parameters t and $\bar{t}$, cf. Figure 3.10.

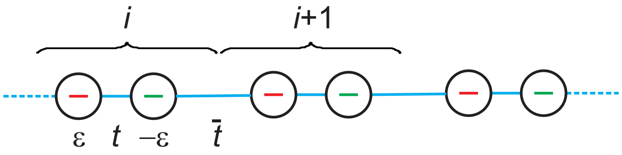

Figure 3.10: The infinite alternating chain.

The Hamiltonian is

$$H = \sum_{i=-\infty}^{\infty} \epsilon \left[|i,1\rangle\langle i,1| - |i,2\rangle\langle i,2|\right] + \left[t\,|i,1\rangle\langle i,2| + \bar{t}\,|i,2\rangle\langle i+1,1| + \text{H.c.}\right] \tag{3.37}$$

By a Fourier transformation we obtain the equivalent notation

$$H = \sum_k \epsilon\left[|k,1\rangle\langle k,1| - |k,2\rangle\langle k,2|\right] + \left[\left[t + \bar{t}\mathrm{e}^{\mathrm{i}k}\right]|k,1\rangle\langle k,2| + \text{H.c.}\right] \tag{3.38}$$

We see that a Fourier transform alone does not diagonalize H. Yet, we obtain a simpler 2×2 eigensystem problem

$$\begin{pmatrix} \epsilon & t + \bar{t}\mathrm{e}^{\mathrm{i}k} \\ t + \bar{t}\mathrm{e}^{-\mathrm{i}k} & -\epsilon \end{pmatrix} \begin{pmatrix} k,1' \\ k,2' \end{pmatrix} = E(k) \begin{pmatrix} k,1' \\ k,2' \end{pmatrix} \tag{3.39}$$

which has the eigenenergies

$$\begin{aligned} E_\pm(k) &= \pm\sqrt{\epsilon^2 + t^2 + \bar{t}^2 + 2t\bar{t}\cos(k)} \\ &= \pm\sqrt{\Delta^2 + 4t\bar{t}\cos^2(\tfrac{k}{2})} \end{aligned} \tag{3.40}$$

where

$$2\Delta \equiv 2\sqrt{\epsilon^2 + \left(t - \bar{t}\right)^2} \tag{3.41}$$

is the band gap between $E_+(k)$ and $E_-(k)$. An example band structure is plotted in Figure 3.11.

Thus the diagonalized Hamiltonian reads

$$H = \sum_k E_+(k)\left|k,1'\right\rangle\left\langle k,1'\right| + E_-(k)\left|k,2'\right\rangle\left\langle k,2'\right| \tag{3.42}$$

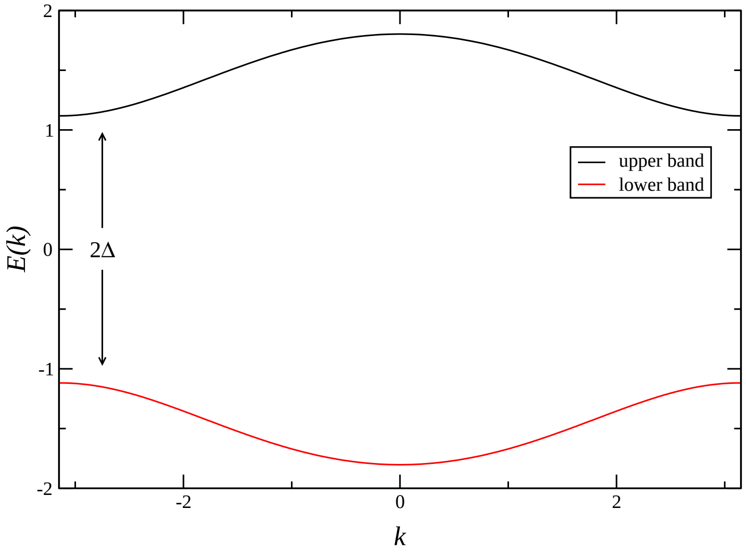

Figure 3.11: Bands $E(k)$ for the alternating chain with the parameters $\epsilon = 1$, $t = 1$, $\bar{t} = 0.5$. The band gap is $2\Delta = 2\sqrt{\epsilon^2 + \left(t - \bar{t}\right)^2} = 2.23$.

with

$$\left|k, 1'\right\rangle = \frac{1}{\sqrt{2}} \left[\left(1 - \frac{\epsilon}{\epsilon + E_+(k)}\right) |k,1\rangle + \left(1 - \frac{\epsilon}{\epsilon + E_+(k)}\right) \frac{E_+(k) - \epsilon}{E_+^2(k)} \mathrm{e}^{\mathrm{i}k} |k,2\rangle \right] \tag{3.43}$$

$$\left|k, 2'\right\rangle = \frac{1}{\sqrt{2}} \left[\left(1 + \frac{\epsilon}{\epsilon - E_-(k)}\right) |k,1\rangle + \left(1 + \frac{\epsilon}{\epsilon - E_-(k)}\right) \frac{E_-(k) - \epsilon}{E_-^2(k)} \mathrm{e}^{\mathrm{i}k} |k,2\rangle \right] \tag{3.44}$$

An alternative notation of the transformation can be found in [31].

3.5 The double chain

Now let us advance to quasi-linear systems and consider the infinite and half-infinite double chain and the transmission through defects in this kind of system.

3.5.1 Hamiltonian and its diagonalization

Like in the case of the linear chain we model the infinite double chain by a tight-binding Hamiltonian.

$$H = \sum_{i=-\infty}^{\infty} \left[|i,1\rangle\langle i+1,1| + |i,2\rangle\langle i+1,2| + t\,|i,1\rangle\langle i,2| + \mathrm{H.c.} \right] \tag{3.45}$$

The first entry (i or $i+1$) of the state vector denotes the position parallel to the chain, the second entry 1 (or 2) denotes lower (or upper) chain. In the definition we have chosen $\epsilon = 0$ for the onsite energies and taken the coupling $t_0 = 1$ along the chain as our energy unit. The Hamiltonian of the half-infinite double chain is just the same, with the only difference

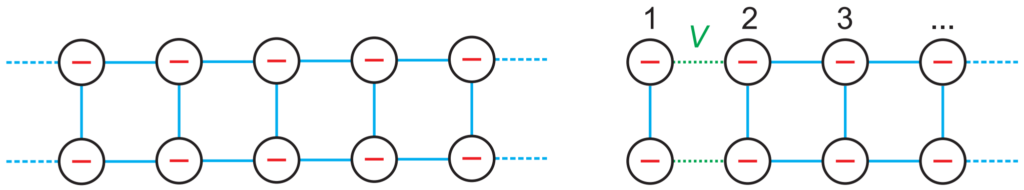

(a) Infinite double chain

(b) Half-infinite double chain

Figure 3.12: Infinite and half-infinite double chains. Like in the linear case, the surface Green function of the half-infinite double chain can be calculated by the Dyson equation.

that the summation over i has to start at 1. Pictures of the infinite and half-infinite double chain can be found in Figure 3.12.

Like in the linear case we look for the eigenvectors of the infinite double chain. First we use the transformation into symmetric ($1'$) and antisymmetric ($2'$) superpositions of the upper and lower chain states:

$$\left\{\begin{array}{l} \left|i,1'\right\rangle = \frac{1}{\sqrt{2}}\left(\left|i,1\right\rangle + \left|i,2\right\rangle\right) \\ \left|i,2'\right\rangle = \frac{1}{\sqrt{2}}\left(\left|i,1\right\rangle - \left|i,2\right\rangle\right) \end{array}\right\} \Leftrightarrow \left\{\begin{array}{l} \left|i,1\right\rangle = \frac{1}{\sqrt{2}}\left(\left|i,1'\right\rangle + \left|i,2'\right\rangle\right) \\ \left|i,2\right\rangle = \frac{1}{\sqrt{2}}\left(\left|i,1'\right\rangle - \left|i,2'\right\rangle\right) \end{array}\right\} \tag{3.46}$$

We obtain the Hamiltonian in the new basis

$$\begin{aligned} H = &\sum_i \left|i,1'\right\rangle\left\langle i+1,1'\right| + \left|i+1,1'\right\rangle\left\langle i,1'\right| + t\left|i,1'\right\rangle\left\langle i,1'\right| \\ &+ \sum_i \left|i,2'\right\rangle\left\langle i+1,2'\right| + \left|i+1,2'\right\rangle\left\langle i,2'\right| - t\left|i,2'\right\rangle\left\langle i,2'\right| \end{aligned} \tag{3.47}$$

which we recognize as the sum of two independent linear chain Hamiltonians (cf. (3.1) with $t \to 1$). Fourier transformations just like in the case of the linear chain lead to the eigenenergies

$$E_{\pm}(k) = \pm t + 2\cos(k) \tag{3.48}$$

where $+$ stems from the symmetric and $-$ from the antisymmetric states.[3] Thus we have two energy bands, split by the tunnel splitting $2t$. If $|t| > 2$, we obtain two separate bands without overlap.

Also the local density of states is a linear combination of the one of the linear chain.

$$D(E) = \left.\frac{\mathrm{d}k}{\pi \mathrm{d}E}\right|_E = \frac{1}{4\pi}\frac{1}{\sqrt{1-\left(\frac{t-E}{2}\right)^2}} + \frac{1}{4\pi}\frac{1}{\sqrt{1-\left(\frac{t+E}{2}\right)^2}} \tag{3.49}$$

It is displayed in Figure 3.13.

In the DOS we can clearly recognize the underlying single-chain DOS and Van-Hove singularities at the band edges. It is interesting to see the similarity with the DOS of a single-walled carbon nanotube as calculated by [42], which is displayed in Figure 3.14.

---

[3] Note that t itself is a signed quantity, cf. the discussion in Footnote 2 on page 15.

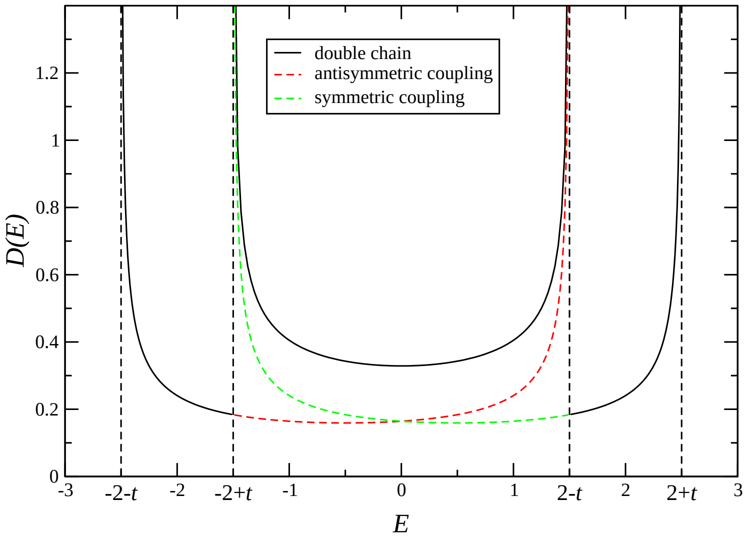

Figure 3.13: Density of states for the infinite double chain as defined in (3.49). The parameter $t = 0.5$ determines the relative shift of the single-chain DOSs: The relative shift between the symmetric (red) and antisymmetric (green) chain is $2t$.

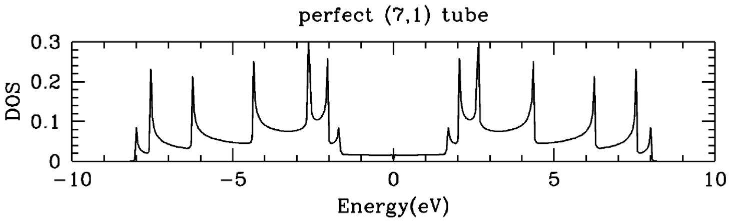

Figure 3.14: Density of states of a single-walled (7,1) carbon nanotube calculated by a tight-binding method, taken from [42]. It shows interesting similarity with the DOS of the double chain.

3.5.2 Surface Green function of the half-infinite double chain

Like in the case of the single chain, we can calculate the surface Green function of the half-infinite double chain with help of the Dyson equation, cf. (3.15)–(3.22). Again, the half-infinite chain is split into its surface and the rest, coupled by the interaction V to form the total system, cf. Figure 3.12.

Again we write

$$\hat{G} = \hat{g} + \hat{g}\hat{V}\hat{G} \tag{3.50}$$

where $\hat{g}$ is the Green function of the unperturbed and $\hat{G}$ of the perturbed system. Because of the fact that the unperturbed system, starting from the second site is the same like the perturbed, we can write

$$\hat{g} = \begin{pmatrix} \hat{g}_{11} & 0 & 0 & \dots \\ 0 & \hat{G}_{11} & \hat{G}_{12} & \dots \\ 0 & \hat{G}_{21} & \hat{G}_{22} & \dots \\ \vdots & \vdots & \vdots & \ddots \end{pmatrix} \qquad \hat{V} = \begin{pmatrix} 0 & \hat{t} & 0 & \dots \\ \hat{t}^{+} & 0 & 0 & \dots \\ 0 & 0 & 0 & \dots \\ \vdots & \vdots & \vdots & \ddots \end{pmatrix} \tag{3.51}$$

where all entries in (3.51) are 2 × 2 matrices (for clarity they wear hats), i.e.

$$\hat{g}_{11} \equiv \begin{pmatrix} E & -t \\ -t & E \end{pmatrix}^{-1} = \frac{1}{E^2 - t^2} \begin{pmatrix} E & t \\ t & E \end{pmatrix} \tag{3.52}$$

and

$$\hat{t} = \begin{pmatrix} 1 & 0 \\ 0 & 1 \end{pmatrix} \tag{3.53}$$

Now for the $(1,1)$ components of the Green function we find just like for the single chain

$$\hat{G}_{11} = \hat{g}_{11} + \hat{g}_{11} \hat{t} \hat{G}_{11} \hat{t}^{+} \hat{G}_{11} = \hat{g}_{11} + \hat{g}_{11} \hat{t}^2 \hat{G}_{11}^2 \tag{3.54}$$

where the difference is that $\hat{G}_{11}$, $\hat{g}_{11}$, and $\hat{t}$ are matrices and thus (3.54) a quadratic matrix equation. A systematic description of how to solve this kind of equations analytically and numerically can be found in [82, 83, 180]. An iterative solution, the so-called decimation technique, is used in Section 3.8. Yet in our case, we can solve (3.54) without an advanced formalism. We begin by writing (3.54) in components.

$$\begin{pmatrix} G_{1111} & G_{1112} \\ G_{1121} & G_{1122} \end{pmatrix} - \frac{1}{E^2 - t^2} \begin{pmatrix} E & t \\ t & E \end{pmatrix} \begin{pmatrix} G_{1111} & G_{1112} \\ G_{1121} & G_{1122} \end{pmatrix}^2 = \frac{1}{E^2 - t^2} \begin{pmatrix} E & t \\ t & E \end{pmatrix} \tag{3.55}$$

As the upper and lower chain are symmetric, also the corresponding Green function elements have to be the same. Thus we can simplify (3.55) using the notation

$$G_1 \equiv G_{1111} = G_{1122} \tag{3.56}$$

$$G_2 \equiv G_{1112} = G_{1121} \tag{3.57}$$

to obtain the nonlinear (quadratic) system of equations

$$\left\{ \begin{array}{l} G_1 - \frac{1}{E^2 - t^2} \left(E \left(G_1^2 + G_2^2 \right) + 2tG_1G_2 \right) = \frac{E}{E^2 - t^2} \\ G_2 - \frac{1}{E^2 - t^2} \left(2EG_1G_2 + t \left(G_1^2 + G_2^2 \right) \right) = \frac{t}{E^2 - t^2} \end{array} \right\} \quad \begin{array}{c} (1) \\ (2) \end{array} \tag{3.58}$$

which can be simplified by considering (1) × E – (2) × t and (1) × t – (2) × E:

$$\left\{ \begin{array}{r} EG_1 - tG_2 - \left(G_1^2 + G_2^2 \right) = 1 \\ tG_1 - EG_2 + 2G_1G_2 = 0 \end{array} \right\} \tag{3.59}$$

We obtain the solutions of (3.59) by MATHEMATICA:

$$\left\{ \begin{array}{l} G_1 = \frac{E}{2} \mp \frac{tE}{\sqrt{2}\sqrt{-4+E^2+t^2 \pm \sqrt{\left(E^2-t^2-4\right)^2 - 16t^2}}} \\ G_2 = -\frac{t}{2} \pm \frac{\sqrt{2}}{4} \sqrt{-4 + E^2 + t^2 \pm \sqrt{\left(E^2 - t^2 - 4\right)^2 - 16t^2}} \end{array} \right\} \tag{3.60}$$

These are four solutions, $\{G_{1-,+}, G_{2+,+}\}$ through $\{G_{1+,-}, G_{2-,-}\}$.[4] Out of the four mathematically possible solutions, for every energy E only one is physical. Like in the case of the single chain, the requirement of a nonnegative local density of states ($\operatorname{Im} G_1 \leq 0$, cf. (2.6)), the normalization of the local density of states ($-\frac{1}{\pi}\int_{-\infty}^{\infty} \mathrm{d}E\ \mathrm{Im}\, G_1(E) = 1$) and the Kramers-Kronig relation (cf. (2.58)) lead to the physical solution (for $t \in [0,2]$)

---

[4] The first sign in G_1 being "+" requires the first sign in G_2 to be "−", whereas the second signs have to be chosen equal.

$$\left\{ \begin{array}{l} G_1 = \frac{E}{2} + \frac{1}{4} \times \begin{cases} \sqrt{(E-t)^2-4} + \sqrt{(E+t)^2-4} & E < -2-t \\ \sqrt{(E-t)^2-4} - \mathrm{i}\sqrt{4-(E+t)^2} & -2-t \leq E \leq -2+t \\ -\mathrm{i}\sqrt{4-(E-t)^2} - \mathrm{i}\sqrt{4-(E+t)^2} & -2+t < E < 2-t \\ -\sqrt{(E+t)^2-4} - \mathrm{i}\sqrt{4-(E-t)^2} & 2-t \leq E \leq 2+t \\ -\sqrt{(E+t)^2-4} - \sqrt{(E-t)^2-4} & 2+t < E \end{cases} \\ G_2 = -\frac{t}{2} + \frac{1}{4} \times \begin{cases} \sqrt{(E-t)^2-4} - \sqrt{(E+t)^2-4} & E < -2-t \\ \sqrt{(E-t)^2-4} + \mathrm{i}\sqrt{4-(E+t)^2} & -2-t \leq E \leq -2+t \\ -\mathrm{i}\sqrt{4-(E-t)^2} + \mathrm{i}\sqrt{4-(E+t)^2} & -2+t < E < 2-t \\ \sqrt{(E+t)^2-4} - \mathrm{i}\sqrt{4-(E-t)^2} & 2-t \leq E \leq 2+t \\ \sqrt{(E+t)^2-4} - \sqrt{(E-t)^2-4} & 2+t < E \end{cases} \end{array} \right\} \tag{3.61}$$

For $t \in [2,\infty)$ the solution has the following form

$$\left\{ \begin{array}{l} G_1 = \frac{E}{2} + \frac{1}{4} \times \begin{cases} \sqrt{(E-t)^2-4} + \sqrt{(E+t)^2-4} & E < -2-t \\ \sqrt{(E-t)^2-4} - \mathrm{i}\sqrt{4-(E+t)^2} & -2-t \leq E \leq -t+2 \\ \sqrt{(E-t)^2-4} - \sqrt{(E+t)^2-4} & -t+2 < E < t-2 \\ -\sqrt{(E+t)^2-4} - \mathrm{i}\sqrt{4-(E-t)^2} & t-2 \leq E \leq t+2 \\ -\sqrt{(E+t)^2-4} - \sqrt{(E-t)^2-4} & 2+t < E \end{cases} \\ G_2 = -\frac{t}{2} + \frac{1}{4} \times \begin{cases} \sqrt{(E-t)^2-4} - \sqrt{(E+t)^2-4} & E < -2-t \\ \sqrt{(E-t)^2-4} + \mathrm{i}\sqrt{4-(E+t)^2} & -2-t \leq E \leq -t+2 \\ \sqrt{(E-t)^2-4} + \sqrt{(E+t)^2-4} & -t+2 < E < t-2 \\ \sqrt{(E+t)^2-4} - \mathrm{i}\sqrt{4-(E-t)^2} & t-2 \leq E \leq t+2 \\ \sqrt{(E+t)^2-4} - \sqrt{(E-t)^2-4} & 2+t < E \end{cases} \end{array} \right\} \tag{3.62}$$

The surface Green functions $G_1(E)$ and $G_2(E)$ for $t \in [0,2]$ and $t \in [2,\infty)$ are plotted in Figures 3.15 through 3.18, respectively.

By comparison of the surface Green functions of the double chain, (3.61) and (3.62), with the one of the single chain (3.22), we find that, like the Hamiltonian, $G_{\text{double chain}}$ is the sum of two $G_{\text{single chain}}$ which are shifted by the tunnel splitting $2t$ in energy. In detail: If $g_1(E)$ is the surface Green function for a single chain shifted up in energy by t and $g_2(E)$

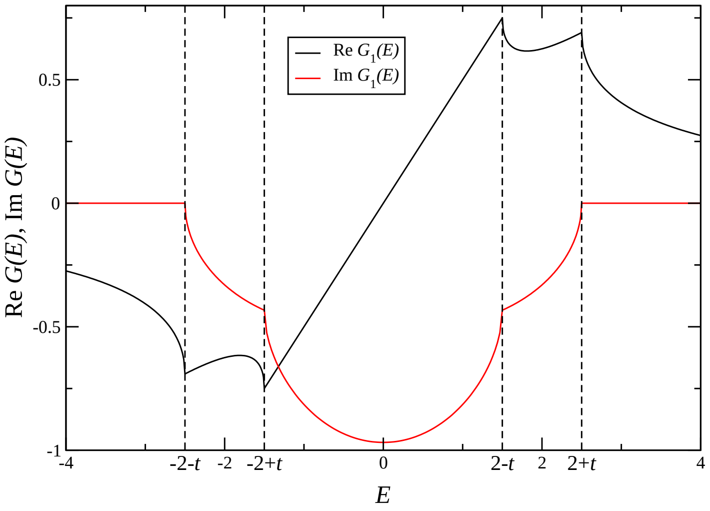

Figure 3.15: Real and imaginary part of the surface Green function G_1 of a half-infinite double chain for $t = 0.5 \in [0, 2]$.

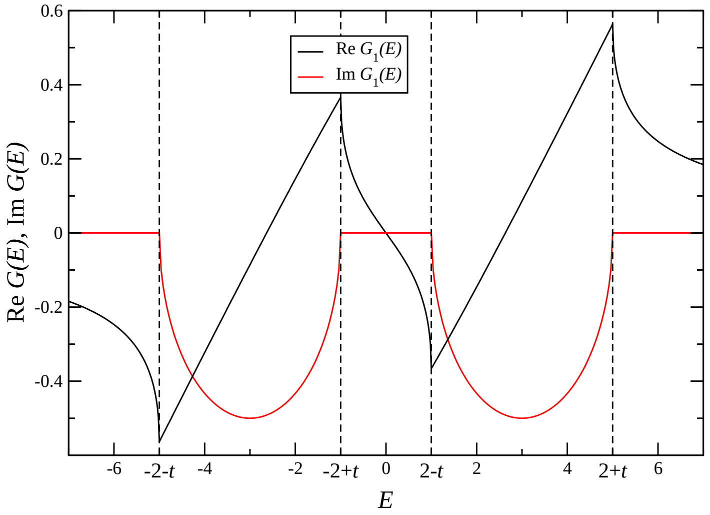

Figure 3.16: Real and imaginary part of the surface Green function G_1 of a half-infinite double chain for $t = 3 \in [2, \infty)$.

is the one shifted down in energy by $-t$, i.e.

$$g_1(E) = \frac{E-t}{2} + \frac{1}{2}\begin{cases} \sqrt{(E-t)^2 - 4} & E - t \leq -2 \\ -\mathrm{i}\sqrt{4-(E-t)^2} & |E-t| < 2 \\ -\sqrt{(E-t)^2-4} & E - t \geq 2 \end{cases} \tag{3.63}$$

$$g_2(E) = \frac{E+t}{2} + \frac{1}{2}\begin{cases} \sqrt{(E+t)^2 - 4} & E + t \leq -2 \\ -\mathrm{i}\sqrt{4-(E+t)^2} & |E+t| < 2 \\ -\sqrt{(E+t)^2-4} & E + t \geq 2 \end{cases} \tag{3.64}$$

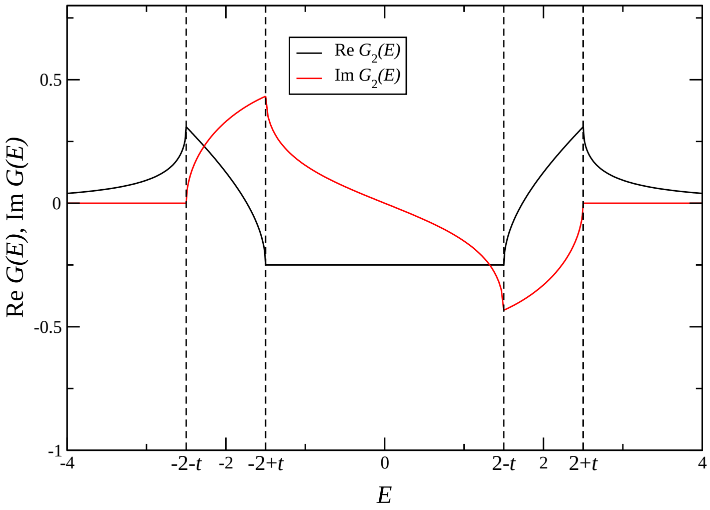

Figure 3.17: Real and imaginary part of the surface Green function G_2 of a half-infinite double chain for $t = 0.5 \in [0, 2]$.

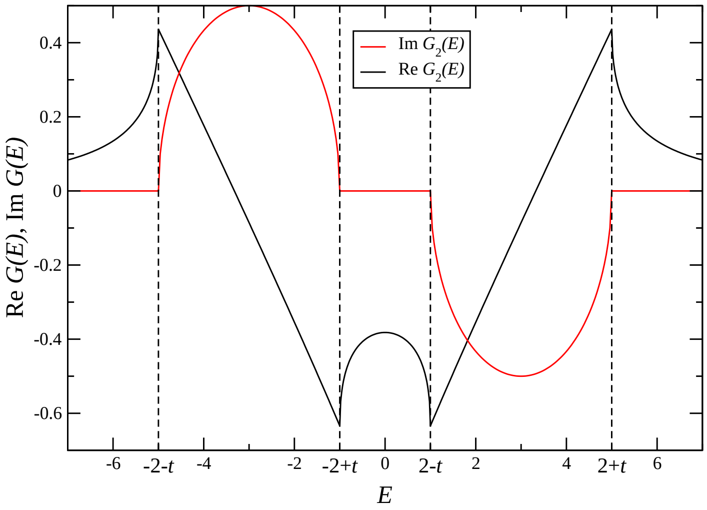

Figure 3.18: Real and imaginary part of the surface Green function G_2 of a half-infinite double chain for $t = 3 \in [2, \infty)$.

then the surface Green function of the double chain is composed of

$$G_1 = \frac{g_1 + g_2}{2} \qquad \text{and} \tag{3.65}$$

$$G_2 = \frac{g_1 - g_2}{2} \tag{3.66}$$

These relations hold independently of the value of t. This is a natural consequence of the base transformation (3.46) which we used for finding the eigenenergies of the double chain Hamiltonian. We will revisit this point in Section 3.7.1, where we discuss the surface Green functions for n-tuple chains.

3.6 The triple chain

In analogy with the double chain we define the infinite triple chain in the following way.

$$H = \sum_{i=-\infty}^{\infty} \left[|i,1\rangle\langle i+1,1| + |i,2\rangle\langle i+1,2| + |i,3\rangle\langle i+1,3| + t\,|i,1\rangle\langle i,2| + t\,|i,2\rangle\langle i,3| + \text{H.c.}\right] \tag{3.67}$$

The Hamiltonian for the half-infinite triple chain is obtained by summing $i = 1 \dots \infty$ instead of $i = -\infty \dots \infty$.

Again we diagonalize by a base transformation

$$\left\{\begin{array}{l} \left|i,1'\right\rangle = \frac{1}{2}\left|i,1\right\rangle + \frac{1}{\sqrt{2}}\left|i,2\right\rangle + \frac{1}{2}\left|i,3\right\rangle \\ \left|i,2'\right\rangle = \frac{1}{\sqrt{2}}\left|i,1\right\rangle - \frac{1}{\sqrt{2}}\left|i,3\right\rangle \\ \left|i,3'\right\rangle = \frac{1}{2}\left|i,1\right\rangle - \frac{1}{\sqrt{2}}\left|i,2\right\rangle + \frac{1}{2}\left|i,3\right\rangle \end{array}\right\} \Leftrightarrow \left\{\begin{array}{l} \left|i,1\right\rangle = \frac{1}{2}\left|i,1'\right\rangle + \frac{1}{\sqrt{2}}\left|i,2'\right\rangle + \frac{1}{2}\left|i,3'\right\rangle \\ \left|i,2\right\rangle = \frac{1}{\sqrt{2}}\left|i,1'\right\rangle - \frac{1}{\sqrt{2}}\left|i,3'\right\rangle \\ \left|i,3\right\rangle = \frac{1}{2}\left|i,1'\right\rangle - \frac{1}{\sqrt{2}}\left|i,2'\right\rangle + \frac{1}{2}\left|i,3'\right\rangle \end{array}\right\} \tag{3.68}$$

and obtain the transformed Hamiltonian

$$\begin{aligned} H = &\sum_i t\sqrt{2}\left|i,1'\right\rangle\left\langle i,1'\right| + \left|i,1'\right\rangle\left\langle i+1,1'\right| + \text{H.c.} \\ &+ \sum_i \left|i,2'\right\rangle\left\langle i+1,2'\right| + \text{H.c.} \\ &+ \sum_i (-t\sqrt{2})\left|i,3'\right\rangle\left\langle i,3'\right| + \left|i,3'\right\rangle\left\langle i+1,3'\right| + \text{H.c.} \end{aligned} \tag{3.69}$$

which we identify as the sum of three independent single chain Hamiltonians (cf. (3.1)), shifted by the energies $+t\sqrt{2}$, 0, and $-t\sqrt{2}$, respectively.

The eigenenergy spectrum and DOS are analogous to the ones of the double chain, cf. (3.48), (3.49), and Figure 3.13.

3.7 The n-tuple chain and the 2d tight-binding grid

What we have learnt from the considerations of the double and triple chain can be generalized for the n-tuple chain. The n-tuple chain Hamiltonian is

$$H = \sum_{i=-\infty}^{\infty} \sum_{j=1}^{n} |i,j\rangle\langle i+1,j| + \text{H.c.} + t \sum_{i=-\infty}^{\infty} \sum_{j=1}^{n-1} |i,j\rangle\langle i,j+1| + \text{H.c.} \tag{3.70}$$

It can be diagonalized by the base transformation

$$\left|i,j'\right\rangle = \sum_{j=1}^{n} \sqrt{\tfrac{2}{n+1}} \sin(j'\frac{j\pi}{n+1})\left|i,j\right\rangle \qquad \Leftrightarrow \qquad \left|i,j\right\rangle = \sum_{j'=1}^{n} \sqrt{\tfrac{2}{n+1}} \sin(j\frac{j'\pi}{n+1})\left|i,j'\right\rangle \tag{3.71}$$

and we obtain

$$H = \sum_{i=-\infty}^{\infty} \sum_{j'=1}^{n} 2t\cos(\tfrac{j'\pi}{n+1})\, |i,j'\rangle\langle i,j'| + |i,j'\rangle\langle i+1,j'| + \text{H.c.} \tag{3.72}$$

Thus the n-tuple chain decomposes into n single chains which are shifted in energy by $2t\cos(\frac{j'\pi}{n+1})$.

Having found the diagonalized Hamiltonian for the n-tuple chain we can proceed to write down its local density of states, which is nothing but the sum of shifted single-chain LDOS. Recalling (3.6) we find

$$D_{n\text{-tuple}}(E) = \begin{cases} \frac{1}{2\pi n} \sum\limits_{j=1}^{n} \frac{1}{\sqrt{1-\left(\frac{E}{2}-t\cos(\frac{j\pi}{n+1})\right)^2}} & |E| < 2+2\,|t|\cos(\frac{\pi}{n+1}) \\ 0 & \text{else} \end{cases} \tag{3.73}$$

Here, only the summands with positive radicand are taken into account (only they appear in the imaginary part of G). For $n \to \infty$ (i.e. an infinite 2d tight-binding grid) the LDOS converts into the integral

$$D_{2\mathrm{d}}(E) = \begin{cases} \frac{1}{2\pi^2} \int\limits_0^{\arccos(\frac{E-2}{2t})} \mathrm{d}j \frac{1}{\sqrt{1-\left(\frac{E}{2}-t\cos(j)\right)^2}} & |E| < 2+2\,|t| \\ 0 & \text{else} \end{cases} \tag{3.74}$$

For $n = 10$ and $n = \infty$, the LDOS is plotted in Figure 3.19. Interestingly, the Van-Hove singularities of the individual chains vanish all but the one in the middle of the band. At the band edges, there is a finite discontinuity. These feature of two-dimensional crystals were already derived in 1953 in the original paper by Van Hove [181].

The Green function and DOS of a two-dimensional tight-binding grid (derived in a completely different way) can also be found in [62, Section 5.3.2].

3.7.1 Surface Green functions for n-tuple chains

Now that we have found a way to diagonalize the n-tuple chain Hamiltonian we can revisit the problem of the surface Green functions, cf. Section 3.5.2. In order to obtain the surface Green function we had to solve (3.54), a quadratic matrix equation. Now let us reconsider the equation:

$$\hat{G}_{11} = \hat{g}_{11} + \hat{g}_{11}\hat{G}_{11}^2 \tag{3.75}$$

where we have taken into account that $\hat{t}$ in (3.54) is the unit matrix.

Now g_{11} is the Green function of the surface Hamiltonian H_{11}. Then, the surface Hamiltonian reads

$$H_{11} = \begin{pmatrix} 0 & t & 0 & \dots & 0 \\ t & 0 & t & & \\ 0 & t & 0 & \ddots & \\ \vdots & & \ddots & \ddots & t \\ 0 & & & t & 0 \end{pmatrix} \tag{3.76}$$

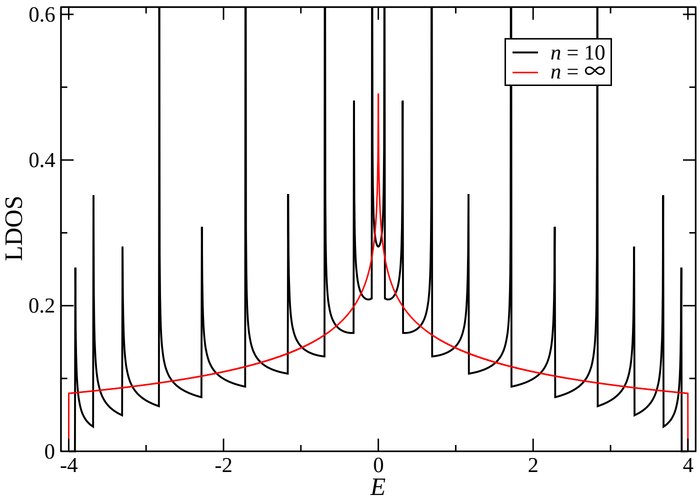

Figure 3.19: Local density of states within a 10-tuple chain and in a 2d tight-binding grid. The integral for the 2d grid, Equation (3.74), was evaluated numerically by Maple. In both cases, $t = 1$. For $n = \infty$, the LDOS has a pole at $E = 0$ and is discontinuous at the band edges, where it jumps from 0 to $\frac{1}{4\pi}$.

We have seen that this matrix has the diagonal form

$$H'_{11} = \begin{pmatrix} 2t\cos(\frac{1\pi}{n+1}) & & & \\ & 2t\cos(\frac{2\pi}{n+1}) & & \\ & & \dots & \\ & & & 2t\cos(\frac{n\pi}{n+1}) \end{pmatrix} \tag{3.77}$$

which is mediated by the base transformation

$$H_{11} = UH'_{11}U^{+} \qquad \text{where} \qquad U = \sqrt{\frac{2}{n+1}} \begin{pmatrix} \sin(1\frac{1\pi}{n+1}) & \sin(1\frac{2\pi}{n+1}) & \dots & \sin(1\frac{n\pi}{n+1}) \\ \sin(2\frac{1\pi}{n+1}) & \sin(2\frac{2\pi}{4}) & \dots & \sin(2\frac{n\pi}{n+1}) \\ \vdots & \vdots & \ddots & \vdots \\ \sin(n\frac{1\pi}{n+1}) & \sin(n\frac{2\pi}{n+1}) & \dots & \sin(n\frac{n\pi}{n+1}) \end{pmatrix} \tag{3.78}$$

In the same basis, by (2.49) also g_{11} is diagonal:[5]

$$g' = \begin{pmatrix} \frac{1}{E-2t\cos(\frac{1\pi}{n+1})} & & & \\ & \frac{1}{E-2t\cos(\frac{2\pi}{n+1})} & & \\ & & \dots & \\ & & & \frac{1}{E-2t\cos(\frac{n\pi}{n+1})} \end{pmatrix} \tag{3.79}$$

Therefore, (3.75) has a diagonal solution in the eigenbasis of H_{11}, namely

$$\begin{aligned} G'_{jj} &= \frac{1}{2g'_{jj}} \pm \sqrt{-1 + \frac{1}{4g'^{2}_{jj}}} \\ &= \frac{E - 2t\cos(\frac{j\pi}{n+1})}{2} \pm \frac{1}{2}\sqrt{\left(E - 2t\cos(\frac{j\pi}{n+1})\right)^2 - 4} \end{aligned} \tag{3.80}$$

---

[5] For clarity, in the following we drop the index 11.

By comparing with (3.22) we find that the correct sign in front of the square root in (3.80) is

$$\pm = \begin{cases} + & \text{for } E - 2t\cos(\frac{j\pi}{n+1}) \leq -2 \\ -\mathrm{i} & \text{for } -2 < E - 2t\cos(\frac{j\pi}{n+1}) < 2 \\ - & \text{for } E - 2t\cos(\frac{j\pi}{n+1}) \geq 2 \end{cases} \tag{3.81}$$

Here the "sign $-\mathrm{i}$" requires the radicand to be multiplied by -1.

Back transformation yields the surface Green function in the original basis

$$G_{ik} = \frac{2}{n+1} \sum_{j=1}^{n} \sin(\tfrac{ij\pi}{n+1}) \sin(\tfrac{jk\pi}{n+1}) G'_{jj} \tag{3.82}$$

These are the surface Green functions which we need for the calculation of self-energies in transmission problems.

With help of the surface Green function we can analyze how the density of states is distributed along the edge of a chain bundle. In Figure 3.20, the local density of states along the end of a bundle of 11 chains is shown.

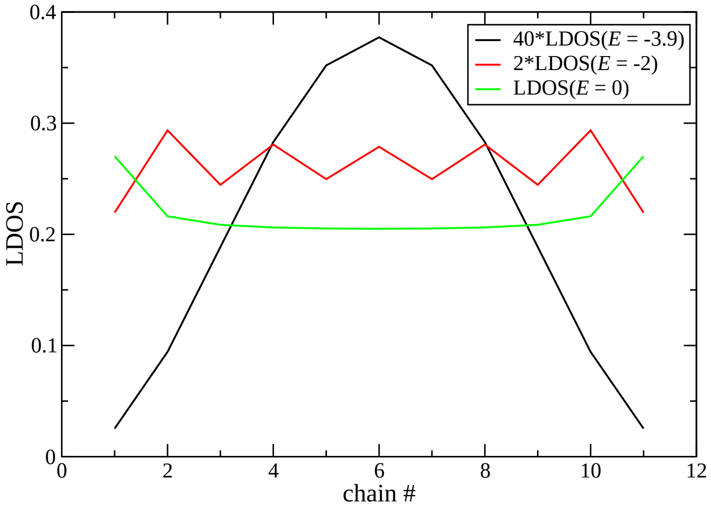

Figure 3.20: Local density of states along the end of an 11-tuple chain for three different energies within the band, using $t = 1$. Note the different scales. We observe that as we go to the band edges ($E \to \pm 4$), the LDOS gets concentrated in the middle of the chain bundle.

3.7.2 Transmission through defects: symmetry effects

The diagonalization of the double chain was done by a symmetric and an antisymmetric linear combination of the original base states, cf. (3.46). The symmetry of the eigenstates of the chain is also reflected in the transmission through defects which depends on the symmetry of the coupling to the left and right chains. We will discuss this using four examples.

For the calculation of the examples, we need the transmission formula (2.45), the definition of the self-energy (2.19), and the surface Green functions of double and triple chain, which here we denote as $G_{d,ij}$ and $G_{t,ij}$, defined in (3.80)–(3.82).

3.7.2.1 Example 1: symmetrically coupled single defect

Here we calculate the transmission through a symmetrically coupled defect (onsite energy ϵ, coupling matrix elements $t_l = t_r$) between two identical half-infinite double chains as defined in (3.45), see Figure 3.21

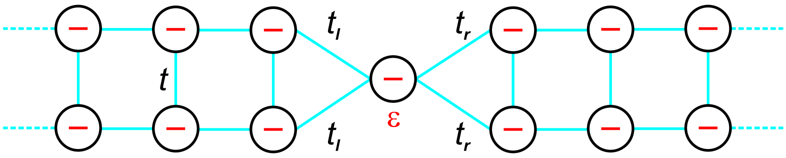

Figure 3.21: A symmetrically coupled defect between two identical half-infinite double chains.

The Green function of the defect is

$$G(E) = \frac{1}{E - \epsilon - \Sigma_L - \Sigma_R} \tag{3.83}$$

where

$$\begin{aligned} \Sigma_L &= \hat{t}_L \hat{G}_{LL} \hat{t}_L^+ \\ &= \begin{pmatrix} t_l & t_l \end{pmatrix} \begin{pmatrix} G_{d,11} & G_{d,12} \\ G_{d,21} & G_{d,22} \end{pmatrix} \begin{pmatrix} t_l \\ t_l \end{pmatrix} \\ &= 2t_l^2 \left(G_{d,11} + G_{d,12} \right) = 2t_l^2 G'_{d,11} \end{aligned} \tag{3.84}$$

and the analogous Σ_R are the self-energies due to the coupling to the left and right double chain.

We find

$$T(E) = \begin{cases} \frac{4t_l^4\left(4-(E-t)^2\right)}{\left(E\left(1-2t_l^2\right)-t\left(\frac{\epsilon}{t}-2t_l^2\right)\right)^2+4t_l^4\left(4-(E-t)^2\right)} & |E-t| < 2 \\ 0 & \text{else} \end{cases} \tag{3.85}$$

which for $\epsilon = t$ and $t_l = t_r = \frac{1}{\sqrt{2}}$ simplifies to

$$T(E) = \begin{cases} 1 & |E-t| < 2 \\ 0 & \text{else} \end{cases} \tag{3.86}$$

We recognize this as the window function we know from the single chain without defect (3.33) shifted by the energy $+t$.

The explanation is the following. As the coupling is symmetric, only the symmetric band of the double chain (which is shifted in energy by $+t$) carries transmitting states. If now the defect matches the energy of the symmetric band ($\epsilon = t$) and the coupling to left and right contact is equivalent to the coupling along the chain ($2t_l^2 = 1$), effectively there is no defect in the symmetric band of the double chain.

3.7.2.2 Example 2: antisymmetrically-symmetrically coupled single defect

Now we consider the situation where the defect is coupled antisymmetrically to the left double chain and symmetrically to the right double chain, cf. Figure 3.22.

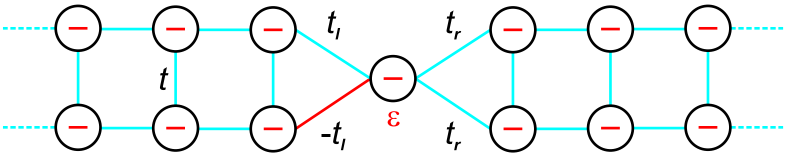

Figure 3.22: A defect coupled antisymmetrically to the left, and symmetrically to the right half-infinite double chain.

The different couplings lead to different self energies: Σ_R is just like in example 1, whereas

$$\begin{aligned}\Sigma_L &= \hat{t}_L \hat{G}_{LL} \hat{t}_L^+ \\ &= \begin{pmatrix} t_l & -t_l \end{pmatrix} \begin{pmatrix} G_{d,11} & G_{d,12} \\ G_{d,21} & G_{d,22} \end{pmatrix} \begin{pmatrix} t_l \\ -t_l \end{pmatrix} \\ &= 2t_l^2 \left(G_{d,11} - G_{d,12}\right) = 2t_l^2 G'_{d,22}\end{aligned} \tag{3.87}$$

With $t_l = t_r$ this leads to the transmission

$$T(E) = \begin{cases} \frac{4t_l^4\sqrt{4-(E-t)^2}\sqrt{4-(E+t)^2}}{\left(E\left(1-2t_l^2\right)-\epsilon\right)^2+t_l^4\left(\sqrt{4-(E-t)^2}+\sqrt{4-(E+t)^2}\right)^2} & |E-t|<2 \ \wedge \ |E+t|<2 \\ 0 & \text{else} \end{cases} \tag{3.88}$$

We see that there is transmission only for energies which belong to both the symmetric *and* the antisymmetric double chain band. If the parameter $|t| > 2$, there is no overlap between the bands, and hence there is no transmission.

An example where there is a band overlap is plotted in Figure 3.23.

3.7.2.3 Example 3: defect coupled to double and triple chain

As the third example we consider a defect (onsite energy 0) between a double and a triple chain. The double chain shall have a shift in energy by ϵ. To the left, the defect is coupled antisymmetrically to the double chain (coupling energy t_l), to the right it is connected to the first and the third strand of the triple chain in an antisymmetric way (coupling energy t_r), cf. Figure 3.24.

In this situation, the self-energy Σ_L is just like in example 2, and

$$\begin{aligned}\Sigma_R &= \hat{t}_R \hat{G}_{RR} \hat{t}_R^+ \\ &= \begin{pmatrix} t_r & 0 & -t_r \end{pmatrix} \begin{pmatrix} G_{t,11} & G_{t,12} & G_{t,13} \\ G_{t,21} & G_{t,22} & G_{t,23} \\ G_{t,31} & G_{t,32} & G_{t,33} \end{pmatrix} \begin{pmatrix} t_r \\ 0 \\ -t_r \end{pmatrix} \\ &= t_r^2 \left(G_{t,11} - 2G_{t,13} + G_{t,33}\right) = 2t_r^2 G'_{t,22}\end{aligned} \tag{3.89}$$

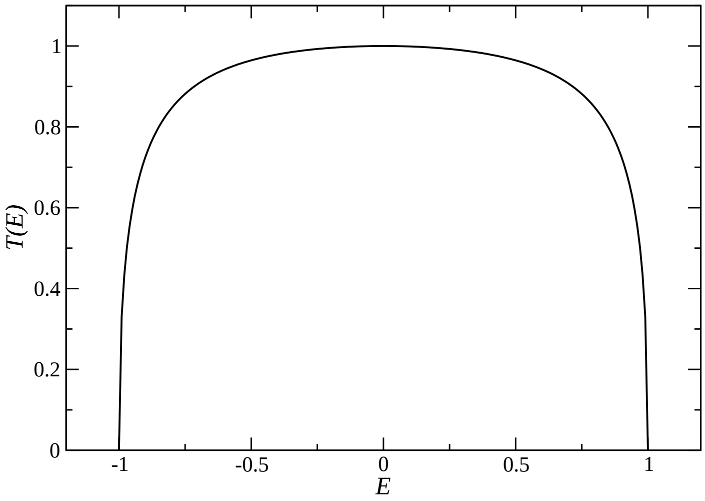

Figure 3.23: Transmission through the antisymmetrically-symmetrically coupled defect. The parameters are $t = 1$, $t_l = t_r = \frac{1}{\sqrt{2}}$ and $\epsilon = 0$. Only where the symmetric and antisymmetric double chain bands overlap, there is transmission.

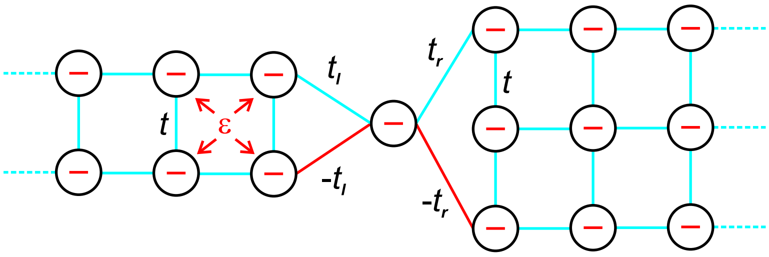

Figure 3.24: A defect coupled to a double chain to the left and a triple chain to the right.

Thus the transmission is

$$T(E) = \begin{cases} \frac{4t_l^2 t_r^2 \sqrt{4-(E-\epsilon+t)^2}\sqrt{4-E^2}}{\left(E\left(1-t_l^2-t_r^2\right)-t_l^2 t+t_l^2\epsilon\right)^2+\left(t_l^2\sqrt{4-(E-\epsilon+t)^2}+t_r^2\sqrt{4-E^2}\right)^2} & |E-\epsilon+t|<2 \ \wedge \ |E|<2 \\ 0 & \text{else} \end{cases} \tag{3.90}$$

We observe that for $\epsilon = t$, $t_l = \frac{1}{\sqrt{2}}$ and $t_r = \frac{1}{\sqrt{2}}$, we obtain again the window function

$$T(E) = \begin{cases} 1 & |E| < 2 \\ 0 & \text{else} \end{cases} \tag{3.91}$$

like in the single chain without defect.

The explanation is the following. With the energy shift ϵ we align the antisymmetric band of the double chain with the second band (antisymmetric coupling of first and third chain) of the triple chain. Both bands are centered at 0, the onsite energy of the defect. By choosing $2t_l^2 = 2t_r^2 = 1$, the effective coupling across the defect (cf. Σ_L and Σ_R) becomes the same like within the chains.

3.7.2.4 Example 4: double defects between double chain

As the final example we study a double defect between two double chains with parameters $\epsilon = 0$ and $t = 1$, cf. Figure 3.25. Let the defect onsite energies be ϵ_1 and ϵ_2, the intra-defect coupling t_d, and the couplings to left and right $t_{l,11}$ through $t_{r,22}$.

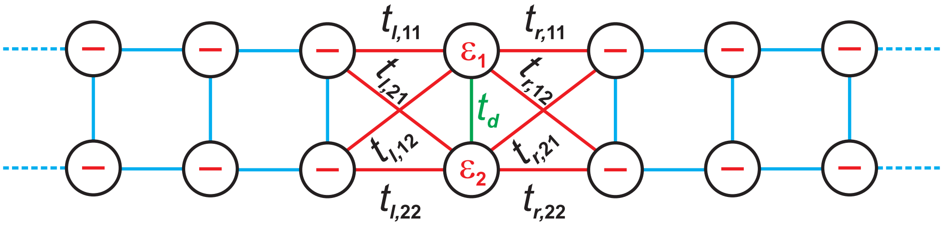

Figure 3.25: A double defect coupled to half-infinite double chains to left and right.

As the first configuration we consider $\epsilon_1 = \epsilon_2 = 0$, $t_{l,11} = t_{r,11} = t_{l,22} = t_{r,22} = t_d = 1$, $t_{l,12} = t_{l,21} = t_{r,12} = t_{r,21} = 0$. In this case, the "defect" in fact is just another chain segment, and as there is no defect, we expect perfect transmission within the bands. The transmission function is displayed in Figure 3.26 as "configuration 1".

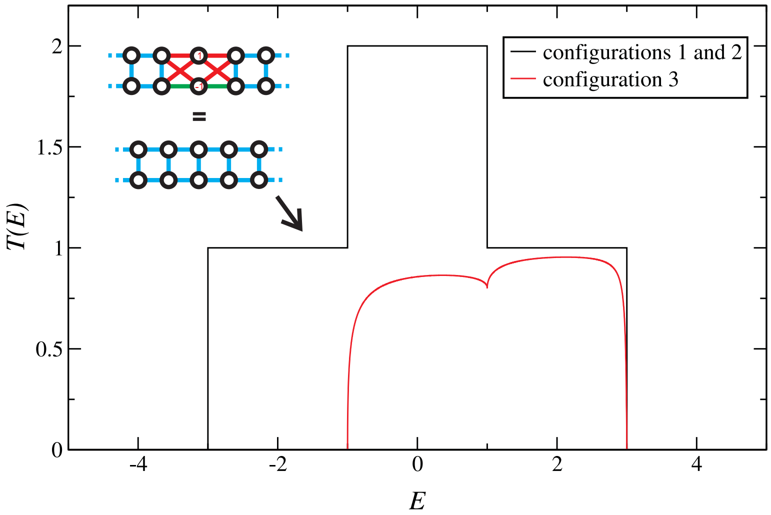

Figure 3.26: Transmission through a double chain with and without double defect, and through different interconnected double chains (see text below). $T(E) = 2$ means that at energy E both double chain bands have perfect transmission, i.e. we have two conducting channels. For the explanation of the different configurations see the text.

What surprises at first is that the transmission function $T(E)$ reaches the value 2. It is easily understood when considering that in the energy range $[-t, t]$ both bands show perfect transmission. See also the discussion at the end of Section 2.3.

Knowing example 1 from above (Section 3.7.2.1) we can design another configuration which shows perfect transmission within both double chain bands. Therefore we couple site one of the defect symmetrically to the left and right chain, $t_{l,11} = t_{l,12} = t_{r,11} = t_{r,12} = \frac{1}{\sqrt{2}}$, and site two antisymmetrically to the chains, $t_{l,21} = -t_{l,22} = t_{r,21} = -t_{r,22} = \frac{1}{\sqrt{2}}$. If furthermore we set the onsite energies of the defect into the middle of the symmetrical and antisymmetrical double chain band, i.e. $\epsilon_1 = 1$, $\epsilon_2 = -1$, and set $t_d = 0$, we obtain the same transmission result, shown as “configuration 2” in Figure 3.26.

If instead, we couple site two antisymmetrically to the left and symmetrically to the right ($t_{l,21} = -t_{l,22} = t_{r,21} = t_{r,22} = \frac{1}{\sqrt{2}}$, rest of the parameters like in configuration 2), the transmission in the antisymmetrical band is suppressed, i.e. there is no transmission for $[-3t, -t]$, cf. “configuration 3” in Figure 3.26. Yet, as this configuration is not perfectly symmetric, also in the symmetric band there is some reflection, and hence $T < 1$.

We can go further and couple two topologically different double chains with each other, cf. Figure 3.27.

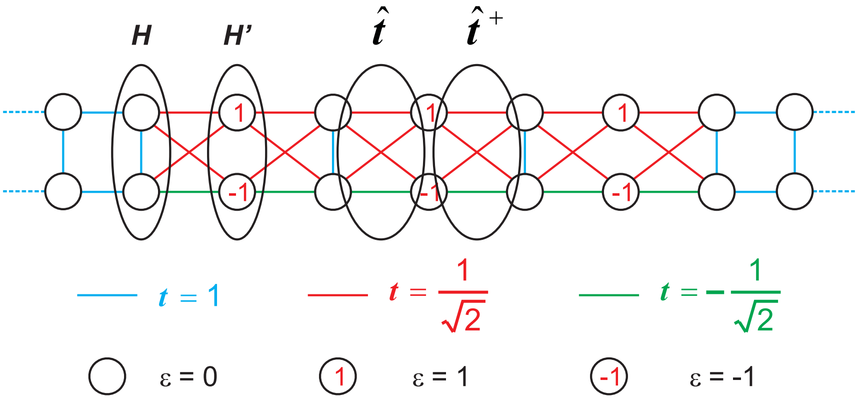

Figure 3.27: Into the infinite double chain (cf. Figure 3.12(a)), we couple a segment of a topologically different chain as a defect. The choice of the parameters is such that no interference occurs. H and H' are the Hamiltonians of the “building blocks” of the two chains, $\hat{t}$ and $\hat{t}^+$ couple between both. This configuration yields perfect double-chain transmission.

Here we find, that for the choice of parameters given in Figure 3.27 there is perfect double-chain transmission, cf. “configuration 1” in Figure 3.26. The reason is the following. The building block of the original double chain has the Hamiltonian

$$H = \begin{pmatrix} 0 & 1 \\ 1 & 0 \end{pmatrix} \tag{3.92}$$

In its eigenbasis:

$$H' = U^+ H U = \begin{pmatrix} 1 & 0 \\ 0 & -1 \end{pmatrix} \quad \text{with} \quad U = U^+ = \begin{pmatrix} \frac{1}{\sqrt{2}} & \frac{1}{\sqrt{2}} \\ \frac{1}{\sqrt{2}} & -\frac{1}{\sqrt{2}} \end{pmatrix} \tag{3.93}$$

Compare this with the notation in Figure 3.27. The example of the two matching double chains is constructed just in a form that the couplings $\hat{t} = U = U^+ = \hat{t}^+$ between every two consecutive double-sites changes the basis. As every second double-site has the vertical coupling $t = 1$, there is perfect match.

Single-walled carbon nanotubes are the perhaps closest relative of the n-tuple chain in Nature. Also there, heterojunctions are discussed and the symmetry-matching plays an important role in how well the heterojunction transmits. For example, Chico *et al.* [41] state that both (12,0) and (6,6) carbon nanotubes transmit at $E = 0$, whereas the

(12,0)/(6,6) matched tube does not transmit at this energy. For the nomenclature and an introduction to carbon nanotubes I recommend the recent review [39]. For further reading [7, 18, 42, 60, 140].

3.8 The DNA chain

As the last example of infinite and half-infinite chains we examine a type of chain which I call "DNA chain" for reasons which we will discuss in Chapter 5. The model is displayed in Figure 3.28.

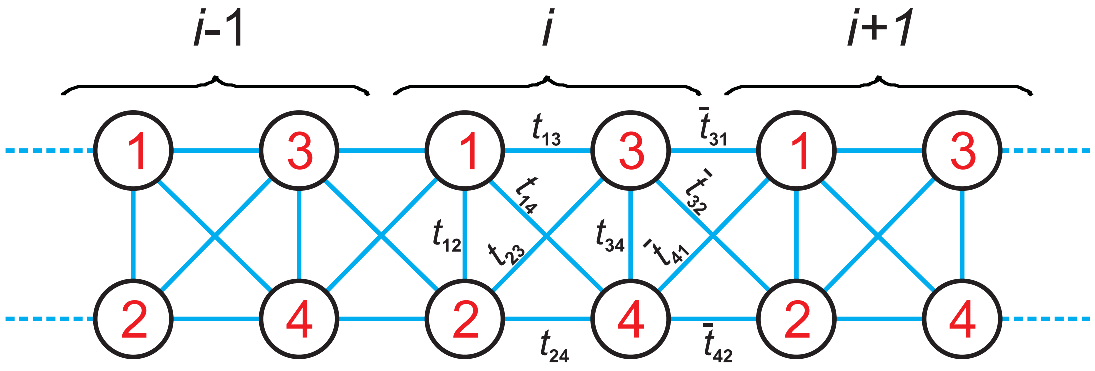

Figure 3.28: The infinite DNA chain. It is composed of repeated sections of four sites with the energies ϵ_1 through ϵ_4. The couplings are named t_{lm} within a section and $\bar{t}_{lm}$ in between two sections. Note that $t_{lm} \neq \bar{t}_{lm}$, in general.

Its real space Hamiltonian is

$$H = \sum_{\substack{i=-\infty \\ m=1}}^{\substack{i=\infty \\ m=4}} \epsilon_m \left|i,m\right\rangle\left\langle i,m\right| + \sum_{i,m\neq n} \left[t_{mn} \left|i,m\right\rangle\left\langle i,n\right| + \bar{t}_{mn} \left|i,m\right\rangle\left\langle i+1,n\right| + \text{H.c.}\right] \tag{3.94}$$

3.8.1 DNA-chain bands

Like usual, we Fourier transform the Hamiltonian, obtaining

$$H = \sum_{k,m=1}^{m=4} \epsilon_m \left|k,m\right\rangle\left\langle k,m\right| + \sum_{k,m\neq n} t_{mn} \left|k,m\right\rangle\left\langle k,n\right| + \bar{t}_{mn}\mathrm{e}^{-\mathrm{i}k} \left|k,m\right\rangle\left\langle k,n\right| + \text{H.c.} \tag{3.95}$$

For the complete diagonalization thus we have to find the eigensystem of

$$H_k = \begin{pmatrix} \epsilon_1 & t_{12} & t_{13}+\bar{t}_{31}\mathrm{e}^{\mathrm{i}k} & t_{14}+\bar{t}_{41}\mathrm{e}^{\mathrm{i}k} \\ t_{12} & \epsilon_2 & t_{23}+\bar{t}_{32}\mathrm{e}^{\mathrm{i}k} & t_{24}+\bar{t}_{42}\mathrm{e}^{\mathrm{i}k} \\ t_{13}+\bar{t}_{31}\mathrm{e}^{-\mathrm{i}k} & t_{23}+\bar{t}_{32}\mathrm{e}^{-\mathrm{i}k} & \epsilon_3 & t_{34} \\ t_{14}+\bar{t}_{41}\mathrm{e}^{-\mathrm{i}k} & t_{24}+\bar{t}_{42}\mathrm{e}^{-\mathrm{i}k} & t_{34} & \epsilon_4 \end{pmatrix} \tag{3.96}$$

As expected, the matrix H_k is hermitian, thus its eigenenergies are real. For a choice of the ϵ_i and t_{mn}, the calculation of the eigenenergies was performed numerically. It is displayed in Figure 3.29.

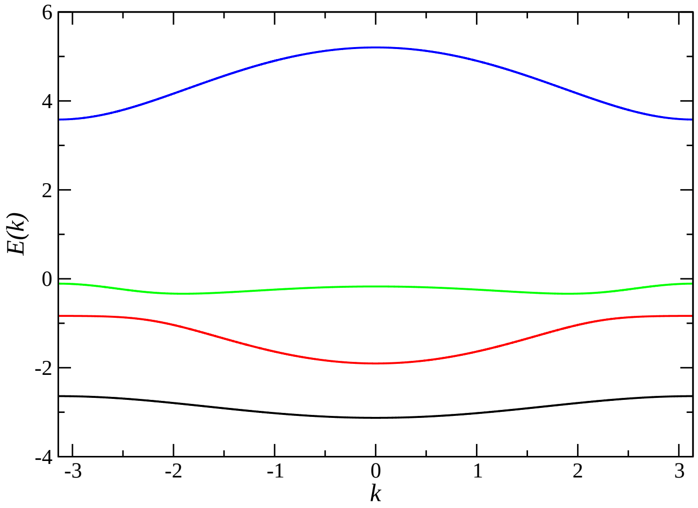

Figure 3.29: Band structure of the DNA chain calculated numerically with MATHEMATICA. The parameters were $\epsilon_1 = -2$, $\epsilon_2 = -1$, $\epsilon_3 = 1$, $\epsilon_4 = 2$, horizontal $t = \bar{t} = 1$, vertical $t_{12} = 1$, $t_{34} = 2$, diagonal $t_{14} = \bar{t}_{32} = \frac{1}{\sqrt{2}}$, $t_{23} = \bar{t}_{41} = \frac{1}{2\sqrt{2}}$.

3.8.2 DNA surface Green function

If we ask for the surface Green function, again we have to consider (3.54),

$$\hat{G}_{11} = \hat{g}_{11} + \hat{g}_{11}\hat{t}\hat{G}_{11}\hat{t}^{+}\hat{G}_{11} \tag{3.97}$$

where now the matrix $\hat{t}$ is not diagonal as it was in the case of the n-tuple chain. Therefore, the quadratic matrix equation (3.97) does not have a straightforward solution. Yet, the so-called decimation technique offers a numerical way to obtain the surface Green function of any periodic half-infinite Hamiltonian. It was derived by [116] in 1985, see also [179, Section 10.6] and [81, 133]. In an iterative way, in the n-th step the decimation technique obtains the surface Green function of 2^n identical layers. Step by step, the interaction of the first 2^n layers with the next 2^n layers becomes smaller and gives an exit condition. For the details, cf. the cited literature. A problem of the decimation technique is that iη, the imaginary part of the energy, is an input parameter and has to be chosen with a finite value. Ideally $\eta \to 0^+$ is infinitesimal, but a too small choice can cause numerical errors. Figures 3.30 and 3.31 show real and imaginary parts of the surface Green function of the DNA chain for different values of η.

We recognize, most clearly in Figure 3.31(a), that the energy range of the bands is just the same as within an infinite DNA chain.

3.9 Transmission of a finite chain

After the discussion of infinite and half-infinite linear systems, which can be used as models for electrical contacts or leads, now we come to finite systems. The transmission of finite systems is essential for the model of decoherence which is described in Chapter 4.

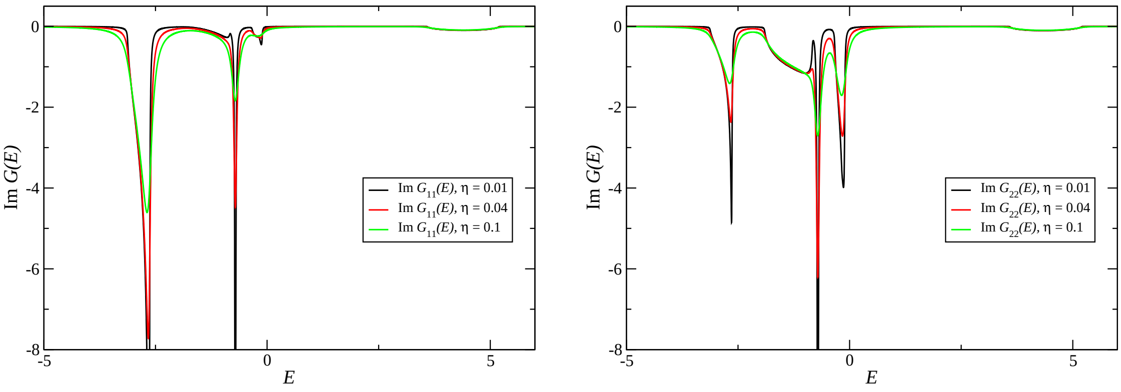

(a) $\mathrm{Im}\, G_{11}(E)$

(b) $\mathrm{Im}\, G_{22}(E)$

Figure 3.30: Surface Green function $\mathrm{Im}\, G(E)$, i.e. $-\pi \times$LDOS at sites 1 and 2, for different parameters η and $n = 10$ decimation iterations. The ϵ and t parameters were chosen like in Figure 3.29.

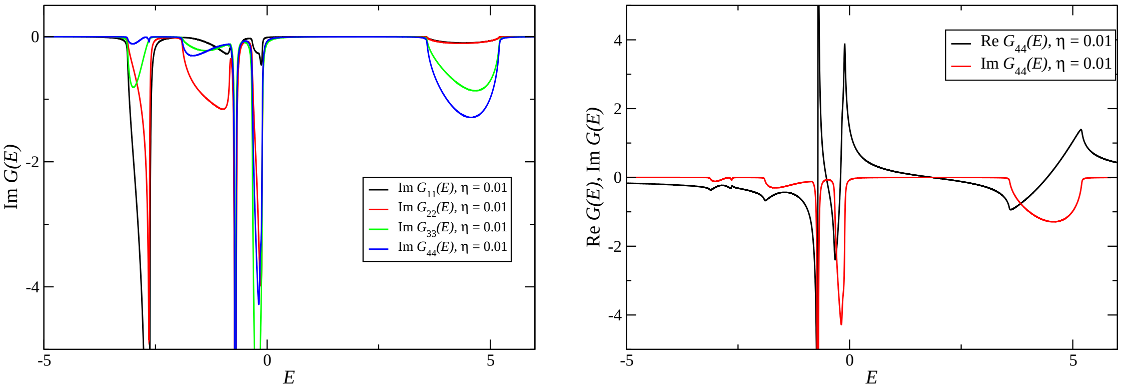

(a)

(b)

Figure 3.31: (a) The imaginary parts of the surface Green functions G_{11} through G_{44} in comparison. We see that the different sites carry states at different energies. (b) Real and imaginary part of the surface Green function $G_{44}(E)$. In the interval $[3; 6]$ we notice a resemblance to the surface Green function of the single chain, cf. Figure 3.4. Due to the distance in energy, the highest band does not mix up as much as the other bands.

The finite chain of N sites which we examine in this section has the Hamiltonian

$$H = \sum_{i=1}^{N} \epsilon_i \, |i\rangle\langle i| + \sum_{i=1}^{N-1} [t_{i,i+1} \, |i\rangle\langle i+1| + \mathrm{H.c.}] \tag{3.98}$$

with the onsite energies ϵ_i and transfer matrix elements $t_{i,i+1}$, cf. Figure 3.32

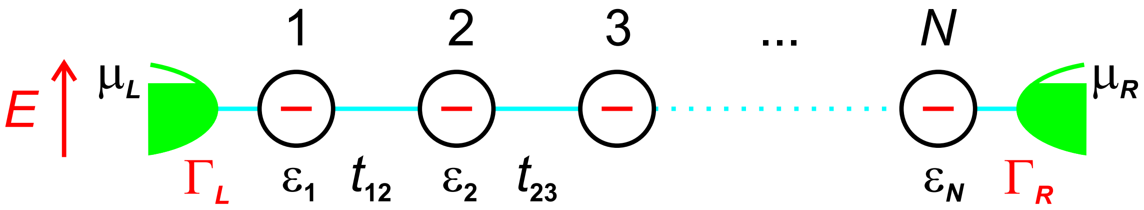

Figure 3.32: A finite linear chain of single-energy sites. In this section, the transfer matrix elements are assumed to be equal along the chain. In the wide-band limit, the self energy of the contacts can be approximated by a constant, leading to a constant broadening $\Gamma = \mathrm{i}\,(\Sigma - \Sigma^{+})$.

3.9.1 The wide-band limit contact

First we define a contact in the wide-band limit. The name stems from the comparison of the channel energy range with the bands of the contacts. If the contact bands range far outside the channel energies, and its density of states is approximately constant, it has a constant purely imaginary self-energy, i.e.

$$\Sigma_{\text{wide band}}(E) = -\frac{\mathrm{i}}{2}\Gamma = \text{const.} \tag{3.99}$$

This is a consequence of the Kramers-Kronig relation (2.57). A constant density of states (and hence constant imaginary part of G) leads to zero real part of G. The assumption of a contact in the wide-band limit is legitimate for many situations in nanoelectronics where e.g. macroscopic gold contacts (band width approximately 8eV) are attached to single molecules for which the energy width of the HOMO or LUMO state is considerably smaller (typically < 0.1eV).

The assumption of wide-band limit for the contacts simplifies the calculation of the transmission:

$$T = 4\,\mathrm{Tr}\left[G\mathrm{Im}(\Sigma_1)G^{+}\mathrm{Im}(\Sigma_2)\right] \overset{\text{wide band}}{=} \Gamma_L\Gamma_R\,|G_{1N}|^2 \tag{3.100}$$

Thus for the calculation of the transmission through a coherent linear system of N sites between two contacts in the wide-band limit we only need to know the element G_{1N} of its Green function and the broadening matrix elements Γ_L and Γ_R.

3.9.2 Transmission of the finite chain without disorder: periodicity in length and tunneling

Before considering the general finite chain between two wide-band contacts we address the finite chain of N sites without disorder. For simplicity, again we choose its onsite energies $\epsilon_i = \epsilon = 0$ as our energy origin and its transfer matrix elements $t_{ij} = t = 1$ as our energy unit, i.e. the uncoupled chain has the Hamiltonian

$$H = \sum_{i=1}^{N-1}\left[|i\rangle\langle i+1| + \text{H.c.}\right] \tag{3.101}$$

On coupling to the contacts we have to consider the broadening matrices $\Gamma_{L,R}$ in the Green function of the channel:

$$G(E) = [E - H - \Sigma_L - \Sigma_R]^{-1} = \begin{pmatrix} E + \mathrm{i}\frac{\Gamma_L}{2} & -1 & 0 & \cdots & 0 \\ -1 & E & -1 & 0 & \vdots \\ 0 & -1 & \ddots & & \\ \vdots & & & & -1 \\ 0 & \cdots & 0 & -1 & E + \mathrm{i}\frac{\Gamma_R}{2} \end{pmatrix}^{-1} \tag{3.102}$$

For the inversion of symmetric tridiagonal matrices, there is an analytic formula, derived e.g. in [192], which yields for G_{1N}:

$$G_{1N} = \frac{1}{p_N} \tag{3.103}$$

where p_N is a recursively defined polynomial:

$$p_0 = 1 \tag{3.104}$$

$$p_1 = E + \mathrm{i}\frac{\Gamma_L}{2} \tag{3.105}$$

$$p_{n+1} = E p_n - p_{n-1} \qquad \forall 1 \le n < N-2 \tag{3.106}$$

$$p_N = \left(E + \mathrm{i}\frac{\Gamma_R}{2}\right) p_{N-1} - p_{N-2} \tag{3.107}$$

Apart from the imaginary part in p_1 and p_N this recursion corresponds to the one of the Chebychev polynomials of the second kind with $E \to 2x$. [6] In our simple case, the recursion can be performed and for $N \ge 3$ we find

$$\begin{aligned} p_N = &\left(E + \mathrm{i}\frac{\Gamma_L}{2}\right)\left(E + \mathrm{i}\frac{\Gamma_R}{2}\right) \sum_{k=0}^{\lfloor\frac{N-2}{2}\rfloor} (-1)^k E^{N-2-2k} \binom{N-2-k}{k} \\ &- \left(2E + \mathrm{i}\frac{\Gamma_L + \Gamma_R}{2}\right) \sum_{k=0}^{\lfloor\frac{N-3}{2}\rfloor} (-1)^k E^{N-3-2k} \binom{N-3-k}{k} \\ &+ \sum_{k=0}^{\lfloor\frac{N-4}{2}\rfloor} (-1)^k E^{N-4-2k} \binom{N-4-k}{k} \end{aligned} \tag{3.111}$$

In this formula, $\lfloor x \rfloor = \max\limits_{i \in \mathbb{N} | i \le x} i$ denotes the floor function. For $\Gamma_L = \Gamma_R \equiv \Gamma$ we can simplify further

$$\begin{aligned} p_N = \frac{1}{S} \Bigg\{ &\left(\frac{E+S}{2}\right)^{N-3} \left[\left(E + \mathrm{i}\frac{\Gamma}{2}\right)\frac{E+S}{2} - 1\right]^2 \\ &- \left(\frac{E-S}{2}\right)^{N-3} \left[\left(E + \mathrm{i}\frac{\Gamma}{2}\right)\frac{E-S}{2} - 1\right]^2 \Bigg\} \end{aligned} \tag{3.112}$$

---

[6] The Chebychev polynomials of the second kind are defined as

$$U_0(x) = 1 \tag{3.108}$$

$$U_1(x) = 2x \tag{3.109}$$

$$U_{n+1}(x) = 2x U_n(x) - U_{n-1}(x) \tag{3.110}$$

For the many interesting properties of these polynomials see e.g. [125, 163].

where

$$S = \sqrt{E^2-4} = \begin{cases} \sqrt{E^2-4} & \text{for } |E| \geq 2 \\ \mathrm{i}\sqrt{4-E^2} & \text{for } |E| < 2 \end{cases} \tag{3.113}$$

Thus, the transmission through a chain of N equal one-level sites

$$T_N(\Gamma_L, \Gamma_R, E) = \Gamma_L \Gamma_R \left| \frac{1}{p_N} \right|^2 \tag{3.114}$$

can easily be calculated.

Figure 3.33 shows the transmission through one to five-site chains in dependence of the energy E.

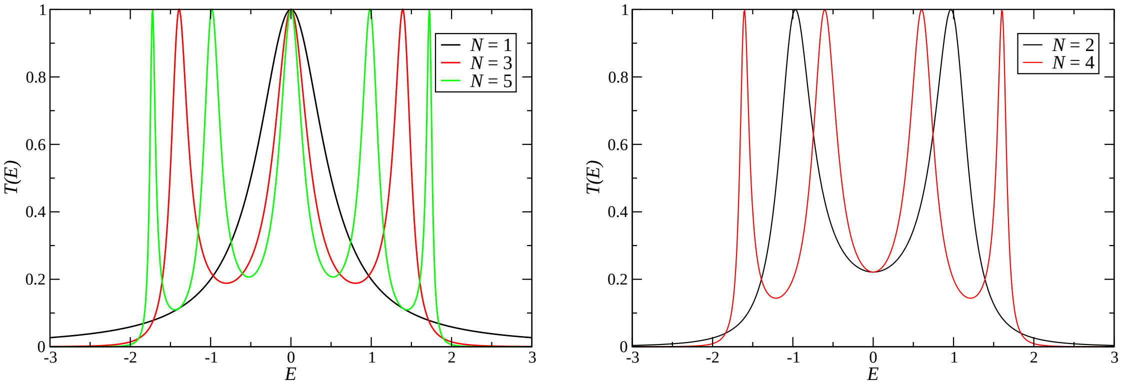

(a) Odd chain length

(b) Even chain length

Figure 3.33: Transmission through (a) one, three, and five identical sites and through (b) two and four sites. The parameters were chosen $\Gamma_L = \Gamma_R = 0.5$. Energy unit $t = 1$.

We find an even-odd behavior of the transmission at energy $E = 0$ that has also been reported by [93]: The zero-energy transmission through a number N of equal sites depends only on whether N is even or odd, not on its actual value. For even N we find:

$$T_N(E=0) = \frac{\Gamma_L \Gamma_R}{\left(1 + \frac{\Gamma_L \Gamma_R}{4}\right)^2} \overset{\Gamma_L = \Gamma_R \equiv \Gamma}{=} \frac{\Gamma^2}{\left(1 + \frac{\Gamma^2}{4}\right)^2} \tag{3.115}$$

whereas for odd N:

$$T_N(E=0) = \frac{4\Gamma_L \Gamma_R}{(\Gamma_L + \Gamma_R)^2} \overset{\Gamma_L = \Gamma_R \equiv \Gamma}{=} 1 \tag{3.116}$$

In both cases, the transmission at $E = 0$ is independent of the number of sites N, and for odd N it does only depend on the ratio $\frac{\Gamma_L}{\Gamma_R}$. The $E = 0$ behavior of the transmission is depicted in Figure 3.34.

For odd N, perfect transmission is achieved when $\Gamma_L = \Gamma_R$. For even N when $1 = \frac{\Gamma_L \Gamma_R}{4}$.

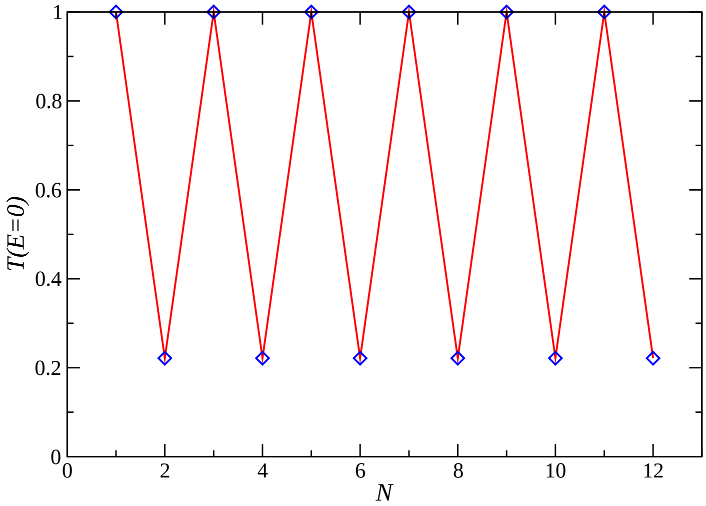

Figure 3.34: Transmission through the finite linear chain at $E = 0$. The transmission value only depends on whether the number N of sites in the chain is even or odd. For this graph, $\Gamma_L = \Gamma_R = 0.5$ was chosen.

3.9.2.1 Location of the transmission maxima

In this Section we consider the case $\Gamma \equiv \Gamma_L = \Gamma_R$. The location of the maxima of $T(E)$ can be found approximately by considering the relation of (3.102) with (3.76). For the surface Green function we have calculated the eigenvalues of a finite tight-binding system without disorder. These are the zeros of the determinant of (3.102) for $\Gamma = 0$. For $\Gamma \to 0^+$, at the same energies there are, mediated through (3.103) and (3.114) the maxima of $T(E)$, i.e. for small Γ, $T(E)$ has maxima near $E = 2\cos(\frac{j\pi}{N+1})$ for $j = 1, \ldots, N$.

In Figure 3.35 we have analyzed the transmission for $N = 3$ in dependence of Γ.

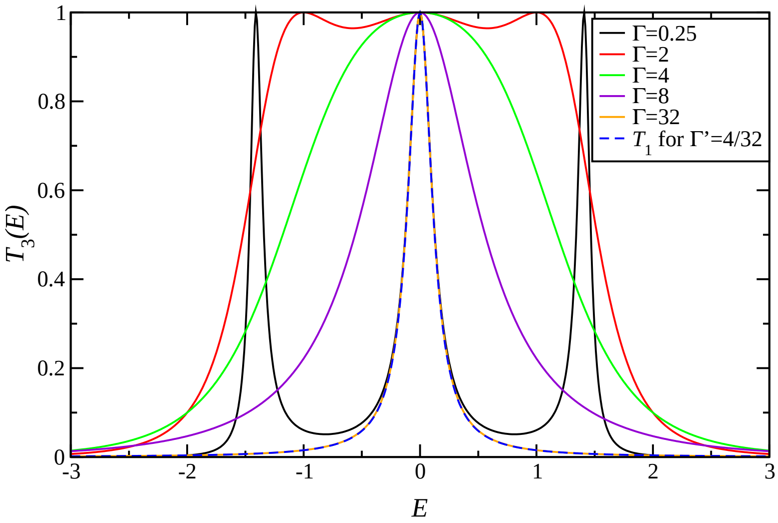

Figure 3.35: Transmission through the finite chain of length $N = 3$ for different values of Γ. We observe that for large Γ, $T_3(\Gamma, E) = T_1(\Gamma', E)$, where $\Gamma' = \frac{4}{\Gamma}$.

We observe that, for large Γ, $T_3(\Gamma, E) \to T_1(\Gamma', E)$, where $\Gamma' = \frac{4}{\Gamma}$. This holds true for any

$N > 2$, i.e. one finds by analyzing (3.111) and (3.114)

$$\lim_{\Gamma\to\infty} \left|T_N(\Gamma, E) - T_{N-2}(\tfrac{4}{\Gamma}, E)\right| = 0 \tag{3.117}$$

for any E. The physical interpretation is the following. Very strong coupling of the first and last site of the chain means that these sites actually belong to the contacts. As $\Gamma \gg 1 = t$ is much larger than the intra-chain coupling, reflection is much more probable than transmission. Only at the very specific resonance energies of the $N-2$ chain, $E = 2\cos(\frac{n\pi}{N-2+1}), n = 1, \ldots, N-2$, perfect transmission $T = 1$ is reached, cf. Figure 3.36.

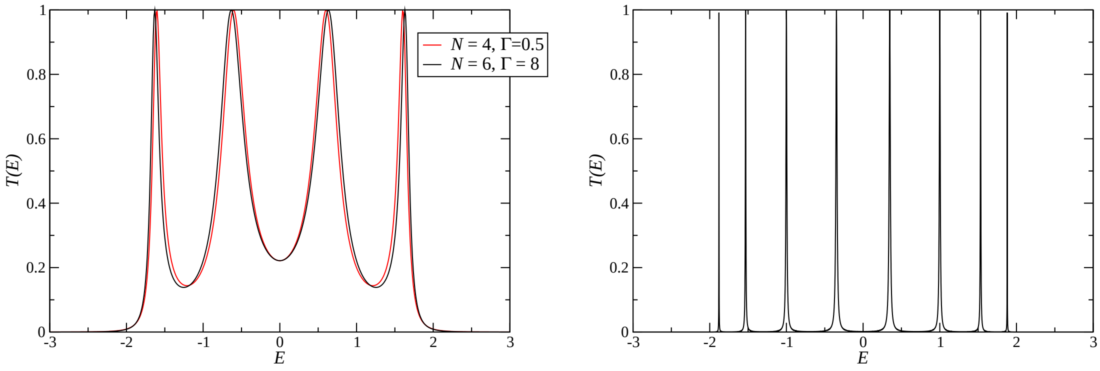

(a) (b)

Figure 3.36: (a) Transmission through the finite chain of length $N = 4$ for $\Gamma = 0.5$ in comparison with the transmission for $N = 6$ and $\Gamma = 8$. (b) Transmission through a chain with length $N = 10$ for $\Gamma = 100$. The transmission peaks lie at the eigenenergies of the uncoupled chain with length 8, $E = 2\cos(\frac{n\pi}{9}), n = 1, \ldots, 8$.

3.9.2.2 Tunneling outside the tight-binding band

If the energy E of the incident electron is outside $[-2, 2]$ (the energy range of the tight-binding chain), the chain corresponds to a tunneling barrier for the electron. Therefore, for $|E| > 2$ we expect the transmission function to decay exponentially with the number of sites in the chain.

Indeed for $E > 2$, (3.112)–(3.114) lead to

$$T \overset{N\to\infty}{\approx} \left(\frac{\Gamma S}{E^2 + \frac{\Gamma^2}{4}}\right)^2 \left(\frac{E+S}{2}\right)^{-2(N-1)} \tag{3.118}$$

where $\Gamma_L = \Gamma_R = \Gamma$. An analog expression holds for $E < -2$. Figure 3.37 shows the transmission in dependence of the chain length N. The parameters were chosen to be $\Gamma_L = \Gamma_R = 0.5$, and $E = 10$.

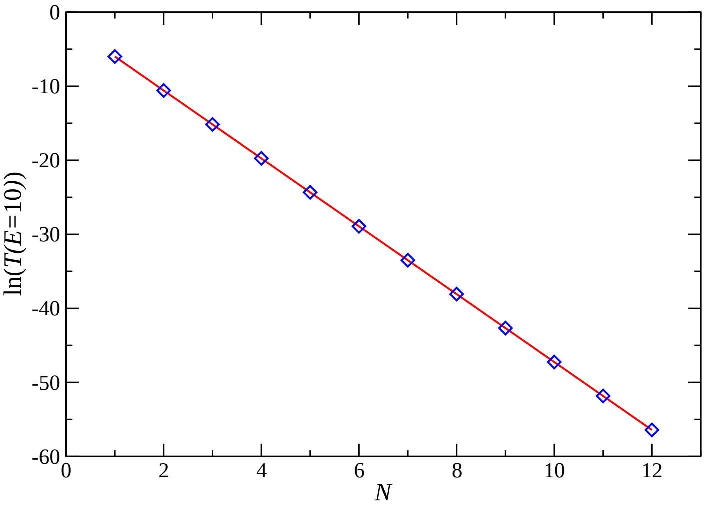

Figure 3.37: The logarithm of the transmission through the finite chain for large E in dependence of the number N of sites. The transmission decays exponentially like expected for a tunnel barrier with increasing length. $\Gamma_L = \Gamma_R = 0.5$.

3.9.2.3 Suprema, infima, periodicity and mean values of $\{T_N(E)\}$

By numerical studies of the $T_N(E)$, for a given $\Gamma = \Gamma_L = \Gamma_R$ we find suprema, infima, a periodicity in N, and mean values of the sets $\{T_N \mid N = 1, 2, \dots\}$. Consider Figure 3.38.

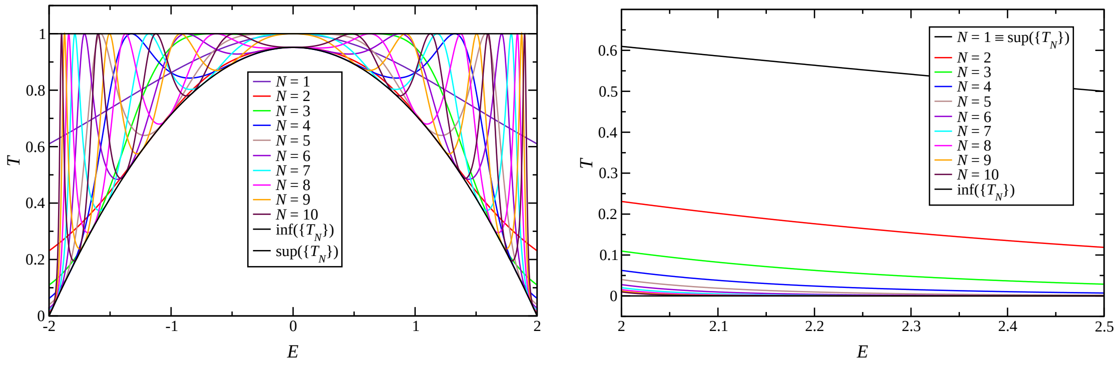

(a)

(b)

Figure 3.38: (a) The transmission function $T_N(E)$ inside the tight-binding band for different N. With increasing N, the area between the infimum and supremum lines becomes densely filled by $T_N(E)$ curves. (b) The transmission function $T_N(E)$ outside the tight-binding band for different N. In both graphs $\Gamma = 2.5$.

We see that within the tight-binding band, $E \in (-2, 2)$, all curves $T_N(E)$ lie between the supremum

$$T_{\text{sup}}(E) = 1 \qquad \text{for } E \in (-2, 2) \tag{3.119}$$

and the infimum

$$T_{\text{inf}}(E) = \frac{\Gamma^2}{\left(1 + \frac{\Gamma^2}{4}\right)^2} \left(1 - \frac{E^2}{4}\right) \qquad \text{for } E \in (-2, 2) \tag{3.120}$$

which was determined empirically with high accuracy from numerical data. Supremum and infimum give us boundaries for $T_N(E)$ for unknown or very large N.

As we have seen in the section before, outside the band, T decays exponentially with N. Thus,

$$T_{\text{sup}}(E) = T_1(E) \qquad \text{for } E \notin [-2, 2] \tag{3.121}$$

is the natural supremum, and

$$T_{\text{inf}}(E) = 0 \qquad \text{for } E \notin [-2, 2] \tag{3.122}$$

is the natural infimum outside the band, cf. Figure 3.38(b).

Another interesting result is that

$$T(E = \pm 2.0) \propto N^{-2} \tag{3.123}$$

which can be drawn from the double logarithmic plot of $T(N, E = 2.0)$ in Figure 3.39 and seen easily from (3.112)–(3.114).

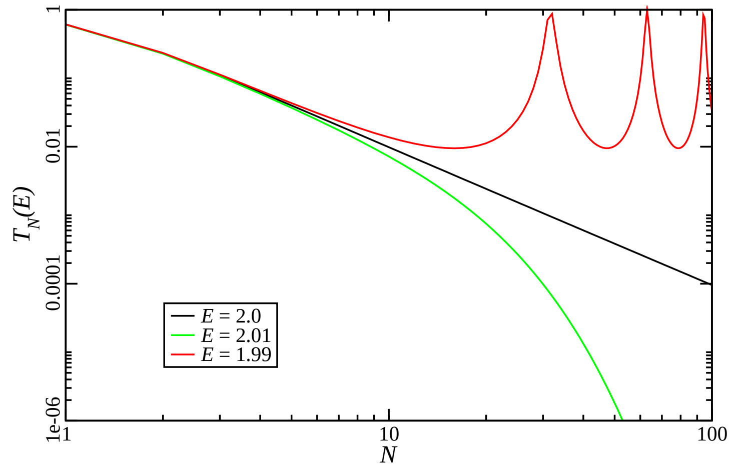

Figure 3.39: The transmission function $T(E)$ near the tight-binding band edge as a function of N. $\Gamma = 2.5$. Whereas $T \propto N^{-2}$ at the band edge $E = 2.0$, for $E > 2.0$ it decays exponentially and for $E < 2.0$ it behaves oscillatory.

Furthermore we observe that the even-odd behavior of T at $E = 0$ is a special case of a general periodic behavior in N for $E \in (-2, 2)$ inside the band. The period P increases from $P = 2$ for $E = 0$ through $P \approx 30$ for $E = 1.99$ in the example of Figure 3.39 to infinity as $E \to 2$. The period does not depend on Γ. We observe that for

$$E = \pm 2 \cos\left(\tfrac{(n-1)\pi}{n}\right) \qquad n = 2, 3, \ldots \tag{3.124}$$

the period is just $P = n$, cf. Figure 3.40(a). The energies in (3.124) for integer periods are eigenenergies of the isolated tight-binding chain of length $n - 1$.

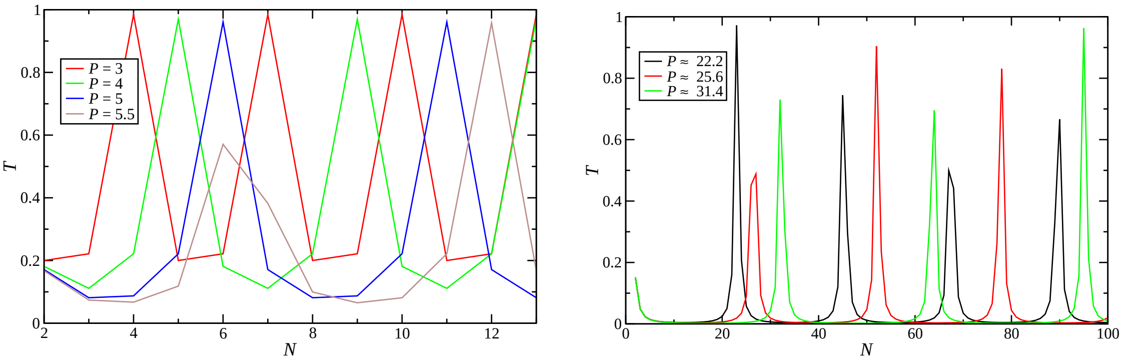

(a) (b)

Figure 3.40: (a) The transmission function T in dependence of the chain length. For the energies $E = \pm 2\cos(\frac{(n-1)\pi}{n})$, $n = 2, 3, \ldots$ it is periodic with an integer period n. The brown curve is an example for a rational $n = 5.5$ period. (b) The transmission function T in dependence of the chain length for larger periods. Close to the maxima, $T \propto (N - N_{\text{max}})^{-2}$. For all curves in both graphs, $\Gamma = 8$.

Solving (3.124) for $P = n$ we find

$$P = \frac{\pi}{\arccos(\frac{E}{2})} \qquad \text{for } E \in (-2, 2) \tag{3.125}$$

a period for any energy $E \in (-2, 2)$. A transmission function $T(N, E)$ with rational period $P = 5.5 \in \mathbb{Q}$ is displayed in Figure 3.40(a). Effectively, the rational period means a correspondingly longer integer period. For the example with $P = 5.5$ we can see just the complete integer period of $2P = 11$ in Figure 3.40(a). For an irrational $P \notin \mathbb{Q}$, any $T \in (T_{\text{inf}}(E), T_{\text{sup}}(E))$ is reached to arbitrary accuracy for some N.

In Figure 3.40(b) we find examples of $T(N, E)$ closer to the band edge, i.e. with longer periods. Numerically we find, that for large periods, $T(N) \propto (N - N_{\text{max}})^{-2}$ near the locations N_{max} of the maxima of T.

For some applications it can be useful to know the average value $\langle T(E)\rangle_N$ of $\{T_N(E) \mid N = 1, 2, \ldots, \infty\}$. As we have observed, $T(E)$ is periodic in N for $E \in (-2, 2)$, and therefore $\langle T(E)\rangle_N$ exists. In Figure 3.41 we have displayed a numerically evaluated $\langle T(E)\rangle_N$ for different values of Γ.

The numerical values lead to the assertion that

$$\langle T(E)\rangle_N = \frac{\Gamma}{1 + \frac{\Gamma^2}{4}} \sqrt{1 - \frac{E^2}{4}} = \sqrt{T_{\text{inf}}(E)} \qquad \text{for } E \in [-2, 2] \tag{3.126}$$

is the exact average for $E \in [-2, 2]$ except for those values of E which lead to integer periods in $T(N)$, clearly notable e.g. for $\Gamma = 8$ at $E = 1$ in Figure 3.41.

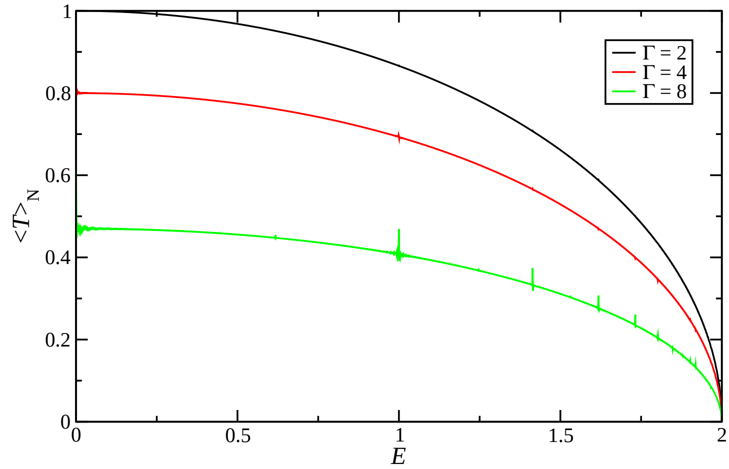

Figure 3.41: The transmission function $\langle T(E)\rangle_N$ averaged over $N = 2, \dots, 1000$ for various values of Γ. Except for values of E which lead to an integer period of $T(N)$ (see (3.124)), $\langle T(E)\rangle_N$ lies on an ellipsis. $\langle T(E)\rangle_N$ is symmetric with respect to $E = 0$, therefore only positive energies are displayed. Curves for $\Gamma' = \frac{4}{\Gamma}$ match those for Γ for the reason observed in Section 3.9.2.1.

3.9.3 Transmission of the finite chain with onsite disorder: localization

The considerations so far concerned the *ordered* linear chain, i.e. a chain where all the onsite-energies ϵ_i and parameters t_{ij} are equal. Of course, the result can be generalized, considering the more general finite-chain Hamiltonian (3.98).

Then, the chain is composed of N sites $1, \dots, N$ with respective onsite-energies $\epsilon_1, \dots, \epsilon_N$ and parameters $t_{12}, \dots, t_{N-1,N}$, and the channel Green function reads (cf. (3.102)):

$$G = \begin{pmatrix} E + \mathrm{i}\frac{\Gamma_L}{2} - \epsilon_1 & -t_{12} & 0 & \cdots & 0 \\ -t_{12} & E - \epsilon_2 & -t_{23} & 0 & \vdots \\ 0 & -t_{23} & \ddots & & \\ \vdots & & & & -t_{N-1,N} \\ 0 & \cdots & 0 & -t_{N-1,N} & E + \mathrm{i}\frac{\Gamma_R}{2} - \epsilon_N \end{pmatrix}^{-1} . \tag{3.127}$$

where, again, Γ_L and Γ_R are the broadening parameters due to left and right contact.

The element of the Green function which is relevant for the transmission, G_{1N}, can be obtained by the generalized recursion from above (cf. (3.103)):

$$G_{1N} = \frac{1}{p_N} \tag{3.128}$$

where:

$$p_0 = 1 \tag{3.129}$$

$$p_1 = \frac{E + \mathrm{i}\frac{\Gamma_L}{2} - \epsilon_1}{t_{12}} \tag{3.130}$$

$$p_n = \frac{1}{t_{n,n+1}} \left[(E - \epsilon_n)\, p_{n-1} - t_{n-1,n} p_{n-2} \right] \qquad n = 2, \dots, N-1 \tag{3.131}$$

$$p_N = \left(E + \mathrm{i}\frac{\Gamma_R}{2} - \epsilon_N \right) p_{N-1} - t_{N-1,N} p_{N-2} \tag{3.132}$$

It is a known fact [6, 98, 99, 136, 137, 176, 200, 202] that in disordered media there exist localized electronic states. For an infinite one-dimensional random system in particular, Mott and Twose [138] could show already in 1961, that all electronic eigenstates are localized. That leads us to expect an exponential decay of the transmission with the chain length for a chain with onsite disorder, i.e.

$$T(E) = T_0 \mathrm{e}^{-\frac{N}{\lambda(E)}} \tag{3.133}$$

where $\lambda(E)$ is the so-called localization length.

For a Gaussian onsite disorder with variance σ^2, i.e. a probability density

$$p_{\mathrm{Gauss}}(\epsilon) = \frac{1}{\sigma\sqrt{2\pi}} \mathrm{e}^{-\frac{\epsilon^2}{2\sigma^2}} \tag{3.134}$$

we have plotted the transmission in dependence of the chain length in Figure 3.42. We also consider uniformly distributed onsite disorder with the same variance σ^2, i.e.

$$p_{\mathrm{uniform}}(\epsilon) = \begin{cases} \frac{1}{2\sqrt{3}\sigma} & -\sigma\sqrt{3} < \epsilon < \sigma\sqrt{3} \\ 0 & \text{else} \end{cases} \tag{3.135}$$

The result for this kind of onsite disorder is displayed in Figure 3.42, too.

For small N we can still recognize the even-odd behavior of the transmission, for larger N it is washed out by the disorder.

By fitting exponential functions (3.133) to the transmission data of Figure 3.42 for $N > 50$, we obtain the localization length in dependence of the disorder strength σ which is listed in Table 3.1.

σ	$\lambda(E=0)$	
	Gaussian	uniformly distributed
0.25	126.6	116.9
0.5	41.6	41.2
0.75	22.8	21.7
1.0	14.7	13.8

Table 3.1: The localization length in dependence of the disorder strength σ for Gaussian and uniformly distributed onsite disorder.

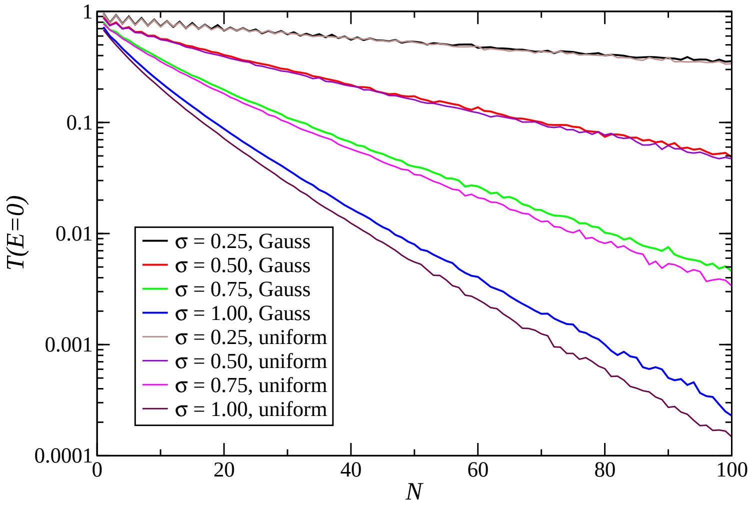

Figure 3.42: Transmission $T(E = 0)$ in dependence of the chain length for different disorder strengths $\sigma = 0.25$, 0.5, 0.75, 1.0 averaged over 1000, 5000, 20000, 150000 disorder configurations, respectively. Considered were Gaussian and uniformly distributed onsite disorder. The broadening was $\Gamma_L = \Gamma_R = 2.5$, all $t_{i,i+1} = 1$ and the mean value for the onsite-energy distributions $\epsilon = 0$.

In the literature [90, 157, 175, 177] we can find a perturbative result for the localization length in the Anderson model concerning the weak disorder limit:

$$\lambda = \frac{8t^2 - 2E^2}{\sigma^2} \tag{3.136}$$

which for $\sigma = 0.25$ and $t = 1$ yields $\lambda(E = 0) = 128$, in good agreement with our values listed in Table 3.1. For larger σ, of course, (3.136), does not agree with our numerical results.

3.10 Conclusions

In this Chapter we have studied the properties of infinite and half-infinite tight-binding systems. Half-infinite tight-binding systems can serve as models for contacts of quantum-mechanical systems due to their continuous density of states. Fourier transformation and diagonalization of the Fourier transformed Hamiltonians lead to the energy spectra and densities of states of the systems.

For the calculation of the transmission through quantum mechanical systems, the contacts only enter through their surface Green functions. In this Chapter we have presented two methods for the calculation of the surface Green function: the Dyson equation (Sections 3.2.1, 3.5.2, 3.7.1) and the direct back transformation (Section 3.2.2). For more complex systems like the DNA-chain we referred to the decimation technique [81, 116, 133, 179].

In Sections 3.3 and 3.7.2 we have studied the transmission through single defects.Depending on the symmetry of the coupling to the defect, the transmission can be suppressed (total reflection), or perfect (no reflection). For double chains we have seen in Section 3.7.2.4 that perfect transmission is also possible through a junction of topologically different chains.

In Section 3.9 we have studied the transmission through finite chains. For electron energies in the middle of the tight-binding band, we found an even-odd behavior of the transmission, which is a special case of a periodic behavior of $T_N(E)$ in N. If the electron energy is outside the band, the chain corresponds to a tunnel barrier and the transmission decays exponentially. Disorder in the chain causes localization. The stronger the diagonal disorder of the energy in the chain, the shorter is the localization length λ. The transmission decays like $T \propto \mathrm{e}^{-N/\lambda}$ with the chain length N. For weak disorder, there are theoretical predictions for λ which agree with our numerical findings.

4 Statistical Model for the Effects of Decoherence on Electron Transport

In this Chapter I present a statistical model for the effects of decoherence on electron transport in large systems. The model and its main results for linear systems have already been published [199], here we will discuss it in detail.

The motivation for our model is the following. We aim at the description of a complex, possibly highly disordered system which on small scale is appropriately described by quantum mechanics, whereas its total dimensions are macroscopic and show classical behavior. An example is a nanoparticle powder: The single nanoparticles show e.g. quantum size effects, whereas on the scale of millimeters we can expect ohmic behavior, i.e. a resistance proportional to the length. Apart from reproducing correctly the behavior on nano and macro-scale, the model should also be computationally less expensive than existing approaches, in order to make the modelling of devices based on nanoparticles possible.

The important ingredient for the transition from quantum to classical behavior is ***decoherence***, i.e. the loss of electronic phase coherence. Once there is no fixed phase-relation between electrons, they cannot interfere with each other (or themselves) anymore and behave as particles. The process of decoherence is understood as a consequence of progressive entanglement of a system with its environment on which information gets lost by tracing out the environmental degrees of freedom and considering the system by a reduced density matrix which only describes the electronic or some of the electronic degrees of freedom. There is a close relationship between the irreversible nature of the total system (system + environment) and the decoherence of the electronic subsystem. For a recent review on the understanding of decoherence and its relation to the measurement process, see [158]. For a general overview on the modelling and effects of decoherence in quantum systems, see [87, 159, 203].

There are many approaches to model decoherence in electronic transport, either by including interaction with the environment into the Hamiltonian, e.g. by a corresponding phenomenological electron-phonon-interaction self-energy [77], [54, Chapter 10] or by the so-called Lindblad master equation [58, 87, 113–115], or e.g. by the so-called Büttiker probes [29, 30, 32, 33, 55, 124, 156] or by random phases introduced into the scattering matrix [144, 145, 197] or a phenomenological imaginary potential [51, 63, 128]. Here we will only discuss the Büttiker probes ansatz as it is related to our model; for an overview of decoherence modelling in electron transport, see the above cited articles and the discussion in [15].

4.1 Büttiker probes

In the Landauer picture of coherent transport in mesoscopic systems (cf. [53, Chapter 2]), scattering in the channel only happens elastically, i.e. no energy is dissipated and the quantum-mechanical phase is conserved. The energy relaxation and phase randomization only happen in the contacts. This has lead to the invention of Büttiker probes as a means for introducing decoherence into the channel. The idea is the following. At the places where the decoherence occurs, a fictitious reservoir is coupled to the channel. As the reservoir is fictitious, no current goes into or comes out of it. This requirement helps to determine the chemical potentials μ of the fictitious reservoirs. As only a part of the electrical current is extracted and re-injected with a random phase at the fictitious reservoirs, no complete phase randomization is reached by any single Büttiker probe.

In practice, the Büttiker probe approach has been applied by D'Amato and Pastawski [55], and subsequently e.g. by Roy and Dhar [156] in the following way. Both consider a linear tight-binding chain to which at all sites but the first (0) and last $(N+1)$, Büttiker probes in form of half-infinite chains (cf. Section 3.2) with onsite energy E_r (r for "fictitious reservoir") and coupling η are attached, see Figure 4.1.

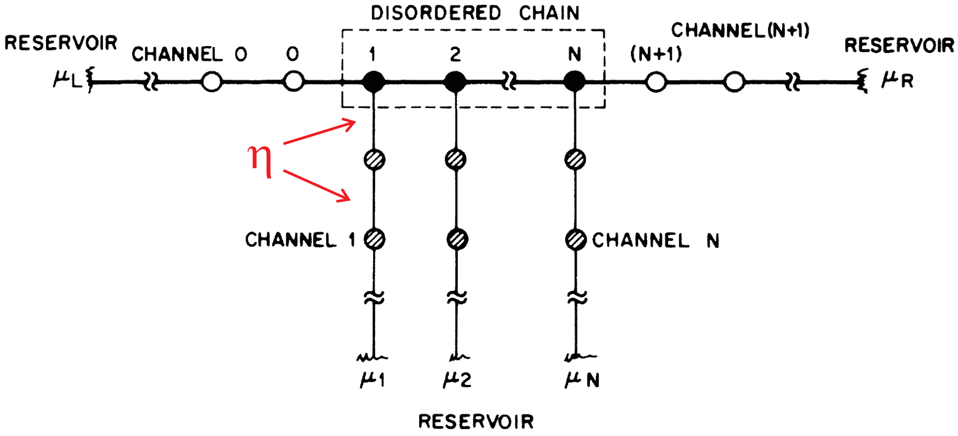

Figure 4.1: Figure 1 of [55], analog to Figure 1 of [156], additional information in red by me. The dephasing model of D'Amato and Pastawski. Along a finite tight-binding chain, to all but the first and last site, half-infinite tight-binding chains are attached.

The self-energy introduced by any of the half-infinite chains Σ_B (B for "Büttiker probe"), for Fermi energies within the tight-binding band, reads

$$\Sigma_B = \eta^2 g_{11,\text{single chain}} = \frac{E - E_r}{2} - \mathrm{i}\sqrt{\eta^2 - \left(\frac{E - E_r}{2}\right)^2} \tag{4.1}$$

In the case that an infinitesimal voltage is applied to the system ($\mu_L \to \mu_R$), by choosing the onsite energy of the fictitious leads equal to the Fermi energy of the contacts ($E_r = E$), the self-energy becomes purely imaginary

$$\Sigma_B = -\mathrm{i}\eta \tag{4.2}$$

Like in Büttiker's original papers [29, 30], the chemical potential at the half-infinite chains is determined in a way, that no net current is going through them. With this model, D'Amato and Pastawski studied the effect of disorder and inelastic scattering on the conductance in the linear system. They introduce an inelastic scattering length $L_{\mathrm{in}} \propto \frac{1}{\eta}$. For a system length $L > L_{\mathrm{in}}$, the system behaves ohmic, i.e. $R \propto \frac{L}{L_{\mathrm{in}}}$. Roy and Dhar extended the model by introducing a finite voltage and temperature bias to study current and heat transport under nonequilibrium conditions in the presence of dephasing. A drawback of these models is that the numerical calculation requires much computation time. The transmission between every pair of reservoirs has to be calculated, and then the chemical potential at each fictitious reservoir to be determined self-consistently such that no net current flows through them.

In the models of D'Amato and Pastwaski and Roy and Dhar, the process of decoherence occurs continuously throughout the system. This is a common feature of the above mentioned models [30, 55, 77, 124, 145, 156, 197].

4.2 Our approach for modelling the effects of decoherence

By contrast, in our approach we assume that decoherence occurs locally and completely in *decoherence regions*, by *statistically independent events*. We assume that the decoherence regions can be described by *electron energy distribution functions*. The energy distribution functions of the different regions are interrelated by *rate equations*. The transition rates of the rate equations are calculated by applying the coherent transport formalism.

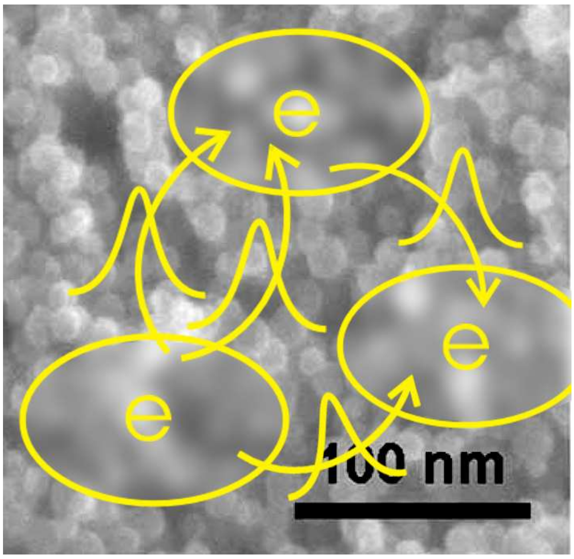

Figure 4.2: Sketch of our approach of modelling decoherence effects in large samples. The decoherence takes place in decoherence regions (within the yellow ellipses); there we assume the electrons can be described by an energy distribution function. In between, the electrons behave quantum-mechanically, i.e. they can interfere. The picture is a Corel-Draw adaptation of the original [150, Fig. 1], a scanning electron micrograph of a Si nano-crystal film.

Before discussing the details of this approach, we have to introduce several physical quantities, for which we use the definitions of [100].

- Mean free path l. The mean free path l is the mean distance an electron can travel before being scattered elastically *or* inelastically. In the Landauer picture, an elastic scattering causes a reduction in the transmission, yet the electron transport still is coherent.
- Localization length λ. For localized electrons it characterizes the exponential decay of the electronic wavefunctions at their boundaries, i.e. $\overline{|\psi(x)|^2|\psi(x')|^2} \approx \mathrm{e}^{-\frac{|x-x'|}{\lambda}}$ for $|x-x'| \to \infty$. Obviously, $\lambda > l$ as localization is a consequence of scattering.
- Phase coherence length L_ϕ. This is the average distance an electron travels before losing its phase coherence. If the decohering mechanism is dissipative it is also called inelastic scattering length. The average time for which an electron conserves phase coherence, is named phase coherence time τ_ϕ.
- System diameter L. Length dimension of the total system under consideration.

We will explain the basic approach of our model in the next Sections 4.2.1–4.2.5. The technical details are explained for the example of a linear chain in Section 4.3.

4.2.1 Decoherence regions

The decoherence regions are the parts of the system where the decoherence occurs. With respect to the rest of the system they act as reservoirs. According to [54, Section 8.4], the central properties of a reservoir are a continuous density of states and the existence of an energy distribution function $f(E)$ for the electrons. This implies the nonexistence of off-diagonal elements in the density matrix, i.e. complete decoherence. The decoherence regions are considered to be located stochastically throughout the system, with the constraint that their average distance corresponds to the phase coherence length. Their position can be fixed in space (e.g. defect regions with inner degrees of freedom), or could move slowly in space, yet on a time-scale much slower than the electronic phase coherence time, such that the assumption of a stationary rate equation for the local energy distribution functions (see below in Section 4.2.4) is reasonable. We do not define their extent and form at this point.[1] In the example of the linear system (Section 4.3) we choose single sites as decoherence regions.

4.2.2 Phase coherence length

The phase coherence length L_ϕ is one of two parameters of our model. In the linear case we discuss below in Section 4.3, $p = \frac{1}{L_\phi}$ is nothing but the spacial density of completely phase randomizing events. For higher dimensions, similar definitions are possible.

For the temperature dependence of the phase coherence length usually a power law is assumed, cf. [3, Chapter 7]

$$L_\phi \propto T^{-\frac{\alpha}{2}} \tag{4.3}$$

---

[1] A reasonable constraint is that the diameter of the decoherence region should be smaller than L_ϕ, as we consider individual dephasing events.

where the exponent α depends on the decohering mechanism and the dimensionality d of the system. Electron-phonon interaction yields $\alpha = 3$, whereas for electron-electron interaction $\alpha = d/2$ for $d = 2, 3$ and $\alpha = 2/3$ for $d = 1$ were found (see [4, 17, 27, 86, 110]).

Independently of the exact decohering mechanism, through the phase coherence length L_ϕ temperature finds its influence in our model.

4.2.3 The decoherence regions as reservoirs: our η parameter

The decoherence regions require a continuous density of states in order to serve as reservoirs. The conceptually easiest way to achieve this is the inclusion of a diagonal purely imaginary self-energy in the Green function of the decoherence regions. Therefore, in Section 4.3 we introduce a parameter η. This is the second parameter of our model. It is introduced in the following way. The decoherence region is modeled by its Green function

$$g_{\mathrm{dec}} \equiv [EI - H + \mathrm{i}I\eta]^{-1} \tag{4.4}$$

where I is the unity operator of the same dimension as H, and $\eta > 0$. Note the resemblance with the usual definition of a Green function (2.4). The difference is that in (4.4), η is no infinitesimal quantity. In the cases of the infinite and half-infinite chains we discussed in Chapter 3, the property of their Green functions to have a non-vanishing imaginary part followed from the Dyson equation because of the translational invariance. The consequence is that the electronic states in the (half-)infinite chains can decay (electrons vanish to infinity). In order to obtain this decay of the electronic states also for the finite decoherence region, the parameter η needs to be finite (no limit $\eta \to 0^+$), else the decoherence regions were closed systems (H is of finite dimension) and no decay of the electronic states would be included in the model. In this way, the parameter η represents the openness of the decoherence regions, be it an openness to the rest of the electronic system or to the environment (e.g. a phononic system).

The influence of the decoherence regions to the coherent transport regions is given by the self-energies

$$\Sigma_{\mathrm{dec}} = t g_{\mathrm{dec}} t^+ \tag{4.5}$$

where t is the coupling matrix between coherent transport region and decoherence region.

Other realizations of the decoherence region Green function are discussed in the application of the model for DNA double strands (cf. Section 5.3).

4.2.4 The rate-equations

To the decoherence regions $n = 1, \ldots, N_d$ we assign electron energy distribution functions $f_n(E)$.

The electronic transport between the decoherence regions causes a redistribution of electrons. At this point we assume that the total number of electrons is not changed within the system.[2] Therefore we can set up a system of electron conservation equations

$$\rho_n \frac{\mathrm{d}f_n(E)}{\mathrm{d}t} = \sum_j T^r_{j,n}(E)(f_j(E) - f_n(E)) \qquad n = 1, \ldots, N_d \tag{4.6}$$

which we will call rate equations in the following. Here, the T^r denote the energy-resolved transition rates between neighboring sites[3], ρ_n is the density of electronic states in decoherence region n, and the index j runs over the neighboring decoherence regions of n. The rate equation as presented in (4.6) is an energy resolved rate equation, i.e. at the decoherence regions the electron energy is conserved and no dissipation takes place. Of course, a damping or recombination term could be introduced[4] but is not necessary in order to introduce decoherence, cf. e.g. [71]. In the literature, for decoherence processes which do not cause energy relaxation, sometimes the term *dephasing* is used. For the real contacts of the system we assume thermal equilibrium such that we assign to them equilibrium Fermi distributions with their respective chemical potentials μ.

Here, we only consider stationary currents, such that the left-hand side of (4.6) equals zero. That requires that the positions of the decoherence regions remain fixed in space over a time much larger than the phase coherence time τ_ϕ.

In the linear system which we discuss below, there are unique neighbors to the left and right of every decoherence region. In this case the decoherence regions make the system fall apart into subsystems making the numerical treatment less expensive. Also a quasi-linear system can be divided into subsystems by the decoherence regions, cf. Chapter 5. In two or three dimensions, decoherence regions do no longer necessarily fragment the system. The question arises how to delimit the coherent regions consistently in this case. Furthermore the question which decoherence regions are neighbors (i.e. interrelated by rate equations) has to be addressed for an extension of the model to higher dimensions.

The transition rates themselves are taken from the coherent transport formalism. As the transition rate $T^r_{n,n+1}(E)$ indicates the rate at which electrons with energy E are transmitted per unit time between decoherence regions $n+1$ and n, the current between them can be written as

$$I_{n,n+1} = \int \mathrm{d}E I_{n,n+1}(E) \tag{4.7}$$

$$= e \int \mathrm{d}E T^r_{n,n+1}(E)\,(f_n(E) - f_{n+1}(E)) \tag{4.8}$$

As the current between the decoherence regions is coherent, we can also apply the coherent current formula (2.46)

$$I_{n,n+1} = \frac{e}{h} \int \mathrm{d}E T(E)\,(f_n(E) - f_{n+1}(E)) \tag{4.9}$$

where $T(E)$ is the transmission function of the channel between the decoherence regions, (2.45). Thus we identify

$$T^r(E) = \frac{1}{h} T(E) \tag{4.10}$$

---

[2] The recombination of electrons and holes will be a future extension of the model.

[3] I.e. $T^r(E)\mathrm{d}E$ is the rate at which electrons with energies in $[E, E + \mathrm{d}E]$ transfer.

[4] This is planned as a future extension of our model.

4.2.5 The statistical approach

Our approach to model decoherence is *statistical* in the sense that we assume decoherence does not occur at regular distances in the system. Therefore the positions of the decoherence regions are chosen according to a probability distribution (in Section 4.3 we discuss a system-wide constant probability p).

In practice we choose a number M of concrete choices of the decoherence regions, which we call *decoherence configurations*, and calculate the physical quantities we are interested in, e.g. the conductance. Afterwards the quantities are ensemble averaged over the M configurations.

4.3 Application of the model to a linear tight-binding system

We consider a finite linear sample of N tight-binding sites with the Hamiltonian

$$H = \sum_{i=1}^{N} \epsilon_i \, |i\rangle\langle i| + t \sum_{i=1}^{N-1} \left[|i\rangle\langle i+1| + \text{H.c.} \right] \tag{4.11}$$

i.e. no off-diagonal disorder is considered.

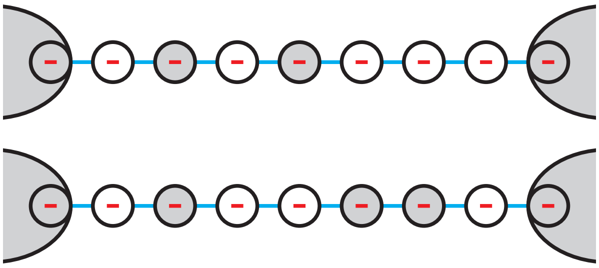

Figure 4.3: The linear system of $N = 7$ sites in two different decoherence configurations.

4.3.1 Model for the decoherence regions: decoherence sites and parameter η

The N_d decoherence regions are modeled as single sites (indices $i_1, \ldots, i_n, \ldots, i_{N_d}$) which are characterized by the Green function according to (4.4) as

$$g_{i_n}(E) = \frac{1}{E - \epsilon_{i_n} + \mathrm{i}\eta} \tag{4.12}$$

They can be interpreted as single sites coupled to contacts in the wide-band limit, cf. (3.99) with η corresponding to $\frac{\Gamma}{2}$. Of course, these wide-band limit contacts are only a model for the coupling to the environment and the rest of the system, and no actual contacts.

4.3.2 Model for contacts and contact coupling

The interaction with the left and right contacts is modeled by a tight-binding Hamiltonian

$$H_I = t_L \left|L\right\rangle\left\langle 1\right| + t_R \left|N\right\rangle\left\langle R\right| + \text{H.c.} \tag{4.13}$$

where only coupling to the surface of the contacts is taken into account. The contacts' surface Green functions are modeled similarly to the decoherence sites:

$$g_{L/R}(E) = \frac{1}{E - \epsilon_{L/R} + \mathrm{i}\eta_{L/R}} \tag{4.14}$$

4.3.3 The decoherence length: parameter p

The decoherence sites are chosen independently according to a probability $p \in [0, 1]$ out of the sites $1, \dots, N$, cf. Figure 4.3. Thus the number of decoherence sites within the system follows a binomial distribution $P(N_d) = \binom{N}{N_d} p^{N_d}(1-p)^{N-N_d}$ and the average number of decoherence sites is

$$\overline{N_d} = \sum_{N_d=0}^{N} N_d P(N_d) = pN \tag{4.15}$$

In this way we define the decoherence length $L_\phi = \frac{1}{p}$ in our system as the average distance between neighboring decoherence sites.

In order to obtain numerical results e.g. for the conductance of the system, we average over M decoherence configurations.

4.3.4 The effective channels and their transmissions

Every decoherence site is considered as an effective contact for the neighboring coherent chains. Thus between two neighboring decoherence sites n and $n+1$ there is an effective channel of $i_{n+1} - i_n - 1$ sites, cf. Figure 4.4.

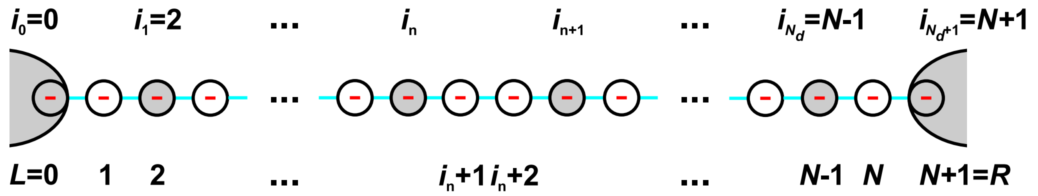

Figure 4.4: The linear system of N sites, its N_d decoherence sites, and the effective channels forming between every two decoherence sites i_n, i_{n+1}.

The effective channel then has the Hamiltonian

$$H_{n,n+1} = \sum_{i=i_n+1}^{i_{n+1}-1} \epsilon_i \left|i\right\rangle\left\langle i\right| + t \sum_{i=i_n+1}^{i_{n+1}-2} \left[\left|i\right\rangle\left\langle i+1\right| + \text{H.c.}\right] \tag{4.16}$$

of the dimension $i_{n+1} - i_n - 1$. The coupling to the effective contacts causes self-energies Σ_n, Σ_{n+1} which are matrices of the same dimension.

$$\Sigma_n = \sum_{i=i_n+1}^{i_{n+1}-1} \delta_{i,i_n+1} t^2 g_{i_n} |i\rangle\langle i| = t^2 g_{i_n} |i_n + 1\rangle\langle i_n + 1| \tag{4.17}$$

$$\Sigma_{n+1} = \sum_{i=i_n+1}^{i_{n+1}-1} \delta_{i,i_{n+1}-1} t^2 g_{i_{n+1}} |i\rangle\langle i| = t^2 g_{i_{n+1}} |i_{n+1} - 1\rangle\langle i_{n+1} - 1| \tag{4.18}$$

Thus we can calculate the effective channel Green function

$$G_{n,n+1}(E) = \left[E - H_{n,n+1} - \Sigma_n - \Sigma_{n+1}\right]^{-1} \tag{4.19}$$

and with this the transmission between two neighboring decoherence sites

$$T_{n,n+1}(E) = 4\,\mathrm{Tr}\left[G_{n,n+1} \mathrm{Im}\,\Sigma_{n+1} G^{+}_{n,n+1} \mathrm{Im}\,\Sigma_n\right] \tag{4.20}$$

To be consistent with the definition of the phase coherence length L_ϕ, we define the length of the subsystem enclosed by decoherence sites i_{n+1} and i_n as *subsystem length* $L_{n+1,n} = i_{n+1} - i_n$, in spite of the fact that the effective channel comprises $i_{n+1} - i_n - 1$ sites.

4.3.5 Rate equations

For the linear system, the general system of rate equations (4.6) reduces to

$$\rho_n \frac{\mathrm{d}f_n(E)}{\mathrm{d}t} = T^r_{n-1,n}(E)\left(f_{n-1}(E) - f_n(E)\right) + T^r_{n,n+1}(E)\left(f_{n+1}(E) - f_n(E)\right) \tag{4.21}$$

where we have used $T^r_{n,n+1} = T^r_{n+1,n}$, and ρ_n is the local density of states at decoherence site n. In the following we will only discuss the stationary case, i.e. $\frac{\mathrm{d}f}{\mathrm{d}t} = 0$. In this case, (4.21) simplifies to

$$0 = T_{n-1,n}(E)\left(f_{n-1}(E) - f_n(E)\right) + T_{n,n+1}(E)\left(f_{n+1}(E) - f_n(E)\right) \qquad n = 1, \ldots, N_d \tag{4.22}$$

where $f_0 \equiv f_L$ and $f_{N_d+1} \equiv f_R$ are the energy distribution functions of the contacts. In (4.22) we have already inserted the transmission functions T according to (4.10) and used the nomenclature $T_{01} \equiv T_{L1}$, $T_{N_d,N_d+1} \equiv T_{N_dR}$. The system (4.22) is a tridiagonal linear system of equations in the f_n of the dimension N_d. We can rewrite it as

$$\begin{pmatrix} T_{L1} + T_{12} & -T_{12} & 0 & \ldots \\ -T_{12} & T_{12} + T_{23} & -T_{23} & \ldots \\ 0 & -T_{23} & \ldots & \ldots \\ \ldots & \ldots & \ldots & \ldots \\ 0 & \ldots & -T_{N_d-1N_d} & T_{N_d-1N_d} + T_{N_dR} \end{pmatrix} \begin{pmatrix} f_1 \\ f_2 \\ \vdots \\ f_{N_d-1} \\ f_{N_d} \end{pmatrix} = \begin{pmatrix} T_{L1} f_L \\ 0 \\ \vdots \\ 0 \\ T_{N_dR} f_R \end{pmatrix} \tag{4.23}$$

This system with tridiagonal matrix of coefficients can be LU transformed and then be solved iteratively, see e.g. [148]:

$$\begin{pmatrix} 1 & 0 & 0 & \dots & 0 \\ m_2 & 1 & 0 & \dots & 0 \\ 0 & m_3 & 1 & \dots & 0 \\ \dots & \dots & \ddots & \ddots & \dots \\ \dots & \dots & \dots & m_{N_d} & 1 \end{pmatrix} \underbrace{\begin{pmatrix} u_1 & c_1 & 0 & \dots & 0 \\ 0 & u_2 & c_2 & \dots & 0 \\ 0 & 0 & u_3 & \ddots & 0 \\ \dots & \dots & \dots & \ddots & \ddots \\ \dots & \dots & \dots & \dots & u_{N_d} \end{pmatrix} \begin{pmatrix} f_1 \\ f_2 \\ \vdots \\ f_{N_d-1} \\ f_{N_d} \end{pmatrix}}_{\equiv \vec{y}} = \begin{pmatrix} T_{L1} f_L \\ 0 \\ \vdots \\ 0 \\ T_{N_d R} f_R \end{pmatrix} \tag{4.24}$$

where

$$u_1 = T_{L1} + T_{12} \tag{4.25}$$

$$y_1 = T_{L1} f_L \tag{4.26}$$

$$c_{n-1} = -T_{n-1,n} \tag{4.27}$$

$$m_n = -\frac{T_{n-1,n}}{u_{n-1}} \tag{4.28}$$

$$u_n = T_{n-1,n} + T_{n,n+1} + m_n T_{n-1,n} \tag{4.29}$$

$$y_n = \delta_{n N_d} T_{N_d R} f_R - m_n y_{n-1} \tag{4.30}$$

for all $1 < n \leq N_d$ and the solution for the fs is

$$f_{N_d} = \frac{y_{N_d}}{u_{N_d}} \tag{4.31}$$

$$f_n = \frac{y_n + T_{n,n+1} f_{n+1}}{u_n} \tag{4.32}$$

For $1 < n < N_d$ the iteration of (4.28)–(4.30) leads to continuous fractions

$$m_n = -\cfrac{T_{n-1,n}}{T_{n-2,n-1} + T_{n-1,n} - \cfrac{T^2_{n-2,n-1}}{T_{n-3,n-2} + T_{n-2,n-1} - \cfrac{T^2_{n-3,n-2}}{\dots}}} \tag{4.33}$$

and similarly for u and y:

$$u_n = T_{n-1,n} + T_{n,n+1} - \cfrac{T^2_{n-1,n}}{T_{n-2,n-1} + T_{n-1,n} - \cfrac{T^2_{n-2,n-1}}{T_{n-3,n-2} + T_{n-2,n-1} - \cfrac{T^2_{n-3,n-2}}{\dots}}} \tag{4.34}$$

$$y_n = -m_n \times (-m_{n-1}) \times (-m_{n-2}) \times (-m_{n-3}) \times \dots \times (-m_2) \times y_1 \tag{4.35}$$

An equivalent notation can be derived by complete induction[5]:

$$m_n = \frac{-\sum\limits_{k=0}^{n-2} \frac{1}{T_{k,k+1}}}{\sum\limits_{k=0}^{n-1} \frac{1}{T_{k,k+1}}} \tag{4.36}$$

$$u_n = T_{n,n+1} + \frac{1}{\sum\limits_{k=0}^{n-1} \frac{1}{T_{k,k+1}}} \tag{4.37}$$

$$y_n = \frac{1}{\sum\limits_{k=0}^{n-1} \frac{1}{T_{k,k+1}}} f_L \tag{4.38}$$

Using (4.30), (4.31) and (4.38) one finds for f_{N_d}:

$$f_{N_d} = \frac{\frac{1}{T_{N_d R}} f_L + \sum\limits_{k=0}^{N_d-1} \frac{1}{T_{k,k+1}} f_R}{\sum\limits_{k=0}^{N_d} \frac{1}{T_{k,k+1}}} \tag{4.39}$$

Thus for the current we find (2.46)

$$I = \frac{e}{h} \int \mathrm{d}E T_{N_d R} \left(f_{N_d} - f_R\right) = \frac{e}{h} \int \mathrm{d}E \left(f_L - f_R\right) \frac{1}{\sum\limits_{k=0}^{N_d} \frac{1}{T_{k,k+1}}} \tag{4.40}$$

which in the small-bias limit $\mu_L \to \mu_R$ yields the conductance of the total system

$$G = \frac{e^2}{h} T_{\text{eff}} = \frac{e^2}{h} \frac{1}{\sum\limits_{k=0}^{N_d} \frac{1}{T_{k,k+1}}} \tag{4.41}$$

and hence the resistance

$$R = \frac{h}{e^2} \sum_{k=0}^{N_d} \frac{1}{T_{k,k+1}} \tag{4.42}$$

which is nothing but the sum of the subsystem resistances $\frac{h}{e^2} \frac{1}{T_{k,k+1}}$. This is already an important property of our model. For a given decoherence configuration, the total resistance equals the sum of the subsystem resistances.

4.3.6 Results for the ordered chain

In this section we consider a tight-binding chain without disorder: all onsite energies $\epsilon_i = \epsilon_L = \epsilon_R = 0$ are equal to zero. Like before, we take $t = 1$ as our energy unit, e.g. μ is measured in units of t. For all calculations $\eta = \eta_L = \eta_R$. For further simplification of the notation we use natural units for the conductance and resistance, i.e. $\frac{e^2}{h} = 1$.

---

[5] Note that $1 < n < N_d$.

4.3.6.1 The conductance $\langle G(\mu)\rangle$ of the system

For an instructive introduction to the numerical results we consider as a first example the ordered chain with length $N = 7$ like in Figure 4.3. Without decoherence sites, its conductance is just $G(\mu) = T_{LR}(\mu) = T_9(E = \mu)$ using the notation $T_N(E)$ of Section 3.9 and taking into account that we model the contacts similar to the decoherence sites. With decoherence sites at $i = 2$ and $i = 4$ like in the first example of Figure 4.3, using (4.42) the resistance of this decoherence configuration reads

$$\frac{1}{G_{\text{config.1}}(\mu)} = R_{\text{config.1}}(\mu) = \frac{2}{T_3(\mu)} + \frac{1}{T_5(\mu)} \tag{4.43}$$

Analogously, for the second example in Figure 4.3, we find

$$\frac{1}{G_{\text{config.2}}(\mu)} = R_{\text{config.2}}(\mu) = \frac{1}{T_2(\mu)} + \frac{2}{T_3(\mu)} + \frac{1}{T_4(\mu)} \tag{4.44}$$

The conductance $G(\mu)$ for the chain without decoherence sites, and for the decoherence configurations of (4.43) and (4.44) is displayed in Figure 4.5. Also the individual transmission functions T_N are displayed there. Compare with Figures 3.33 and 3.35, where the same T_N (for different $\eta = \frac{\Gamma}{2}$) are displayed.

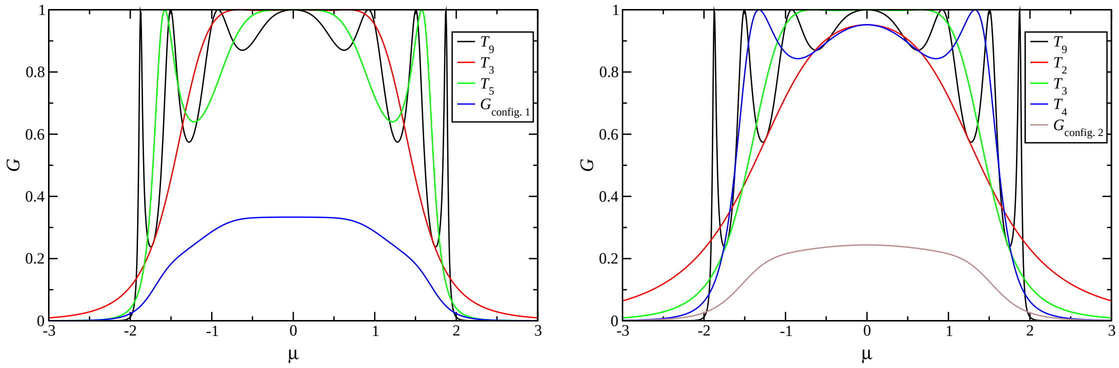

Figure 4.5: Conductance G of the example configurations of Figure 4.3 as a function of the Fermi energy μ of the contacts. For comparison, also the transmission functions which go into the conductances are displayed. $\eta = 1.25$.

Now, in order to obtain the conductance $\langle G(\mu)\rangle$ of the system for a given parameter p we choose a number of M decoherence configurations and average the single-configuration conductances. For the chain of length $N = 7$ with $p = 0.2$ and $M = 100$, this is done in Figure 4.6.

In this Figure 4.6 we compare the curves $\langle G(\mu)\rangle$ averaged over different decoherence configurations for every energy μ (black curve), and averaged over the same decoherence configurations (red curve). Of course, the red curve is continuous and differentiable, whereas the black one fluctuates. Yet we observe that the fluctuations of the black curve are of the same size as the standard error of the mean $\sigma_M(G) = \sqrt{\frac{1}{M}\langle G^2 - \langle G\rangle^2\rangle}$ which was evaluated for the red curve. We conclude that averaging over the same decoherence configurations for different energies is justified, having in mind that the average is subject to an error measurable by the standard error of the mean σ_M.

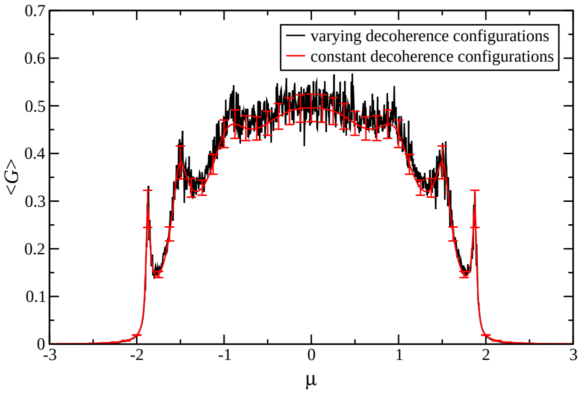

Figure 4.6: Averaged conductance $\langle G\rangle$ for a chain with $N = 7$ as a function of the Fermi energy μ of the contacts. $p = 0.2$, $\eta = 1.25$. Whereas for the black curve, the $M = 100$ decoherence configurations were chosen independently for every energy μ, for the red curve the same $M = 100$ decoherence configurations were taken for every energy. The error bars in the red curve are the standard errors of the mean conductance, $\sigma_M = \sqrt{\frac{1}{M}\langle G^2 - \langle G\rangle^2\rangle}$, and in good accordance with the fluctuations of the black curve.

We have also performed numerical calculations for a chain of $N = 100$ sites with $\eta = 1.25$. Figure 4.7 shows the results for the conductance in dependence of the Fermi energy μ of the contacts. The conductance was averaged over $M = 400$ decoherence configurations which were the same for all energies μ.

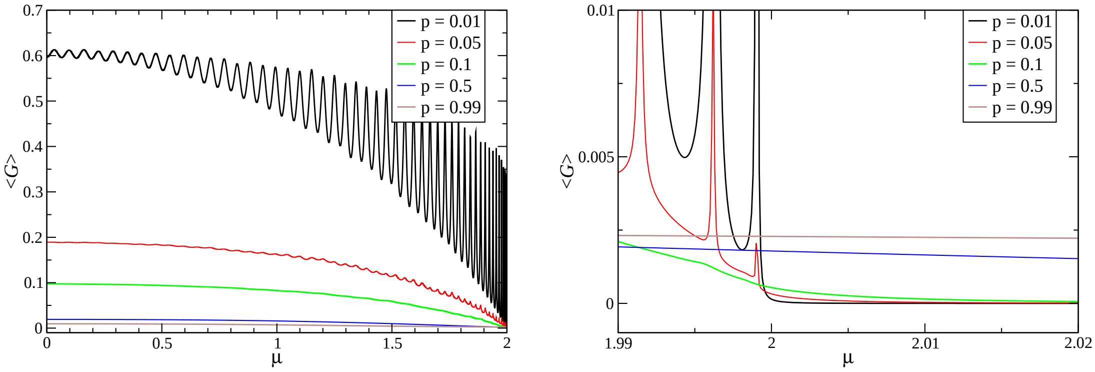

(a) μ inside the band

(b) μ at the band edge

Figure 4.7: Averaged conductance $\langle G\rangle$ of the ordered chain as a function of the Fermi energy μ of the contacts for different parameters p. The conductance $\langle G(\mu)\rangle$ is symmetric with respect to $\mu = 0$, therefore only $\langle G(\mu > 0)\rangle$ is displayed. The $M = 400$ decoherence configurations over which the average was taken, were the same for all energies μ. $\eta = 1.25$.

In Figure 4.7(a) for $p = 0.01$ we can still see the energy spectrum of the finite tight-binding chain, cf. (3.77). At the eigenenergies of the isolated chain, $\langle G\rangle$ has maxima. The reason is that for many of the decoherence configurations at $p = 0.01$ no decoherence in the system was present. For higher values of p, the maxima are washed out as their locations vary for different lengths of the coherent subsystems. To the edges of the tight-binding band

$\mu \to \pm 2$, the conductance is reduced, just like in the model of Roy and Dhar [156], whose result is displayed in Figure 4.8.

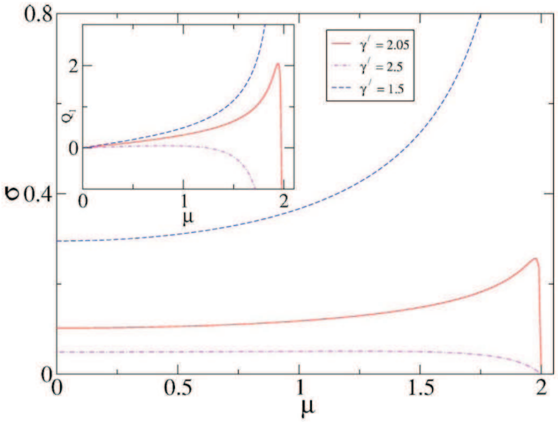

Figure 4.8: Figure 2 of [156]. The electrical and thermal (inset) conductivity of an infinite chain of the setup of Figure 4.1. Here the conductivity is understood as length × conductance of an infinite subsystem infinitely far from the left and right contacts. γ' corresponds to the parameter η in Figure 4.1. The conductivity σ is given in units of $\frac{e^2}{2h}$ and μ in units of the coupling along the chain. For large dephasing parameter $\gamma' = 2.5$, the curve $\sigma(\mu)$ has a similar behavior as our $G(\mu)$ for $p > 0.05$, cf. Figure 4.7.

4.3.6.2 Fluctuations of $G(\mu)$

In the same way like the conductance we calculate the conductance fluctuations as a function of the Fermi energy μ of the contacts by averaging over different decoherence configurations. In Figure 4.9 these fluctuations are displayed for a system of length $N = 100$ averaged over 400 configurations.

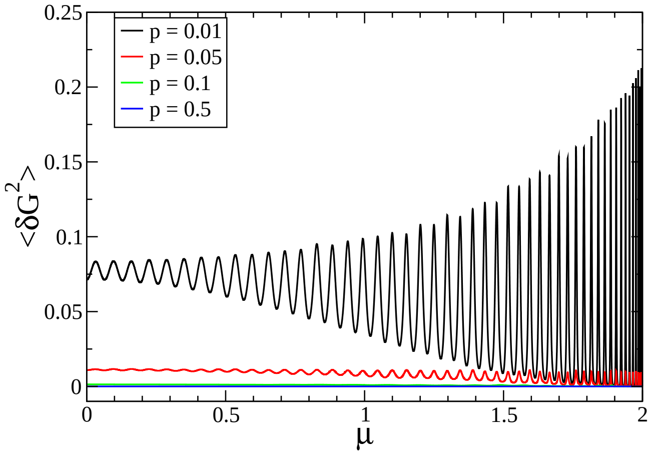

Figure 4.9: Conductance fluctuations $\langle \delta G^2 \rangle$ of the ordered chain as a function of the Fermi energy μ of the contacts for different parameters p. We see that the decoherence strongly suppresses the fluctuations. Like G, also its fluctuations are symmetrical with respect to $\mu = 0$. $\eta = 1.25$.

For $p > 0.05$ we find a strong suppression of the conductance fluctuations by decoherence. That means that apart from the average over M decoherence configurations, also within a single configuration the distribution of decoherence sites causes a self-averaging which reduces the fluctuations. The strong fluctuations towards the band edge for $p = 0.01$ are explained by the fact that near the band edge, the tight-binding system has the highest density of eigenenergies. Thus a decoherence site in the system is more likely to modify the transmission near the band edges.

4.3.6.3 $\langle G(p)\rangle$ and $\langle R(p)\rangle$ for $\mu = 0$

Furthermore we have analyzed the dependence of the conductance on the density p of decoherence sites, $\langle G(\mu, p)\rangle$. At each decoherence site there is a momentum relaxation. Therefore a loss of conductance is expected. Numerical results are displayed in Figure 4.10.

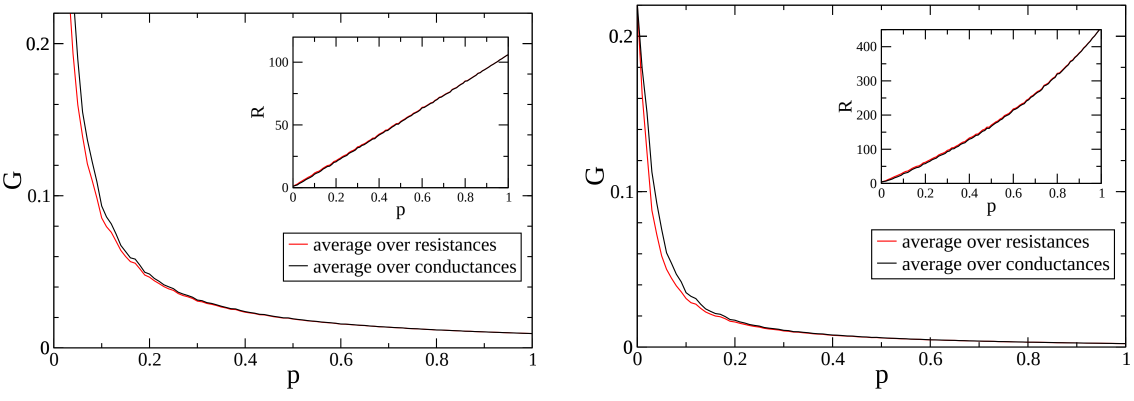

(a)

(b)

Figure 4.10: (a) Conductance and resistance (inset) of a chain with $N = 100$ at $\mu = 0$ as a function of the decoherence parameter p which corresponds to the average decoherence site density. $\eta = 1.25$. The averages were taken over $M = 400$ decoherence configurations. For the black curves, the conductance was averaged over the decoherence configurations, and the resistance calculated as the inverse averaged conductance, i.e. $R = \frac{1}{<G>}$, whereas for the red curve, the resistance was averaged over the decoherence configurations, and $G = \frac{1}{<R>}$. As expected, the conductance decreases with p, the average density of decoherence sites. (b) Except for $\eta = 4.0$ all parameters are the same like in (a). In the inset we observe that the resistance does not increase linearly with p. Like in (a), the type of average affects the resulting resistance and conductance, specially for small values of p.

In Figure 4.10, two different averages are considered. For the black curves, the conductance was averaged over the different decoherence configurations, whereas for the red curves, the resistance was averaged. The seemingly linear dependence of $\langle R(p)\rangle$ and $1/\langle G(p)\rangle$ in Figure 4.10(a) is a coincidence for the chosen parameter η. For $\eta = 4$ we observe a nonlinearity, cf. the Figure 4.10(b).

When to take which average

The averages over the conductance and the resistance correspond to different experimental situations. Whereas the average over the conductances is adequate for a situation where for a fixed voltage the current is measured as the reaction of the system, the average over the resistances is adequate when a fixed current is imposed on the system and the caused potential drop is measured.

If we consider the linear chain as a representative of a current path in a 3d medium between 2d contacts, it is natural to average over the conductance. If instead we consider the chain as a representative subsystem of a very long linear system (like below for the calculation of the resistivity), the average has to be taken over the resistances.

Below we will see that under certain circumstances, an ohmic resistivity of the infinite chain can be defined. For a large system size, both conductance and resistance can be described well by the resistivity. Then the question of which average to take becomes irrelevant.

Analytical calculation of $\langle R(p, \mu = 0)\rangle$

As we have seen in Section 3.9.2, at $E = \mu = 0$, the transmission $T_N(E)$ of the coherent ordered chain only depends on the even-odd parity of the chain length. This gives us a means to calculate $\langle R(p)\rangle$ of Figure 4.10 analytically.

The way we defined the contacts and decoherence sites in Sections 4.3.1 and 4.3.2, between every two contacts and decoherence sites we have $i_{n+1} - i_n - 1$ coherent sites which correspond to ordered chains of length $i_{n+1} - i_n + 1$ between contacts in the wide-band limit like in Section 3.9.2. If furthermore we choose $\eta_L = \eta_R = \eta$, the total resistance[6] at $\mu = 0$ of a decoherence configuration, (4.42), simplifies to

$$R = \frac{A_u}{T_u} + \frac{A_g}{T_g} \tag{4.45}$$

where A_u is the number of segments of odd length ($i_{n+1} - i_n + 1$ odd), and A_g is the corresponding number of even segments ($i_{n+1} - i_n + 1$ even). As we have seen in Section 3.9.2 (equations (3.115) and (3.116) with $\Gamma = 2\eta$, see also [199, Section 5]), the transmission $T_N(E = 0)$ through an odd-length ordered chain for $\eta_L = \eta_R = \eta$ and $t = 1$ is

$$T_u = 1 \tag{4.46}$$

and for an even-length chain

$$T_g = \frac{4\eta^2}{(1+\eta^2)^2} \tag{4.47}$$

The average number of odd segments in the chain is

$$\langle A_u(p, N)\rangle = \frac{2\,(1-p)^2\left[1-(p-1)^N\right] + pN\,(1-p)\,(2-p)}{(2-p)^2} \tag{4.48}$$

---

[6] Note that we use natural units $\frac{e^2}{h} = 1$ in this Section.

and the average number of even segments in the chain is

$$\langle A_g(p,N)\rangle = \frac{2-p^2+pN\,(2-p)+2\,(1-p)^2\,(p-1)^N}{(2-p)^2} \tag{4.49}$$

For the derivation of the formulae (4.48) and (4.49), which involves using a matrix product ansatz, see the Appendix C.

Knowing these exact averages, the averaged resistance is

$$\langle R\rangle_{\text{exact}} = \frac{\langle A_u\rangle}{T_u} + \frac{\langle A_g\rangle}{T_g} \tag{4.50}$$

A comparison of numerical and exact averages of R is displayed in Figure 4.11.

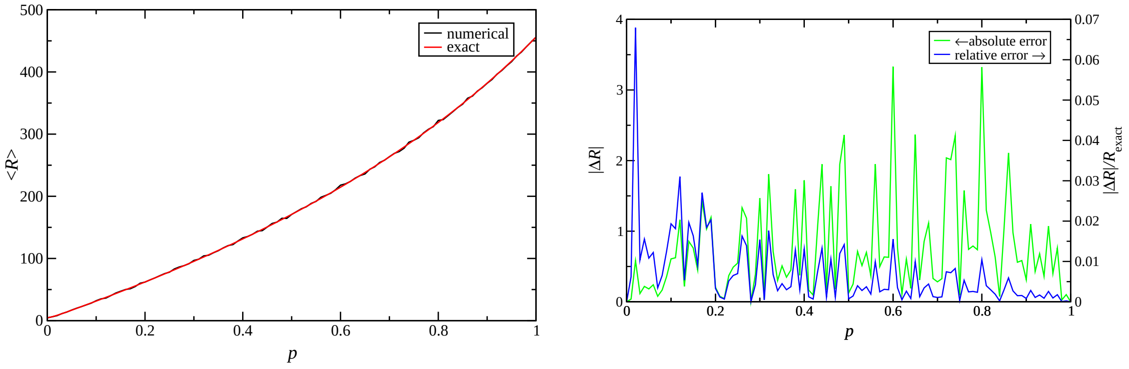

(a) (b)

Figure 4.11: Resistance of a ordered chain of length $N = 100$, $\eta = 4.0$. (a) $R(p)$ as a numerical average over 400 decoherence configurations (black) and as the exact average (red). (b) Absolute (green) and relative (blue) error of the numerical average. Note the two different y axes in the right graph.

The relative error between numerical average and exact average is also shown in Figure 4.11. As we can see, already the average over 400 decoherence configurations (out of $2^{100} \approx 1.3 \times 10^{30}$ possible) yields relative errors in the averaged resistance of less than 7%. Figure 4.12 shows the dependence of the relative error on the number M of decoherence configurations over which the average is taken.

We can see that for $N = 100$ and $\eta = 4.0$ a reliable numerical average with an error $< 5\%$ is already reached on averaging over only 700 decoherence configurations.

4.3.6.4 The resistivity of infinite chains

Now let us consider the averaged resistance $\langle R\rangle_{\text{exact}}$, equation (4.50), in the limit $N \to \infty$. As $p \in [0,1]$, we find the ohmic resistivity

$$\rho(\mu=0,p) = \lim_{N\to\infty} \frac{\langle R(p,\mu=0)\rangle_{\text{exact}}}{N} = \frac{p(1-p)}{2-p}\frac{1}{T_u} + \frac{p}{2-p}\frac{1}{T_g} = \frac{p(1-p)}{2-p} + \frac{p}{2-p}\frac{\left(1+\eta^2\right)^2}{4\eta^2} \tag{4.51}$$

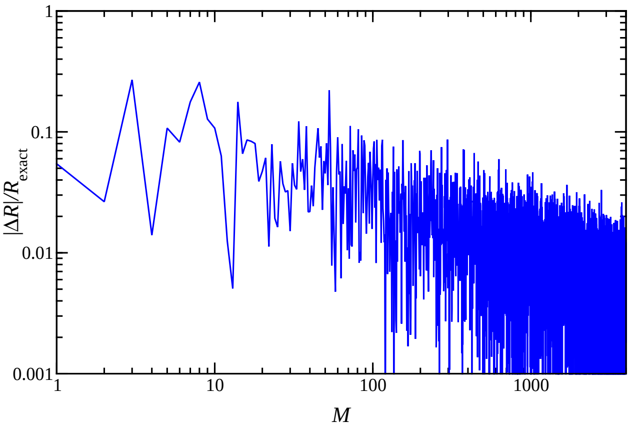

Figure 4.12: Relative error of the resistance as a function of the number M of decoherence configurations over which the numerical average is taken. $N = 100$, $\eta = 4.0$. For more than 700 decoherence configurations, the relative error is smaller than 5%. Note the logarithmic scales.

for a linear ordered system at $\mu = 0$. The resistivity $\rho(p = 0) = 0$, does not mean that a completely coherent conductor has a resistance $R = 0$, but only that it does no longer increase with the length.

Also for $\mu \neq 0$ we can define a resistivity of infinite chains in the following way:

$$\rho(\mu, p) = \frac{1}{L_\phi}\left[\frac{p}{T_2(\mu)} + \frac{p(1-p)}{T_3(\mu)} + \frac{p(1-p)^2}{T_4(\mu)} + \dots\right] = p^2 \sum_{j=0}^{\infty} \frac{(1-p)^j}{T_{j+2}(\mu)} \tag{4.52}$$

where L_ϕ is the average subsystem length, p the relative frequency of subsystems of length $i_{n+1} - i_n = 1$ (transmission function T_2), $p(1-p)$ the relative frequency of subsystems of length 2, etc. The sum in (4.52) converges for $\mu \in (-2, 2)$ because $\frac{1}{T_{\mathrm{inf}}(\mu)} \sum_{j=0}^{\infty}(1-p)^j = \frac{1}{pT_{\mathrm{inf}}(\mu)}$ converges and $\frac{1}{T_{\mathrm{inf}}(\mu)} \geq \frac{1}{T_j(\mu)} > 0$ is a majorant for all j, cf. Section 3.9.2.3.

The majorant also yields an estimate for the error in the numerical evaluation of $\rho(\mu \in (-2, 2))$. If we add the first J terms of the sum ($= \rho_J$), the maximum error is

$$\rho - \rho_J \leq \frac{p^2}{T_{\mathrm{inf}}(\mu)} \sum_{j=J+1}^{\infty} (1-p)^j = \frac{p\,(1-p)^{J+1}}{T_{\mathrm{inf}}(\mu)} \tag{4.53}$$

Thus we know which J to choose for any desired accuracy of ρ.

For $\mu = \pm 2.0$, where, according to (3.123), $T_j \propto j^{-2}$, the series (4.52) converges for all $p \in [0, 1]$, as the generalized ratio test for the summands shows.

For μ outside the band, we can apply (3.118),[7] in order to determine those p for which a resistivity can be defined. For $\mu > 2$, the summands of (4.52) for large j can be approximated by

$$\frac{p^2(1-p)^j}{T_{j+2}(\mu)} \overset{j \gg 1}{\approx} \frac{p^2(\mu^2+\eta^2)^2(\mu+\sqrt{\mu^2-4})^2}{16\eta^2\,(\mu^2-4)} \left[\left(\frac{\mu+\sqrt{\mu^2-4}}{2}\right)^2 (1-p)\right]^j \tag{4.54}$$

---

[7] Use $\Gamma = 2\eta$.

Thus the series (4.52) has the same tail (i.e. large j-part) like a geometric series with summands (4.54). Therefore also for $\mu \notin [-2, 2]$ we have ohmic behavior for infinite chains, if the convergence criterion for ρ is fulfilled:

$$\left(\frac{\mu+\sqrt{\mu^2-4}}{2}\right)^2 (1-p) \begin{cases} < 1 & \text{resistivity } \rho \text{ exists} \\ \geq 1 & \text{resistivity } \rho \text{ does not exist} \end{cases} \tag{4.55}$$

We conclude that if

$$L_\phi < L^* = \frac{1}{1 - \left[\frac{2}{\mu+\sqrt{\mu^2-4}}\right]^2} \qquad \text{or equivalently} \qquad p > p^* = 1 - \left[\frac{2}{\mu + \sqrt{\mu^2-4}}\right]^2 \tag{4.56}$$

ohmic behavior is reached.[8]

We observe, that whether or not for a given $|\mu| > 2$ a resistivity can be defined, only depends on the parameter p. The parameter η only enters into the absolute value of ρ.

For large finite systems, the resistivity of the infinite system yields an approximate value for the resistance $R \approx \rho N$ and conductance $G \approx \frac{1}{\rho N}$. Then also the question of whether to average over the resistances or conductances becomes irrelevant as the resistance for every decoherence configuration becomes self-averaging for large N. We will discuss this in the next paragraph.

One could imagine to use the first summands of (4.52) to approximate the resistance R of a finite system with size N also for $\mu > 2, p < p^*$ (i.e. when ρ does not exist):

$$R \approx N\rho_N \qquad \text{wrong!} \tag{4.57}$$

Yet, this approximation leads to wrong results because the summands for $j \approx N$, which contribute most to ρ_N, have wrong statistical weight for a finite chain. Anyway we expect a super-linear resistance increase.

$\langle G(p, \mu \neq 0)\rangle$ and $\langle R(p, \mu \neq 0)\rangle$

Above in Section 4.3.6.3 using an analytic calculation we have seen that $\langle R(p, \mu = 0)\rangle$ increases monotonously with p. Here we examine this function numerically also for other values of μ. See Figure 4.13.

First we notice that $\rho N \approx \langle R\rangle \approx 1/\langle G\rangle$ is not valid for small values of $p < \frac{1}{N}$, i.e. when the system size is smaller than the coherence length. Then, of course, the use of the resistivity of an infinite system makes no sense.

We see in Figure 4.13 that for all values $\mu \notin (-2, 2)$ outside the tight-binding band of the ordered chain, $\langle G\rangle$ increases with p. The reason is the following. As we have seen in Section 3.9.2.2, the transmission $T_N(E)$ of the ordered chain decays exponentially with

---

[8] Already for $\mu = 2.1$ the required phase coherence $L_\phi < 2.14$ reaches the order of magnitude of the lattice constant.

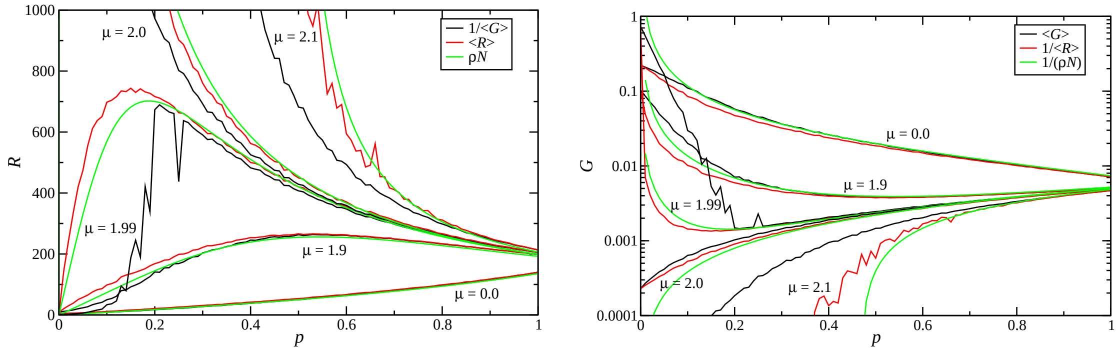

(a) Resistance

(b) Conductance

Figure 4.13: Resistance (a) and conductance (b) of an ordered chain with $N = 30$ as a function of p. The averages $\langle G\rangle$ (black lines) and $\langle R\rangle$ (red lines) were taken over $M = 1000$ decoherence configurations. For comparison also the conductance and resistance calculated from ρ are depicted in the graphs (green lines). In (a), $\mu = 0.0, 1.9, 1.99, 2.0, 2.1$ from bottom to top groups of three lines. In (b), $\mu = 0.0, 1.9, 1.99, 2.0, 2.1$ from top to bottom. Note the logarithmic G-axis in (b). $\eta = 4.0$.

$N \to \infty$ for $|E| > 2$. Now, with growing p the number of decoherence sites in the chain increases and thus the average subsystem length decreases, leading to an increase in $\langle G(p)\rangle$ for $|\mu| \geq 2$.

Now we explain the behavior for $\mu \in (-2, 2)$. With p, the number of decoherence sites in the system increases. For every additional decoherence site in a decoherence configuration, according to (4.42) we have an additional summand adding to the resistance with a value between $\frac{1}{T_{\text{sup}}}$ and $\frac{1}{T_{\text{inf}}}$.[9] For $\mu \approx 0$, as we can see in Figure 3.38(a) on page 49, T_{inf} and T_{sup}, are of the same order of magnitude for $\eta = 4.0$, thus the increase in the number of decoherence sites causes an approximately linear increase of R. For $\mu \to \pm 2$, i.e. $T_{\text{inf}} \to 0$, we find that the resistance first increases and then decreases with p. This is the crossover between the behavior at the middle of the band and outside the band. The crossover can be understood by considering Figures 3.38 and 3.41 on pages 49 and 52. We see in Figure 3.41 that the average transmission $\langle T(\mu \to 2)\rangle_N \to 0$ approaches zero whereas for $N = 2$, as we can see in Figure 3.38(b), $T_2(\mu \to 2) > 0$ has a value clearly larger than zero. Now, whereas for small p, any additional decoherence site causes a large increase in resistance (as $1/\langle T\rangle_N \gg 1$) of the configuration, for large p most of the coherent subsystems have the length 1 and contribute only $1/T_2 \sim 1$ to the resistance of the configuration. The large discrepancy of the individual values of T that contribute to $\langle R\rangle$ for $\mu \to 2$ is also the reason for the large differences in averaging over resistances or conductances in Figure 4.13(a) for $\mu = 1.99$.

---

[9] For the definitions of T_{sup} and T_{inf}, see Section 3.9.2.3, page 49.

4.3.6.5 The resistance of the finite chain, and how the ohmic limit is reached

The length dependence of the resistance $1/\langle G(N)\rangle$ is displayed in Figures 4.14 and 4.15.

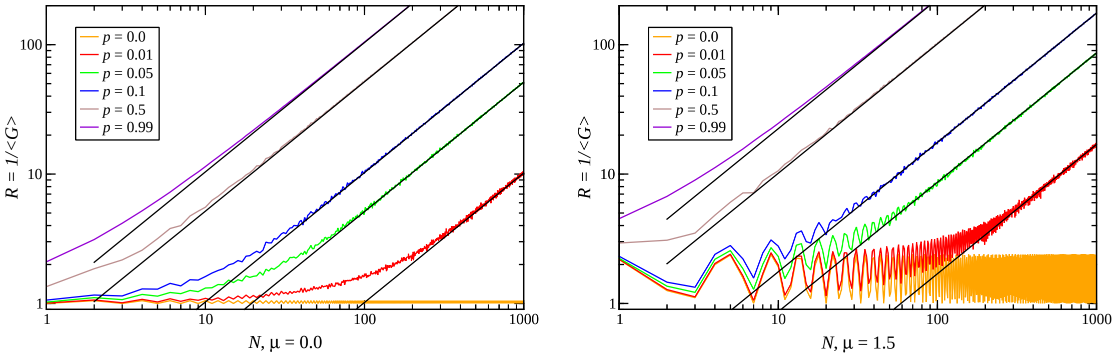

(a) In the middle of the band

(b) Inside the band

Figure 4.14: The length dependence of the resistance $R = 1/\langle G\rangle$ where the average was taken over $M = 400$ decoherence configurations. Note the double logarithmic axes. For comparison, in black we have drawn the straight lines $R = \rho(\mu, p)N$ of ohmic resistance with the resistivity for infinite chains. For all curves, $\eta = 1.25$.

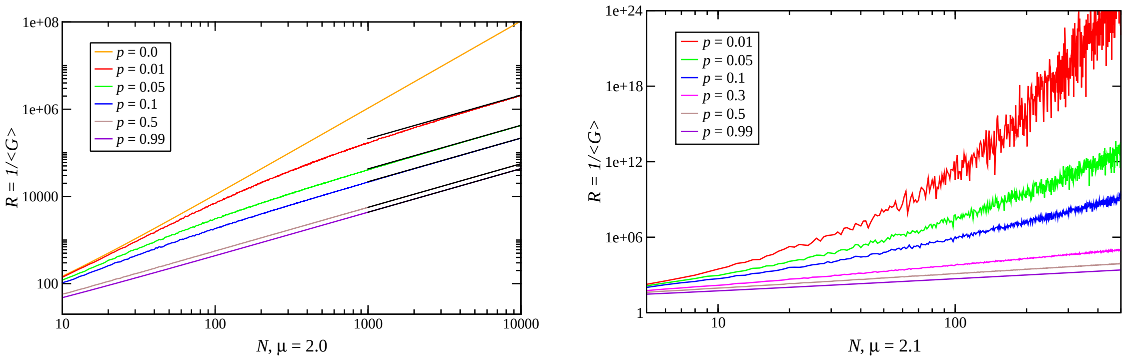

(a) At the band edge

(b) Outside the band

Figure 4.15: The same as Figure 4.14 for different choices of μ. For $\mu = 2.0$ we observe the power law $R \propto N^2$ for $p = 0.0$ (compare with Figure 3.39), whereas for $p > 0$, finally $R \propto N$ is reached. For $\mu = 2.1$ outside the band we observe a nonlinear increase of R except for $p > p^*$.

We notice that for large N, the resistance increases ohmically, i.e. proportional to N, for all $\mu \in (-2, 2)$ inside the tight-binding band of the chain. For comparison, also the resistances calculated from the resistivity ρ according to (4.52) are plotted in Figure 4.14. They give very good estimates for large system sizes.

As we can see from Figure 4.15(a), for $\mu = 2.0$ at the band edge, the proportionality $R \propto N$ is reached for large N. Only for $p = 0.0$ (which shows oscillatory curves for $|\mu| < 2.0|$), we find $R \propto N^2$, in accordance with (3.123).

For $|\mu| > 2.0$, the large N behavior of R depends on p. For $p < p^*$ (cf. (4.56)), R behaves nonlinear, increasing the steeper the smaller p is. For $p > p^*$, we expect a linear relationship $R \propto N$ for $N \to \infty$.

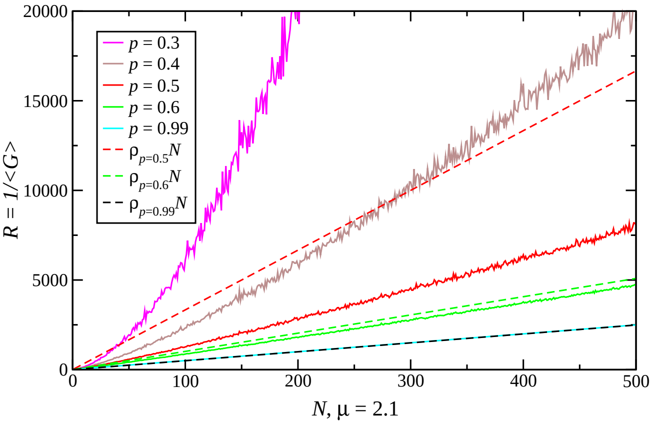

Figure 4.16: A magnification of Figure 4.15(b) (now using linear axes) including additional choices of p. For comparison, also $N\rho(p, \mu)$ is depicted for those choices of p, for which it can be defined. For the parameters chosen in this plot, $p^* = 0.467$.

Indeed we find, as displayed in Figure 4.16, examples of linear behavior $R \propto N$ for $\mu = 2.1$. There we have also displayed the resistances calculated from the resistivity of the infinite chain. Whereas for $p = 0.99$ and $p = 0.6$, the resistivity ρ of the infinite chain comes close to the slope of R, for $p = 0.5 \gtrsim 0.467 = p^*$ there is a large discrepancy. The reason is that subsystems of an almost vanishing statistical weight contribute significantly to the resistivity (defined in (4.52)). For example, for $p = 0.5$ and $\mu = 2.1$, subsystems of length $L > 20$ which have a statistical weight of $1 - p(1 - p)^{19} = 9.5 \times 10^{-7}$ contribute more than 29% to the resistivity. Even subsystems of length $L > 73$ (statistical weight 1.0×10^{-22}) contribute more than 1% to ρ. Thus, as we approach $p \to p^*$ from above, an accordance of the system resistance with the resistivity is only reached for larger and larger N. The number of decoherence configurations M over which we average the conductance, has to increase drastically in order to find agreement with the value calculated from the resistivity ρ. Computationally this becomes soon impossible. If ρ has significant contributions for subsystem lengths $L > N$ larger than the system, it can no longer be used to approximate the finite system resistance.

This could also have observable experimental consequences. Although a large sample can have a material-specific resistivity (corresponding to our ρ), smaller systems (still much larger than the phase coherence length) of the same material can have unpredictable resistances, if the locations of decoherence events cannot be controlled.

In Figure 4.17 we analyze how the ohmic limit of the conductance is reached.

For $\mu = 0.0$ we find that the way the ohmic conductance is reached is similar to that found with the model of Roy and Dhar [156]. In this situation we find a correspondence of the "dissipation constant γ'" of [156] (the η of Figure 4.1) with our decoherence site density p. See also the discussion in [199, End of Section 5].

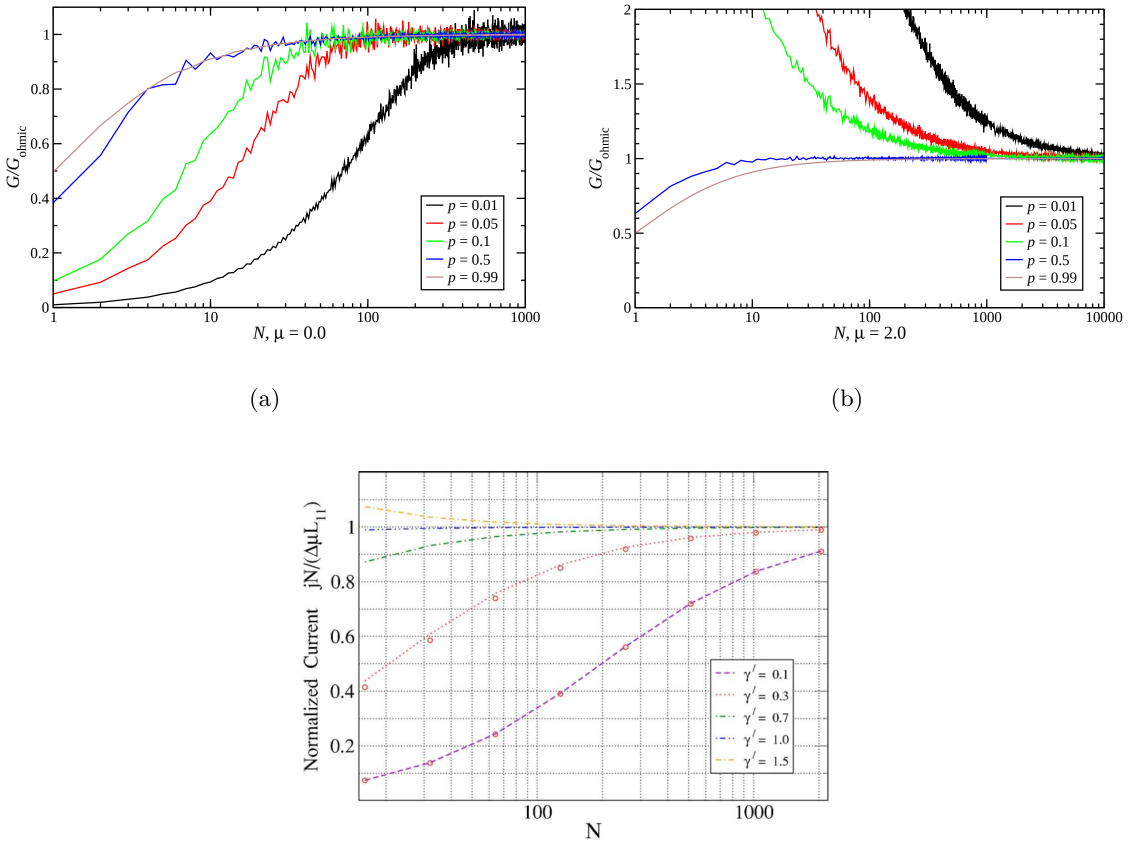

(a)

(b)

(c)

Figure 4.17: $\langle G\rangle\rho N$ as a function of the chain length for $\mu = 0.0$ (a) and $\mu = 2.0$ (b). The conductance was averaged over $M = 400$ decoherence configurations. $\eta = 1.25$. For $\mu = 0.0$ we see a nice analogy with Figure 4 of [156], displayed in (c). With decreasing phase coherence length $1/p$ (increasing "dissipation constant γ'" of [156]) the ohmic limit is reached faster. Note the logarithmic N axis in the graphs.

4.3.6.6 The fluctuations $\langle\delta G^2\rangle$

Now we come to the fluctuations of the conductance. The fluctuations $\langle\delta G^2\rangle = \langle G^2 - \langle G\rangle^2\rangle$ as a function of the chain length N are displayed in Figure 4.18 and 4.19 for different values of μ.

In Figure 4.18 we see the conductance fluctuations for $\mu = 0$ in the middle of the band. The maxima of the fluctuations lie at about $N = \frac{1}{p}$ i.e. when there is most probably either 0 or 1 decoherence site in the system. As we can see in the log-log plot (Figure 4.18(b)), the fluctuations for $\mu = 0.0$ behave like $\langle\delta G^2\rangle \propto N^{-3}$ as $N \to \infty$.

In Figure 4.19(a) we find that the proportionality $\langle\delta G^2\rangle \propto N^{-3}$ also holds for $\mu = 1.99$ near the band edge. Consider the periodicity of the oscillations in Figures 4.18(a) and 4.19(a). We identify them with the periodicity of $T_N(E)$ (cf. Section 3.9.2.3): Whereas

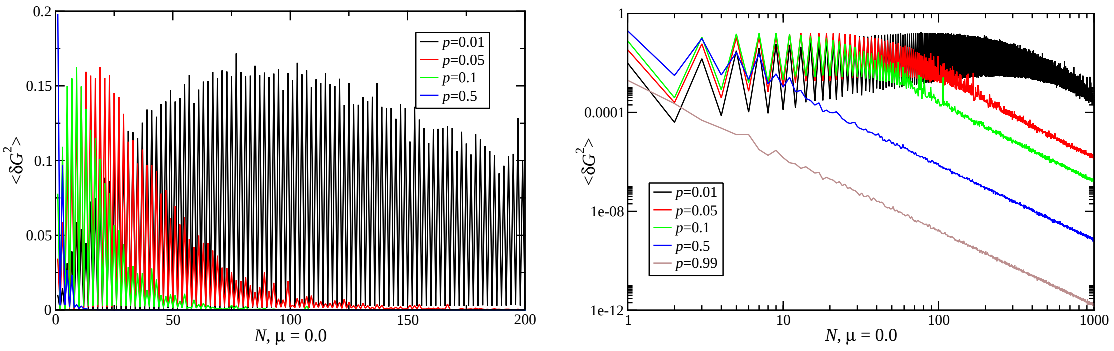

(a) $\mu = 0.0$

(b) $\mu = 0.0$, log-log plot

Figure 4.18: The length dependence of the fluctuations $\langle \delta G^2 \rangle$ for $\eta = 4.0$ and different values of p. Average over $M = 400$ decoherence configurations.

at $\mu = 0$ we find the period $P = 2$ (even-odd behavior), at $\mu = 1.99$ we find the period $P = 31.4$ given by (3.125). With any $N > kP, k = 1, 2, \ldots$, the chain can comprise one more subsystem of the length P, which has a transmission close to 1, whereas subsystems of other lengths have transmissions close to 0 (cf. Figure 3.40(b)).

In Figure 4.19(b) we can see the fluctuations for $\mu = 2.1$ outside the band. We can see that for $p > p^* = 0.463$ (cf. (4.56)), when ohmic behavior is reached, the fluctuations decay also like $\langle \delta G^2 \rangle \propto N^{-3}$. On the other hand for $p < p^*$, the fluctuations decay faster (but not faster than the conductance itself, see Section 4.3.6.7).

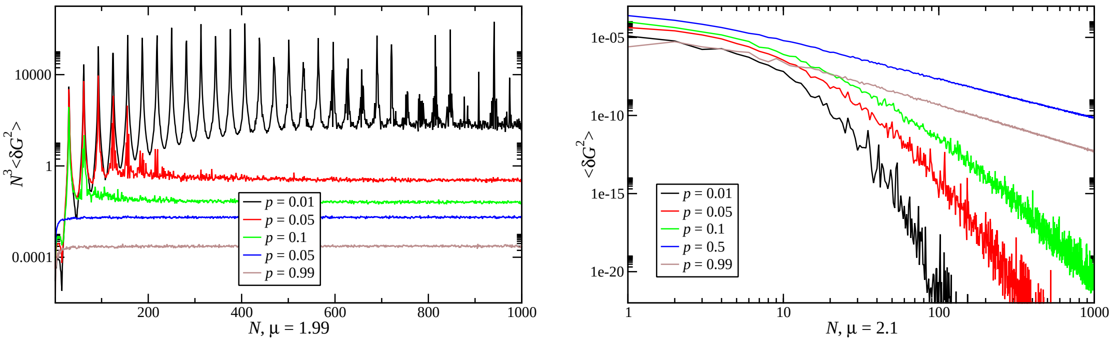

(a) $\mu = 1.99$

(b) $\mu = 2.1$, log-log plot

Figure 4.19: The length dependence of the fluctuations $\langle \delta G^2 \rangle$. Note that in (a) $N^3 \langle \delta G^2 \rangle$ is plotted in dependence of N. Apart from μ, parameters like in 4.18.

The reason for the decay for $N \to \infty$ for a fixed number of decoherence configurations M is that, when the ohmic limit exists, for long chains the resistance of every decoherence configuration approaches the same value given by $R = N\rho$ due to self-averaging. If the ohmic limit does not exist, the subsystems predominantly act as tunneling barriers, and therefore their respective conductance and condunctance fluctuations decay exponentially with the chain length.

4.3.6.7 The relative standard error of the mean $\frac{\sqrt{\langle \delta G^2 \rangle}}{\langle G \rangle \sqrt{M}}$

The relative standard error of the mean $\frac{\sqrt{\langle \delta G^2 \rangle}}{\langle G \rangle \sqrt{M}}$ is displayed in Figure 4.20.

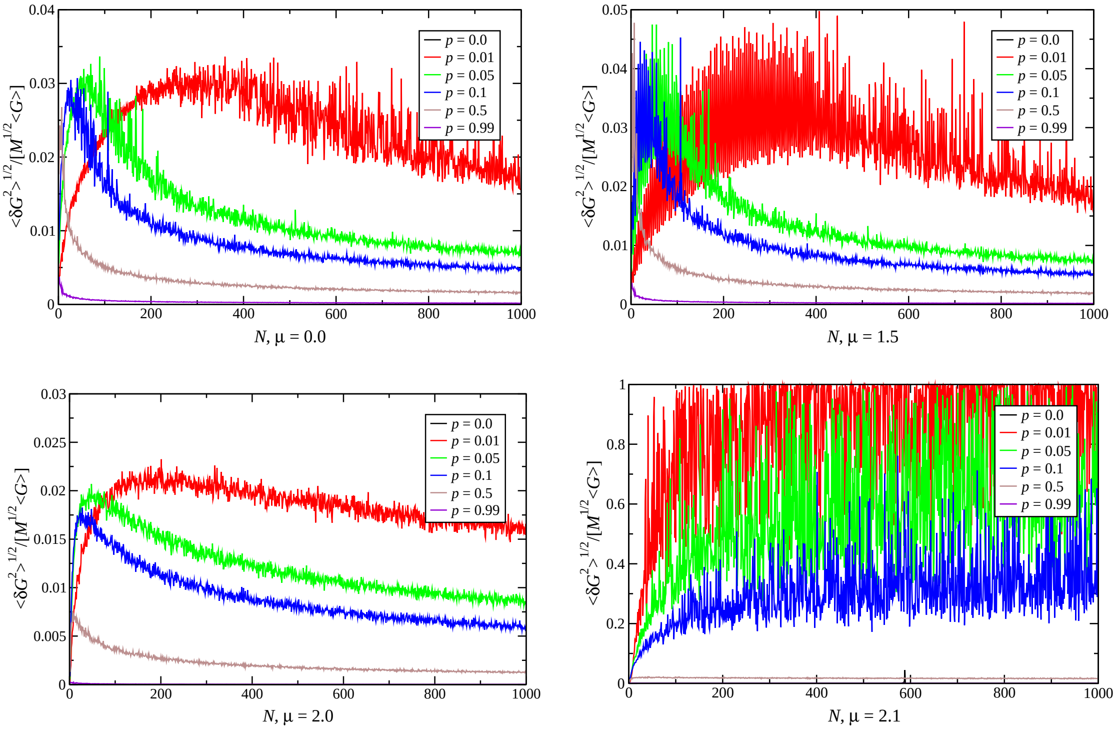

Figure 4.20: The length dependence of the relative standard error of the mean $\frac{\sqrt{\langle \delta G^2 \rangle}}{\langle G \rangle \sqrt{M}}$. For all figures the average was taken over $M = 400$ configurations at $\mu = 0, 1.5, 2.0, 2.1$ from upper left to lower right. For all curves, $\eta_L = \eta_R = \eta = 1.25$.

Whereas inside the band and at the band edge, the relative standard error of the mean decays with N, independently of p, for μ outside the band (and $p < p^*$) the error remains high and even increases the steeper the smaller p is. The fact that the relative error of the mean is up to 1 for small p, is reflected in the extreme fluctuations of R displayed in Figure 4.15(b). The reason for the large relative fluctuations of G is the following. As we have seen in Section 3.9.2.3, for energies outside the tight-binding band, the coherent transmission through an ordered chain decays exponentially with the chain length. The resistance of an individual coherent chain thus increases exponentially with the chain length. For small values of p, the length of the longest coherent chain in a decoherence configuration (which dominates the resistance) fluctuates strongly, and thus the resistances of the individual decoherence configurations fluctuate by orders of magnitude. This is not the case for μ inside the band. There, as we have seen in Section 3.9.2.3, the transmission of the individual coherent segments has an infimum $T_{\text{inf}} > 0$ for every energy, and therefore the resistances of the individual decoherence configurations only fluctuate linearly as the number of decoherence sites in the chain fluctuates.

We conclude that due to the large resistance fluctuations in cases for which ρ does not exist, the resistance obtained by averaging over a small number of decoherence configurations does no longer describe the statistical ensemble of all decoherence configurations of the ordered chain significantly. Compare the discussion of Figure 4.16 on page 78.

4.3.7 Results for a linear chain with onsite disorder

In this section we consider a tight-binding chain with Gaussian onsite disorder, i.e. the onsite energies ϵ_i are chosen according to a Gaussian probability density

$$p(\epsilon) = \frac{1}{\sigma\sqrt{2\pi}} \mathrm{e}^{-\frac{\epsilon^2}{2\sigma^2}} \tag{4.58}$$

with mean value $\epsilon = 0$ and variance σ^2. We do not consider off-diagonal disorder and take $t = 1$ as our energy unit. The onsite energies of the left and right contact are fixed, i.e. $\epsilon_L = \epsilon_R = 0$. Like before, we set $\eta_L = \eta_R = \eta$, and choose natural units for the conductance, i.e. $\frac{e^2}{h} = 1$.

In Section 3.9.3 we have already seen that the coherent transmission through a chain with Gaussian disorder decays exponentially with the length N. Before introducing decoherence into the system, let us consider the coherent transmission through disordered chains.

In Figure 4.21 we display three different disorder realizations for a chain with $N = 20$ and $\sigma = 1.0$ with their respective transmissions for $\eta = 1.25$. Although the concrete transmission functions for the different disorder realizations show little similarity, the averaged transmission function $\langle T\rangle$ displayed in Figure 4.21(d) has a transmission value $\langle T\rangle$ significantly larger than zero for all energies μ of the tight-binding band of the chain without disorder.

4.3.7.1 $\langle G(\mu)\rangle$ and its fluctuations

If now we introduce decoherence into the system, we can examine, like in the case of the ordered chain, the behavior $\langle G(\mu)\rangle$ of the average conductance in dependence of the Fermi energy of the contacts. Here, we perform the average over both energy disorder and decoherence configurations. We generate L sets of random onsite energies $\{\epsilon_i \mid i = 1, \ldots, N\}$ according to the Gaussian energy distribution (4.58). Furthermore we choose M decoherence configurations like in the case of the ordered chain of Section 4.3.6. For every one of the L disorder realizations we calculate the average conductance over the M decoherence configurations. For comparability, we use the same set of disorder and decoherence configurations for every energy μ, cf. the discussion in Section 4.3.6.1. In Figures 4.22 and 4.23 we show the results for $\langle G(\mu)\rangle$ and $\sqrt{\langle\delta G(\mu)^2\rangle}$ for $\sigma = 0.1$ and $\sigma = 1.0$, respectively.

Whereas in the case of $\sigma = 0.1$, the underlying energy structure of the ordered tight-binding chain is clearly visible for $p = 0.0$ and $p = 0.01$ (in the oscillations of $\langle G\rangle$, cf. Figures 4.7 and 3.33), the disorder washes it out for $\sigma = 1.0$. Comparing the Figures 4.22 and 4.23, we also find that for strong disorder ($\sigma = 1.0$), a higher parameter p increases the conductance. We will explain the reasons in the following Section 4.3.7.2. Whereas in the case of $\sigma = 0.1$, the fluctuations $\sqrt{\langle\delta G^2\rangle}$ are mostly due to the different decoherence

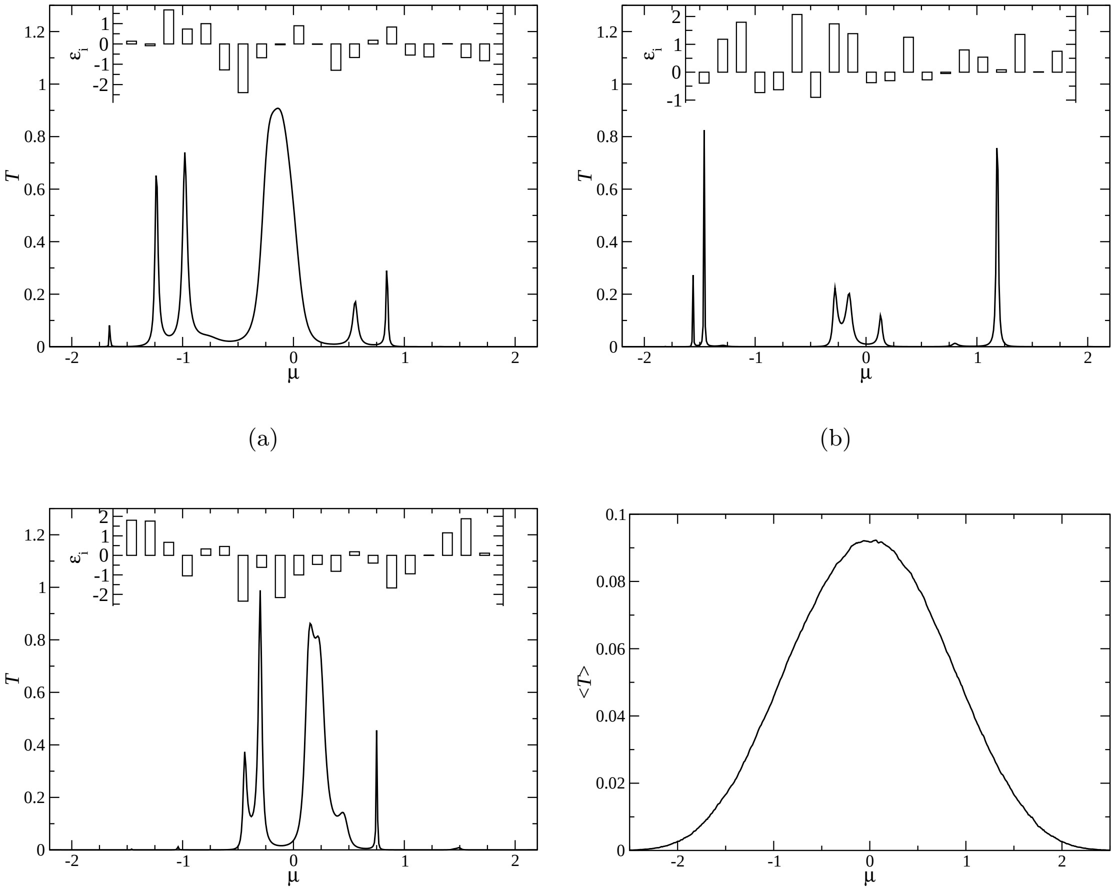

(a)

(b)

(c)

(d)

Figure 4.21: The transmission through three different disordered chains of length $N = 20$ with $\sigma = 1.0$. The transmission function varies clearly for every disorder realization. Note the slightly different energy scales in the insets. Figure (d) shows the transmission averaged over 150,000 different disorder configurations. $\eta = 1.25$.

configurations (therefore the similarity with Figure 4.9), in the case of $\sigma = 1.0$, they are mostly due to the very strongly energy-dependent transmission functions of the coherent subsystems (cf. Figure 4.21).

4.3.7.2 $\langle G(p) \rangle$ and $\langle R(p) \rangle$

Like in the case of the ordered chain, in this section we study the dependence of the average conductance on the concentration of decoherence sites p for a fixed chain length N, cf. Figure 4.24.

Whereas for $\sigma = 0.5$ we observe a similar behavior like for the ordered chain ($\sigma = 0.0$), we observe an increase in p for the conductance $\langle G(p) \rangle$ for $\sigma = 1.0$ and $\sigma = 1.5$. Comparing with Figure 4.13(b), we find the behavior for $\sigma = 1.0$ and $\sigma = 1.5$ is analogous for the

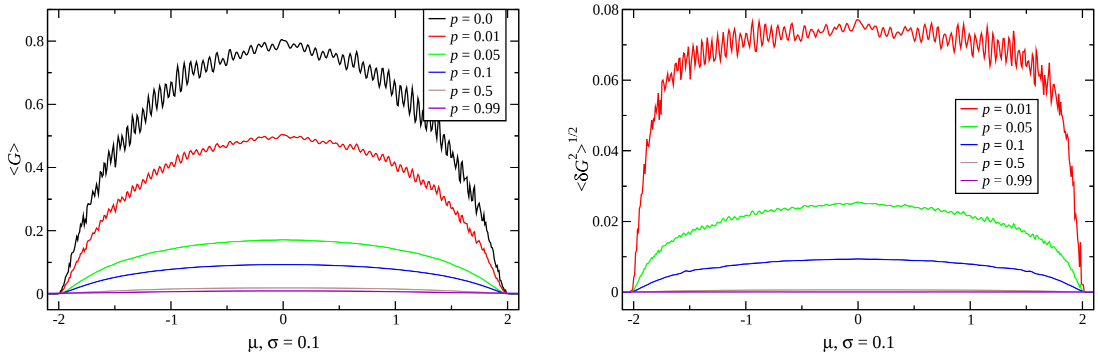

(a) (b)

Figure 4.22: (a) Averaged conductance $\langle G \rangle$ of the disordered chain of length $N = 100$ with $\sigma = 0.1$ as a function of the Fermi energy μ of the contacts for different parameters p. (b) Mean fluctuations of the conductance $\sqrt{\langle \delta G^2 \rangle}$. For both graphs the $M = 400$ decoherence configurations as well as the $L = 400$ disorder configurations over which the average was taken, were the same for all energies μ. $\eta = 1.25$.

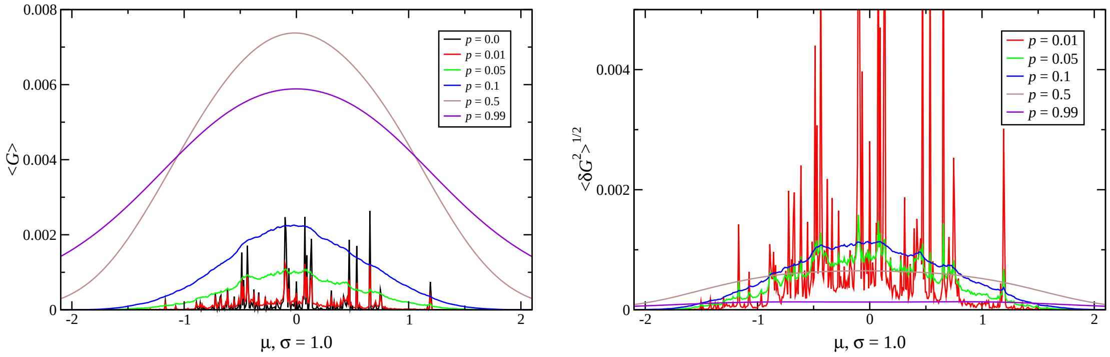

Figure 4.23: Like Figure 4.22. The only parameter difference: Here $\sigma = 1.0$.

one of $\langle G(p) \rangle$ of the ordered chain for μ outside the band. The reason is also the same. Whereas the increase in decoherence sites causes an increase of the resistance linear in p, it is overcompensated by the increase of the transmission which is exponential.

4.3.7.3 Resistance and resistivity of the disordered chain

In this section we consider the resistance of the disordered chain as a function of the chain length N. Therefore we take an ensemble of chains with onsite disorder of variance σ, and for each of the chains we consider a number of decoherence configurations. For every decoherence configuration we calculate the conductance, and then we average over both decoherence configurations, and disorder. Numerical results are displayed in Figure 4.26.

Like for the chain without disorder, we examine under which conditions a resistivity exists

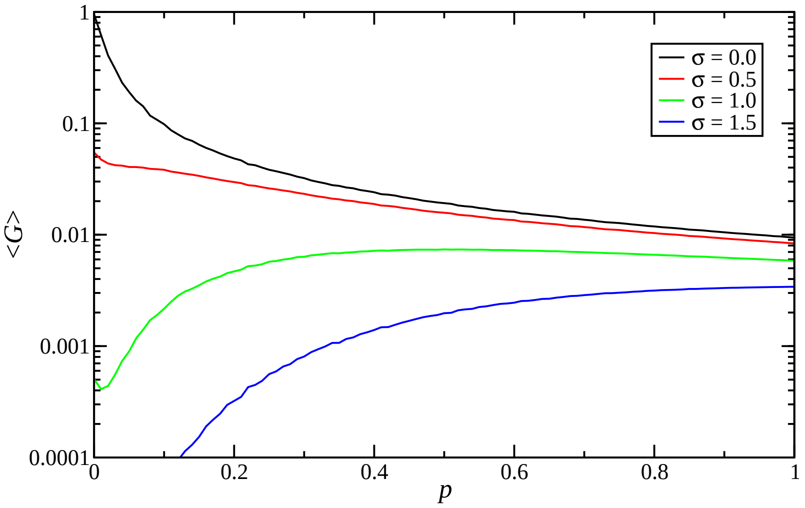

Figure 4.24: Conductance $\langle G(p, \mu = 0.0)\rangle$ of a disordered chain with $N = 100$ for different disorder strengths σ. The average was taken over $L = 1000$ disorder and $M = 400$ decoherence configurations. $\eta = 1.25$.

for disordered chains. In analogy with (4.52), the resistivity for the disordered chain reads

$$\rho_{\text{disorder}}(\mu, p) = p^2 \sum_{j=0}^{\infty} (1-p)^j \left\langle \frac{1}{T_{j+2}(\mu)} \right\rangle_{\text{disorder}} \tag{4.59}$$

i.e. each subsystem has to be weighted by the disorder averaged inverse transmission. As we have seen in Section 3.9.3, the coherent transmission (3.133) of the disordered chain decays exponentially with the chain length, $\langle T_j \rangle \propto \mathrm{e}^{-\frac{j}{\lambda}}$, where λ is the localization length. Thus we expect $\langle \frac{1}{T_j} \rangle \propto \mathrm{e}^{\frac{j}{\xi}}$ to increase exponentially according to some length ξ, which according to the different average, in general differs from λ. Numerical calculations confirm the exponential behavior of $\langle \frac{1}{T_j} \rangle$, cf. Figure 4.25.

The values which we find for ξ by fitting exponential functions to the graphs in 4.25 for $J > 500$ are listed in Table 4.1.

σ	ξ	
	Gaussian	uniformly distributed
0.25	46.5	40.5
0.5	13.6	12.6
0.75	6.21	5.90
1.0	3.85	3.54

Table 4.1: The length ξ in dependence of the disorder strength σ for Gaussian and uniformly distributed onsite disorder. Found by fitting to Figure 4.25.

As, using $\langle \frac{1}{T_j} \rangle \propto \mathrm{e}^{\frac{j}{\xi}}$, (4.59) contains a geometric series, it depends on the product $\mathrm{e}^{\frac{1}{\xi}}(1-p)$ whether the resistivity exists or not:

$$\mathrm{e}^{\frac{1}{\xi}}(1-p) \begin{cases} < 1 & \text{resistivity } \rho \text{ exists} \\ \geq 1 & \text{resistivity } \rho \text{ does not exist} \end{cases} \tag{4.60}$$

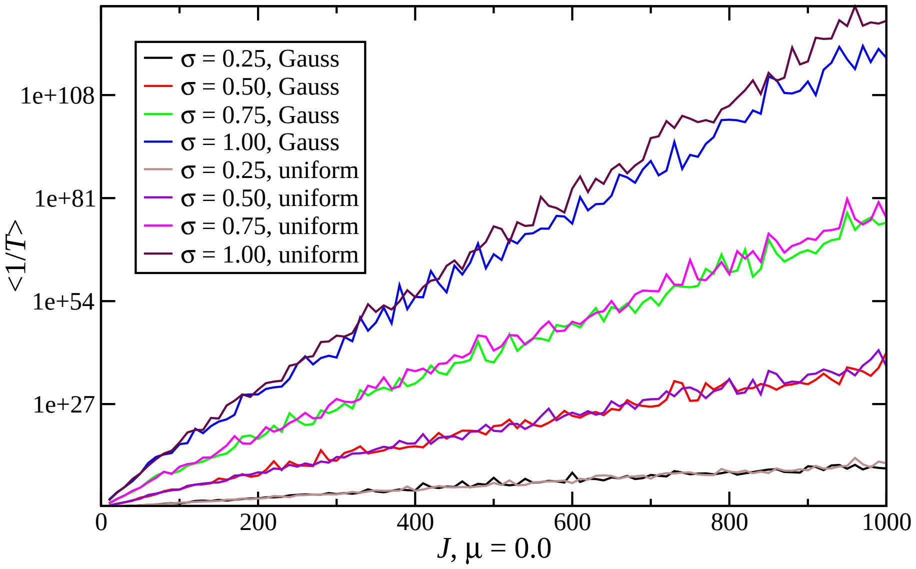

Figure 4.25: The averaged inverse transmission function $\langle \frac{1}{T} \rangle_L$ for Gaussian and uniformly distributed disorder, averaged over $L = 1000$ disorder configurations, $\eta = 1.25$, $\mu = 0.0$.

we conclude that for

$$(1-p)\,\mathrm{e}^{\frac{1}{\xi}} < 1 \quad \Leftrightarrow \quad p > p^*_{\text{disorder}} = 1 - \mathrm{e}^{-\frac{1}{\xi}} \quad \Leftrightarrow \quad L_\phi < \frac{1}{1-\mathrm{e}^{-\frac{1}{\xi}}} \overset{\xi \gg 1}{\approx} \xi \tag{4.61}$$

the series converges and a resistivity can be defined.

In practice we examine the series (4.59) numerically. We average each $\langle \frac{1}{T_j} \rangle$ over L randomly chosen disorder configurations. Then we evaluate the sums

$$\rho_J(\mu,p) = p^2 \sum_{j=0}^{J} (1-p)^j \left\langle \frac{1}{T_{j+2}(\mu)} \right\rangle_L \tag{4.62}$$

and examine whether for large J

$$|\rho_{J+1} - \rho_J| \to 0 \tag{4.63}$$

within a satisfactory numerical accuracy.

An example calculation for $R(N) = \frac{1}{\langle G(N) \rangle}$ is presented in Figure 4.26.

With the parameters chosen in Figure 4.26, for $p > p^*_{\text{Gaussian}} = 0.07$ and $p > p^*_{\text{uniform}} = 0.08$ the resistance should increase linearly for $N \to \infty$ and converge to $R = N\rho(\mu,p,\sigma)$. Whereas for $p = 0.5$ we have already almost perfect match, and for $p = 0.2$ the resistances differ about 7% (Gaussian) and 4% (uniform), for $p = 0.1 \approx p^*$, $N\rho$ and $1/\langle G \rangle$ differ significantly, compare the dashed and continuous green curves in Figure 4.26(a). For the uniform disorder, $N\rho(p = 0.1) = 4176N$ is outside the ranges chosen for Figure 4.26(b). Approaching $p \to p^*$ from above, the closer we come to p^*, the more summands of the series ρ (cf. (4.59)) become relevant. This involves averaging larger and larger

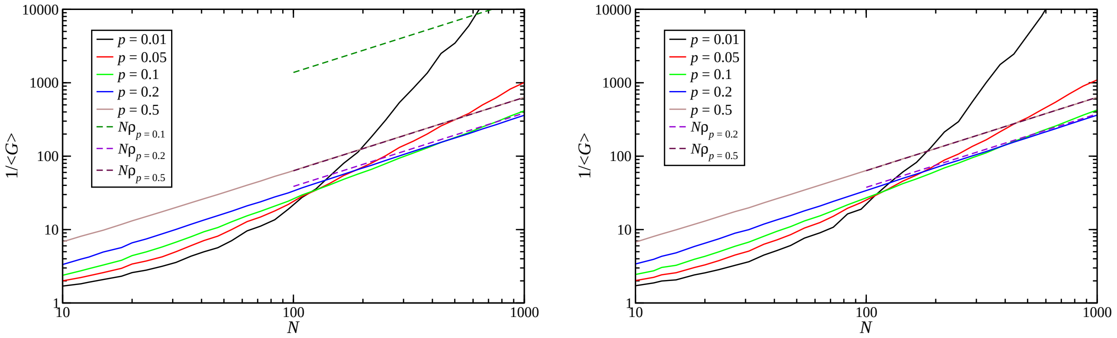

(a) Gaussian disorder, $\sigma = 0.5$

(b) uniform disorder, $\sigma = 0.5$

Figure 4.26: Length dependence of the resistance $1/\langle G \rangle$ for a chain with onsite disorder: (a) with Gaussian, (b) with uniform disorder. In both cases $\mu = 0.0$, $\eta = 1.25$. The average was taken over 1000 disorder and 1000 decoherence configurations. In dashed lines: The resistances calculated from the resistivity $\rho_{J=1000}$ for $L = 1000$.

quantities $\langle \frac{1}{T_j} \rangle$, which fluctuate over orders of magnitude (cf. the already averaged curves in Figure 4.25). The criterion (4.63) for ρ becomes harder and harder to reach, both for computational accuracy as for computation time reasons. The same holds true for the computation of $1/\langle G \rangle$ of the finite system. The individual conductances for every decoherence configurations differ very much making an increasing ensemble of decoherence and disorder configurations necessary. Once $p < p^*$, the system cannot reasonably be described by a resistivity.

4.4 Conclusions and outlook

In this chapter we have studied a model for the effects of decoherence on the electron transport in large systems. The concepts of the model have already been published previously [199]. We have discussed the model using the example of a linear tight-binding chain with and without diagonal disorder. The major results are the following.

- **Modelling approach.** Our model uses two parameters η and p. With η, the purely imaginary self-energy of the decoherence regions, we describe within a single parameter the strength of the coupling of decoherence regions to the environment and/or the rest of the system. As we do not pretend to model the decoherence itself but only the *effects* of decoherence, this is the simplest possible approach. We have seen that despite its simplicity important results can be obtained. The parameter p describes the density of decoherence regions in the system, which in one dimension is the inverse phase coherence length, i.e. $p = \frac{1}{L_\phi}$.

  In this thesis linear systems and single sites as decoherence regions are studied. The quantum-mechanical transport description is only used between neighboring decoherence sites. Beyond this length scale, via the rate equation, a classical description is used. The rate equation is considered in the stationary case. That means the positions of the decoherence sites have to be constant on a time scale much longer than the time between any two decoherence processes.

In linear systems, the decoherence sites make the system fall apart into small-size subsystems. This reduces the computational cost in comparison with other phenomenological decoherence models.

- **Outlook to future extensions.** So far we have only discussed linear systems. If we wish to apply our model for higher dimensions, we have to take into account that by introducing single decoherence sites, the system does no longer fall apart into disconnected subsystems. That raises the questions of how to delimit the quantum-mechanical descriptions (the main computing time-saving advantage of our approach), and how to choose neighboring decoherence sites/regions for the rate equation.

  The rate equation (4.6) does not mix energies, i.e. no energy is lost or gained due to decoherence or interaction at the decoherence sites, and conserves the number of charge carriers. Future extensions of the model are to include electron-hole recombination on the one hand, and non-infinitesimal bias on the other hand. For these extensions, energy mixing in the rate equation might be required. Then also finite temperatures play a role. A finite bias requires a self-consistent modification of the onsite energies of the system. Using the Hartree approximation, this modification is being done in a diploma thesis [170] at the moment.

- **Significance of linear chains.** We have analyzed our model for linear tight-binding chains at infinitesimal bias. The experimental significance we think of does not only extend to truly linear and quasi-linear systems like chains of nanoparticles, chains of gold atoms, or linear molecules like DNA, but also to three-dimensional media between two-dimensional electrodes, as long as the conduction essentially occurs along linear paths and if in-plane interactions play a minor role.

- **Results for linear tight-binding chains.** We have studied finite linear tight-binding systems, and analyzed how they behave as their length increases. For a given system length we have studied ensemble averages of decoherence site configurations with a given decoherence site density p.

  - **Properties of coherent subsystems remain visible.** For low concentrations p of decoherence sites, in the ensemble averaged conductance we can see following properties of the coherent subsystems which we have presented in Section 3.9. The spectrum of the transmission $T_N(E)$ with maxima at the eigenenergies of the N-site tight-binding chain can be recognized in the averaged conductance $\langle G(\mu)\rangle$ of a system with length N (compare Figures 3.36 and 4.7(a)). The conductance fluctuates the stronger the closer μ is to the band edge $\mu = \pm 2$, as there the density of the eigenenergies is the highest (cf. Figure 4.9). In the length dependence of the fluctuations (Figures 4.18 and 4.19) we recognize the periodicity in N of the transmission function T_N.
  - **Transition from coherent to ohmic behavior.** Studying the length dependence of $R = 1/\langle G\rangle$ we find that it approaches linearity $R \propto N$ under the following conditions. For the chain without disorder inside the band $\mu \in [-2, 2]$ it is reached for any p. Outside the band $|\mu| > 2$ there exists a critical density p^* (see (4.56)), such that for $p > p^*$ the proportionality $R \propto N$ is reached. The

critical density p^* depends only on μ, i.e. the relative alignment of the Fermi energy of the contacts with respect to the onsite energies (using the tight-binding coupling t as energy unit). For $p < p^*$, the tunneling-barrier character of the subsystems dominates the resistance, and thus R increases nonlinear with N. Under this condition, the average $1/\langle G\rangle$ fluctuates strongly. In an experimental situation which fulfills this condition, resistance measurements would be irreproducible (seemingly identical systems have resistances which could differ by orders of magnitude).

For the chain with disorder, the coherent subsystems experience localization, i.e. the subsystem transmissions decay exponentially. Anyway there exists a critical density p^*_{disorder}, for which the system resistance $R = 1/\langle G\rangle$ approaches linear increase with size. The value of p^*_{disorder} is determined by the disorder strength σ, according to (4.61) via a σ-dependent length $\xi = \frac{\partial \ln(\langle 1/T\rangle_{\text{disorder}})}{\partial N}$.

- **Definition of a resistivity.** For the resistivity of infinite linear systems we have found definitions via series, (4.52) in the ordered case and (4.59) in the disordered case. The convergence of the series is given for $p > p^*$ and $p > p^*_{\text{disorder}}$, respectively. For large systems, instead of a ensemble average over decoherence configurations, the use of the resistivity, if it exists, is computationally much more convenient.

5 Model for Decoherence Effects Applied on the Conductance of DNA Double Strands

In this Chapter I will present an application of our statistical model for the effects of decoherence (Chapter 4) on a real system: A DNA double strand between two gold scanning tunnelling microscope (STM) tips. The reason for this choice is the following. DNA, apart from its importance in biochemistry, is also a promising tool in self-assembling microelectronics.[1] DNA, like the chains discussed in Chapter 4, is an essentially linear molecule, thus the concepts from the linear chains are transferable. Furthermore, experimental conductance measurements[2] have been performed, the results of which we aim to explain with decoherence effects.

5.1 Structure of DNA double strands

As is widely known, the genetic information of all life-forms on Earth is encoded in the DNA double helices. The abbreviation DNA stands for deoxyribonucleic acid. A DNA molecule is a concatenation of nucleotides, which themselves are composed of deoxyribose (a pentose sugar, i.e. a sugar with five C-Atoms), the encoding aromatic bases (guanine, adenine, cytosine, and thymine), and a phosphate group. The chemical structure formula of a nucleic acid and the double-helical structure of B-DNA are displayed in Figure 5.1.

As we can see in Figure 5.1(a), the nucleotides are chemically bound along the phosphates and the sugar rings, which form the so-called strand, whereas the aromatic bases are not chemically bound among themselves (yet they may interact due to H-bridges). The carbon atoms of the sugar rings are numbered $1'$ through $5'$. At the positions $5'$ and $3'$, the phosphate groups attach. By convention, the polynucleotide sequence is written with its $5'$ end at the left, and its $3'$ end at the right. E.g. in Figure 5.1(a), we find the sequence $5'$-ATCG-$3'$. In this sense, a polynucleotide is a directed molecule. Depending on its environment, DNA double strands form different 3-dimensional structures. In the nuclei of living cells, we find the so-called B-DNA, displayed in Figure 5.1(b). B-DNA is composed of two anti-parallel, right-handed polynucleotide strands. The two strands are bound by H-bridges between the bases, where G only couples with C and A only couples with T forming the Watson-Crick base-pairs $\mathrm{G\cdot C}$ and $\mathrm{A\cdot T}$, named after the discoverers of the double helix structure [187]. As the base pairing is unique, the sequence of the single strand already contains the information of the double strand. Therefore in the following we use the single-strand notation for the double strand. E.g. Figure 5.2 shows the double strand with sequence $5'$-GC$(\mathrm{AT})_2$GC-$3'$.

---

[1] Recently [127], self assembly of carbon nanotubes using DNA has been reported.

[2] See below in Section 5.2.

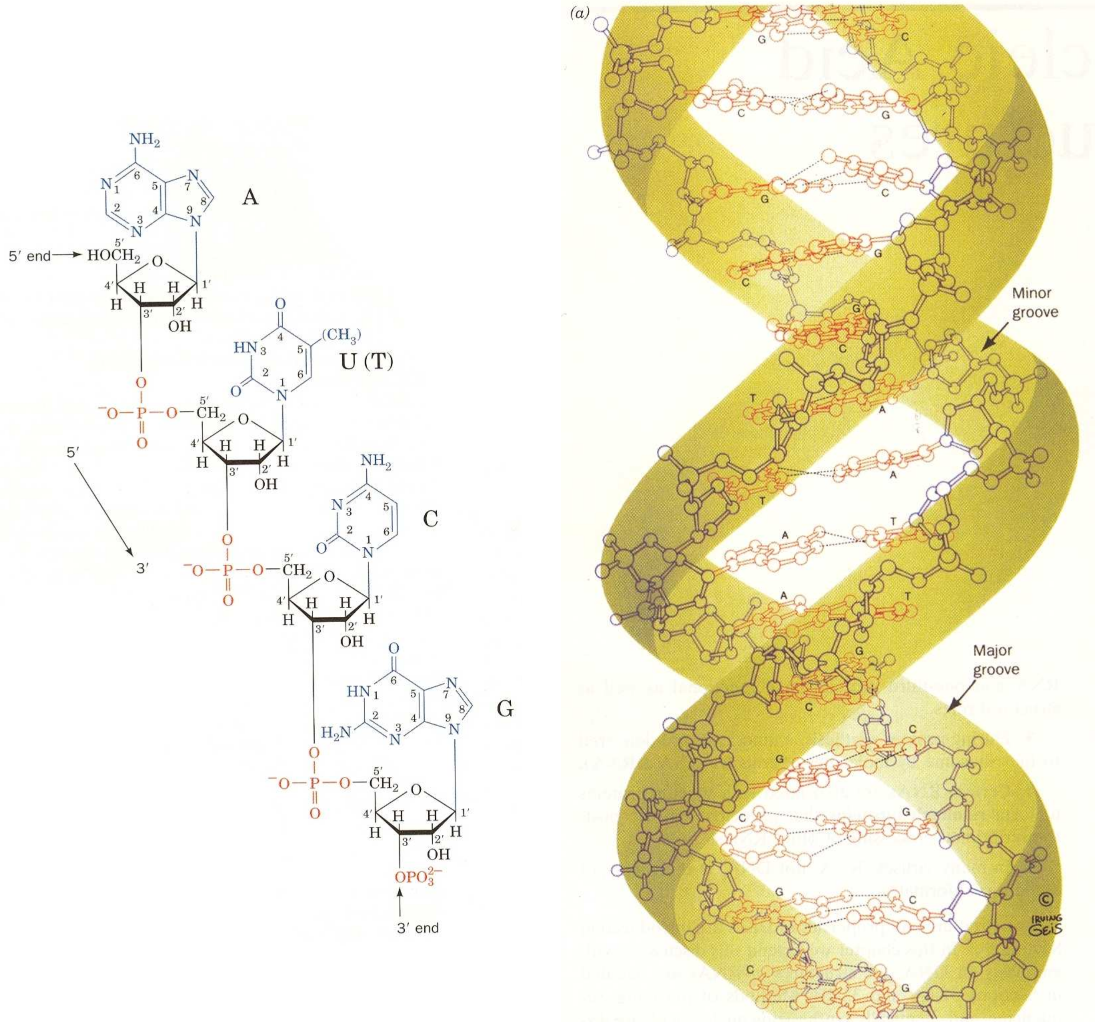
A
5′ end
HOCH$_2$
U (T)
(CH$_3$)
5′
3′
C
G
OPO$_3^{2-}$
3′ end
(a)
Minor groove
Major groove
© Irving Geis

(a) (b)

Figure 5.1: (a) Figure 5-2 of [182]. Chemical structure of a DNA-strand with the bases Adenine, Uracil (Thymine when the CH_3-group in parentheses is present), Cytosine, Guanine from the 5′ to the 3′ end. (b) Figure 29-1 of [182]. Local 3-dimensional structure of a B-DNA double helix.

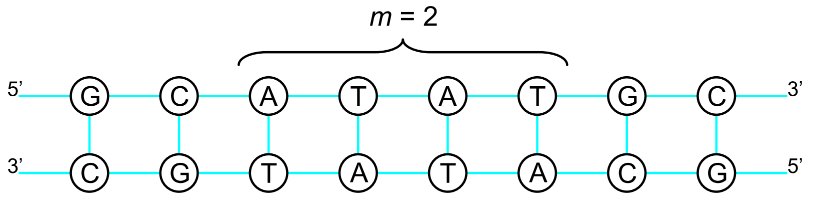
$m = 2$
5’
G
C
A
T
A
T
G
C
3’
3’
C
G
T
A
T
A
C
G
5’

Figure 5.2: The DNA double strand 5′-GC$(AT)_{m=2}$GC-3′.

5.2 Electronic properties of DNA

The literature on electronic properties and device applications of DNA is abundant, see the recent review articles and books [38, 59, 67, 147, 166] and references therein. First transport measurements have been photochemical experiments [76, 111, 129, 152]. The charge transport mechanism in DNA double strands has been and still is controversial, as electron transport measurements by directly contacting single DNA molecules have shown insulating [28, 172], semiconducting [44, 146], ohmic [70, 89, 191, 194], and even superconducting (when bridging superconducting metals) [89] behavior. Most widely accepted today is the fact that hole-transfer along the π orbitals of the aromatic rings is the most important ingredient in the conductance of DNA double strands.

5.2.1 Direct measurements of conductance of DNA double strands

Several groups have managed to contact individual DNA double strands between two electrodes and perform direct current measurements [28, 44, 89, 121, 146, 165, 172, 186, 191, 194]. Here we wish to present the results of [191].

They managed to contact single DNA double strands between two gold electrodes via thiol linkers, labeled with the S for sulphur in Figure 5.3.

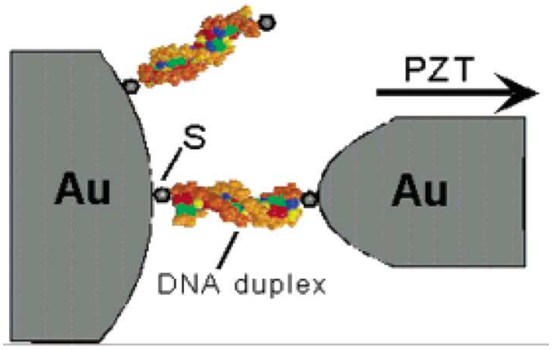

Figure 5.3: Figure 1-a of [191]. Individual DNA double strand between a gold electrode and a gold piezoelectric transducer (PZT) in aqueous solution. The PZT was approached and withdrawn from the gold electrodes until only a single DNA double strand bridged the contacts.

Comparing different DNA double strands, they managed to find a length dependent conductance, cf. Figure 5.4.

The conductance of the DNA double strand with a sequence 5'-GCGC$(AT)_m$GCGC-3' was observed to decay exponentially with the number of base pairs (see Figure 5.4(a))

$$G = A\mathrm{e}^{-2m/\lambda_0} \tag{5.1}$$

where $A = (1.3 \pm 0.1) \times 10^{-3} G_0$, ($G_0 = \frac{2e^2}{h}$ is the conductance quantum[3]), and $\lambda_0 \approx 0.68$.[4]

---

[3] An assumed spin degeneracy is the reason for the 2 in the numerator.

[4] Equation (5.1) is given in [191]. For the conversion of their parameter β to λ_0, the geometrical information about B-DNA given in [182, Table 29-1] was used.

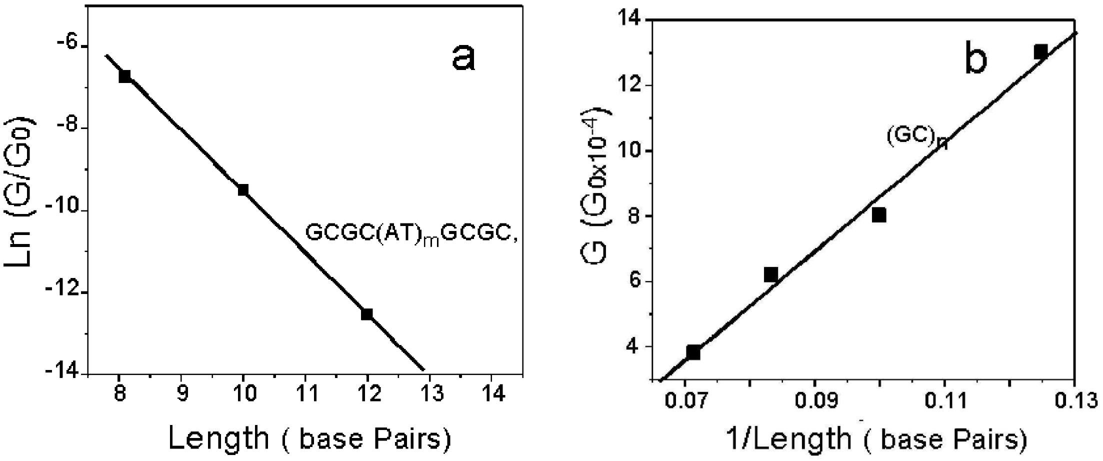

(a)

(b)

Figure 5.4: (a) Figure 3a and (b) Figure 3b of [191]. For sequences (a) 5'-GCGC(AT)$_m$GCGC-3' the authors of [191] find that the conductance decays exponentially with the number of base pairs, whereas for sequences (b) 5'-(GC)$_n$-3' they find that the conductance is inversely proportional to the number of base pairs.

By contrast, for sequences 5'-(GC)$_n$-3' a conductance which is inversely proportional to the number of base pairs was claimed by the authors of [191] (see Figure 5.4(b))

$$G = C + \frac{B}{2n} \tag{5.2}$$

where $B \approx 0.0167 G_0$ and $C \approx -8.1 \times 10^{-4} G_0$.[5]

Although the data base is not abundant, the change in length dependence of the conductance from exponential to inversely proportional is clear. As we have observed a similar change in the length dependence of the conductance for the linear chains discussed in Chapter 4, we have a clear motivation for applying our model for the effects of decoherence for DNA molecules.

5.2.2 Tight-binding models for DNA

A great variety of tight-binding models for DNA double strands have been proposed, many of which are presented in [50, 118]. The simplest one, the line model, is just a linear tight-binding chain, where each site (onsite energy $\epsilon_i = \epsilon_{\mathrm{A \cdot T}}, \epsilon_{\mathrm{G \cdot C}}$) corresponds to a base pair and the coupling t_i to the π-π overlap integrals between adjacent base pairs, cf. Figure 5.5(a).

The line model in combination with a D'Amato-Pastawski dephasing was used e.g. by [112] to fit experimentally [146] measured I-V characteristics with a satisfactory agreement.

---

[5] The relation (5.2) was found by fitting to Figure 5.4(b). The authors of [191] just state $G \approx 1/L$.

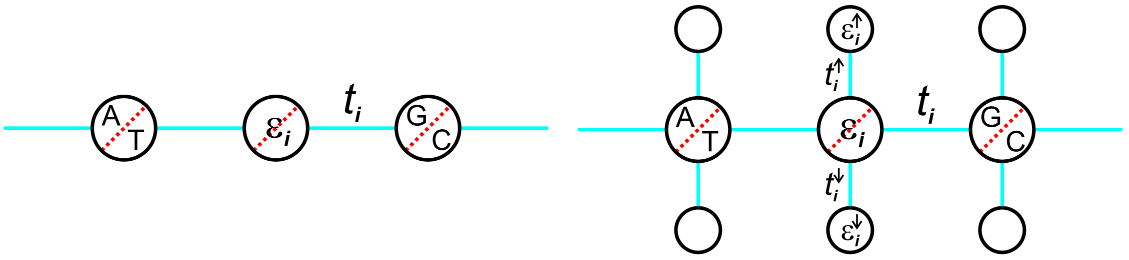
A
T
ε_i
t_i
G
C
$\varepsilon_i^\uparrow$
$t_i^\uparrow$
$t_i^\downarrow$
$\varepsilon_i^\downarrow$

(a) Line model

(b) Fishbone model

Figure 5.5: Tight-binding models for DNA double strands.

Using an alternating chain (cf. Section 3.4) as an effective model and including D'Amato-Pastawski dephasing, the author of [193] gives his explanation to the measurements of [191]. Of course, the line-model cannot distinguish sequences 5'-GA-3' from 5'-GT-3' etc.

The fishbone model (see Figure 5.5(b)) is an extension of the line model, and takes into account the interaction of the bases with the respective strands (couplings $t_i^\uparrow, t_i^\downarrow$, onsite energies $\epsilon_i^\uparrow, \epsilon_i^\downarrow$). It was used e.g. by [49] to explain a semiconductor-like gap in the I-V curve of [146], without recurring to decoherence.

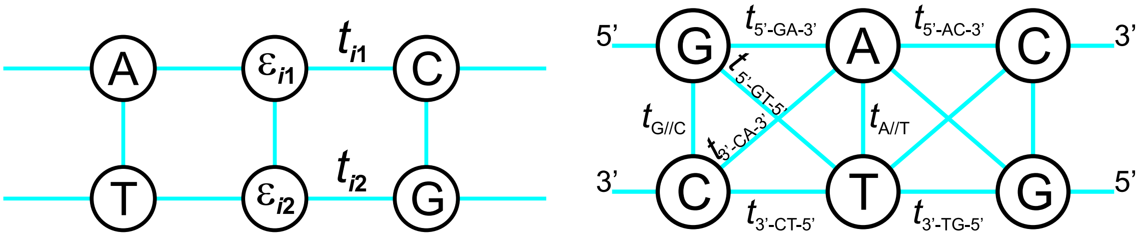
A
T
ε_{i1}
ε_{i2}
t_{i1}
t_{i2}
C
G
5'
3'
$t_{5'\text{-GA-3'}}$
$t_{5'\text{-AC-3'}}$
$t_{5'\text{-GT-5'}}$
$t_{3'\text{-CA-3'}}$
$t_{G//C}$
$t_{A//T}$
$t_{3'\text{-CT-5'}}$
$t_{3'\text{-TG-5'}}$

(a) Simple ladder model

(b) Extended ladder model

Figure 5.6: Tight-binding models for DNA double strands.

In order to account for arbitrary base sequences, the bases of a base pair have to be treated individually, e.g. within the simple ladder model (Figure 5.6(a)) used e.g. by [85]. Ab-initio calculations [164, 196] have shown that the diagonal inter-strand transfer matrix elements can be more relevant than the intra-strand coupling. Thus the extended ladder model (Figure 5.6(b)) has been proposed [164, 196]. In both ladder models presented in Figure 5.6, the strands have been neglected. Yet also ladder models including interaction with the strands have been examined [96, 154].

In Section 5.3, we will apply our model for the effects of decoherence on the extended ladder model. For the energy parameters we will essentially rely on the well-established parameters found by [164].

5.2.3 The extended ladder model

We have already studied the infinite and half-infinite translationally invariant versions of the extended ladder model in Section 3.8. Here we treat its general, non-periodic version of length N with the Hamiltonian

$$H = \sum_{i,m=1}^{i=N,m=2} \epsilon_{i,m} \left|i,m\right\rangle\left\langle i,m\right| + \sum_{i,m\neq n} t_{i,mn} \left|i,m\right\rangle\left\langle i,n\right| + \sum_{i,m,n} \left[t_{i,i+1,mn} \left|i,m\right\rangle\left\langle i+1,n\right| + \text{H.c.}\right] \tag{5.3}$$

where $\epsilon_{i,m} = \epsilon_{\mathrm{G}}, \epsilon_{\mathrm{A}}, \epsilon_{\mathrm{C}}, \text{or } \epsilon_{\mathrm{T}}$, depending on the respective base, $t_{i,mn} = t_{\mathrm{G//C}}$ or $t_{\mathrm{A//T}}$, depending on the base pair, and $t_{i,i+1,mn} = t_{\text{5'-XY-3'}}, t_{\text{3'-XY-5'}}, t_{\text{5'-XY-5'}},$ or $t_{\text{3'-XY-3'}}$ depending on the respective bases and geometry, cf. Figure 5.6(b). The base pairs are indexed $i = 1, \ldots, N$.

In this chapter we use parameters ϵ, t found with DFT calculations for DNA double strands [164] which are widely used in the literature, e.g. [161, 162]. Similar hopping parameters have been found by [37, 103, 131, 173, 183–185]. Yet the onsite-energy parameters differ significantly in the literature, compare, e.g. the ones listed in [103, Table 1], [196, Table II], and [164, Table 2], depending on the method by which they were calculated or measured.

We list the parameters in eV in Table 5.1. The onsite energies are the mean values of [164, Table 2] for every base. For the nomenclature, see Figure 5.6(b). The onsite energies are named ϵ_{X}, the intra-strand couplings $t_{\text{5'-XY-3'}}$ and $t_{\text{3'-XY-5'}}$ for the upper and lower strand, the intra base-pair couplings $t_{\mathrm{G//C}}$ and $t_{\mathrm{A//T}}$, and the inter-strand couplings $t_{\text{5'-XY-5'}}$ and $t_{\text{3'-XY-3'}}$, where X and Y stand for any of the four bases G, A, C, and T.

We note that because of the directionality of the DNA strands, $t_{\text{5'-XY-3'}} \neq t_{\text{5'-YX-3'}} = t_{\text{3'-XY-5'}}$ for X $\neq$ Y. However, due to symmetry $t_{\text{5'-XY-5'}} = t_{\text{5'-YX-5'}}$ and $t_{\text{3'-XY-3'}} = t_{\text{3'-YX-3'}}$ for all X, Y.

Using the parameters of Table 5.1, we can calculate the local densities of states of infinite DNA double strands by (3.96). The LDOS of some example molecules are displayed in Figure 5.7.

We observe the typical van-Hove singularities for linear systems, cf. Sections 3.5 and 3.7. In Figure 5.7(b) they are suppressed on the base A because the intra-strand coupling $t_{\text{5'-AA-3'}}$ is very small (cf. Table 5.1(b)). The local densities of states on every base are located mostly around the respective onsite energy. Important contributions from other energies are found where the coupling between the bases is strong, e.g. the LDOS on the G base at the onsite energy of T in Figure 5.7(f).

As we have seen in Chapter 4, the relative alignment of the Fermi energy of the contacts with the band(s) of the channel determines whether the channel subsystems act as tunnel barriers. We expect ohmic behavior of the DNA double strand when Fermi energy and at least one band are aligned, or for very strong decoherence.

ϵ_G	ϵ_A	ϵ_C	ϵ_T	$t_{G//C}$	$t_{A//T}$
8.178	8.631	9.722	9.464	-0.055	-0.047

(a) Onsite and intra base pair parameters

X\Y	G	A	C	T
G	0.053	- 0.077	-0.114	0.141
A	-0.010	-0.004	0.042	-0.063
C	0.009	-0.002	0.022	-0.055
T	0.018	-0.031	-0.028	0.180

(b) $t_{5'\text{-XY-}3'}$

X\Y	G	A	C	T
G	0.053	-0.010	0.009	0.018
A	-0.077	-0.004	-0.002	-0.031
C	-0.114	0.042	0.022	-0.028
T	0.141	-0.063	-0.055	0.180

(c) $t_{3'\text{-XY-}5'}$

X\Y	G	A	C	T
G	0.012	-0.013	0.002	-0.009
A	-0.013	0.031	-0.001	0.007
C	0.002	-0.001	0.001	0.0003
T	-0.009	0.007	0.0003	0.001

(d) $t_{5'\text{-XY-}5'}$

X\Y	G	A	C	T
G	-0.032	-0.011	0.022	-0.014
A	-0.011	0.049	0.017	-0.007
C	0.022	0.017	0.010	-0.004
T	-0.014	-0.007	-0.004	0.006

(e) $t_{3'\text{-XY-}3'}$

Table 5.1: Parameters for the extended ladder model (in eV). The onsite energies in (a) were taken from [164, Table 2] by calculating the mean value for every base. The intra base-pair couplings can be found in [164, below Equation 3]. (b)–(e) taken from [164, Table 3, columns 3, 6, 9, and 12].

5.3 Application of the decoherence model for DNA double strands

In order to apply our statistical model for the effects of decoherence on the extended ladder model for DNA double strands, we have to define the decoherence regions, and the contacts.

We choose to replace single base pairs by decoherence regions[6], and model every decoherence region as under the influence of a virtual contact. For the decoherence regions we examine the three models displayed in Figure 5.8.

5.3.1 Decoherence region 1

The first model for the decoherence region is the one displayed in Figure 5.8(a) which is just the same decoherence region we chose in Chapter 4 (cf. (4.12)), i.e. it has a Green

---

[6] This way, the system falls apart into subsystems.

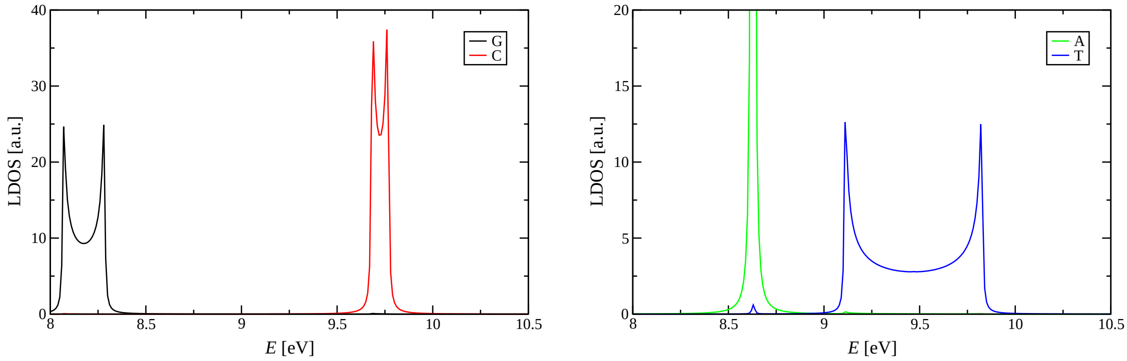

(a) 5'-$(GG)_\infty$-3' (b) 5'-$(AA)_\infty$-3'

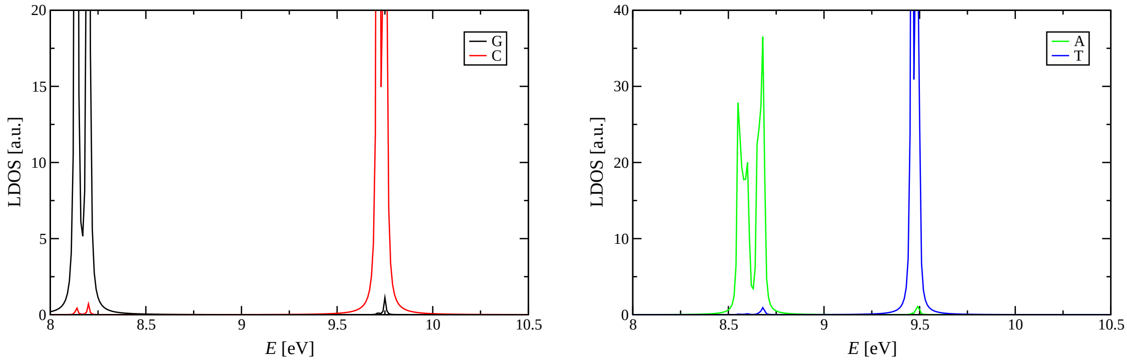

(c) 5'-$(GC)_\infty$-3' (d) 5'-$(AT)_\infty$-3'

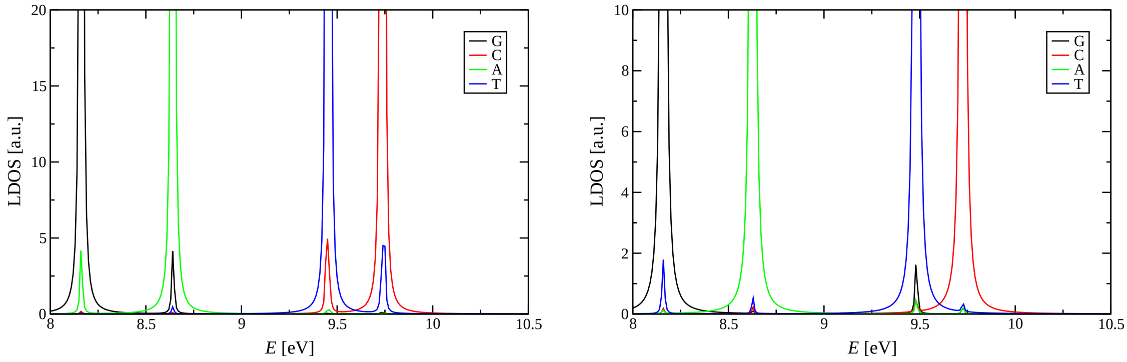

(e) 5'-$(GA)_\infty$-3' (f) 5'-$(GT)_\infty$-3'

Figure 5.7: Local densities of states for infinite DNA double strands.

function

$$g = \frac{1}{E - \epsilon_d + \mathrm{i}\eta} \tag{5.4}$$

where we choose $\epsilon_d = \frac{1}{2}(\epsilon_{i1} + \epsilon_{i2})$, and η is our decoherence strength parameter. The coupling to decoherence region 1 is dependent on the original base pair which is replaced. If, e.g. we replace the middle base pair $(\mathrm{A} \cdot \mathrm{T})$ of Figure 5.6(b) by a decoherence region,

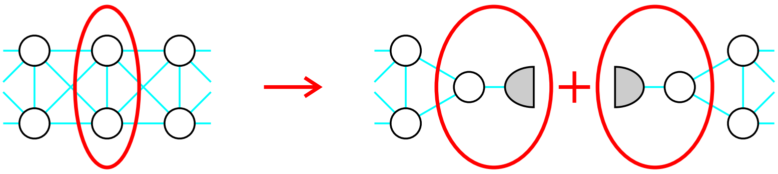

(a) Decoherence region 1

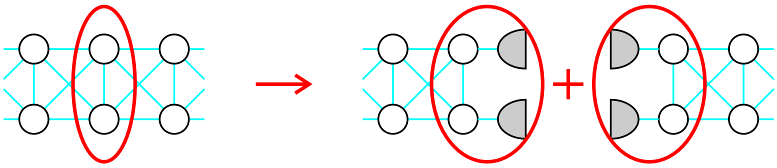

(b) Decoherence region 2

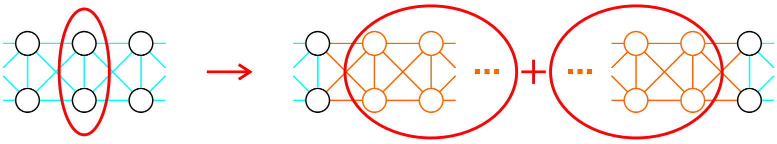

(c) Decoherence region 3

Figure 5.8: Models for the decoherence regions in DNA double strands.

the coupling to G to the left is

$$t_{l1} = \frac{1}{\sqrt{2}}(t_{\text{5'-GA-3'}} + t_{\text{5'-GT-5'}}) \tag{5.5}$$

and analogously

$$t_{l2} = \frac{1}{\sqrt{2}}(t_{\text{3'-CA-3'}} + t_{\text{3'-CT-5'}}) \tag{5.6}$$

$$t_{r1} = \frac{1}{\sqrt{2}}(t_{\text{5'-AC-3'}} + t_{\text{5'-AG-5'}}) \tag{5.7}$$

$$t_{r2} = \frac{1}{\sqrt{2}}(t_{\text{3'-TC-3'}} + t_{\text{3'-TG-5'}}) \tag{5.8}$$

to the other bases to left and right.

The decoherence region 1 offers a continuous density of states around the mean value of the onsite energies of the original base pair it replaces. Depending on the η parameter it represents a stronger or weaker coupling to the environment.

5.3.2 Decoherence region 2

The second model for the decoherence region is displayed in Figure 5.8(b). In this case, we attach wide-band contacts (cf. Section 3.9.1) to each of the bases of the decoherence region, thus the decoherence region Green function is

$$g = [(E + \mathrm{i}\eta)\, I - H_{\text{base pair}}]^{-1} \tag{5.9}$$

i.e. we add a diagonal $-i\eta$ to the Hamiltonian of the original base pair. The coupling to the left and to the right remains unchanged. The decoherence region has a LDOS peaked at the onsite energies of the bases it comprises, cf. Figure 5.9.

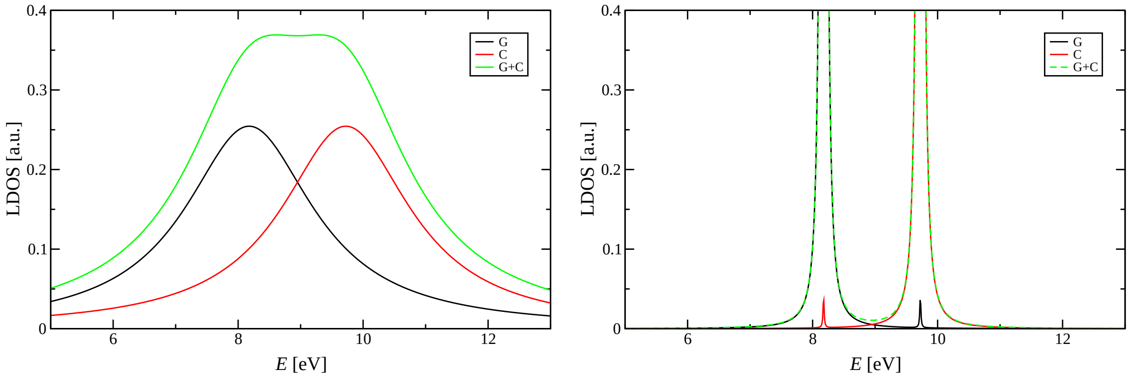

(a) $\eta = 1.25$

(b) $\eta = 0.01$

Figure 5.9: LDOS of the decoherence region 2 replacing a G·C base pair for two different choices of η. In black: the LDOS on G, in red on C, in green the sum of both.

The decoherence region 2 offers a finite density of states around both the onsite energies of the original base pair. In comparison with decoherence region 1, the coupling of the decoherence region to the coherent subsystems does not have to be modified.

5.3.3 Decoherence region 3

The third model for the decoherence region is displayed in Figure 5.8(c). It is a half-infinite repetition of the original base pair. Thus the Green function of the decoherence region 3 reads

$$g = [E - H_{\text{half-infinite DNA chain}}]^{-1}_{\text{surface}} \tag{5.10}$$

It can be calculated in the way described in Section 3.8.2. The coupling to left and right is the original coupling of the base pair which is replaced by the decoherence region 3. Like for decoherence regions 2, we display the LDOS of the surface of the decoherence region 3 in Figure 5.10.

Decoherence region 3 idealizes one aspect of the decoherence regions in general (cf. Sections 4.2.1 and 4.2.3): Electrons can decohere by going into other states of the rest of the system, *not* its environment. Comparing Figures 5.9 and 5.10, we notice that this implies that decoherence region 3 receives electrons within a clearly reduced range of energy compared with decoherence region 2.

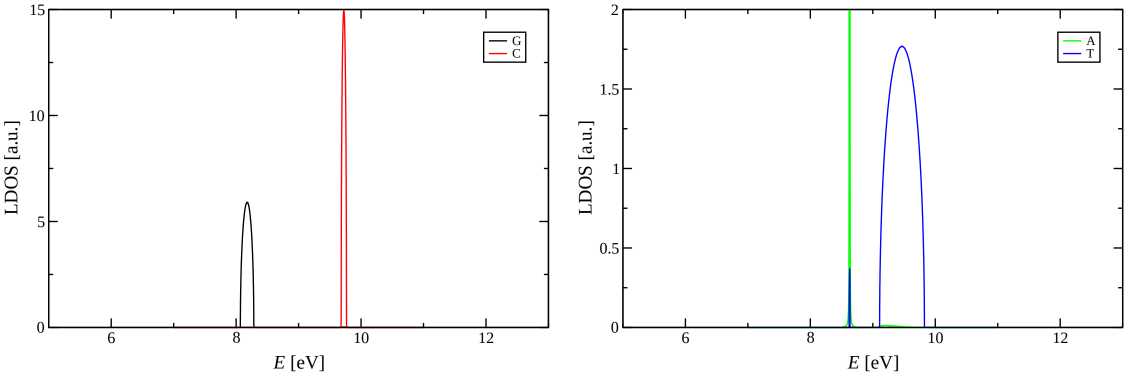

(a) G·C base pair

(b) A·T base pair

Figure 5.10: LDOS of the decoherence region 3 replacing (a) a G·C and (b) an A·T base pair.

5.3.4 Contact model 1

Apart from the models for the decoherence regions, also the contacts have to be defined. The first approach is to model the contacts in the wide-band limit, i.e. like the decoherence region 2, with independent η parameters η_L and η_R for left and right contact.

5.3.5 Contact model 2

The second contact model (see Figure 5.11(a)) is a double chain like of Section 3.5, in analogy with Wei and Chan [188], with the Hamiltonian, e.g. for the left contact

$$H_L = \sum_{i=1,j=1}^{i=\infty,j=2} \chi_{L,j}\, |L,i,j\rangle\langle L,i,j| + \rho_L \sum_{i=1,j=1}^{i=\infty,j=2} [|L,i,j\rangle\langle L,i+1,j| + |L,i,j\rangle\langle L,i,j+1| + \text{H.c.}] \tag{5.11}$$

where the onsite energies $\chi_{L,1} = \epsilon_{1,1}$, $\chi_{L,2} = \epsilon_{1,2}$ are taken from the first base pair of the DNA double strand such that energetic alignment is achieved. The parameter ρ_L determines the band width of the double chain. The right contact is defined analogously with an analog parameter ρ_R. The coupling between contact and DNA double strand is mediated by parameters λ_L and λ_R.

5.3.6 Contact model 3

The third alternative for the contact is displayed in Figure 5.11(b) which is a reduced version of contact model 2. Single chains with Hamiltonians

$$H_L = \sum_{i=1}^{\infty} \chi_L\, |L,i\rangle\langle L,i| + \rho_L \sum_{i=1}^{\infty} [|L,i\rangle\langle L,i+1| + \text{H.c.}] \tag{5.12}$$

and analogous H_R are coupled via transfer matrix elements λ_L and λ_R to the lower left and upper right base of the DNA double strand. Also for contact model 3, the onsite energies $\chi_L = \epsilon_{1,2}$ and $\chi_R = \epsilon_{N,1}$ are aligned with the onsite energies of the bases to which the contacts are attached.

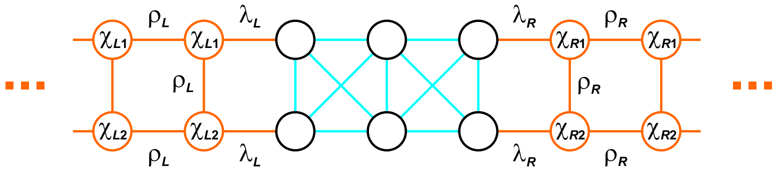

(a) Contact model 2

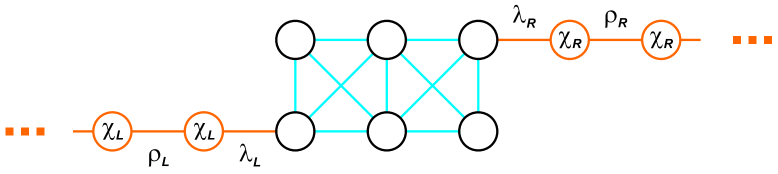

(b) Contact model 3

Figure 5.11: Models for the contacts to DNA double strands.

This choice of the contact is made in analogy with the experimental realization of [191]. There, only the 3'-ends of the strands are attached to the gold contacts via a thiol-linker.

5.3.7 Conductance calculations for different base sequences

In this Section we study how the conductance depends on the base sequence of the DNA double strand under examination. We examine the double strands measured by [191], i.e. 5'-GCGC$\,(\mathrm{AT})_m\,$GCGC-3' and 5'-$(\mathrm{GC})_n$-3' in dependence of the number of base pairs in the molecules. For all calculations, we choose symmetric contacts, i.e. $\eta_L = \eta_R$ for contact 1, and $\rho_L = \rho_R$ and $\lambda_L = \lambda_R$ for contacts 2 and 3.

The Fermi energy of gold (which is the contact metal in [191]) is known to be about $E_F = 5.1$eV.[7] Yet as the absolute values of the onsite energy parameters depend on the method by which they were calculated or measured, we consider also the Fermi energy as a variable parameter.

For the simulations we used the parameters given in Table 5.2.

With this set of parameters, for the DNA-double strands examined by [191] we obtain the conductance results displayed in Figures 5.12–5.14, in comparison with the experimental data of [191].

Choosing contact 2 and decoherence region 2 we obtain results which are quantitatively

---

[7] This is the value e.g. used by [75].

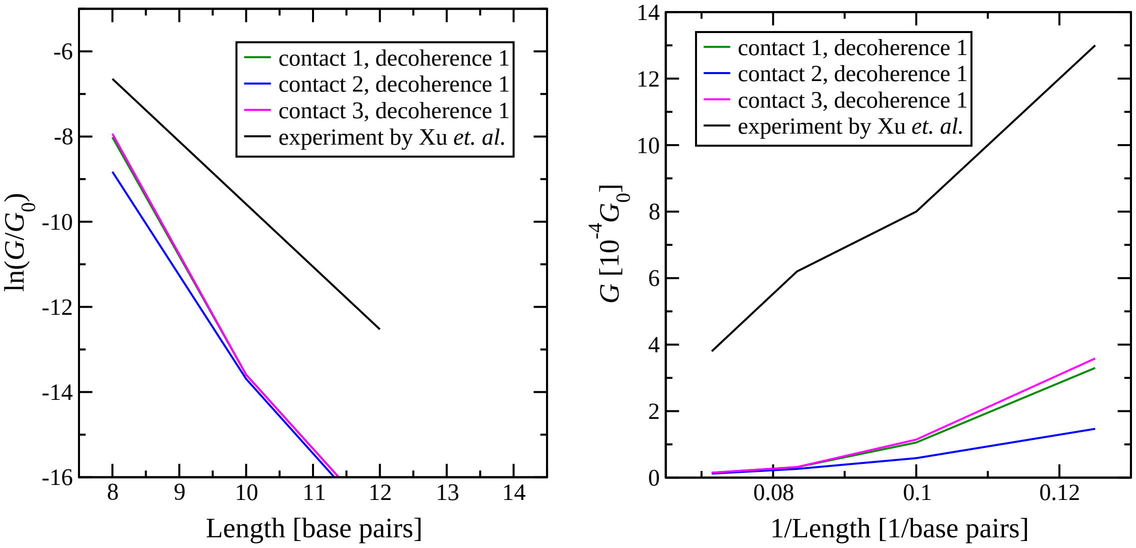

(a) 5'-GCGC(AT)$_m$GCGC-3', dec. region 1 (b) 5'-(GC)$_n$-3', dec. region 1

Figure 5.12: Conductance for different DNA double strands calculated with the extended ladder model, the three contact models and the decoherence region 1. For all calculations, $M = 1000$ decoherence configurations were considered.

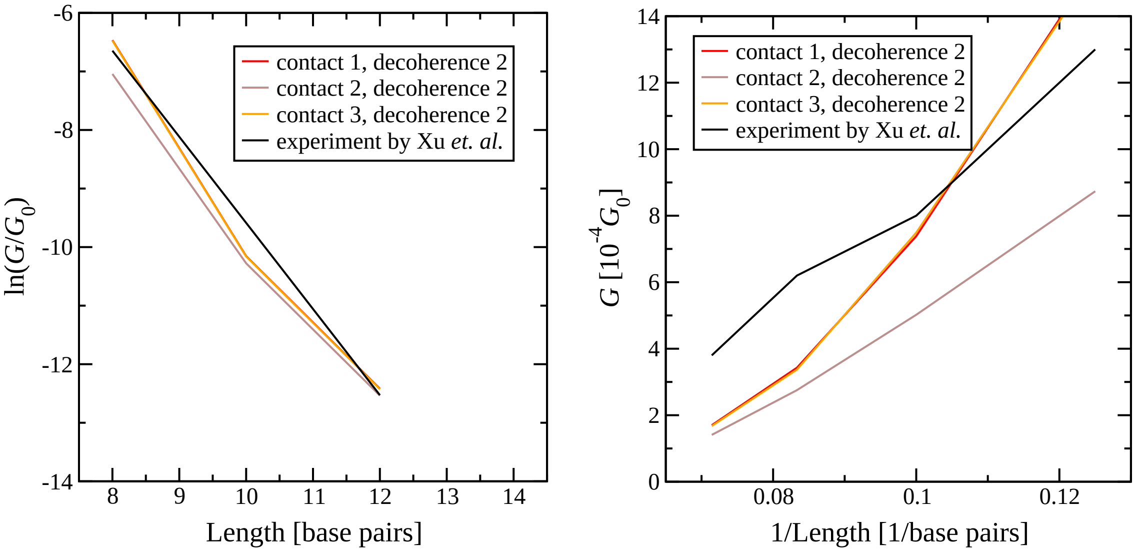

(a) 5'-GCGC(AT)$_m$GCGC-3', dec. region 2 (b) 5'-(GC)$_n$-3', dec. region 2

Figure 5.13: Conductance for different DNA double strands calculated with the extended ladder model, the three contact models and the decoherence region 2. For all calculations, $M = 1000$ decoherence configurations were considered.

contact	E_F	$\eta_L = \eta_R$	$\lambda_L = \lambda_R$	$\rho_L = \rho_R$
1	8.178	0.12	-	-
2	8.178	-	0.12	4.8
3	8.178	-	0.7	4.8

(a) Contacts

dec. region	η	p
1	1.2	0.24
2	1.2	0.24
3	-	0.24

(b) Decoherence Regions

Table 5.2: Simulation parameters for the contacts and decoherence regions. All energies in eV.

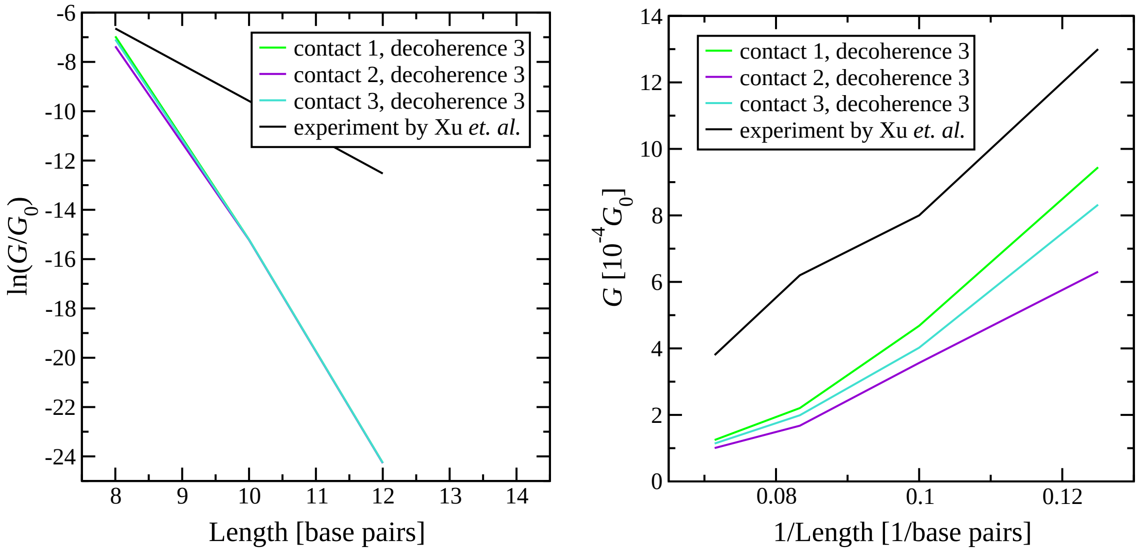

(a) 5'-GCGC(AT)$_m$GCGC-3', dec. region 3

(b) 5'-(GC)$_n$-3', dec. region 3

Figure 5.14: Conductance for different DNA double strands calculated with the extended ladder model, the three contact models and the decoherence region 3. For all calculations, $M = 1000$ decoherence configurations were considered.

comparable with the ones of [191] displayed in Figure 5.4. For all combinations of contacts and decoherence regions we find that the conductance decreases steeper by augmenting A·T than by augmenting G·C base pairs. Yet, whereas the exponential decrease in conductance (5.1) by augmenting A·T base pairs is reproduced, the inversely proportional behavior (5.2) for augmenting G·C base pairs (ohmic behavior) is not as clearly reproduced. Yet, for higher values of p or longer molecules, ohmic behavior should be reached.

Some words to the choice of parameters for the simulation (cf. Table 5.2). First of all, we choose the Fermi energy $E_F = 8.178$eV to be aligned with the onsite energy ϵ_{G} of the G base. A justification is that the onsite-energy parameters ϵ_X are controversial in the literature, compare [103], [196], and [164]. As we do not include energy relaxation in the model of decoherence nor consider finite voltages, the energetic alignment of Fermi energy and one of the bands of the channel is indispensable for obtaining significant conductance. For the coupling λ of contact 2 and η of contact 1 we have chosen a value which corresponds to the larger $t_{5'\text{-XY-}3'}$ values given in Table 5.1, while the values of $\rho = 4.8$eV correspond to half of the band-width of the conduction band of gold.[8] The further parameters (η for decoherence regions 1 and 2, and λ for contact 3) have been chosen such to best fit the experimental data of [191].

5.4 Conclusions and outlook

In this chapter we have presented structure, electronic properties, and experimental results for the conductance of DNA double strands. We believe that the controversial results for the conductance of DNA double strands [191] yielding exponential or inversely proportional decay with the length of the double strand, can be explained by effects of decoherence. As we have seen in Chapter 4, for energetic alignment of the contact Fermi energy and the onsite energies of an ordered chain, decoherence effects lead to ohmic behavior. On the other hand, if the Fermi energy is outside of the band of the channel, only for short decoherence length (large parameter p), we find ohmic behavior, else the channel can behave as a tunneling barrier, and exponential conductance decay is expected.

We have discussed several tight-binding models for DNA which have been used in the literature. The extended ladder model presented in Section 5.2.3 is one of the most realistic tight-binding models for which widely accepted transfer matrix elements have been found by DFT calculations [164].

We examined this model for different contact and decoherence region models in Section 5.3.7, and find qualitative and (to orders of magnitude) quantitative agreement with the experiments by [191] in the sense that for A·T base pairs introduced into a 5'-(GC)$_n$-3' double strand the conductance reduces notably stronger than for additional G·C base pairs. The reason is that the energetic difference in the onsite-energies between A·T and G·C make the A·T base pairs act as tunneling barriers between G·C base pairs. The absolute values of the conductance we find are quantitatively comparable in orders of magnitude. Yet, so far we could not find a satisfactory agreement between our model results and the experiment of [191]. The conductance decay we find for introducing A·T base pairs is not clearly exponential, and the additional G·C base pairs do not clearly increase the resistance linearly.

There are various reasons why the agreement has not been achieved. Firstly, the onsite-energy parameters for the model, the correct Fermi energy, and the correct contact model might require a complete DFT calculation of the system and the contacts. As presented in this chapter, too many of the parameters remain free-choice parameters. Secondly, energy relaxation on decoherence events can play an important role in the transport process. If, by relaxation, e.g. the energy of the transferring hole aligns or misaligns with the surrounding bases, transport is enhanced or inhibited. The inclusion of energy relaxation can be a future extension of our model for the effects of decoherence. Thirdly, as the system of [191], is a DNA double strand in aqueous solution, the energy landscape of the double strand is strongly influenced by the (movement of the) counter-ions (mostly Na$^+$), cf. [11, 74]. The modifications of onsite energies and charge-transfer integrals by interaction with the solvent have been studied by [79, 102]. To include the dynamical potential modifications can be a future extension of the model.

---

[8] The conduction band has a width of about 10eV, cf. [94, 101].

Summarizing we have found qualitative and quantitative (orders-of-magnitude) agreement between our model and experiments by [191]. For better quantitative agreement, extensions of our model would have to be considered.

6 Conclusions and Outlook

Decoherence, or the transition from the quantum-mechanical to the classical description of Nature is the phenomenon at the core of ohmic conductance. If it were not for the electrons to scatter and lose their phase coherence due to interaction, there would not be a material quantity named resistivity ρ, and in school we would not learn that the resistance increases linearly with the length of a wire.

While in this thesis we did not consider *why* the electron loses its phase during conduction—via phonon scattering, electron-electron interaction, or light absorption to name but a few decohering processes—, we have seen a way to describe *how* this affects the conduction. During statistically independent events we take out electrons from decoherence regions and then re-inject them to the coherent rest of the system suppressing any interference. This occurs at distances which on average equal the phase coherence length (see Chapter 4). In this way, the symmetries of coherent electronic states, and the way they affect the interference patterns at local defects (see Chapter 3) do not play a role on scales larger than the coherence length. Similarly, the localization of electronic states due to disorder, which suppresses the conduction exponentially with increasing coherent transport distance, does not necessarily cause an exponential increase of resistance with length on scales which are larger than the phase coherence length. In Section 4.3 we have seen how and under which conditions the transition from coherent to incoherent transport allows us to define a resistivity using our model for the effects of decoherence. The interference patterns, the even-odd effects, and the behavior as tunneling barriers, of finite coherent systems are replaced by a material parameter ρ.

The results of Chapters 3, 4, and 5 are summarized in their respective conclusions, see pages 54, 87, and 105. The main results can also be found in the summary, Chapter 7.

For DNA double strands which we considered in Chapter 5, experiments [191] have shown a “turnover from tunneling to hopping”[1] conduction. This is just what we have described before: the transition from a coherent behavior, to an effective decoherent description by a material parameter. This is why we discussed the application of the model for the effects of decoherence on DNA double strands in Chapter 5. In the context of DNA we have already seen that extensions of this model should be considered. How can we include energy relaxation which is believed to be intrinsically tied to decoherence? What about the absorption and emission of photons we have spoken about in the Introduction? How to address Coulomb blockade in the framework of our model? What changes, if we consider two and three-dimensional systems? There is truly much way to go to a consistent description of electron transport in a nanoparticulate system which locally catches the quantum-mechanical basis of the nanoparticles, and globally is described by effective material parameters.

---

[1] Words used by [72, page 20].

Nevertheless, let us look at closer goals. The consideration of finite bias voltages within our model is in preparation and will make comparison with experimental I-V characteristics possible. The DNA chain model is a multiply connected system. In this and similar quasi-linear models, the influence of a transversal magnetic field on the current (Aharonov-Bohm effect) can be studied.

And there are promising results already for the model as it is presented in this thesis. Ohm's law is retrieved and a resistivity of linear systems can be defined also for systems experiencing localization, as long as a critical decoherence site density is reached. This is the nature of a model. It is but a way to understand some aspects of reality.

7 Summary

After the Introduction, Chapter 2 provides an excerpt of the framework of quantum transport used in this thesis.

In Chapter 3, for coherent transport in linear and quasi-linear tight-binding systems we have described various methods to calculate the Green functions and surface Green functions, which give us information about the total and local densities of states at the surface of the system. The surface Green functions are needed when considering half-infinite tight-binding systems as models for contacts in quantum transport. We have also studied how the symmetries of the Hamiltonians of the half-infinite systems affect the transmission through defects. An example is the reflectionless transmission through double-chain like defect coupled to topologically different half-infinite double chains. Furthermore we have studied the transmission through finite tight-binding chains. Without disorder, the transmission function shows maxima at the locations of the eigenenergies of the tight-binding system. Outside the eigenenergy spectrum, the transmission through finite chains decreases exponentially, i.e. the chains behave like tunnelling barriers for incoming electrons. Within the energy range of the eigenenergy spectrum, the transmission function is periodic with respect to the chain length. We develop formulae to describe the period, infima, and suprema of the transmission function. Concluding Chapter 3 we analyze the transmission through disordered tight-binding chains, and find an exponential decrease of transmission with the chain length, as expected for systems in localization regime.

Chapter 4 contains the core of this thesis, the description of the statistical model for the effects of decoherence on the transport properties of large samples. Conceptually we divide a large sample into regions of coherent transport, and decoherence regions which act as reservoirs with respect to the coherent regions. To the decoherence regions we assign electron energy distribution functions which are interrelated by transition rates derived from the coherent transport between neighboring decoherence regions. In the linear case, by the decoherence regions (decoherence sites in the discussed example), the system falls apart into subsystems which do not interfere quantum-mechanically. For linear systems we find, by solving the rate equations in the stationary current case, that every decoherence region configuration leads to a total system resistance which is the sum of the subsystem resistances. As an example for the application of the model of the effects of decoherence we study decoherence effects on transport in linear tight-binding systems without and with onsite (diagonal) disorder. For the case without disorder we find that the resistance $1/\langle G\rangle$ [1] reaches an ohmic limit (proportionality with the total system length) for all contact Fermi energies μ in the range of the tight-binding eigenenergies of the chain. For Fermi energies outside this range, there exists a critical decoherence site density p^* such that for all $p > p^*$ an ohmic limit is reached, whereas for $p < p^*$, the tunneling-barrier properties of the subsystems dominate transport, and the resistance increases non-linearly. Analogously, also for the decoherence effects on transport through disordered tight-binding systems we find a critical decoherence site density p^*_{disorder} such that for $p > p^*_{\text{disorder}}$ an ohmic large-system limit is reached, although the subsystems show an exponentially increasing resistance (due to localization). Finally we determine series expressions for the ohmic resistivity of infinite ordered and disordered systems, and their convergence criteria.

---

[1] The system conductance is averaged over an ensemble of statistically independent decoherence configurations.

We discuss the application of the model of the effects of decoherence on DNA double strands in Chapter 5. There, we present various tight-binding models for DNA molecules. We study three models for the contacts and three models for the decoherence regions in the DNA double strand. Using energy parameters from the literature and choosing our contact and decoherence parameters adequately we can qualitatively and, to orders of magnitude, quantitatively reproduce experimental data.

A Recommended Literature

Much time during a PhD-thesis is spent with literature studies. Specially as I was a newcomer in the field of Quantum Transport of Nanostructures and a pioneer within Prof. Wolf's working group, this was an important part of my work. For the sake of future students and scientists taking their first step in a new area similar to the one of this thesis, I wish to present a list of personal literature recommendations.

A.1 Solid state physics

The experimentally-oriented textbook by **Ashcroft and Mermin** [8] has nice introductory chapters 1–8 on the first electron transport theory, **Drude theory**, and its limits, on crystal structures and reciprocal lattices, as well as Bloch's theorem.

The introductory book by theorist **Charles Kittel** [95] serves as a nice **reference book on solid state theory**. It comprises short definitions and derivations, e.g. on phonons, band-structure calculations or plasmons. It is specially nice because it does not use too much overhead and its chapters are largely independent. Since the edition of 2004 it also comprises a **short chapter on nanostructures** which can serve as a starting-point.

A rather didactic, but read-through approach is followed by **Ziman** [201]. Of special interest is its **chapter on transport properties**, which presents the classical **Boltzmann approach for conduction**.

Because of the emphasis on the **tight-binding method**, I can recommend the textbook by **Walter Harrison** [80], which is also an introductory book on solid-state theory. Yet, still the best understanding of the tight-binding method and its usefulness can be achieved by carefully studying the classic 1954-paper of **Slater and Koster** [167] where the method is presented in detail, the important remarks by **Löwdin** [117] and the paper of **Mehl and Papaconstantopoulos** [130] where the method is applied for parameterization of first-principles electronic structure calculations.

A **modern presentation** of solid-state physics is given by **Grosso and Pastori Parravicini**. Specially chapter 1 with the tridiagonal matrices arising with the tight-binding method and the related continued fractions has applications in Sections 3.9 and 4.3.5 of this thesis.

A.2 Green functions and many-particle physics

For the description of transport physics, a treatment with Green functions is virtually indispensable. It offers the concept of a propagator which is at the basis of many-particle physics, specially Wick's theorem and the Dyson equation which are required for nonequilibrium physics.

To my taste, **Economou**'s book [62] is the **best starting point** for a study of Green functions. It gives **short definitions** and derives the **mathematical properties of Green functions** clearly separated from the physical applications.

For many-particle physics I refer to two classics: **Fetter and Walecka** [69], with emphasis on chapters 1–7, gives a **systematic approach** to the aspects of many-particle physics which are necessary for this thesis, and **Mahan** [120] which discusses also many **concrete example systems**.

Another classic book on many-particle physics is by **Abrikosov** [1], which I did not use much though.

A.3 Nanostructures and nanoparticles

A good starting point to get familiar with nanoparticles is **Günter Schmid**'s book [160]. It gives a physically intuitive **first insight** into the most important properties of nanoparticles.

Furthermore I recommend the book by **Delerue and Lannoo** [57], which amongst others offers an introduction into **quantum confinement** and a chapter about **transport in nanostructures**.

A.4 Mesoscopic physics

The physics of quantum transport has, to a large extend, evolved from the field of mesoscopic physics. The concepts of **localization, dephasing, decoherence**, and the very important **Landauer formula** are findings within the framework of mesoscopic physics. Two standard books are available. The one by **Imry** [86], and the one by **Akkermans and Montambaux** [3] which I prefer personally.

A.5 Quantum transport

Here I come to the core literature for my thesis. Most of what I needed to know I found in the two great books by **Supriyo Datta**. **"Electronic transport in mesoscopic**

systems" [53] comes from the mesoscopic physics and advances through to the nonequilibrium Green function formalism. His most recent book **"Quantum Transport. From Atom to Transistor"** [54] is the result of his lectures for students of Electrical Engineering. In a very didactical style he motivates and derives all the necessary physics and formalism for the modelling of nanoscale electronic devices.

Furthermore, I consulted the book by **Ferry and Goodnick** [68] which contains a lot of **experimental findings**, and transport description from the different viewpoints.

A recent book by **Di Ventra** [58] comprises all the **different levels of transport description**, from macroscopic Drude theory to Landauer's approach to nonequilibrium Green functions formalism with clear remarks about the limits of each description. Without going into so much detail, but offering a broader view of the field, **Nazarov and Blanter** [141] have written a good didactical book.

I am already very curious about **Carlos Cuevas**' book on **Molecular Electronics** [48] which is to be published in 2010. Knowing his PhD thesis [46] this will be a complete overview over the field containing **the necessary knowledge to start in this field**.

Last but not least I wish to cite the works on which all the field of quantum transport is based. Martin and Schwinger [122], Kadanoff and Baym [88], Keldysh [91], Caroli et. al. [34–36, 45], Danielewicz [52], Rammer and Smith [151], Mahan [119], Khan et. al. [92], and Meir and Wingreen [132].

A.6 Biochemistry

New land for surely many physicists. I recommend **Voet and Voet**'s didactical book about **biologically relevant molecules** [182] and their functions in live cells, and also their physical properties and structures.

B Green functions in transport theory

This chapter gives a short introduction into Green functions in general, with respect to quantum mechanics and specifically to quantum transport.

The introductory section B.1 follows [62, chapter 1 and 2].

B.1 Definition and basic properties of time-independent Green functions

Time independent Green functions are solutions of partial differential equations of the following type:

$$(z - L(\vec{r}))\, G(\vec{r}, \vec{r}'; z) = \delta(\vec{r} - \vec{r}') \tag{B.1}$$

where z is a complex number with $\mathrm{Re} z = \lambda$ and $\mathrm{Im} z = s$, and L a time-independent, linear, Hermitian differential operator, e.g. the Hamiltonian. The Green function is defined uniquely given a set of boundary conditions for $G(\vec{r}, \vec{r}'; z)|_{(\vec{r}, \vec{r}') \in S}$ on the surface S of the domain Ω of $\vec{r}$, $\vec{r}'$.

L as an Hermitian operator possesses a complete set of eigenfunctions, i.e.

$$L(\vec{r})\phi_n(\vec{r}) = \lambda_n \phi_n(\vec{r}) \tag{B.2}$$

where the $\{\phi_n(\vec{r})\}$ are subject to the same boundary conditions as G.

The eigenfunctions ϕ_n can be taken, without loss of generality, as a set of orthogonal functions

$$\int\limits_{\Omega} \mathrm{d}^3 r \phi_i^*(\vec{r})\phi_j(\vec{r}) = \delta_{ij} \tag{B.3}$$

The completeness of the set of eigenfunctions means

$$\sum_n \phi_n^*(\vec{r}')\phi_n(\vec{r}) = \delta(\vec{r} - \vec{r}') \tag{B.4}$$

where the $\sum_n$ is to be understood as $\sum_n = \sum_{n'} + \int \mathrm{d}n$ a sum or an integral, for the discrete and continuous part of the spectrum of L respectively.

The notation for this introductory section can be simplified by using Dirac's abstract bra-ket-formulation, abstract in the sense that it can be used without a concrete basis.

The above equations translate into the bra-ket-notation by the following relations:

$$\phi(\vec{r}) \equiv \langle \vec{r}|\phi\rangle \tag{B.5}$$

$$\delta(\vec{r}-\vec{r}')L(\vec{r}) \equiv \left\langle \vec{r}|L|\vec{r}'\right\rangle \tag{B.6}$$

$$G(\vec{r},\vec{r}';z) \equiv \left\langle \vec{r}|G(z)|\vec{r}'\right\rangle \tag{B.7}$$

$$\delta(\vec{r}-\vec{r}') \equiv \left\langle \vec{r}|\vec{r}'\right\rangle \tag{B.8}$$

$$\int \mathrm{d}^3r\ |\vec{r}\rangle\langle\vec{r}| = 1 \tag{B.9}$$

Thus we have the defining equations

$$(z-L)\,G(z) = 1 \tag{B.10}$$

with

$$L|\phi_n\rangle = \lambda_n|\phi_n\rangle \tag{B.11}$$

$$\langle\phi_n|\phi_m\rangle = \delta_{nm} \tag{B.12}$$

$$\sum_n |\phi_n\rangle\langle\phi_n| = 1 \tag{B.13}$$

Taking the $\langle\vec{r}|, |\vec{r}'\rangle$ matrix element of (B.10), we recover (B.1):

$$\left\langle \vec{r}|(z-L)G(z)|\vec{r}'\right\rangle = \left\langle \vec{r}|1|\vec{r}'\right\rangle = \delta(\vec{r}-\vec{r}')$$

and thus

$$\begin{aligned} zG(\vec{r},\vec{r}';z) &- \left\langle \vec{r}|LG(z)|\vec{r}'\right\rangle \\ &= zG(\vec{r},\vec{r}';z) - \int \mathrm{d}^3r''\left\langle \vec{r}|L|\vec{r}''\right\rangle\left\langle \vec{r}''|G(z)|\vec{r}'\right\rangle \\ &= zG(\vec{r},\vec{r}';z) - L(\vec{r})G(\vec{r},\vec{r}';z) = \delta(\vec{r}-\vec{r}') \end{aligned} \tag{B.14}$$

The bra and ket notation (B.10) can be solved for G for all $z \neq \{\lambda_n\}$, formally as

$$G(z) = \frac{1}{z-L} \tag{B.15}$$

i.e., multiplying by (B.13)

$$G(z) = \frac{1}{z-L}\sum_n |\phi_n\rangle\langle\phi_n| = \sum_n \frac{|\phi_n\rangle\langle\phi_n|}{z-\lambda_n} \tag{B.16}$$

which, in $\vec{r}$-representation is

$$G(\vec{r},\vec{r}';z) = \sum_n \frac{\phi_n^*(\vec{r}')\phi_n(\vec{r})}{z-\lambda_n} \tag{B.17}$$

The equations (B.16) and (B.17) are usually called the spectral or Lehmann representation of the Green function.

By the last equation we can easily see that the simple poles of the Green function $G(z)$ give the discrete spectrum of L.

B.2 Non-equilibrium Green functions: the Keldysh formalism

This Section B.2 follows [123].

Green functions are used as a method for solving linear inhomogeneous differential equations. In electrodynamics, for example, they are used for solving the inhomogeneous wave equation that gives the fields for a time-dependent current distribution. In quantum mechanics, Green functions are often called "propagators" which reminds us that they are used for the calculation of propagation probability amplitudes: The probability amplitude to find an electron at $\vec{r}'$ at time t' given it had been at $\vec{r}$ at time t:

$$G^c(\vec{r}',t';\vec{r},t) = -\mathrm{i}\langle\Psi_0|\mathbf{T}[\psi(\vec{r}',t')\psi^+(\vec{r},t)]|\Psi_0\rangle \tag{B.18}$$

where Ψ_0 is the ground-state wave function of the system in the Heisenberg picture, $\mathbf{T}$ is the time-ordering operator according to Wick, and the $\psi^{(+)}(\vec{r},t)$ are field annihilation (creation) operators. Spin dependency has been neglected.

In (B.18) we have defined the so-called "causal" Green function G^c. For some calculations, the definition of the "retarded" and "advanced" Green function, G^r and G^a are useful:

$$G^{r,a}(\vec{r}',t';\vec{r},t) = \mp\mathrm{i}\theta(\pm(t-t'))\langle\Psi_0|[\psi(\vec{r}',t'),\psi^+(\vec{r},t)]_+|\Psi_0\rangle, \tag{B.19}$$

where $[,]_+$ denotes the anti-commutator.

In the following we will use the creation and annihilation operator notation, i.e. $\psi(\vec{r},t) \rightarrow c_i(t)$, $\psi^+(\vec{r},t) \rightarrow c_i^+(t)$.

B.2.1 Perturbation theory in equilibrium

Perturbation theory allows the description of a system governed by a Hamiltonian

$$H = H_0 + V, \tag{B.20}$$

with a single-electron unperturbed Hamiltonian H_0 with known eigenstates and eigenvalues[1] , and a perturbation V, which, e.g., can describe interaction or an external potential. The goal is to calculate the expectation values of arbitrary operators.

B.2.1.1 The interaction picture

In perturbation theory, it is convenient to use the interaction picture of quantum mechanics. It is related to both the Heisenberg and the Schrödinger picture through unitary transformations.

---

[1] In this case, single-electron Hamiltonian denotes a Hamiltonian without electron-electron correlations. It can always be written in terms of creation and annihilation operators of one-electron states: $H = \sum_{ij} c_i^+ H_{ij} c_j$. The N-electron-wavefunctions corresponding to a Hamiltonian of this kind can be represented by a Slater determinant.

The wave function in the interaction picture is defined as

$$\Psi_I(t) = \mathrm{e}^{\mathrm{i}H_0 t}\Psi_S(t) \tag{B.21}$$

where $\Psi_S(t)$ is the corresponding Schrödinger wave function.

The operators transform correspondingly:

$$O_I(t) = \mathrm{e}^{\mathrm{i}H_0 t} O_S \mathrm{e}^{-\mathrm{i}H_0 t} \tag{B.22}$$

with the operator O_S in the Schrödinger picture. As we can see, the operators in the interaction picture are nothing but the Heisenberg operators of the unperturbed system.

Time evolution of operators and wave functions in the interaction picture Starting from (B.22), we can derive the time evolution of an operator in the interaction picture:

$$\begin{aligned} &\frac{\partial}{\partial t} O_I(t) = \mathrm{i}H_0 O_I(t) - \mathrm{i}O_I(t) H_0 \\ \Rightarrow \quad &\mathrm{i}\frac{\partial}{\partial t} O_I(t) = [O_I(t), H_0] \end{aligned} \tag{B.23}$$

i.e. the time-evolution of the operators is the same as in the Heisenberg picture. Note that the operators in the interaction picture evolve in time as if the system were unperturbed.

Now let us consider the time evolution of the wave functions in the interaction picture. Using the definition of $\Psi_I(t)$ (B.21) and the Schrödinger equation we can see that

$$\begin{aligned} \frac{\partial}{\partial t}\Psi_I(t) &= \mathrm{i}H_0 \mathrm{e}^{\mathrm{i}H_0 t}\Psi_S(t) - \mathrm{i}\mathrm{e}^{\mathrm{i}H_0 t} H \Psi_S(t) \\ \Rightarrow \quad \mathrm{i}\frac{\partial}{\partial t}\Psi_I(t) &= \mathrm{e}^{\mathrm{i}H_0 t}\left(H - H_0\right)\Psi_S(t) \\ &= \mathrm{e}^{\mathrm{i}H_0 t}\left(H - H_0\right)\mathrm{e}^{-\mathrm{i}H_0 t}\mathrm{e}^{\mathrm{i}H_0 t}\Psi_S(t) \\ &= V_I(t)\Psi_I(t) \end{aligned} \tag{B.24}$$

This means that in the interaction picture, the time evolution of the wave function only depends on the interaction.

For completeness we also give a summary of the unitary transformations that relate the interaction and the Heisenberg picture:

$$\Psi_I(t) = \mathrm{e}^{\mathrm{i}H_0 t}\mathrm{e}^{-\mathrm{i}Ht}\Psi_H \tag{B.25}$$

$$O_I(t) = \mathrm{e}^{\mathrm{i}H_0 t}\mathrm{e}^{-\mathrm{i}Ht} O_H(t) \mathrm{e}^{\mathrm{i}Ht}\mathrm{e}^{-\mathrm{i}H_0 t} \tag{B.26}$$

$$\Psi_H = \mathrm{e}^{\mathrm{i}Ht}\mathrm{e}^{-\mathrm{i}H_0 t}\Psi_I(t) \tag{B.27}$$

$$O_H(t) = \mathrm{e}^{\mathrm{i}Ht}\mathrm{e}^{-\mathrm{i}H_0 t} O_I(t) \mathrm{e}^{\mathrm{i}H_0 t}\mathrm{e}^{-\mathrm{i}Ht} \tag{B.28}$$

The time-evolution operator Like in the Schrödinger picture, we define a time-evolution operator $S(t, t_0)$ for the wave function:

$$\Psi_I(t) \equiv S(t, t_0)\Psi_I(t_0) \tag{B.29}$$

Using (B.21) and the time-evolution operator in the Schrödinger picture we obtain

$$\begin{aligned} \Psi_I(t) &= \mathrm{e}^{\mathrm{i}H_0 t}\Psi_S(t) \\ &= \mathrm{e}^{\mathrm{i}H_0 t}\mathrm{e}^{-\mathrm{i}H(t-t_0)}\Psi_S(t_0) \\ &= \mathrm{e}^{\mathrm{i}H_0 t}\mathrm{e}^{-\mathrm{i}H(t-t_0)}\mathrm{e}^{-\mathrm{i}H_0 t_0}\Psi_I(t_0) \\ \Rightarrow \quad S(t,t_0) &= \mathrm{e}^{\mathrm{i}H_0 t}\mathrm{e}^{-\mathrm{i}H(t-t_0)}\mathrm{e}^{-\mathrm{i}H_0 t_0} \end{aligned} \tag{B.30}$$

The unitary transformations (B.25–B.28) can be expressed in terms of the time-evolution operator, using $S(0,t) = \exp(\mathrm{i}Ht)\exp(-\mathrm{i}H_0 t)$:

$$\Psi_H = S(0,t)\Psi_I(t) \tag{B.31}$$

$$O_H = S(0,t)O_I(t)S(t,0) \tag{B.32}$$

The equation of motion for the time-evolution operator reads

$$\mathrm{i}\frac{\partial}{\partial t}S(t,t_0) = V_I(t)S(t,t_0) \tag{B.33}$$

like for the wave function itself.

B.2.1.2 The perturbation expansion

Equation (B.24) can be written as an integral equation:

$$\Psi_I(t) = \Psi_I(t_0) - \mathrm{i}\int_{t_0}^{t} \mathrm{d}t' V_I(t')\Psi_I(t') \tag{B.34}$$

which, by iteration, leads to the perturbation expansion for $\Psi_I(t)$

$$\Psi_I(t) = \left[1 + \sum_{n=1}^{\infty}(-\mathrm{i})^n \int_{t_0}^{t} \mathrm{d}t_1 V_I(t_1) \int_{t_0}^{t_1} \mathrm{d}t_2 V_I(t_2) \times \cdots \times \int_{t_0}^{t_{n-1}} \mathrm{d}t_n V_I(t_n)\right]\Psi_I(t_0) \tag{B.35}$$

Now, note that the integrands in this expression have decreasing time arguments from left to right, i.e. $t_1 > t_2 > \cdots > t_n$. Let us introduce the time-ordering operator[2], which is defined as

$$\mathbf{T}\left[V(t_1)V(t_2) \times \cdots \times V(t_n)\right] = V(t_{l_1})V(t_{l_2}) \times \cdots \times V(t_{l_n}) \tag{B.36}$$

where $\{l_i\}$ is the permutation of $(1,2,\dots,n)$ which fulfils $t_{l_1} > t_{l_2} > \cdots > t_{l_n}$.

With this definition we can rewrite (B.35) as

$$\Psi_I(t) = \left[1 + \sum_{n=1}^{\infty}\frac{(-\mathrm{i})^n}{n!} \int_{t_0}^{t} \mathrm{d}t_1 \int_{t_0}^{t} \mathrm{d}t_2 \cdots \int_{t_0}^{t} \mathrm{d}t_n \mathbf{T}\left[V_I(t_1)V_I(t_2)\cdots V_I(t_n)\right]\right]\Psi_I(t_0) \tag{B.37}$$

---

[2] The time-ordering operator is not a physical operator in the sense that it corresponds to an observable; it is just a mathematical tool, like e.g. a commutator.

where the factor $\frac{1}{n!}$ takes care of the fact that the change of the integration limits from (B.35) to (B.37) generates $n!$ integrals of the type in (B.35).

More generally, the time-ordering operator is defined as

$$\mathbf{T}[c_i(t)c_j^+(t')] = \begin{cases} c_i(t)c_j^+(t') & \text{for } t > t' \\ \pm c_j^+(t')c_i(t) & \text{for } t' > t \end{cases} \tag{B.38}$$

where the +-sign is for bosons, and the −-sign for fermions, i.e. it changes the sign for every interchange of a pair of Fermi creation and annihilation operators. This definition agrees with (B.36), as in the perturbation the creation and annihilation operators always appear in pairs.

Comparing (B.37) with (B.29) we obtain the perturbation expansion for the time-evolution operator

$$S(t, t_0) = 1 + \sum_{n=1}^{\infty} \frac{(-\mathrm{i})^n}{n!} \int_{t_0}^{t} \mathrm{d}t_1 \int_{t_0}^{t} \mathrm{d}t_2 \cdots \int_{t_0}^{t} \mathrm{d}t_n \mathbf{T}\left[V_I(t_1)V_I(t_2)\cdots V_I(t_n)\right] \tag{B.39}$$

which we can formally write as

$$S(t, t_0) = \mathbf{T}[\exp(-\mathrm{i} \int_{t_0}^{t} \mathrm{d}t' V_I(t'))] \tag{B.40}$$

B.2.1.3 The adiabatic hypothesis

The perturbation expansion for the time-evolution operator in the interaction picture can be used to relate the Heisenberg wavefunction of the unperturbed system to the interaction-picture wavefunction of the perturbed system.

We assume the perturbation to be “turned on and off” exponentially slow via

$$H = H_0 + V\mathrm{e}^{-\eta|t|} \tag{B.41}$$

Thus the perturbation tends to zero as $t \to \pm\infty$ and reaches its real value in the range of $1/\eta$ around $t = 0$.

It is reasonable to assume that the ground state of a system described by (B.41) approaches the unperturbed ground state $|\phi_0\rangle$ as $t \to \pm\infty$ and the perturbed ground state $|\Psi_H\rangle$[3] at $t = 0$. This statement, named the adiabatic hypothesis, was proved by Gell-Mann and Low [73], nicely explained in [69].

B.2.1.4 Calculation of expectation values

In this section we will show how to make use of the perturbation expansion in order to calculate expectation values.

---

[3] or a phase factor times $|\Psi_H\rangle$

Let us assume we want to calculate the expectation value of an operator $\mathbf{T}\left[A_H(t)B_H(t')\right]$. We choose this kind of operator, as the causal Green function is an operator of this kind. In the Heisenberg picture, the expectation value of this operator is defined by

$$I = \frac{\langle \Psi_H | \mathbf{T}\left[A_H(t)B_H(t')\right] | \Psi_H \rangle}{\langle \Psi_H | \Psi_H \rangle} \tag{B.42}$$

Now, we transform both the operator and the wave function into the interaction picture by using the unitary transformations (B.31) and (B.32):

$$I = \frac{\langle \phi_0 | S(\infty, 0)\mathbf{T}\left[S(0,t)A_I(t)S(t,t')B_I(t')S(t',0)\right] S(0,-\infty) | \phi_0 \rangle}{\langle \phi_0 | S(\infty, -\infty) | \phi_0 \rangle} \tag{B.43}$$

As $t = \pm\infty$ are the first and latest occurring times in this expression, the time-evolution operators can be included into the time ordering, i.e.

$$I = \frac{\langle \phi_0 | \mathbf{T}\left[A_I(t)B_I(t')S(\infty, -\infty)\right] | \phi_0 \rangle}{\langle \phi_0 | S(\infty, -\infty) | \phi_0 \rangle} \tag{B.44}$$

As the many-particle wavefunctions are defined in a Fock space, the quantum operators can always be written in terms of creation and annihilation operators, i.e. (B.43) corresponds to a sum of expectation values of the form

$$\left\langle \phi_0 | \mathbf{T}\left[c_i^+(t)c_j(t') \cdots c_k^+(t_1) \cdots c_l(t_n)\right] | \phi_0 \right\rangle \tag{B.45}$$

The time-ordered product of Fermi operators can be simplified by using the anti-commutation rules. This is done in the so-called Wick theorem [189] which states that, e.g.

$$\begin{aligned} \langle \phi_0 | \mathbf{T}[c_i(t)c_j^+(t')c_k(t_1)c_l^+(t_2)] | \phi_0 \rangle &= \langle \phi_0 | \mathbf{T}[c_i(t)c_j^+(t')] | \phi_0 \rangle \langle \phi_0 | \mathbf{T}[c_k(t_1)c_l^+(t_2)] | \phi_0 \rangle \\ &- \langle \phi_0 | \mathbf{T}[c_i(t)c_l^+(t_2)] | \phi_0 \rangle \langle \phi_0 | \mathbf{T}[c_k(t_1)c_j^+(t')] | \phi_0 \rangle \end{aligned} \tag{B.46}$$

i.e. a time-ordered product of n creation and n annihilation operators can be decomposed into the sum of all products of time-ordered pairs of annihilation and creation operators. Depending on the number of pair interchanges P that is necessary to obtain the order of a certain product, starting from the original order, each product carries the corresponding sign $(-1)^P$.

The proof of this theorem can be found in many field theory textbooks, e.g. [69, 120, 135, 153].

The proof now stated here follows [135]. Let there be $2p$ fermion operators b_r, $r = 1, 2, \ldots, 2p$ in the interaction picture. They are time-dependent, i.e. b_1 is taken at t_1, etc. All of the operators can be decomposed into a creation and an annihilation part:

$$\begin{aligned} b_r &= b_r^{(1)} + b_r^{(2)+} \qquad \text{with} \\ b_r^{(1)}\Phi_0 &= 0 \\ b_r^{(2)}\Phi_0 &= 0 \end{aligned} \tag{B.47}$$

where Φ_0 is the ground state for N fermions.

The theorem then can be stated as

$$\langle \mathbf{T}[\prod_1^{2p} b_r] \rangle_0 = \sum_{\text{all pairs } (r,s)} (-1)^P \prod \langle \mathbf{T}[b_r b_s] \rangle_0 \tag{B.48}$$

where $<>_0$ means the mean value in the ground state. Now, what the time-ordering operator does, is to sort the operators according to time, with the latest time on the left. Let us define another $2p$ operators c_r which are the operators b_r ordered according to time. If t_q is the latest of the times t_r, then by this definition

$$c_1 = b_q \tag{B.49}$$

and

$$\mathbf{T}[\prod_{r=1}^{2p} b_r] = (-1)^{P_1} c_1 \prod_{r=2}^{2p} c_r \tag{B.50}$$

where P_1 is the number of permutations necessary in rearranging the b_r to the c_r.

This operator can now be inserted into the left hand side of the theorem (B.48), i.e.

$$\begin{aligned}\langle \mathbf{T}[\prod_{r=1}^{2p} b_r]\rangle_0 &= (-1)^{P_1} \langle c_1 \prod_{r=2}^{2p} c_r\rangle_0 \\ &= (-1)^{P_1} \langle c_1^{(1)} \prod_{r=2}^{2p} c_r\rangle_0\end{aligned} \tag{B.51}$$

as $\langle c_1^{(2)+}| = 0$ by definition (B.47). Now, by a series of commutations, $c_1^{(1)}$ in (B.51) can be shovelled through to the right by applying the anti-commutation rules. Then at the right, $|c_1^{(1)}\rangle_0 = 0$ is used to obtain

$$\langle \mathbf{T}[\prod_{r=1}^{2p} b_r]\rangle_0 = (-1)^{P_1} \sum_{r=2}^{2p} (-1)^r [c_1, c_r] \langle \prod_{\substack{l\neq r\\ l\neq 1}} c_l\rangle_0 \tag{B.52}$$

As the anti-commutator is a complex number, replacing it with its expectation value does not change anything. Using this fact and (B.47) we get

$$\begin{aligned}[c_1^{(1)}, c_r] &= \langle [c_1^{(1)}, c_r]\rangle_0 \\ &= \langle c_1^{(1)} c_r\rangle_0 \\ &= \langle c_1 c_r\rangle_0 \\ &= \langle \mathbf{T}[c_1 c_r]\rangle_0\end{aligned} \tag{B.53}$$

Inserting this into (B.52) we obtain

$$\langle \mathbf{T}[\prod_{r=1}^{2p} b_r]\rangle_0 = (-1)^{P_1} \sum_{r=2}^{2p} (-1)^r \langle \mathbf{T}[c_1 c_r]\rangle_0 \langle \mathbf{T} \prod_{\substack{l\neq r\\ l\neq 1}} c_l\rangle_0. \tag{B.54}$$

Here we have included the time-ordering operator in the last expectation value. This does not make a change because $\prod_{l\neq r, l\neq 1} c_l$ is already a time-ordered product. The equation (B.54) is a recursion formula, which by assumption holds for $p = 1$, and by induction leads to the Wick theorem (B.48).

The important fact is that, by the Wick theorem, any operator can be decomposed into a sum of products of Green functions of the unperturbed state:

$$\begin{aligned}\langle\phi_0|\mathbf{T}[c_i(t)c_j^+(t')c_k(t_1)c_l^+(t_2)]|\phi_0\rangle &= \langle\phi_0|\mathbf{T}[c_i(t)c_j^+(t')]|\phi_0\rangle\langle\phi_0|\mathbf{T}[c_k(t_1)c_l^+(t_2)]|\phi_0\rangle \\ &\quad - \langle\phi_0|\mathbf{T}[c_i(t)c_l^+(t_2)]|\phi_0\rangle\langle\phi_0|\mathbf{T}[c_k(t_1)c_j^+(t')]|\phi_0\rangle \quad \text{(B.55)} \\ &= G_{il}^{(0)}(t,t_2)G_{kj}^{(0)}(t_1,t') - G_{ij}^{(0)}(t,t)'G_{kl}^{(0)}(t_1,t_2)\end{aligned}$$

where we have used the definition of a time-dependent causal Green function $G_{ij}^{(0)}(t,t') = -\mathrm{i}\langle\phi_0|\mathbf{T}[c_i(t)c_j^+(t')]|\phi_0\rangle$. The decomposition of the perturbed time-evolution operator into propagators of the unperturbed system is the starting point for the description of perturbed systems by Feynman diagrams.

B.2.2 Perturbation theory in non-equilibrium

The above formalism for the description of perturbed systems in equilibrium can be extended to non-equilibrium systems. This extension is due to Keldysh [91], and is nicely explained e.g. in [46]. The extension to non-equilibrium systems is fundamental for the description of transport processes like electric current.

In non-equilibrium, the Hamiltonian can be written as

$$H(t) = H_0 + V(t), \quad \text{(B.56)}$$

where, like in (B.20), the unperturbed Hamiltonian H_0 has known eigenvalues and eigenstates. Unlike in (B.20), the perturbation operator has a time dependence.

A different approach for the calculation of the expectation values is necessary because it does no longer hold the assumption that for adiabatic turning on and off of the perturbation for time $t \to \infty$ the ground state of the unperturbed system $|\phi_0\rangle$ is approached.

The expectation value of an operator thus cannot be calculated by (B.44). But, assuming that like in equilibrium for $t \to -\infty$ the system is in the ground state of the unperturbed system, we can write the expectation value of an operator A at time t as

$$\langle A\rangle(t) = \frac{\langle\phi_0|S(-\infty,0)S(0,t)A_I(t)S(t,0)S(0,-\infty)|\phi_0\rangle}{\langle\phi_0|S(-\infty,t)S(t,-\infty)|\phi_0\rangle}. \quad \text{(B.57)}$$

Now, the expression in the numerator cannot be subsumed under the usual time ordering operator. But by defining a new time order, along the so-called Keldysh contour $\mathcal{C}$, a formally analog expression for the expectation value holds true:

$$\langle A\rangle = \frac{\langle\phi_0|\mathbf{T}_c[A(t)S_c(\infty,-\infty)]|\phi_0\rangle}{\langle\phi_0|S_c(\infty,-\infty)|\phi_0\rangle} \quad \text{(B.58)}$$

Here, $\mathbf{T}_c$ orders the time along the Keldysh contour $\mathcal{C}$, and S_c is the corresponding time-evolution operator

$$S_c(\infty,-\infty) = S_-(-\infty,\infty)S_+(\infty,-\infty) \quad \text{(B.59)}$$

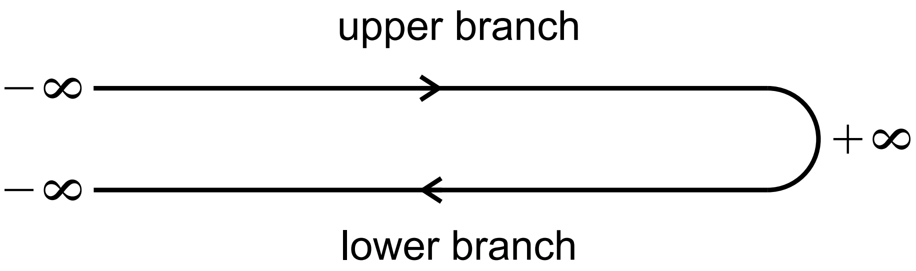

Figure B.1: The Keldysh contour.

where the index "+" indicates times on the upper branch and "−" on the lower branch of the Keldysh contour.

The expression (B.58) can be expanded into a perturbation expansion which is formally analog to (B.37), using the Keldysh time ordering operator and integrating time over $\mathcal{C}$.

$$G_{c,ij}(t_\alpha, t_\beta) = g_{c,ij}(t_\alpha, t_\beta) + \int\limits_{\mathcal{C}} \mathrm{d}t_1 \int\limits_{\mathcal{C}} \mathrm{d}t_2 \, [g_c(t_\alpha, t_1)\Sigma(t_1, t_2)G_c(t_2, t_\beta)]_{ij} \tag{B.60}$$

where g_c is the Green function of the unperturbed system, G_c the nonequilibrium Green function, and Σ the proper self energy of the perturbation. The contour ordered Green function involved in (B.60) reads

$$G_{c,ij}(t_\alpha, t_\beta) = -\mathrm{i}\frac{\langle \Psi_H | \mathbf{T}_c[c_i(t_\alpha)c_j^+(t_\beta)] | \Phi_H \rangle}{\langle \Psi_H | \Psi_H \rangle} \tag{B.61}$$

where $t_\alpha, t_\beta \in \mathcal{C}$.

We can restrict the domain of the times to $t, t' \in (-\infty, \infty)$, but then, instead of (B.61) we have to differentiate between four different Green functions, the so-called Keldysh Green functions, depending on the branch where t and t' stem from.

- $t = t_+$, $t' = t'_+$

  $$G_{ij}^{++}(t, t') = -\mathrm{i}\langle \mathbf{T}[c_i(t)c_j^+(t')] \rangle \tag{B.62}$$

  equals the usual definition of the causal Green function (cf. (B.18)).

- $t = t_+$, $t' = t'_-$

  $$G_{ij}^{+-}(t, t') = \mathrm{i}\langle c_j^+(t')c_i(t) \rangle \tag{B.63}$$

  As t_- is always "later" than t_+ along the Keldysh contour, no time-ordering operator is required.[4]

- $t = t_-$, $t' = t'_+$

  $$G_{ij}^{-+}(t, t') = -\mathrm{i}\langle c_i(t)c_j^+(t') \rangle \tag{B.64}$$

  Again we do not need a time-ordering operator in this definition.[5]

---

[4] This Green function is often named "lesser" Green function $G_{ij}^{<}(t, t')$.

[5] This Green function is often named "greater" Green function $G_{ij}^{>}(t, t')$.

- $t = t_-$, $t' = t'_-$

$$G_{ij}^{--}(t,t') = -\mathrm{i}\langle\tilde{\mathbf{T}}[c_i(t)c_j^+(t')]\rangle \tag{B.65}$$

  Here $\tilde{\mathbf{T}}$ is the anti-time ordering operator (latest times come to the right). Anti-time ordering on the lower branch of $\mathcal{C}$ corresponds to contour-time ordering.

We merge the four Green functions into the matrix

$$\mathbf{G} = \begin{pmatrix} G^{++} & G^{+-} \\ G^{-+} & G_{--} \end{pmatrix} \tag{B.66}$$

This kind of matrices are elements of the so-called Keldysh space. It can be shown [46, Appendix A] that also the Green functions in Keldysh space fulfil a Dyson equation

$$\mathbf{G}(t,t') = \mathbf{g}(t,t') + \int\limits_{-\infty}^{\infty} \mathrm{d}t_1 \int\limits_{-\infty}^{\infty} \mathrm{d}t_2\, \mathbf{g}(t,t_1)\mathbf{\Sigma}(t_1,t_2)\mathbf{G}(t_2,t') \tag{B.67}$$

which for stationary problems can be Fourier transformed to yield

$$\mathbf{G}(E) = \mathbf{g}(E) + \mathbf{g}(E)\mathbf{\Sigma}(E)\mathbf{G}(E) \tag{B.68}$$

B.2.3 Properties of the Keldysh Green functions

The four Keldysh Green functions fulfil the following relations:

$$G^{++} + G^{--} = G^{+-} + G^{-+} \tag{B.69}$$

$$G^{++} - G^{+-} = -G^{--} + G^{-+} = G^r \tag{B.70}$$

$$G^{++} - G^{-+} = -G^{--} + G^{+-} = G^a \tag{B.71}$$

which can be proved by inserting the definitions (B.19), (B.62)–(B.65). By these relations, the four Keldysh Green functions are not independent, and by a rotation in Keldysh space we can rewrite (B.66) as a triangular matrix

$$\tilde{\mathbf{G}} = \begin{pmatrix} 0 & G^a \\ G^r & G^F \end{pmatrix} = \mathbf{R}\mathbf{G}\mathbf{R}^{-1} \quad \text{with} \quad \mathbf{R} = \frac{1}{\sqrt{2}}\begin{pmatrix} 1 & -1 \\ 1 & 1 \end{pmatrix} \tag{B.72}$$

where $G^F = G^{+-} + G^{-+}$. Similarly the Dyson equation (B.68) can be written in a triangular form

$$\tilde{\mathbf{G}} = \tilde{\mathbf{g}} + \tilde{\mathbf{g}}\tilde{\mathbf{\Sigma}}\tilde{\mathbf{G}} \tag{B.73}$$

where

$$\tilde{\mathbf{\Sigma}} = \mathbf{R}\mathbf{\Sigma}\mathbf{R}^{-1} = \begin{pmatrix} \Omega & \Sigma^r \\ \Sigma^a & 0 \end{pmatrix} \tag{B.74}$$

with $\Omega = -[\Sigma^{+-} + \Sigma^{-+}]$.

Evaluating the matrix entries of (B.72) we find

$$G^a = g^a + g^a \Sigma^a G^a \tag{B.75}$$
$$G^r = g^r + g^r \Sigma^r G^r \tag{B.76}$$
$$G^F = g^F + g^r \Omega G^a + g^r \Sigma^r G^F + g^F \Sigma^a G^a \tag{B.77}$$

Also for the Keldysh Green functions G^{+-} and G^{-+} one finds Dyson equations[6]

$$G^{+-} = (1 + G^r \Sigma^r) g^{+-} (1 + \Sigma^a G^a) + G^r \Sigma^{+-} G^a \tag{B.78}$$
$$G^{-+} = (1 + G^r \Sigma^r) g^{-+} (1 + \Sigma^a G^a) + G^r \Sigma^{-+} G^a \tag{B.79}$$

B.2.4 Derivation of the current formula

Using creation and annihilation operators, the electrical charge at a site can be described by the operator

$$\rho_j = -e n_j = -e c_j^+ c_j \tag{B.80}$$

with the elementary charge e. Its equation of motion is

$$\frac{\partial \rho_j(t)}{\partial t} = \frac{\mathrm{i}}{\hbar}[H, \rho_j(t)] \tag{B.81}$$

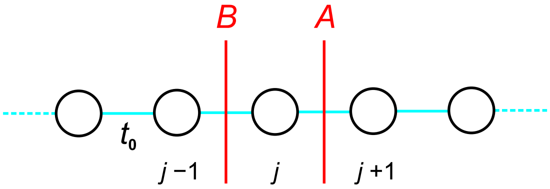

Figure B.2: A linear system. We consider the current through planes A and B.

For a linear system like displayed in Figure B.2 with the Hamiltonian $H = t_0 \sum_j [c_j^+ c_{j+1} + \text{H.c.}]$, the charge continuity requires

$$I_A - I_B + \frac{\partial \rho_j}{\partial t} = 0 \tag{B.82}$$

where I_A (I_B) is the current through plane A (B). Inserting (B.81) we find

$$\begin{aligned} I_A - I_B &= \frac{\mathrm{i}}{\hbar}[\rho_j(t) H - H \rho_j(t)] \\ &= \frac{\mathrm{i}et_0}{\hbar}\left(\sum_i [c_{i+1}^+ c_i + c_i^+ c_{i+1}] c_j^+ c_j - \sum_i c_j^+ c_j [c_{i+1}^+ c_i + c_i^+ c_{i+1}]\right) \\ &= \frac{\mathrm{i}et_0}{\hbar}\left(c_{j+1}^+ c_j - c_j^+ c_{j+1} + c_{j-1}^+ c_j - c_j^+ c_{j-1}\right) \end{aligned} \tag{B.83}$$

where we have used the commutation rules for fermions, and we identify

$$I_A = \frac{\mathrm{i}et_0}{\hbar}\left(c_{j+1}^+ c_j - c_j^+ c_{j+1}\right) \qquad I_B = \frac{\mathrm{i}et_0}{\hbar}\left(c_{j-1}^+ c_j - c_j^+ c_{j-1}\right) \tag{B.84}$$

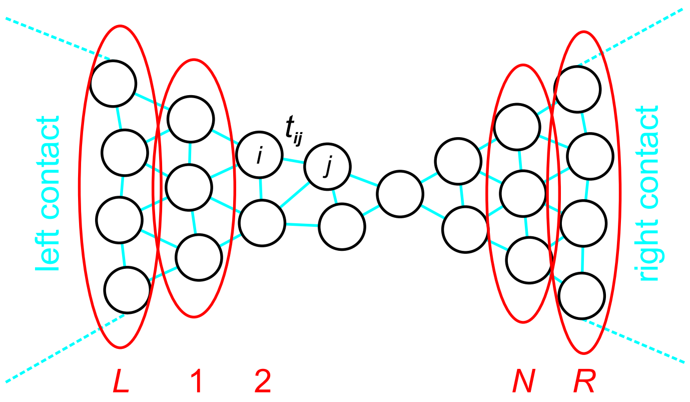

Figure B.3: Channel consisting of N planes between left and right contact. In analogy with [46, Figure E.1].

as these terms involve the adjacent sites of intersection A and B.

Generalizing, the operator of an electrical current from sites of a plane L to sites of a neighboring plane 1 (cf. Figure B.3) reads

$$I(t) = \frac{\mathrm{i}e}{\hbar} \sum_{\substack{i \in L \\ j \in 1}} t_{ij} [c_i^+(t) c_j(t) - c_j^+(t) c_i(t)] \tag{B.85}$$

and its expectation value, using (B.63),

$$\langle I(t) \rangle = \frac{e}{\hbar} \sum_{\substack{i \in L \\ j \in 1}} t_{ij} \left[G_{ji}^{+-}(t,t) - G_{ij}^{+-}(t,t) \right] \tag{B.86}$$

which, in the stationary case can be Fourier transformed yielding

$$\langle I \rangle = \frac{e}{\hbar} \sum_{\substack{i \in L \\ j \in 1}} t_{ij} \int \frac{\mathrm{d}E}{2\pi} \left[G_{ji}^{+-}(E) - G_{ij}^{+-}(E) \right] \tag{B.87}$$

Equivalently we can write

$$\langle I \rangle = \frac{e}{h} \int \mathrm{d}E \, \mathrm{Tr}[G_{1L}^{+-}(E) t_{L1} - t_{1L} G_{L1}^{+-}(E)] \tag{B.88}$$

where t_{1L} is the matrix $(t_{ij})_{i \in 1, j \in L}$.

Now, considering the coupling to the contacts as perturbation, and $\Sigma^{+-} = 0$ (no interaction within the channel), using (B.78) and (B.79), we replace

$$G_{1L}^{+-} = G_{11}^{+-} t_{1L} g_{LL}^a + G_{11}^r t_{1L} g_{LL}^{+-} \tag{B.89}$$

$$G_{L1}^{+-} = g_{LL}^{+-} t_{L1} G_{11}^a + g_{LL}^r t_{L1} G_{11}^{+-} \tag{B.90}$$

and using $G^{+-} - G^{-+} = G^a - G^r$ and (2.9) we rewrite (B.88) as

$$\langle I \rangle = \frac{e}{h} \int \mathrm{d}E \, \mathrm{Tr}[G_{1N}^r t_{NR} 2\mathrm{iIm}\{g_{LL}^a\} t_{RN} G_{N1}^a t_{1L} 2\mathrm{iIm}\{g_{LL}^a\} t_{L1}] (f_L(E) - f_R(E)) \tag{B.91}$$

$$= \frac{e}{h} \int \mathrm{d}E T(E) (f_L(E) - f_R(E)) \tag{B.92}$$

---

[6] Use $(AB \cdots YZ)^{+-} = A^{+-} B^a \cdots Z^a + A^r B^{+-} C^a \cdots Z^a + \cdots + A^r \cdots Y^r Z^{+-}$.

and arrive again at the Landauer-Büttiker formula (2.46), identifying

$$T(E) = 4\,\mathrm{Tr}[G^r_{1N}\mathrm{Im}\{\Sigma_R\}G^a_{N1}\mathrm{Im}\{\Sigma_L\}] \tag{B.93}$$

where

$$\Sigma_L = t_{1L}g^a_{LL}t_{L1} \quad \text{and} \quad \Sigma_R = t_{NR}g_{RR}t_{RN} \tag{B.94}$$

C Derivation of equations (4.48) and (4.49)

In this appendix we will derive the equations (4.48) and (4.49), i.e. the average number of odd and even distances between occupied sites on a lattice ring. The solution was found with help of [190].

In order to obtain formulae with the same nomenclature as in Chapter 4, we consider the following setup (cf. Figure C.1). A ring with $N+1$ sites the first of which is always occupied. The other sites are occupied according to a probability p, or unoccupied. What we are looking for is the average number of odd and even distances between neighboring occupied sites, where distance is defined as the number of unoccupied sites between two occupied sites. If there is no unoccupied site between two occupied sites, we count the distance as even.

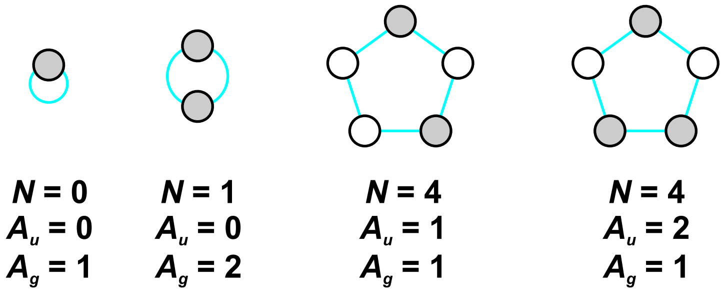

Figure C.1: Different realizations of a ring with $N = 0, 1,$ and 4. A_u and A_g are the numbers of odd and even distances in these concrete configurations.

The solution to this problem is found with the Matrix product ansatz. We represent a configuration $(1, \tau_1, \dots, \tau_N)$, $\tau_i = 0, 1$, of the ring by the matrix product

$$\mathcal{P}(1, \tau_1, \dots, \tau_N) = \mathrm{Tr}[D \prod_{\mu=1}^{N} \{\tau_\mu D + (1-\tau_\mu)E\}] \tag{C.1}$$

where the matrices

$$D = \begin{pmatrix} y & x \\ 0 & 0 \end{pmatrix} \qquad \text{and} \qquad E = \begin{pmatrix} 0 & 1 \\ 1 & 0 \end{pmatrix} \tag{C.2}$$

represent occupied and empty sites of the ring. The definition of the matrices is chosen such that

$$E^{2n} = \begin{pmatrix} 1 & 0 \\ 0 & 1 \end{pmatrix} \qquad E^{2n+1} = E = \begin{pmatrix} 0 & 1 \\ 1 & 0 \end{pmatrix} \tag{C.3}$$

$$DE^{2n} = D = \begin{pmatrix} y & x \\ 0 & 0 \end{pmatrix} \qquad DE^{2n+1} = DE = \begin{pmatrix} x & y \\ 0 & 0 \end{pmatrix} \tag{C.4}$$

i.e. the $(1,1)$ component of DE^j indicates whether the number j of consecutive empty sites behind a occupied one is odd or even. With (C.3) and (C.4), the matrix product for any given configuration can be calculated, e.g. the third in Figure C.1 reads

$$\begin{aligned}\mathcal{P}(1,0,1,0,0) &= \mathrm{Tr}\,[DEDEE] = \mathrm{Tr}\left[\begin{pmatrix} x & y \\ 0 & 0\end{pmatrix}\begin{pmatrix} y & x \\ 0 & 0\end{pmatrix}\right] \\ &= xy\end{aligned} \tag{C.5}$$

and for the fourth example in Figure C.1

$$\mathcal{P}(1,0,1,1,0) = x^2 y \tag{C.6}$$

We see that in the matrix product of a configuration, the exponent of x indicates the number of odd distances, and the exponent of y the one of even distances in this configuration.

Now we consider the so-called partition function of the matrix product

$$Z_N(x,y) = \mathrm{Tr}[D\underbrace{(pD+(1-p)E)^N}_{\equiv C^N}] \tag{C.7}$$

where

$$C = \begin{pmatrix} py & px+1-p \\ 1-p & 0\end{pmatrix} \equiv \begin{pmatrix} a & b \\ c & 0\end{pmatrix} \tag{C.8}$$

As it is defined, the partition function is the sum of all combinatorially possible matrix products $\mathcal{P}$, weighted by their respective probability. Thus we find

$$\langle A_u(N)\rangle = \partial_x Z_N(x,y)|_{x=y=1} \tag{C.9}$$

$$\langle A_g(N)\rangle = \partial_y Z_N(x,y)|_{x=y=1} \tag{C.10}$$

a way to calculate the desired averages. The only missing step is the evaluation of the partition function. This can be done by diagonalizing C.

$$C = PJP^{-1} \quad \Leftrightarrow \quad J = P^{-1}CP \quad \Rightarrow \quad C^N = PJ^NP^{-1} \tag{C.11}$$

where

$$J = \begin{pmatrix} \lambda_+ & 0 \\ 0 & \lambda_-\end{pmatrix} \tag{C.12}$$

is the diagonal form of C

$$\lambda_\pm = \frac{a \pm \sqrt{a^2+4bc}}{2} = \frac{py \pm \sqrt{p^2y^2+4(1-p)\,[px+1-p]}}{2} \tag{C.13}$$

are the eigenvalues, and

$$P = \frac{1}{\sqrt{a^2+4bc}}\begin{pmatrix} \lambda_+ & -\lambda_- \\ c & c\end{pmatrix} \qquad P^{-1} = \begin{pmatrix} 1 & -\lambda_-/c \\ 1 & -\lambda_+/c\end{pmatrix} \tag{C.14}$$

the transformation matrices. Knowing the diagonal representation of C, we find

$$\begin{aligned} Z_N &= \mathrm{Tr}\left[DPJ^NP^{-1}\right] = \mathrm{Tr}\left[P^{-1}DP\begin{pmatrix} \lambda_+^N & 0 \\ 0 & \lambda_-^N\end{pmatrix}\right] \\ &= \mathrm{Tr}\left[\frac{1}{\sqrt{a^2+4bc}}\begin{pmatrix} y\lambda_+ + xc & -(y\lambda_- + xc) \\ y\lambda_+ + xc & -(y\lambda_- + xc)\end{pmatrix}\begin{pmatrix} \lambda_+^N & 0 \\ 0 & \lambda_-^N\end{pmatrix}\right] \\ &= \frac{[y\lambda_+ + (1-p)x]\,\lambda_+^N - [y\lambda_- + (1-p)x]\,\lambda_-^N}{\lambda_+ - \lambda_-}\end{aligned} \tag{C.15}$$

Inserting the last line (C.15) into (C.9) and (C.10) we find with help of Maple

$$\langle A_u(p,N)\rangle = \frac{2\,(1-p)^2\,[1-(p-1)^N] + pN\,(1-p)\,(2-p)}{(2-p)^2} \tag{C.16}$$

$$\langle A_g(p,N)\rangle = \frac{2-p^2+pN\,(2-p)+2\,(1-p)^2\,(p-1)^N}{(2-p)^2} \tag{C.17}$$

These are just the equations (4.48) and (4.49) which were to derive.

Bibliography

[1] A. Abrikosov, L. Gorkov, and I. Dzyaloshinski. *Methods of quantum field theory in statistical physics*. Dover, 1963.

[2] C. J. Adkins. Conduction in granular metals–variable-range hopping in a Coulomb gap? *J. Phys. Condens. Matter*, 1:1253–1259, 1989.

[3] E. Akkermans and G. Montambaux. *Mesoscopic Physics of Electrons and Photons*. Cambridge University Press, 2007.

[4] B. Altshuler, A. Aronov, M. Gershenson, and Y. Sharvin. Quantum effects in disordered metal films. *Sov. Sci. Rev., Sect. A*, 39:223–354, 1987.

[5] M. G. Ancona, W. Kruppa, R. W. Rendell, A. W. Snow, D. Park, and J. B. Boos. Coulomb blockade in single-layer Au nanocluster films. *Phys. Rev. B*, 64:033408, 2001.

[6] P. W. Anderson. Absence of diffusion in certain random lattices. *Phys. Rev.*, 109:1492–1505, 1958.

[7] T. Ando. Theory of electronic states and transport in carbon nanotubes. *J. Phys. Soc. Jpn.*, 74:777–817, 2005.

[8] N. W. Ashcroft and N. D. Mermin. *Solid State Physics*. Saunders College, 1976.

[9] M. Y. Azbel, A. Hartstein, and D. DiVincenzo. T dependence of the conductance in quasi one-dimensional systems. *Phys. Rev. Lett.*, 52:1641–1644, 1984.

[10] I. Balberg, E. Savir, J. Jedrzejewski, A. Nassiopoulou, and S. Gardelis. Fundamental transport processes in ensembles of silicon quantum dots. *Phys. Rev. B*, 75:235329, 2007.

[11] R. N. Barnett, C. L. Cleveland, A. Joy, U. Landman, and G. B. Schuster. Charge migration in DNA: Ion-gated transport. *Science*, 294:567–571, 2001.

[12] T. Baron, P. Gentile, N. Magnea, and P. Mur. Single-electron charging effect in individual Si nanocrystals. *Appl. Phys. Lett.*, 79:1175–1177, 2001.

[13] A. V. Barzykin and M. Tachiya. Mechanism of charge recombination in dye-sensitized nanocrystalline semiconductors: Random flight model. *J. Phys. Chem. B*, 106:4356–4363, 2002.

[14] C. Beenakker. Theory of Coulomb-blockade oscillations in the conductance of a quantum dot. *Phys. Rev. B*, 44:1646–1656, 1991.

[15] C. W. Beenakker. Random-matrix theory of quantum transport. *Rev. Mod. Phys.*, 69:731–808, 1997.

[16] I. Beloborodov, A. Lopatin, V. Vinokur, and K. Efetov. Granular electronic systems. *Rev. Mod. Phys.*, 79:469–518, 2007.

[17] G. Bergmann. Weak localization in thin films. *Phys. Rep.*, 107:1–58, 1984.

[18] J. Bernholc, D. Brenner, M. Buongiorno Nardelli, V. Meunier, and C. Roland. Mechanical and electrical properties of nanotubes. *Annu. Rev. Mater. Res.*, 32:347–375, 2002.

[19] C. A. Berven and M. N. Wybourne. Effect of self-capacitance on the tunneling thresholds in linear arrays of nanoparticles. *Appl. Phys. Lett.*, 78:3893–3895, 2001.

[20] K. C. Beverly, J. F. Sampaio, and J. R. Heath. Effects of size dispersion disorder on the charge transport in self-assembled 2-d Ag nanoparticle arrays. *J. Phys. Chem. B*, 106:2131–2135, 2002.

[21] K. C. Beverly, J. L. Sample, J. F. Sampaio, F. Remacle, J. R. Heath, and R. D. Levine. Quantum dot artificial solids: Understanding the static and dynamic role of size and packing disorder. *Proc. Natl. Acad. Sci. USA*, 99:6456–6459, Apr 30 2002.

[22] A. Bezryadin, R. M. Westervelt, and M. Tinkham. Self-assembled chains of graphitized carbon nanoparticles. *Appl. Phys. Lett.*, 74:2699–2701, 1999.

[23] F. Bloch. Über die Quantenmechanik der Elektronen in Festkörpern. *Z. Phys.*, 52:555–600, 1928.

[24] I. V. Blonskyy, A. Y. Vakhnin, V. N. Kadan, and A. K. Kadashchuk. New mechanisms of localization of charge carriers in nanosilicon. *Phys. Solid State*, 46(1):45–48, 2004.

[25] M. Blunt, M. Suvakov, F. Pulizzi, C. Martin, E. Pauliac-Vaujour, A. Stannard, A. Rushforth, B. Tadic, and P. Moriarty. Charge transport in cellular nanoparticle networks: Meandering through nanoscale mazes. *Nano Lett.*, 7:855–860, 2007.

[26] H. Böttger and V. V. Bryksin. *Hopping conduction in solids.* VCH, 1985.

[27] H. Bouchiat. Experimental signatures of phase coherent transport. In E. Akkermans, G. Montambaux, J.-L. Pichard, and J. Zinn-Justin, editors, *Mesoscopic Quantum Physics: Proceedings of the Les Houches Summer School, Session LXI, 28 June–29 July 1994*. Elsevier, 1995.

[28] E. Braun, Y. Eichen, U. Sivan, and G. Ben-Yoseph. DNA-templated assembly and electrode attachment of a conducting silver wire. *Nature*, 391:775–778, 1998.

[29] M. Büttiker. Small normal-metal loop coupled to an electron reservoir. *Phys. Rev. B*, 32:1846–1849, 1985.

[30] M. Büttiker. Role of quantum coherence in series resistors. *Phys. Rev. B*, 33:3020–3026, 1986.

[31] F. D. Buzatu and G. Jackeli. Alternating chain with Hubbard-type interactions: Renormalization group analysis. *Phys. Lett. A*, 246:163–171, 1998.

[32] M. Büttiker. Coherent and sequential tunneling in series barriers. *IBM J. Res. Dev.*, 32(1):63–75, 1988.

[33] M. Büttiker. Capacitance, charge fluctuations and dephasing in Coulomb coupled conductors. In R. Haug and H. Schoeller, editors, *Interacting Electrons in Nanostructures*, Lecture Notes in Physics, pages 149–164. Springer, 2001.

[34] C. Caroli, R. Combescot, D. Lederer, P. Nozieres, and D. Saint-James. A direct calculation of the tunnelling current. II. Free electron description. *J. Phys. C*, 4(16):2598–2610, 1971.

[35] C. Caroli, R. Combescot, P. Nozieres, and D. Saint-James. Direct calculation of the tunneling current. *J. Phys. C*, 4(8):916–929, 1971.

[36] C. Caroli, R. Combescot, P. Nozieres, and D. Saint-James. A direct calculation of the tunnelling current: IV. Electron-phonon interaction effects. *J. Phys. C*, 5(1):21–42, 1972.

[37] E. Cauët, D. Dehareng, and J. Lievin. Ab initio study of the ionization of the DNA bases: Ionization potentials and excited states of the cations. *J. Phys. Chem. A*, 110:9200–9211, 2006.

[38] T. Chakraborty, editor. *Charge migration in DNA: Perspectives from Physics, Chemistry & Biology*. Springer, 2007.

[39] J.-C. Charlier, X. Blase, and S. Roche. Electronic and transport properties of nanotubes. *Rev. Mod. Phys.*, 79:677–732, 2007.

[40] J. Chen, L. Yang, H. Yang, and J. Dong. Electronic and transport properties of a carbon-atom chain in the core of semiconducting carbon nanotubes. *Phys. Lett. A*, 316:101–106, 2003.

[41] L. Chico, L. X. Benedict, S. G. Louie, and M. L. Cohen. Quantum conductance of carbon nanotubes with defects. *Phys. Rev. B*, 54:2600–2606, 1996.

[42] L. Chico, V. H. Crespi, L. X. Benedict, S. G. Louie, and M. L. Cohen. Pure carbon nanoscale devices: Nanotube heterojunctions. *Phys. Rev. Lett.*, 76:971–974, 1996.

[43] C.-H. Cho, B.-H. Kim, and S.-J. Park. Room-temperature Coulomb blockade effect in silicon quantum dots in silicon nitride films. *Appl. Phys. Lett.*, 89:013116, 2006.

[44] H. Cohen, C. Nogues, R. Naaman, and D. Porath. Direct measurement of electrical transport through single DNA molecules of complex sequence. *Proc. Natl. Acad. Sci. USA*, 102(33):11589–11593, Aug 16 2005.

[45] R. Combescot. A direct calculation of the tunnelling current. III. Effect of localized impurity states in the barrier. *J. Phys. C*, 4(16):2611–2622, 1971.

[46] J. C. Cuevas. *Electronic transport in normal and superconducting nanocontacts*. PhD thesis, Universidad Autónoma de Madrid, 1999.

[47] J. C. Cuevas, A. Levy Yeyati, and A. Martín-Rodero. Microscopic origin of conducting channels in metallic atomic-size contacts. *Phys. Rev. Lett.*, 80:1066–1069, 1998.

[48] J. C. Cuevas and E. Scheer. *Molecular Electronics.* World Scientific, 2010.

[49] G. Cuniberti, L. Craco, D. Porath, and C. Dekker. Backbone-induced semiconducting behavior in short DNA wires. *Phys. Rev. B*, 65:241314, 2002.

[50] G. Cuniberti, E. Maciá, A. Rodriguez, and R. Römer. Tight-binding modeling of charge migration in DNA devices. In T. Chakraborty, editor, *Charge migration in DNA: Perspectives from Physics, Chemistry & Biology*, NanoScience and Technology, chapter 1, pages 1–20. Springer, 2007.

[51] G. Czycholl and B. Kramer. Nonvanishing zero temperature static conductivity in one dimensional disordered systems. *Solid State Commun.*, 32(11):945–951, 1979.

[52] P. Danielewicz. Quantum theory of nonequilibrium processes, I. *Ann. Phys. (N.Y.)*, 152(2):239–304, 1984.

[53] S. Datta. *Electronic transport in mesoscopic systems.* Cambridge University Press, 1995.

[54] S. Datta. *Quantum Transport: Atom to Transistor.* Cambridge University Press, 2005.

[55] J. L. D'Amato and H. M. Pastawski. Conductance of a disordered linear chain including inelastic scattering events. *Phys. Rev. B*, 41:7411–7420, 1990.

[56] C. Dekker and M. A. Ratner. Electronic properties of DNA. *Physics World*, 14:29–33, Aug 2001.

[57] C. Delerue and M. Lannoo. *Nanostructures.* Springer, 2004.

[58] M. Di Ventra. *Electrical Transport in Nanoscale Systems.* Cambridge University Press, 2008.

[59] M. Di Ventra and M. Zwolak. DNA electronics. In H. S. Nalwa, editor, *Encyclopedia of Nanoscience and Nanotechnology*, volume 2, pages 475–493. American Scientific, 2004.

[60] M. S. Dresselhaus, editor. *Carbon nanotubes. Synthesis, structure, properties and applications.* Springer, 2001.

[61] P. Drude. Zur Elektronentheorie der Metalle. *Ann. Phys. (Leipzig)*, 306(3):566–613, 1900.

[62] E. N. Economou. *Green's functions in quantum physics.* Springer, 1990.

[63] K. B. Efetov. Temperature effects in quantum dots in the regime of chaotic dynamics. *Phys. Rev. Lett.*, 74:2299–2302, 1995.

[64] K. B. Efetov and A. Tschersich. Coulomb effects in granular materials at not very low temperatures. *Phys. Rev. B*, 67:174205, 2003.

[65] A. Efros and B. I. Shklovskii. Coulomb gap and low temperature conductivity of disordered systems. *J. Phys. C*, 8(4):L49–L51, 1975.

[66] K. Elteto, E. G. Antonyan, T. T. Nguyen, and H. M. Jaeger. Model for the onset of transport in systems with distributed thresholds for conduction. *Phys. Rev. B*, 71:064206, 2005.

[67] R. G. Endres, D. L. Cox, and R. R. P. Singh. Colloquium: The quest for high-conductance DNA. *Rev. Mod. Phys.*, 76:195–214, 2004.

[68] D. K. Ferry and S. M. Goodnick. *Transport in Nanostructures.* Cambridge University Press, 1997.

[69] A. L. Fetter and J. D. Walecka. *Quantum theory of many-particle systems.* McGraw-Hill, 1971.

[70] H.-W. Fink and C. Schönenberger. Electrical conduction through DNA molecules. *Nature*, 398:407–410, 1999.

[71] G. W. Ford and R. F. O'Connell. Decoherence without dissipation. *Phys. Lett. A*, 286:87–90, 2001.

[72] M. Galperin, M. A. Ratner, and A. Nitzan. Molecular transport junctions: vibrational effects. *J. Phys. Condens. Matter*, 19:103201, 2007.

[73] M. Gell-Mann and F. Low. Bound states in quantum field theory. *Phys. Rev.*, 84:350–354, 1951.

[74] F. L. Gervasio, P. Carloni, and M. Parrinello. Electronic structure of wet DNA. *Phys. Rev. Lett.*, 89:108102, 2002.

[75] A. W. Ghosh, F. Zahid, S. Datta, and R. R. Birge. Charge transfer in molecular conductors – oxidation or reduction? *Chem. Phys.*, 281:225–230, 2002.

[76] B. Giese, J. Amaudrut, A.-K. Köhler, M. Spormann, and S. Wessely. Direct observation of hole transfer through DNA by hopping between adenin bases and by tunnelling. *Nature*, 412:318–320, 2001.

[77] R. Golizadeh-Mojarad and S. Datta. Nonequilibrium Green's function based models for dephasing in quantum transport. *Phys. Rev. B*, 75:081301, 2007.

[78] I. Gradshteyn and I. Ryzhik. *Table of Integrals, Series, and Products.* Academic Press, Boston, 1980.

[79] R. Gutiérrez, R. A. Caetano, B. P. Woiczikowski, T. Kubar, M. Elstner, and G. Cuniberti. Charge transport through biomolecular wires in a solvent: Bridging molecular dynamics and model Hamiltonian approaches. *Phys. Rev. Lett.*, 102:208102, 2009.

[80] W. A. Harrison. *Elementary electronic structure.* World Scientific, 1999.

[81] J. Henk and W. Schattke. A subroutine package for computing Green's functions of relaxed surfaces by the renormalization method. *Comput. Phys. Commun.*, 77:69–83, 1993.

[82] N. J. Higham and H.-M. Kim. Numerical analysis of a quadratic matrix equation. *IMA J. Numer. Anal.*, 20:499–519, 2000.

[83] N. J. Higham and H.-M. Kim. Solving a quadratic matrix equation by Newton's method with exact line searches. *SIAM Journal on Matrix Analysis and Applications*, 23(2):303–316, 2001.

[84] T. Horiguchi. Lattice Green's function for the simple cubic lattice. *J. Phys. Soc. Jpn.*, 30:1261–1272, 1971.

[85] K. Iguchi. Semiconductivity and band gap of a double strand of DNA. *J. Phys. Soc. Jpn.*, 70:593–597, 2001.

[86] Y. Imry. *Introduction to mesoscopic physics.* Oxford University Press, 2002.

[87] E. Joos, H. Zeh, C. Kiefer, D. Giulini, J. Kupsch, and I.-O. Stamatescu. *Decoherence and the Appearance of a Classical World in Quantum Theory.* Springer, 2003.

[88] L. P. Kadanoff and G. Baym. *Quantum statistical mechanics. Green's function method in equilibrium and non-equilibrium problems.* Benjamin/Cummings, 1962.

[89] A. Kasumov, M. Kociak, S. Guéron, B. Reulet, V. Volkov, D. Klinov, and H. Bouchiat. Proximity-induced superconductivity in DNA. *Science*, 291:280–282, 2001.

[90] T. Kaya. Hamiltonian map approach to 1d Anderson model. *Eur. Phys. J. B*, 67:225–230, 2009.

[91] L. V. Keldysh. Diagram technique for nonequilibrium processes. *Sov. Phys. JETP*, 20(4):1018–1026, 1965.

[92] F. S. Khan, J. H. Davies, and J. W. Wilkins. Quantum transport equations for high electric fields. *Phys. Rev. B*, 36:2578–2597, 1987.

[93] T.-S. Kim and S. Hershfield. Even-odd parity effects in conductance and shot noise of metal–atomic-wire–metal (superconducting) junctions. *Phys. Rev. B*, 65:214526, 2002.

[94] F. Kirchhoff, M. Mehl, N. Papanicolaou, D. Papaconstantopoulos, and F. Khan. Dynamical properties of Au from tight-binding molecular-dynamics simulations. *Phys. Rev. B*, 63:195101, 2001.

[95] C. Kittel. *Introduction to Solid State Physics.* John Wiley & Sons, 8th edition, 2004.

[96] D. Klotsa, R. A. Römer, and M. S. Turner. Electronic transport in DNA. *Biophys. J.*, 89:2187–2198, 2005.

[97] J. König and Y. Gefen. Coherence and partial coherence in interacting electron systems. *Phys. Rev. Lett.*, 86:3855–3858, 2001.

[98] B. Kramer, G. Bergmann, and Y. Bruynseraede, editors. *Localization, Interaction, and Transport Phenomena.* Springer, 1985.

[99] B. Kramer and A. MacKinnon. Localization: theory and experiment. *Rep. Prog. Phys.*, 56:1469–1564, 1993.

[100] B. Kramer and J. Mašek. Influence of the phase coherence length on ballistic transport. *Z. Phys. B*, 76:457–462, 1989.

[101] W. Krolikowski and W. Spicer. Photoemission studies of the noble metals. II. Gold. *Phys. Rev. B*, 1:478–487, 1970.

[102] T. Kubar and M. Elstner. What governs the charge transfer in DNA? The role of DNA conformation and environment. *J. Phys. Chem. B*, 112:8788–8798, 2008.

[103] T. Kubar, P. B. Woiczikowski, G. Cuniberti, and M. Elstner. Efficient calculation of charge-transfer matrix elements for hole transfer in DNA. *J. Phys. Chem. B*, 112:7937–7947, 2008.

[104] S. Kumar, N. Pimparkar, J. Y. Murthy, and M. A. Alam. Theory of transfer characteristics of nanotube network transistors. *Appl. Phys. Lett.*, 88:123505, 2006.

[105] J. König and Y. Gefen. Aharonov-Bohm interferometry with interacting quantum dots: Spin configurations, asymmetric interference patterns, bias-voltage-induced Aharonov-Bohm oscillations, and symmetries of transport coefficients. *Phys. Rev. B*, 65:045316, 2002.

[106] S. Lamba and D. Kumar. Variable-range hopping: Role of Coulomb interactions. *Phys. Rev. B*, 59:4752–4765, 1999.

[107] R. Landauer. Spatial variation of currents and fields due to localized scatterers in metallic conduction. *IBM J. Res. Dev.*, 1(3):223–231, 1957.

[108] R. Landauer. Spatial variation of currents and fields due to localized scatterers in metallic conduction. *IBM J. Res. Dev.*, 32(3):306–316, 1988.

[109] E. Lebanon, A. Schiller, and F. Anders. Coulomb blockade in quantum boxes. *Phys. Rev. B*, 68:041311, 2003.

[110] P. A. Lee and T. V. Ramakrishnan. Disordered electronic systems. *Rev. Mod. Phys.*, 57:287–337, 1985.

[111] F. D. Lewis, X. Liu, J. Liu, S. E. Miller, R. T. Hayes, and M. R. Wasielewski. Direct measurement of hole transport dynamics in DNA. *Nature*, 406:51–53, 2000.

[112] X.-Q. Li and Y. Yan. Electrical transport through individual DNA molecules. *Appl. Phys. Lett.*, 79:2190–2192, 2001.

[113] G. Lindblad. Entropy, information and quantum measurements. *Commun. Math. Phys.*, 33:305–322, 1973.

[114] G. Lindblad. Completely positive maps and entropy inequalities. *Commun. Math. Phys.*, 40:147–151, 1975.

[115] G. Lindblad. On the generators of quantum dynamical semigroups. *Commun. Math. Phys.*, 48:119–130, 1976.

[116] M. López Sancho, J. López Sancho, and J. Rubio. Highly convergent schemes for the calculation of bulk and surface Green functions. *J. Phys. F*, 15(4):851–858, 1985.

[117] P.-O. Löwdin. On the non-orthogonality problem connected with the use of atomic wave functions in the theory of molecules and crystals. *J. Chem. Phys.*, 18:365–375, 1950.

[118] E. Maciá. Charge transfer in DNA: effective Hamiltonian approaches. *Z. Kristallogr.*, 224:91–95, 2009.

[119] G. D. Mahan. Quantum transport equation for electric and magnetic fields. *Phys. Rep.*, 145:251–318, 1987.

[120] G. D. Mahan. *Many-Particle Physics.* Kluwer Academic/Plenum, 2000.

[121] A. K. Mahapatro, K. J. Jeong, G. U. Lee, and D. B. Janes. Sequence specific electronic conduction through polyion-stabilized double-stranded DNA in nanoscale break junctions. *Nanotechnology*, 18:195202, 2007.

[122] P. C. Martin and J. Schwinger. Theory of many-particle systems. I. *Phys. Rev.*, 115:1342–1373, 1959.

[123] A. Martín-Rodero and J. C. Cuevas. *Curso de Doctorado.* Lecture Notes of a course taught at the Universidad Autónoma de Madrid, 2005.

[124] K. Maschke and M. Schreiber. Electron transport along a spatially disordered chain in the presence of dissipation. *Phys. Rev. B*, 49:2295–2305, 1994.

[125] J. C. Mason and D. Handscomb. *Chebyshev Polynomials.* Chapmann & Hall/CRC, 2003.

[126] R. D. Mattuck. *A guide to Feynman diagrams in the many-body problem.* McGraw-Hill, 1967.

[127] H. T. Maune, S.-p. Han, R. D. Barish, M. Bockrath, W. A. Goddard, III, P. W. Rothemund, and E. Winfree. Self-assembly of carbon nanotubes into two-dimensional geometries using DNA origami templates. *Nat. Nanotechnol.*, 5:61–66, 2009.

[128] E. McCann and I. V. Lerner. Mesoscopic conductance fluctuations in dirty quantum dots with single channel leads. *J. Phys. Condens. Matter*, 8:6719–6728, 1996.

[129] E. Meggers, M. E. Michel-Beyerle, and B. Giese. Sequence dependent long range hole transport in DNA. *J. Am. Chem. Soc.*, 120:12950–12955, 1998.

[130] M. J. Mehl and D. A. Papaconstantopoulos. Tight-binding parametrization of first-principles results. In C. Fong, editor, *Topics in Computational Materials Science*, chapter 5, pages 169–213. World Scientific, 1998.

[131] H. Mehrez and M. P. Anantram. Interbase electronic coupling for transport through DNA. *Phys. Rev. B*, 71:115405, 2005.

[132] Y. Meir and N. S. Wingreen. Landauer formula for the current through an interacting electron region. *Phys. Rev. Lett.*, 68:2512–2515, 1992.

[133] G. Metalidis. *Electronic Transport in Mesoscopic Systems.* PhD thesis, Martin-Luther-Universität Halle-Wittenberg, 2007.

[134] A. A. Middleton and N. S. Wingreen. Collective transport in arrays of small metallic dots. *Phys. Rev. Lett.*, 71:3198–3201, 1993.

[135] R. Mills. *Propagators for many-particle systems.* Gordon and Breach Science Publishers, 1969.

[136] N. Mott. Electrons in disordered structures. *Adv. Phys.*, 16(61):49–144, 1967.

[137] N. Mott, M. Pepper, S. Pollitt, R. H. Wallis, and C. J. Adkins. The Anderson transition. *Proc. R. Soc. London, Ser. A*, 345(1641):169–205, Aug 30 1975.

[138] N. Mott and W. Twose. The theory of impurity conduction. *Adv. Phys.*, 10(38):107–163, 1961.

[139] N. F. Mott and E. Davis. *Electronic processes in non-crystalline materials.* Oxford University Press, 1979.

[140] M. B. Nardelli. Electronic transport in extended systems: Application to carbon nanotubes. *Phys. Rev. B*, 60:7828–7833, 1999.

[141] Y. V. Nazarov and Y. M. Blanter. *Quantum Transport.* Cambridge University Press, 2009.

[142] E. Neshataeva, T. Kümmell, G. Bacher, and A. Ebbers. All-inorganic light emitting device based on ZnO nanoparticles. *Appl. Phys. Lett.*, 94:091115, 2009.

[143] H. Onneken. *Leitfähigkeit von selbstorganisierten Eisennanodrähten.* Diplomarbeit, Universität Duisburg-Essen, 2006.

[144] M. Pala and G. Iannaccone. Modeling decoherence effects on the transport properties of mesoscopic devices. *J. Comput. Electron.*, 2:393–396, 2003.

[145] M. G. Pala and G. Iannaccone. Statistical model of dephasing in mesoscopic devices introduced in the scattering matrix formalism. *Phys. Rev. B*, 69:235304, 2004.

[146] D. Porath, A. Bezryadin, S. de Vries, and C. Dekker. Direct measurement of electrical transport through DNA molecules. *Nature*, 403:635–638, 2000.

[147] D. Porath, G. Cuniberti, and R. D. Felice. Charge transport in DNA-based devices. *Top. Curr. Chem.*, 237:183–227, 2004.

[148] W. H. Press, S. A. Teukolsky, W. T. Vetterling, and B. P. Flannery. *Numerical Recipes in C.* Cambridge University Press, 1990.

[149] M. Rafiq, Z. Durrani, H. Mizuta, A. Colli, P. Servati, A. Ferrari, W. Mine, and S. Oda. Room temperature single electron charging in single silicon nanochains. *J. Appl. Phys.*, 103:053705, 2008.

[150] M. Rafiq, Y. Tsuchiya, H. Mizuta, S. Oda, S. Uno, Z. Durrani, and W. Milne. Hopping conduction in size-controlled Si nanocrystals. *J. Appl. Phys.*, 100:014303, 2006.

[151] J. Rammer and H. Smith. Quantum field-theoretical methods in transport theory of metals. *Rev. Mod. Phys.*, 58:323–359, 1986.

[152] M. Ratner. Electronic motion in DNA. *Nature*, 397:480–481, 1999.

[153] E. Rebhan. *Theoretische Physik II.* Spektrum, 2005.

[154] A. Rodríguez, R. A. Römer, and M. S. Turner. Sequence dependence of electronic transport in DNA. *Phys. Status Solidi B*, 243(2):373–377, 2006.

[155] H. E. Romero and M. Drndic. Coulomb blockade and hopping conduction in PbSe quantum dots. *Phys. Rev. Lett.*, 95:156801, 2005.

[156] D. Roy and A. Dhar. Electron transport in a one dimensional conductor with inelastic scattering by self-consistent reservoirs. *Phys. Rev. B*, 75:195110, 2007.

[157] R. Römer and H. Schulz-Baldes. Weak-disorder expansion for localization lengths of quasi-1d systems. *Europhys. Lett.*, 68:247–253, 2004.

[158] M. Schlosshauer. Decoherence, the measurement problem, and interpretations of quantum mechanics. *Rev. Mod. Phys.*, 76:1267–1305, 2005.

[159] M. Schlosshauer. *Decoherence and the Quantum-to-Classical Transition.* Springer, 2007.

[160] G. Schmid, editor. *Nanoparticles.* Wiley-VCH, 2004.

[161] B. B. Schmidt, M. H. Hettler, and G. Schön. Influence of vibrational modes on the electronic properties of DNA. *Phys. Rev. B*, 75:115125, 2007.

[162] B. B. Schmidt, M. H. Hettler, and G. Schön. Nonequilibrium polaron hopping transport through DNA. *Phys. Rev. B*, 77:165337, 2008.

[163] H. R. Schwarz and N. Köckler. *Numerische Mathematik.* Teubner, 2006.

[164] K. Senthilkumar, F. C. Grozema, C. F. Guerra, F. M. Bickelhaupt, F. D. Lewis, Y. A. Berlin, M. A. Ratner, and L. D. A. Siebbeles. Absolute rates of hole transfer in DNA. *J. Am. Chem. Soc.*, 127:14894–14903, 2005.

[165] T. Shigematsu, K. Shimotani, C. Manabe, H. Watanabe, and M. Shimizu. Transport properties of carrier-injected DNA. *J. Chem. Phys.*, 118:4245–4252, 2003.

[166] O. Shoseyov and I. Levy, editors. *NanoBioTechnology.* Humana Press, 2008.

[167] J. C. Slater and G. F. Koster. Simplified LCAO method for the periodic potential problem. *Phys. Rev.*, 94:1498–1524, 1954.

[168] C. A. Stafford and S. Das Sarma. Collective Coulomb blockade in an array of quantum dots: A Mott-Hubbard approach. *Phys. Rev. Lett.*, 72:3590–3593, 1994.

[169] D. Stauffer. *Introduction to percolation theory.* Taylor & Francis, 1985.

[170] T. Stegmann. Diplomarbeit, 2010.

[171] A. D. Stone and P. Lee. Effect of inelastic processes on resonant tunneling in one dimension. *Phys. Rev. Lett.*, 54:1196, 1985.

[172] A. Storm, J. van Noort, and C. Dekker. Insulating behavior for DNA molecules between nanoelectrodes at the 100 nm length scale. *Appl. Phys. Lett.*, 79:3881–3883, 2001.

[173] H. Sugiyama and I. Saito. Theoretical studies of GG-specific photocleavage of DNA via electron transfer: Significant lowering of ionization potential and 5'-localization of HOMO of stacked GG bases in B-form DNA. *J. Am. Chem. Soc.*, 118:7063–7068, 1996.

[174] J. Sée, P. Dollfus, S. Galdin, and P. Hesto. From wave-functions to current-voltage characteristics: overview of a Coulomb blockade device simulator using fundamental physical parameters. *J. Comput. Electron.*, 5:35–48, 2006.

[175] L. Tessieri and F. Izrailev. One-dimensional tight-binding models with correlated diagonal and off-diagonal disorder. *Physica E*, 9:405–417, 2001.

[176] D. Thouless. Electrons in disordered systems and the theory of localization. *Phys. Rep.*, 13:93–142, 1974.

[177] D. J. Thouless. Percolation and localization. In R. Balian, R. Maynard, and G. Toulouse, editors, *Ill-condensed matter: Proceedings of the Les Houches Summer School, Session XXXI, 3 July–18 August 1978*, pages 1–62. North-Holland, 1979.

[178] F. Tremblay, R. J. Jansen, R. Newbury, M. J. Kelly, and G. Hill. Electronic wavefunctions in lightly doped semiconductors, in the presence of strong magnetic fields. *J. Phys. Condens. Matter*, 2:6763–6770, 1990.

[179] I. Turek, V. Drchal, J. Kudrnovský, M. Sob, and P. Weinberger. *Electronic structure of disordered alloys, surfaces and interfaces.* Kluwer Academic, 1997.

[180] H. Uhlig. A toolkit for analyzing nonlinear dynamic stochastic models easily. In R. Marimon and A. Scott, editors, *Computational Methods for the Study of Dynamic Economies*, chapter 3, pages 30–61. Oxford University Press, 1999.

[181] L. Van Hove. The occurrence of singularities in the elastic frequency distribution of a crystal. *Phys. Rev.*, 89:1189–1193, 1953.

[182] D. Voet and J. G. Voet. *Biochemistry.* John Wiley & Sons, 3rd edition, 2004.

[183] A. A. Voityuk, J. Jortner, M. Bixon, and N. Rosch. Electronic coupling between watson–crick pairs for hole transfer and transport in desoxyribonucleic acid. *J. Chem. Phys.*, 114:5614–5620, 2001.

[184] A. A. Voityuk, J. Jortner, M. Brixon, and N. Rösch. Energetics of hole transfer in DNA. *Chem. Phys. Lett.*, 324:430–434, 2000.

[185] A. A. Voityuk, N. Rosch, M. Bixon, and J. Jortner. Electronic coupling for charge transfer and transport in DNA. *J. Phys. Chem. B*, 104:9740–9745, 2000.

[186] H. Watanabe, C. Manabe, T. Shigematsu, K. Shimotani, and M. Shimizu. Single molecule DNA device measured with triple-probe atomic force microscope. *Appl. Phys. Lett.*, 79:2462–2464, 2001.

[187] J. Watson and F. Crick. A structure for deoxyribose nucleic acid. *Nature*, 171:737–738, 1953.

[188] J. Wei and K. Chan. Charge transport in polyguanine-polycytosine DNA molecules. *J. Phys. Condens. Matter*, 19:286101, 2007.

[189] G. C. Wick. The evaluation of the collision matrix. *Phys. Rev.*, 80:268–272, 1950.

[190] M. Wölki. Private communication, Dec. 2009.

[191] B. Xu, P. Zhang, X. Li, and N. Tao. Direct conductance measurement of single DNA molecules in aqueous solution. *Nano Lett.*, 4:1105–1108, 2004.

[192] H. Yamani and M. Abdelmonem. The analytic inversion of any finite symmetric tridiagonal matrix. *J. Phys. A*, 30:2889–2893, 1997.

[193] J. Yi. Analytic study of charge tunneling through DNA under dissipation. *Phys. Rev. B*, 77:193109, 2008.

[194] K.-H. Yoo, D. H. Ha, J.-O. Lee, J. W. Park, J. Kim, J. J. Kim, H.-Y. Lee, T. Kawai, and H. Y. Choi. Electrical conduction through poly(dA)-poly(dT) and poly(dG)-poly(dC) DNA molecules. *Phys. Rev. Lett.*, 87:198102, 2001.

[195] D. Yu, C. J. Wang, B. L. Wehrenberg, and P. Guyot-Sionnest. Variable range hopping conduction in semiconductor nanocrystal solids. *Phys. Rev. Lett.*, 92:216802, 2004.

[196] H. Zhang, X.-Q. Li, P. Han, X. Y. Yu, and Y. Yan. A partially incoherent rate theory of long-range charge transfer in deoxyribose nucleic acid. *J. Chem. Phys.*, 117:4578–4584, 2002.

[197] H. Zheng, Z. Wang, Q. Shi, X. Wang, and J. Chen. Statistical model for analyzing the dephasing effects in a one-dimensional scattering chain. *Phys. Rev. B*, 74:155323, 2006.

[198] C. Zhou and R. N. Bhatt. One-dimensional chain with random long-range hopping. *Phys. Rev. B*, 68:045101, 2003.

[199] M. Zilly, O. Ujsághy, and D. E. Wolf. Statistical model for the effects of dephasing on transport properties of large samples. *Eur. Phys. J. B*, 68:237–246, 2009.

[200] J. M. Ziman. Localization of electrons in ordered and disordered systems II. Bound bands. *J. Phys. C*, 2(7):1230–1247, 1969.

[201] J. M. Ziman. *Principles of the theory of solids.* Cambridge University Press, 1972.

[202] J. M. Ziman. *Models of disorder.* Cambridge University Press, 1979.

[203] W. H. Zurek. Decoherence, einselection, and the quantum origins of the classical. *Rev. Mod. Phys.*, 75:715–775, 2003.

Zusammenfassung

Die vorliegende Arbeit befasst sich mit kohärentem Quantentransport in linearen System und wie er durch Dekohärenz beieinflusst wird. Daher wird nach der Einführung in Kapitel 2 eine kurzer Abriss des verwendeten Quantentransport-Formalismus gegeben.

In Kapitel 3 wird der kohärente Transport in linearen und quasilinearen Tight-binding-Systemen untersucht. Dazu werden verschiedene Methoden zur Berechnung der (Oberflächen-)Greenfuntionen vorgestellt. Die Greenfunktionen geben Aufschluss über die totale und lokale (Oberflächen-)Zustandsdichte und werden für die Modellierung von Kontakten benötigt. Weiterhin werden die Symmetrien der betrachteten Hamilton-Operatoren und deren Einfluss auf die Transmission durch Defekte untersucht. Ein Beispiel ist die reflexionslose Kopplung eines Doppelketten-artigen Defekts an zwei topologisch verschiedene halbunendliche Doppelketten. Außerdem wird die Transmission durch endliche Tight-binding-Ketten untersucht. Ohne Unordnung weist die Transmissionsfunktion Maxima bei den Eigenenergien des zugrundeliegenden Tight-binding-Systems auf. Für Energien außerhalb des Eigenenergie-Spektrums fällt die Transmission exponentiell mit der Länge ab, d.h. die Kette verhält sich wie eine Tunnelbarriere für einlaufende Elektronen. Innerhalb des Eigenenergie-Spektrums ist die Transmissionsfunktion periodisch in der Systemlänge. Formeln zur Periodizität, den Infima und Suprema der Transmissionsfunktion werden angegeben. Zum Abschluss des Kapitels 3 werden ungeordnete Tight-binding-Ketten untersucht, für die die Transmission, wie erwartet für Systeme mit Anderson-Lokalisierung, exponentiell mit der Länge abfällt.

Kapitel 4 enthält den Kern dieser Dissertation, die Beschreibung des statistischen Modells für die Effekte von Dekohärenz auf das Transportverhalten großer Systeme. Ein großes System wird in Regionen kohärenten Transport und Dekohärenzregionen unterteilt. Diesen werden Elektronenenenergie-Verteilungsfunktionen zugeordnet, die untereinander durch Übergangsraten verknüpft sind, die aus dem kohärenten Transport-Formalismus ermittelt werden. Für lineare System zerfällt das Gesamtsystem durch Einfügen von Dekohärenz-Regionen (Dekohärenz-Sites im besprochenen Beispiel) in Untersysteme, die quantenmechanisch nicht miteinander interferieren. Aus den Ratengleichungen ergibt sich für lineare Systeme, dass sich der Widerstand jeder Dekohärenz-Konfiguration additiv aus den Widerständen der Subsysteme zusammensetzt. Am Beispiel linearer Tight-binding-Ketten ohne und mit diagonaler Unordnung werden die Dekohärenz-Effekte auf den Transport untersucht. Für den Fall ohne Unordnung ergibt sich, dass der Widerstand $1/\langle G\rangle$ [1] den ohmschen Limes (Widerstand proportional zur Systemlänge) für alle Kontakt-Fermienergien μ, die innerhalb des von den Eigenenergien des Tight-binding-Bands der Kette liegen, erreicht. Für Fermi-Energien außerhalb des Bandes gibt es eine kritische Dichte p^* von Dekohärenz-Sites, jenseits derer der ohmsche Limes erreicht wird. Für $p < p^*$ hingegen

---

[1] Der Leitwert des Systems wird über statistisch unabhängige Dekohärenz-Konfigurationen gemittelt.

dominiert der Einfluss der Subsysteme als Tunnelbarrieren und der Gesamt-Widerstand nimmt überlinear zu. Analog ergibt sich auch für ungeordnete Systeme eine kritische Dekohärenzsite-Dichte p^*_{disorder}, ab der ohmsches Verhalten für große Systeme erreicht wird, obwohl die Subsysteme wegen Lokalisierung exponentiell anwachsende Einzelwiderstände aufweisen. Der spezifische Widerstand kann, falls ohmsches Verhalten erreicht wird, als Reihe dargestellt werden. Kriterien für deren Konvergenz werden angegeben.

In Kapitel 5 wird das statistische Modell für Dekohärenzeffekte auf DNA-Doppelstränge angewandt. Tight-binding-Modelle für DNA-Moleküle werden vorgestellt. Für die Kontakte zu und die Dekohärenz-Regionen in DNA-Doppelsträngen werden jeweils drei Modelle eingeführt. Unter Verwendung von Energieparamtern aus der Literatur und durch geeigneter Wahl der Parameter der hier vorgestellten Modelle können experimentelle Ergebnisse qualitativ und auf die Größenordnung genau quantitativ reproduziert werden.

Danke

Zu guter Letzt möchte ich danke sagen.

An erster Stelle danke ich Herrn Professor Dietrich Wolf für die Ermöglichung dieser Doktorarbeit an seinem Lehrstuhl, für die zahlreichen Diskussionen, die zur Entstehung des hier vorgestellten Modells beigetragen haben und für die Ermöglichung sehr fruchtbarer Auslandsaufenthalte und Konferenzteilnahmen.

Orsolya Újsághy danke ich ganz besonders für die gemeinsame Arbeit an dem Modell, für viele inspirierende Diskussionen, ihre Gastfreundschaft in Budapest und zahlreiche Anmerkungen zum vorliegenden Text.

Carlos Cuevas von der Universidad Autónoma de Madrid und Supriyo Datta von der Purdue University in West Lafayette danke ich für ihre Gastfreundschaft bei meinen Auslandsaufenthalten und für vieles, das ich von ihnen lernen konnte.

Weiterhin danke ich:

Professor Markus Winterer, dem Sprecher des Graduiertenkollegs “Nanotronics”, in das meine Doktorarbeit eingegliedert ist, für die Organisation der Spring Courses, International Workshops und der Ringvorlesung. Ihm und Monika Lünsmann danke ich für Hilfestellungen zu organisatorischen Fragen insbesondere bezüglich der Auslandsaufenthalte.

André Ebbers und der Evonik-Degussa für die Zusammenarbeit mit dem Graduiertenkolleg und die Summerschools in Marl.

Alfred Zawadowski für kritische Fragen zum Modell und Gastfreundschaft in Budapest.

Marko Wölki für den Anstoß zu Anhang C und einige Anmerkungen zum Text.

Lothar Brendel für stete Hilfsbereitschaft zu Computerfragen und physikalische Diskussionen.

Thomas Stegmann für seine Anmerkungen zum Text.

Meinen Kollegen aus dem Graduiertenkolleg und aus der Arbeitsgruppe Wolf für zahlreiche physikalische und nicht-physikalische Gespräche.

Nicht zuletzt möchte ich mich bei meinen Eltern, Brüdern und meiner lieben Frau für ihre Unterstützung und Motivation während meiner Doktorarbeit herzlich bedanken.

Erklärung

Ich versichere, dass ich die von mir vorgelegte Dissertation selbständig angefertigt, die benutzten Quellen und Hilfsmittel vollständig angegeben und die Stellen der Arbeit – einschließlich der Abbildungen –, die anderen Werken im Wortlaut oder dem Sinn nach entnommen sind, in jedem Einzelfall als Entlehnung kenntlich gemacht habe; dass diese Dissertation noch keiner anderen Fakultät oder Universität zur Prüfung vorgelegen hat; dass sie – abgesehen von unten angegebenen Teilpublikationen – noch nicht veröffentlicht worden ist sowie, dass ich eine solche Veröffentlichung vor Abschluss des Promotionsverfahrens nicht vornehmen werde. Die Bestimmungen dieser Promotionsordnung sind mir bekannt. Die von mir vorgelegte Dissertation ist von Herrn Professor Dr. Dietrich Wolf betreut worden.

Duisburg, den 26. Februar 2010

Teilpublikation

M. Zilly, O. Ujsághy, and D. E. Wolf. Statistical model for the effects of dephasing on transport properties of large samples. *Eur. Phys. J. B*, 68:237–246, 2009.

Lebenslauf

Persönliche Daten

Name:	Matías Zilly
Geburtsdatum:	01.03.1979
Geburtsort:	Mülheim an der Ruhr
Familienstand:	verheiratet, eine Tochter

Schulbildung

1985 – 1989	Landwehrschule (Grundschule), Oberhausen
1989 – 1998	Heinrich-Heine-Gymnasium, Oberhausen, Abitur

Zivildienst

1998 – 1999	Sozialdienst im Haus Alexandra (Altenpflegeheim), Oberhausen

Hochschulstudium

Okt. 1998 – Sept. 1999	FiPS (Früheinstieg ins Physik-Studium), Fernstudium an der Universität Kaiserslautern
Okt. 1999	Immatrikulation an der Gerhard-Mercator Universität Duisburg
Sept. 2001	Vordiplom Physik
Apr. 2004 – März 2005	Diplomarbeit “Algorithms for Optical Measurement of Granular Matter” bei Prof. Dr. D. Wolf in Kooperation mit Fa. Retsch Technology
März 2005	Diplom-Physiker
Seit April 2005	Doktorarbeit bei Prof. Dr. D. Wolf im Graduiertenkolleg 1240 “Nanotronics” in Kooperation mit Fa. Evonik-Degussa

Gastaufenthalte

Okt. – Dez. 2005	Bei Carlos Cuevas (Universidad Autónoma de Madrid, Spanien)
Dez. 2007 – März 2008	Bei Supriyo Datta (Purdue University, West Lafayette, USA)
Nov. 2009	Bei Orsolya Újsághy (Budapest University of Technology and Economics, Ungarn)

Beschäftigungsverhältnisse

1999 – 2005	Werkstudent bzw. Studentische Hilfskraft bei Prof. Dr. D. Wolf (Computational Physics) und Prof. Dr. M. Schreckenberg (Physik von Transport und Verkehr)
Seit Juni 2005	Wissenschaftlicher Mitarbeiter am Lehrstuhl für Computational Physics